LIÈGE université
Sciences Appliquées

SAFRAN
SAFRAN AERO BOOSTERS

Assessment of a Viscous Through-Flow Model for Predicting the Effects of Geometric Variability on the Performance of Modern Low-Pressure Compressors

Thesis submitted in partial fulfillment of the requirements for the degree of Doctor of Philosophy (PhD) in Engineering Science

by

Arnaud BUDO

Supervisor: Vincent E. TERRAPON

Co-supervisor: Koen HILLEWAERT

DOCTORAL COLLEGE IN AEROSPACE AND MECHANICS

2026

Examination committee:

Prof. Vincent E. Terrapon, University of Liège (supervisor)
Prof. Koen Hillewaert, University of Liège (co-supervisor)
Prof. Boyan Mihaylov, University of Liège (president)
Prof. Maarten Arnst, University of Liège
Dr. Xavier Ottavy, Ecole centrale de Lyon
Dr. Vincent Valentin, Safran Aero Boosters
Dr. Armandojanni Petrucci Orefice, Safran Tech

Department of Aerospace and Mechanical Engineering, University of Liège
Academic Year 2025-2026

This work is jointly funded by the Walloon region, under grant no. 7900, Safran Aero Boosters in the frame of the project MARIETTA, and the University of Liège. The present research benefited from software made available by Safran Tech, Safran Aero Boosters and Onera.

"All we have to decide is what to do with the time that is given us."

J. R. R. Tolkien

Abstract

An important question for turbomachine designers is how to deal with blade and flowpath geometric variabilities stemming from the manufacturing process or erosion during the component lifetime. The challenge consists in identifying where stringent manufacturing tolerances are absolutely necessary and where looser tolerances can be used, as some geometric variations have little or no effects on performance, while others do have a significant impact. Because numerical simulations based on Reynolds Averaged Navier-Stokes (RANS) equations are computationally expensive for a stochastic analysis, an alternative approach is proposed, in which these simulations are complemented by cheaper through-flow (TF) simulations to provide a finer exploration of the range of variations, in particular in a context of robust design. The overall goal of the present study is to evaluate the adequacy of a viscous time-marching TF solver to predict geometric variability effects on compressor performance and, in particular, to capture the main trends. Although the computational efficiency of such a low-fidelity solver is useful for parametric studies, it is known that the involved assumptions and approximations associated with the TF approach introduce errors in the performance prediction. Thus, the model is first evaluated with respect to its underlying assumptions and correlations. To do so, TF simulations are compared to RANS simulations applied to the CME2 compressor stage and a modern low-pressure compressor designed by Safran Aero Boosters. On the one hand, the TF simulations are fed with the exact radial distribution of the correlation parameters using RANS input data in order to isolate the modeling error from correlation empiricism. Moreover, in the context of multi-fidelity optimisation, such distributions can be predicted using the more detailed RANS simulations which are performed on selected operating points. On the other hand, correlations from the literature are assessed and improved. It is shown that the solver provides realistic predictions of performance but is highly sensitive to the underlying correlations. Then, two modeling aspects linked to the blade leading edge, namely the incidence correction and the camber line computation, are discussed. As geometric variability precisely at the blade leading edge has a significant impact on the performance, we assess how these two aspects influence the variability propagation in this region. Moreover, we propose a strategy to mitigate these model uncertainties. Finally, within the scope of this preliminary study, the perturbations are introduced in the low-pressure compressor through variations in blade angle, blade thickness, rotor tip clearance, three-dimensional positioning of the undeformed blades, and hub and shroud contour deformations. Their range is defined based on the tolerance limits typically imposed in the industry and on observed manufacturing variability. It is found that the TF model can broadly provide realistic predictions of performance variations resulting from the imposed geometric variations, although several limitations are also identified and discussed. These results are a promising first step towards the use of the through-flow modeling approach for geometric uncertainty quantification.

Acknowledgments

This section is intentionally written in French in order to more directly express my gratitude to the many people who accompanied me throughout this work, although it is impossible to be entirely exhaustive.

"*A PhD is not a sprint, but rather a marathon with occasional sprints in the wrong direction*"

Anonymous

Une thèse de doctorat est une aventure des plus singulières: on accepte d'abord la mission sans en connaître réellement le chemin, ni même la durée. C'est une épreuve où la ténacité est une qualité indispensable. On avance souvent seul face aux doutes et aux questions qui surgissent inévitablement au fil de la recherche. Pourtant, cette aventure n'est jamais tout à fait solitaire. Cette thèse doit ainsi son aboutissement à un grand nombre de personnes. Les quelques mots qui suivent expriment ma sincère gratitude envers celles et ceux qui m'ont accompagné durant cette aventure.

J'ai eu la chance de pouvoir bénéficier, tout au long de ce travail, d'un encadrement à la fois académique et industriel de grande qualité. À l'Université de Liège, je tiens tout d'abord à remercier Vincent Terrapon pour son investissement et sa disponibilité constante tout au long de ces années. Sa confiance, son sens de la rigueur et son exigence scientifique ont été essentiels à la réalisation de ce travail. J'ai énormément appris à ses côtés, tant sur le plan scientifique que sur la manière de structurer, communiquer et diffuser un travail de recherche. J'ai également eu la chance de bénéficier des conseils précieux de Koen Hillewaert, que je tiens à remercier pour ses explications éclairantes et pour les échanges particulièrement enrichissants que nous avons eus autour des turbomachines. Je souhaite également remercier Maarten Arnst de m'avoir accueilli au sein de son équipe de recherche et pour nos échanges autour de la quantification d'incertitude, bien que nous n'ayons pas pu aller aussi loin que nous l'aurions souhaité dans ce domaine.
J'aimerais également remercier les membres de Safran Tech, et plus particulièrement Sophie Mouriaux et Benoit Rodriguez, pour leur aide précieuse lors de la prise en main du code `ASTEC`. Je tiens aussi à remercier Simon Martin pour m'avoir guidé dans l'utilisation des outils de génération géométrique compatibles avec `ASTEC`. Ensuite, j'aimerais remercier Florent Kravtsoff pour l'entraide dont j'ai pu bénéficier grâce à nos échanges autour de nos développements mutuels dans le code `ASTEC`.
De plus, je souhaite exprimer ma gratitude au groupe Safran pour m'avoir offert l'opportunité de tester le modèle développé dans le cadre de cette thèse sur des configurations industrielles réelles, ce qui a largement contribué à enrichir ce travail. En particulier, j'aimerais remercier Jules Bartholet, Stéphane Hiernaux, Gaël Schmetz et Thibault Le Men pour leur aide et leur investissement dans ce projet.

Je te tiens aussi à remercier Xavier Ottavy, Armandojanni Petrucci Orefice, Vincent Valentin et Boyan Mihaylov pour le temps qu'ils ont consacré à la lecture de mon manuscrit.

Cette thèse a également été rythmée par de nombreux allers-retours entre le Bâtiment 52 de l'Université de Liège et Safran Aero Boosters. Je tiens à remercier chaleureusement les équipes des deux côtés pour leur convivialité, les nombreux échanges et l'ambiance de travail particulièrement agréable. Que ce soit lors des discussions durant les temps de midi ou lors de nos sorties en fin de journée, ces moments ont largement contribué à rendre ces années de thèse aussi enrichissantes qu'agréables. Une mention particulière à Amaury B., Paul D., Adrien C., Nayan L. et Thomas G., pour les nombreuses bouffées d'air que nous avons prises ensemble, avec la complicité de ceux qui savent qu'ils naviguent sur la même mer parfois agitée. J'aimerais également remercier Bart Ruis, Camille Dufour, Martin Jolis et Yohan Kulhaneck, pour avoir partagé un petit bout de chemin avec moi sur la voie des modèles méridiens.

Je voudrais aussi remercier ma famille et mes amis, qui ont su m'apporter l'équilibre nécessaire tout au long de ces années. Je pense tout particulièrement à mes parents, qui m'ont accompagné durant toute ma formation et m'ont permis de suivre la voie que j'avais choisie dans les meilleures conditions. À une époque où la poursuite d'études longues n'est toujours pas accessible à tous, je leur suis profondément reconnaissant de m'avoir offert cette opportunité.

"*Il arrive que parfois, très rarement, un monde naît entre deux personnes. Un petit microcosme, dans lequel vous pouvez toujours vous sauver du monde qui s'effondre.*"

H. Arendt

Mes derniers mots vont d'une part à ma femme, qui m'a encouragé tout au long de ces années et qui m'a soutenu malgré les nombreuses difficultés rencontrées sur ce chemin. Sa présence et son soutien indéfectible ont été précieux dans l'aboutissement de ce travail. *Maureen*, merci pour ton amour, ta patience et ton soutien sans faille.
Ces derniers mots vont d'autre part à mon fils, *Mathias*, qui n'a jamais semblé tenir rigueur à son papa de passer tant de temps à rédiger ce manuscrit. Il a pris son mal en patience, notamment en passant des appels vidéo réguliers, ou encore en partageant certaines séances de travail sur mes genoux. Par sa gaieté constante, son amour et sa curiosité, il m'a rappelé chaque jour qu'au-delà du travail et des échéances, il est essentiel de profiter pleinement de chaque instant.
Enfin, j'adresse aussi une pensée toute particulière à une petite étoile qui occupe une place à part dans nos cœurs.

Contents

Nomenclature

Abbreviations

2D	Two-dimensional
3D	Three-dimensional
ASTEC	Aerodynamic Source Terms for Efficient Computations
AVDR	Axial Velocity Density Ratio
CFD	Computational Fluid Dynamics
BET	Blade Element Theory
BFM	Body Force Modeling
CFL	Courant–Friedrichs–Lewy
DNS	Direct Numerical Simulation
DOF	Degree Of Freedom
EoS	Equations of state
FDM	Finite Difference method
FVM	Finite Volume method
FEM	Finite Element method
IBMSG	Immersed Boundary with Smeared Geometry
IGV	Inlet Guide Vane
ISRE	Isentropic Simplified Radial Equilibrium
LE	Leading Edge
LES	Large Eddy Simulation
NS	Navier-Stokes
NIPOD	Non-Intrusive Proper Orthogonal Decomposition
PDF	Probability Density Function
QOI	Quantity Of Interest
RANS	Reynolds Averaged Navier-Stokes
ROI	Return On Investment
RPM	Rotations per minute
SLC	Streamline curvature
TE	Trailing Edge
TF	Through-Flow
UHBR	Ultra High Bypass Ratio

Physical quantities

A	Angle of attack [°]
a	Speed of sound [m s^{-1}]
b	Tangential blockage factor [-]
C_D	Drag coefficient [-]
c	chord [m]
c_p	heat capacity at constant pressure [J kg^{-1} K^{-1}]
c_v	Heat capacity at constant volume [J kg^{-1} K^{-1}]
e	Energy source term [W m^{-3}]
f	Blade force [kg m^{-2} s^{-2}]
E	Internal energy [J kg^{-1}]
H	Enthalpy [J kg^{-1}]
i	Incidence angle [°]
K_{stall}	Stall margin [−]
k	Thermal conductivity [W m^{-1} K^{-1}]
M	Mach number [−]
$\dot{m}$	Mass-flow rate [kg s^{-1}]
N	Number of blades per row [-]
$\mathbf{n}$	vector normal to the mean flow path [−]
q	Heat flux [W m^{-2}]
r_{gas}	Gas constant [J kg^{-1} K^{-1}]
$\mathbb{S}$	Stator row
S	Source terms
s	Entropy [J kg^{-1} K^{-1}]
s_b	Blade pitch [m]
T	Temperature [K]
t_b	Blade thickness [m]
p	Pressure [kg m^{-1} s^{-2}]
$\mathbb{R}$	Rotor row
U/V	Velocity in the relative/absolute frame [m s^{-1}]
W	Local velocity [m s^{-1}]
$w_{s,\mathrm{eff}}$	Effective suction-side height [m]
x, r, θ	Cylindrical coordinates
α	Tangential flow angle [°]
β	Local tangential flow angle [°]
Γ	Circulation [m^2 s^{-1}]
γ	Heat capacity ratio [−]
δ	deviation angle [°]
η	Efficiency [−]
κ	Blade angle [°]

λ	Stagger angle [°]
μ	Dynamic vicosity [kg m^{-1} s^{-1}]
ρ	Density [kg m^{-3}]
π	Total pressure ratio [−]
Π	Total pressure ratio [−]
ϕ	Meridional flow angle [−]
ψ	Stream function [kg s^{-1}]
σ	Solidity [−]
τ	Shear stress [kg m^{-1} s^{-2}]
Ω	Rotation speed of the considered blade row [s^{-1}]
ω	Loss coefficient [−]

Subscripts

b	Blade
cl	Camber line
i, v	Inviscid/viscous
is	Isentropic
in	Inlet
m	Meridional
n	Normal
out	Outlet
p	Parallel
r	Radial
s	Stress
t	Total quantities
U	Relative, i.e. in the relative frame of reference
V	Absolute, i.e. in the absolute frame of reference
W	Local, i.e. in the frame of the considered blade row
x	Axial
θ	Circumferential

Superscripts

$-$	Reynolds average
$'$	Reynolds fluctuation
$\sim$	Favre average
$''$	Favre fluctuation
$*$	Design conditions
a	Passage-to-passage average
c	Circumferential average
e	Ensemble (Reynolds) average
t	Time average

Chapter 1

Introduction

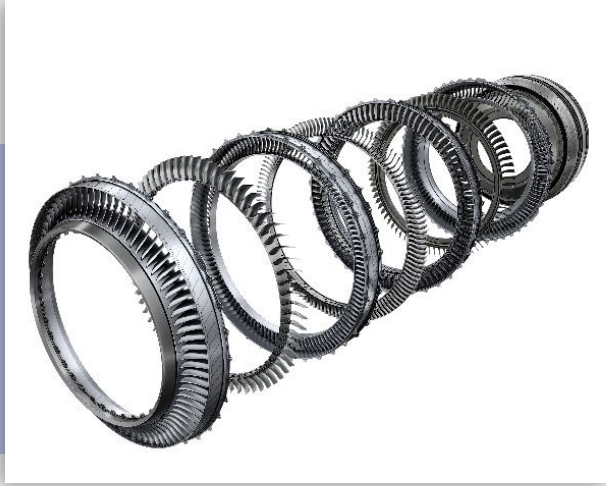

1.1 Context of the aircraft engine market

Global aviation is characterized by significant and sustained growth in the aircraft fleet. Despite the COVID-19 pandemic, which caused widespread order cancellations, production slowdowns, and workforce reductions [184], the recovery of the airline industry has been strong. By 2023, short- and medium-haul capacity exceeded pre-COVID levels from 2019 [164, 177], and the number of flights per year is inevitably increasing. However, this crisis had deep implications for the aircraft industry, leading to unprecedented disruptions and challenges. Aircraft manufacturers, who had adjusted their production to cope with the COVID-19 crisis, are once again increasing production, with an emphasis on resilience to future disruptions and cost-effective solutions.

In addition, environmental concerns have played an increasingly important role in recent years. The global objective of achieving "net zero" carbon emissions by 2050 has intensified efforts to develop more fuel-efficient and lower-emission aircraft. The aeronautics market is thus driven by a continuous quest for enhanced product performance. As a critical component of aviation technology, aircraft engines significantly influence the efficiency and environmental impact of air travel. The demand for new aircraft thereby fuels the need for advanced engines. Competition among various players in this market, such as Rolls-Royce, Pratt & Whitney, General Electric, and Safran, also results in strong pressure on costs. These major players are at the forefront of technological advances and continuously invest in research and development to maintain a competitive advantage. For instance, technological progresses such as the current Ultra High Bypass Ratio (UHBR) engine family, along with other innovative proposals like the renewed interest in the open-rotor concept, are driving the evolution of the aeronautics market.

1.2 The MARIETTA project

One strategy among others to stay competitive is to manage the impact of manufacturing tolerances on the technical and economic performance of both new architectures and operational aircraft engines. The manufacturing tolerance of the axial low-pressure compressor, and in particular of its blade rows, is a good example: blade shape has a high impact on aerodynamic performance while ensuring high geometric accuracy entails a severe manufacturing cost. Most modern compressor blades have traditionally been designed without considering geometric variations although manufactured blades inevitably differ from the nominal geometry due to imperfections, component assembly, or erosion during flight operations. Nonetheless, the impact of geometric variations can induce unacceptable performance variability and a degradation of the mean performance, due to a lack of design robustness [18]. Typically, a blade with an aerodynamic defect can either be scrapped or exempted. Replacing the blade means milling it out and welding a new one, which is expensive but can save the entire assembly. If the defect is in the shroud of a stator row, the inner shroud can be replaced, but if the outer shroud is defective, the entire assembly may have to be scrapped. The decision to exempt or scrap a part is based on manufacturing tolerances which are traditionally set as a compromise between production costs, past experience, and designer requirements. The result of the metrology analysis is usually a map of "out of tolerance" situations. The processing of this metrology data must therefore be referred back to the aerodynamic designer, who must process it directly with standard calculation tools. This requires significant time, cost and human resources, over and above the costs directly associated with repair or replacement. Furthermore, these tolerances are not directly linked to the performance robustness specified by the design criteria. Instead, they are largely empirical, reflecting production capabilities rather than being driven by performance requirements.

Owing to the increasing computational power combined with powerful new numerical techniques for optimization and uncertainty propagation, such questions related to design robustness with respect to manufacturing variability can now be tackled as part of the design process method: recent works [16, 66, 100, 119, 141] on this topic rely on Computational-Fluid-Dynamics (CFD) simulations to propagate variability of the geometry to that of performance, using a Monte-Carlo-based approach. However, most of the work in the literature to date has focused on optimizing the nominal blade geometry for a given set of manufacturing tolerances. One exception is the work of Goodhand et al. [70] and Dow and Wang [53], who demonstrated, in the context of compressor design, that the optimum geometry from a robust design perspective depends on manufacturing tolerances only when a bifurcation in the dominant loss mechanism is observed. To optimize blade performance, the goal is therefore to reduce manufacturing tolerances selectively in the areas of the blade that have the greatest impact on average performance. In this context, the MARIETTA[1] project [170], funded by the Walloon Region and Safran Aero Boosters (SAB), aims to optimize the balance between performance and manufacturing cost by identifying early in the design process where stringent manufacturing tolerances are absolutely necessary and where looser tolerances can be used. This approach can streamline the manufacturing process and simplify the treatment of poorly manufactured parts during quality control while reducing pollution emissions and both manufacturing and operating costs.

The projected return on investment (ROI) is quite significant: based on prior year figures for the target market, Safran Aero Boosters forecasts 38,000 aircraft deliveries to airlines between 2024 and 2043, of which 70% are expected to be medium-haul aircraft (mainly Airbus A320neo and Boeing 737 max) and 20% long-haul aircraft (mainly Airbus A350 and Boeing 777). In terms of market share, this represents an annual production of around 2,000 engines of the various architectures developed by Safran Aero Boosters, including LEAP, GE9X, Passport, etc. The project estimated outcomes include a

[1]MAîtRIsE Technico-économique des Tolérances de fAbrication.

10% reduction in the time spent processing waivers, and a 20% increase in acceptance of parts currently scrapped, i.e., 0.2% of the parts produced. These improvements are expected to yield cumulative cost savings of over €1 million annually.

In practical terms, the project methodology is divided into three steps, as shown in Fig. 1.1. In the characterization phase, the geometrical variabilities are first quantified from blade measurements. Optical measurement techniques, such as structured light or 3D X-ray scanning, are employed to capture deviations of compressor blades from their nominal geometry. This metrological analysis therefore produces a three-dimensional point cloud of the measured blade. The amount of data increases drastically as the number of scanned blades grows, especially given the large sample size required to obtain a statistically valid distribution of the degrees of freedom (DOF). This enormous dataset is thus unusable in its raw form: traditional approaches, such as Monte Carlo simulations, are unable to handle such a large number of parameters due to the prohibitively high computational cost involved. A deterministic model including blade parameters is thus required to conduct this kind of simulation-based analysis. To address this challenge, dimensionality reduction techniques, such as those developed by Lange et al. [118, 120], are essential for efficiently processing and analyzing these geometric variabilities.

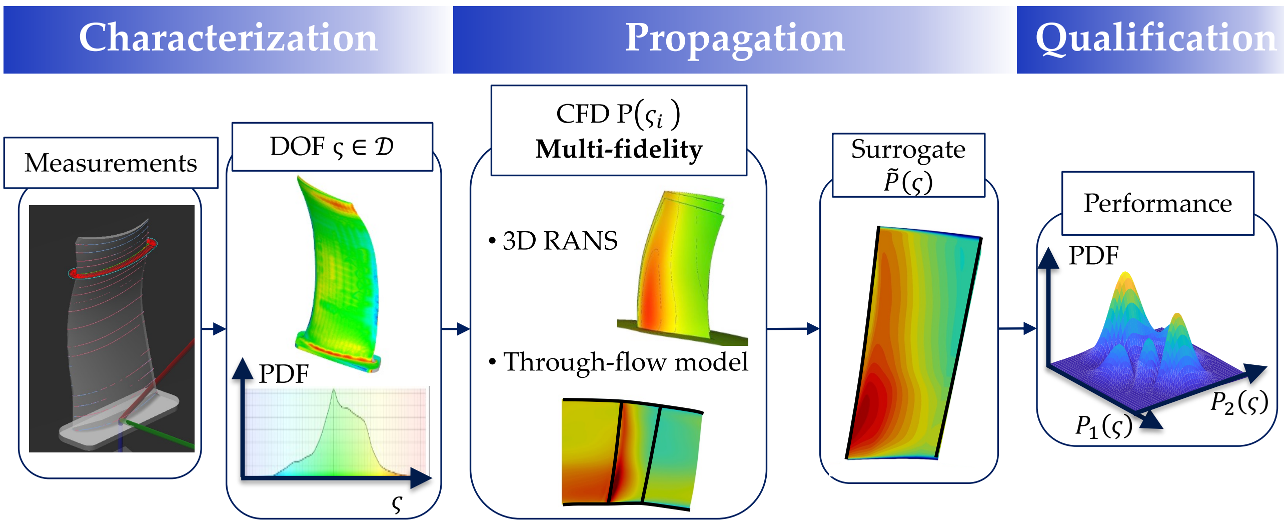

Figure 1.1: Flowchart of the MARIETTA project methodology for the robust design of axial compressors. Geometrical variabilities are first quantified from blade measurements, leading to the construction of a reduced-order model that describes these variations through degrees of freedom ς derived from the measured variability field $\mathcal{D}$. The probability distribution function (PDF) of these geometric inputs is then sampled to generate probabilistic realizations ς_i. These sampled inputs are introduced into multi-fidelity CFD simulations to assess aerodynamic performance variations P_i. A surrogate model, trained based on the simulations, enables a computationally efficient mapping between geometric variations and aerodynamic performance.

Subsequently, the geometrical uncertainties are propagated through CFD simulations, specifically using 3D Reynolds Averaged Navier-Stokes (RANS) simulations. These results are then used to train a surrogate model based on a non-intrusive proper orthogonal decomposition (NIPOD) approach [17], enabling direct performance prediction. This method allows the model to be constructed with a limited number of simulations while significantly accelerating response surface predictions. Finally, the impact of manufacturing variability on performance dispersion is assessed during the qualification phase. This enables the establishment of a feedback loop between production and design, resulting in optimized tolerancing that enhances design robustness while reducing production costs.

In the context of industrial design, RANS simulations are the most commonly employed type of CFD analysis due to their favorable trade-off between computational efficiency and predictive accuracy. High-fidelity methods like direct numerical simulation (DNS), which resolve all turbulence scales, and large eddy simulations (LES), which model smaller turbulence scales while resolving larger ones, are not feasible during design phases because of their prohibitively high computational cost. As a result, RANS remains the standard choice for aerodynamic performance assessments in the design of turbomachinery components.

Nevertheless, the cost of RANS simulations required can still be prohibitively high, as the already non-negligible cost of a single simulation is further compounded by the large number of simulations required. However, it is of utmost importance to be able to predict the effects of tolerances on the performance dispersion, within a time scale compatible with the design process. To further reduce computational effort, high quality simulations can be complemented by cheaper approaches to provide a finer exploration of the parameter space while hopefully still capturing the main trends [137]. In this context, the computational efficiency of through-flow (TF) solvers is useful for parametric studies during design improvement phases in which robust design is targeted. Through-flow models are low-fidelity CFD tools that solve the circumferentially averaged flow in the meridional (hub-to-casing) plane of turbomachinery components. They provide fast estimates of aerodynamic performance during preliminary design by relying on an averaged flow representation and empirical closure models, which are specifically introduced to account for the additional terms arising from the averaging process. For instance, the blades do not appear explicitly as solid surfaces within the computational domain. These empirical models are therefore essential to represent the key aerodynamic effects, including losses, deviations, and blockage. Additional background and formulation details on through-flow models are provided in Chapter 2.

1.3 Challenges and limitations of through-flow models in robust design

Through-flow modeling has been used for decades in axial turbomachines, either for blade design based on stage target performance, or for further analysis during the design process in case of design revaluation. Although its role in the past years has diminished in favour of more expensive yet higher-fidelity Computational-Fluid-Dynamics methods, it remains an essential tool in turbomachinery design [50, 95, 154]. Its ability to perform fast computations is particularly valuable for parametric studies during design optimization phases, where multiple parameters are involved [9, 82, 107, 151]. Another key advantage is its capability to efficiently reconstruct the aerodynamic flow field within an entire machine using experimental data. There has been a renewed industrial and academic interest in through-flow models and in their improvement [59, 62, 143, 160, 161, 200] because the computational cost of RANS simulations still remains too large for such simulations to be used at the initial design stage.

It is however known that such an averaged two-dimensional CFD modeling approach is fundamentally limited in its ability to represent some turbomachinery flow features, due to the intrinsic limitations of the through-flow equations and the approximations and assumptions made in the closure models [168]. For instance, a through-flow model, even based on Navier-Stokes equations, cannot predict the prerotation of the flow upstream of a blade row due to the axisymmetry assumption on which the model is based [13]. In the analysis mode, the flow angles in the bladed region are imposed by a blade flow deflection force. Therefore, a discontinuity occurs at the leading edge if the flow incidence is not aligned with the mean blade camber. This discontinuity leads to a sudden and non-physical increase of entropy and a spurious loss generation. A common fix consists in modifying the blade angle in the leading-edge region so that it adapts to the incident flow. As a result, the blade geometry is locally modified by this numerical artifact; this modification can thereby smooth any impact of variabilities at the leading edge on the performance.

Furthermore, modern optimized airfoils are directly described by a distribution of points along the suction and pressure airfoil surface, unlike NACA airfoils which are parameterized classically based on a camberline/thickness distribution description; the latter is generally used for through-flow simulations. Therefore, the section outline splitting into mean camber line and thickness distribution has to be achieved through an inverse computation algorithm. However, in the vicinity of the leading edge (LE) and trailing edge (TE), algorithms determining a mean camber line can be unreliable [118]. This epistemic uncertainty, although having usually a small impact, can still completely mask geometric variability in the leading edge region.

Another main challenge lies in the reliance on empirical correlations used to close the additional terms stemming from the averaging process, which can be particularly problematic when applied to modern, highly optimized blades. It is then unclear whether the low computational cost of through-flow models can be leveraged for the practical quantification and propagation of geometric variability.

1.4 Objectives and thesis outline

The objective of the present work is thus to evaluate the adequacy of the through-flow modeling approach to quantify the impact of geometric variability on the performance of axial compressors. To achieve this, two main questions are investigated:

- How accurate is the through-flow approach compared to higher fidelity methods such as RANS simulations for robust design of modern achitectures?
- Can a viscous through-flow solver capture key performance variations induced by geometric tolerances?

Thus, the originality of this work lies in assessing the feasibility of incorporating a through-flow model into a multi-fidelity approach to evaluate the impact of tolerancing on compressor performance. Although the incorporation of through-flow models in the robust aerodynamic design of compressors has been investigated for over a decade [83], very few references have fundamentally analyzed the relevance and the ability of the through-flow modeling approach to quantify the impact of geometric variability on compressor performance. Furthermore, the impact of TF modeling aspects on variability propagation remains an open question, as it has not yet been thoroughly investigated in existing research. The aim of this thesis is to address this gap by demonstrating the feasibility of using through-flow models for uncertainty quantification and identifying the areas in which the model must be improved to accurately account for geometric variability. Therefore, this critical assessment of the second part of the MARIETTA project and, more generally, of the use of through-flow models in robust design, represents an interesting and useful contribution to the community. This is thus the focus of the present work. In this respect, aspects related to surrogate modeling and the probabilistic representation of geometric uncertainties, while both interesting and challenging, are beyond the scope of this work.

The study focuses specifically on subsonic axial compressors, with two test cases centered on low-pressure compressor stages. While the methodologies developed in this work can be extended to other types of turbomachinery, including turbines and transonic compressors, the current scope is limited to subsonic designs. The first test case is the CME2 axial compressor stage [43, 72], a well-known benchmark in the turbomachinery community. The second test case is a modern highly-loaded multi-stage axial low-pressure compressor developed by Safran Aero Boosters. The analysis of such a modern multi-stage compressor is not commonly found in the literature.

The viscous through-flow approach developed in this thesis is based on the Navier-Stokes equations and its predictions are mainly compared with those of steady 3D RANS simulations. The analysis includes a sensitivity analysis of critical compressor performance metrics—mass flow rate, pressure ratio, isentropic efficiency and stability margin— under different operating conditions. It is important to emphasize that, because of the axisymmetry assumption underlying the TF model and the assumed periodicity of the RANS reference simulations, the geometric variabilities are intrinsically assumed to be identical on each blade of a given row, so that the analysis of mistuned blade rows is not possible. Nevertheless, the relevance of the present study is motivated by the analysis of recurring systematic deformation patterns related to tolerances and the blade manufacturing process. Mistuned blade rows, where each blade can exhibit slightly different geometric deviations, could nonetheless be tackled by such an axisymmetric approach, in a statistical sense, by averaging the blade row geometries and by using propagation of the uncertainty/variation on blade geometry to the variation of the performance. Another prospective approach to address mistuning could be the through-flow approach extended to three-dimensional body forces [27].

This thesis is organized as follows. In Chapter 2, the theoretical framework of through-flow solvers is presented in the context of axial-flow compressors. The general equations governing the TF solver are derived, and the modeling aspects of their unclosed terms are discussed, including correlations and their associated sources of error. This chapter provides the state-of-the-art and background for the developments and contributions presented in the following chapters. The thesis is addressed to a knowledgeable readership: no detailed reminders on compressor or turbomachinery fundamentals are provided, as excellent references already exist in standard textbooks [10, 38].

Chapter 3 is dedicated to the numerical implementation of the viscous through-flow solver developped in this thesis. Both the pre-existing implementation of the finite volume method, using the CFD solver `elsA`, coupled to the baseline source terms implemented in the `ASTEC` module, and the author's contribution are presented. The finite volume method coupled to a time-marching procedure is used, and the standard algorithms are briefly described. The particularities of the numerics associated with the through-flow modeling are discussed.

Chapter 4 focuses on the validation of the through-flow solver. The TF model is assessed using the two test cases presented above, covering both design and off-design conditions through an analysis formulation. Several modifications to the correlations, implemented during this thesis, are proposed to enhance prediction accuracy. This chapter demonstrates the predictive capabilities of the TF solver and provides a quantitative assessment of its ability to capture the major trends in the flow field. It serves as an insightful answer to the first key question of this thesis, as stated above.

Chapter 5 presents the sensitivity analysis of the current TF model with respect to the propagation of geometric variabilities in the low-pressure compressor, with a focus on identifying where the TF approach can effectively capture the effects of geometric variations and where its limitations prevent accurate predictions, as well as prioritizing the effects of geometric variabilities on compressor performance. Strategies to mitigate inherent model uncertainties are also proposed. The geometric variabilities considered in this study are based on the blade leading edge angle, the blade thickness, the rotor tip-gap the three-dimensional position of undeformed blades, and the deformation of the hub/shroud geometry of the second test case. This study does not rely on a probabilistic model or measured distributions of geometric variations; instead, it is based on theoretical variations that remain consistent with industry-imposed tolerances. The sensitivity of the correlation outputs with respect to the geometric variabilities are also discussed. This chapter presents an investigation in response to the second key question of this thesis related to the overall study of geometric variabilities.

Finally, Chapter 6 concludes the thesis by summarizing the main contributions and discussing the implications for TF-based multi-fidelity approaches in the context of robust design. Recommendations for future research in the short and long term are also provided.

1.5 Main contributions of this thesis

This thesis provides a critical assessment of a viscous, Navier-Stokes-based through-flow model for modern axial compressors under geometric variability. The key contributions are:

- **Model evaluation and validation:**
  - A thorough benchmarking of the TF solver against 3D RANS simulations on a modern low-pressure compressor.
  - Analysis of modeling errors introduced by empirical correlations, model assumptions, and closure models.
- **Improved correlation models:**
  - Integration of closure models into the existing CFD solver along with modifications to classical empirical correlations for deviation angle and loss coefficient. These enhancements incorporate Mach number effects and refined slope parameters to better capture the behavior of modern blade profiles and improve overall predictive accuracy.
- **Modeling aspects at blade leading edge:**

  - Assessment of the incidence correction technique and its numerical artifacts.
  - Evaluation of epistemic uncertainty due to the camber line reconstruction in modern airfoils.

- **Geometric sensitivity analysis:**
  - A parametric study using variations of geometric degrees of freedom (blade stagger, axial/pitchwise displacement, hub/casing deformation, blade thickness variation).
  - Comparison of TF and RANS predictions to identify where TF captures variability trends reliably, and where its limitations appear.
  - Insight into the impact of geometric perturbations on performance metrics and prioritization of these uncertainties.

Many of these contributions were already presented in conference papers [22, 23, 21] and are further described in a peer-reviewed journal article [24]. In addition to the modeling and analysis work, a significant effort was dedicated to software development and implementation, as the original version of the in-house through-flow solver was at an early stage and required development to support the objectives of this thesis. This included

- bug fixes in the original code, including those relaled to CGNS output generation, blockage factor computation, incidence correction, and vector rotation methodology,
- correction and clarification of angle conventions to ensure consistency across modules,
- development of data extractors and preprocessing routines for the application of non-uniform boundary conditions in both stationary and rotating frames, including field initialization from non-uniform solutions,
- extension of the solver to handle multi-stage configurations and enhancement of mesh generation tools for improved versatility and robustness,
- implementation of missing viscous terms and empirical correlations for the blade forces,
- implementation of correlations including profile loss, tip-gap flows, and endwall loss,
- automation of key workflows, including a full computational chain for geometric variability datasets compatible with existing Safran tools,
- addition of post-processing capabilities such as the wall distance computation and residual monitoring,
- implementation of one-dimensional inviscid through-flow solver based on the finite volume method,
- implementation of the capability to impose user-defined source terms directly within the solver.

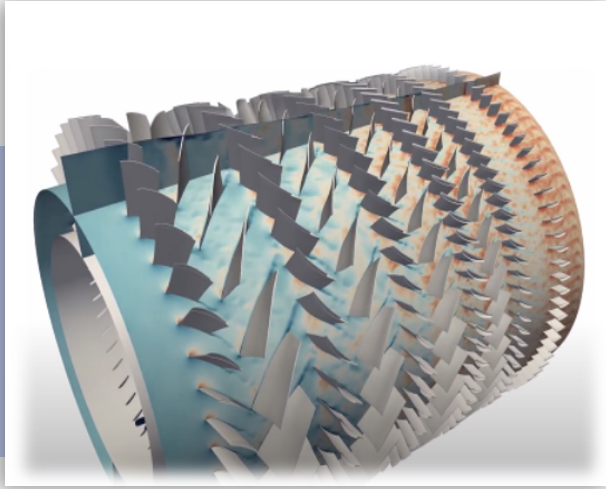

Chapter 2

Through-flow model

2.1 General considerations on turbomachinery design

The aerodynamic design of turbomachinery components, as shown in Fig 2.1, is nowadays primarily based on Computational Fluid Dynamics methods [50, 87, 154]. Historically, the development of high-fidelity CFD methods, such as DNS or LES, was even expected to eventually replace both experimental testing and low-fidelity tools, driven by the continuous increase in available computing power [88]. Due to the absence of modeling hypotheses, these simulations are indeed an ideal form of virtual experiments, as all details of the flow can be observed without limitations on probe placement or probe-flow interference that typically corrupt physical experiment. However, this substitution has not been achieved in practice: the inherent complexity and the three-dimensional nature of wall-bounded flows in gas turbines, particularly in turbofan engines used for aircraft propulsion, still pose challenges for industrial applications. The flow exhibits strong unsteadiness, involving a very wide range of length and time scales, leading to the need for a very fine resolution with respect to the geometry. The computational cost of such simulations scales with the cube of the Reynolds number, making DNS and, to a lesser extent, LES impractical for iterative design processes requiring rapid performance evaluation, as the resources required to efficiently explore multiple design configurations would still be too prohibitive [190]. As a result, RANS are still, and will be for some time to come, the industry standard for performance predictions during the design process. However, instrumented test benches remain essential in the design final stages due to the limitations of RANS, including modeling approximations and uncertainties in turbulence and loss predictions [49].

In the early stages of the design process, lower-fidelity models remain widely used to provide fast and reliable approximations before refining the design with higher-fidelity methods. Moreover, lower-fidelity models have found renewed relevance as complementary tools in multi-fidelity design frameworks [18]. As illustrated in Fig. 2.2, these low-fidelity methods are mainly based on two complementary computational surfaces [204], whose coupling is commonly referred to in the literature as the quasi-three-dimensional (*quasi-3D*) method: the blade-to-blade plane and the meridional plane. The blade-to-blade plane is a two-dimensional representation of the flow along a blade passage at a specific stream surface, corresponding to a specific spanwise location. Through a conformal transformation that preserves the relative angles, the blade geometry is mapped onto a periodic array of equally spaced two-dimensional blades, forming a planar stream surface called a blade *cascade*.

Cascade flow theory allows for the design and the analysis of velocity triangles and local blade loading.

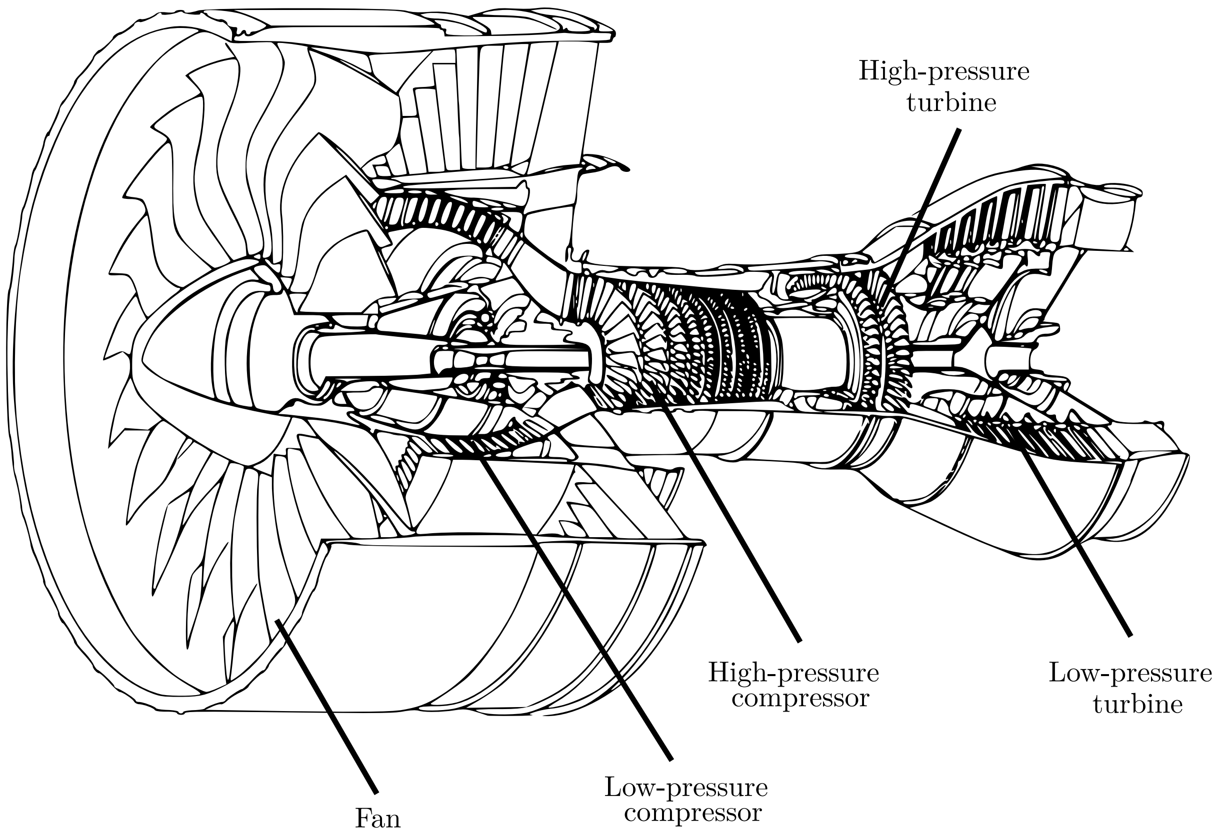

Figure 2.1: Bladed components of a turbofan engine (adapted from Salvat [165]).

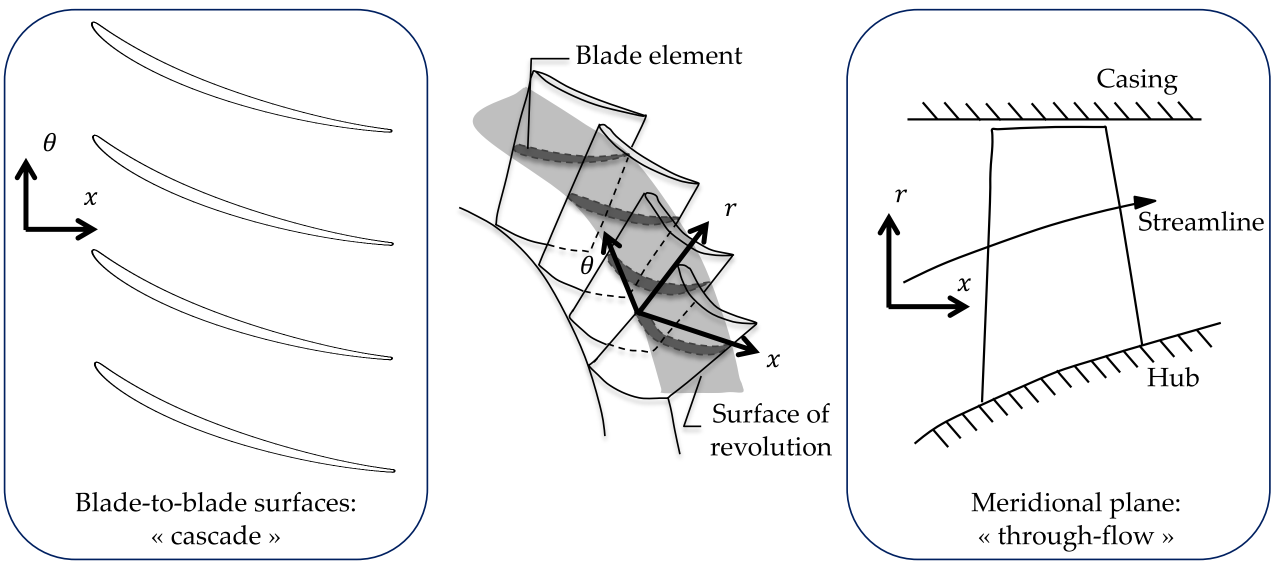

Figure 2.2: Schematic representation of the two surfaces used in the early design stages of turbomachinery: the blade-to-blade plane and the meridional plane, where x, r, θ are the stream-wise, span-wise and pitch-wise coordinates, respectively (adapted from Cumpsty [38]).

The meridional plane, on the other hand, provides a hub-to-tip view of the axisymmetric flow, averaged in the azimuthal direction. It naturally enforces compatibility conditions between adjacent stream surfaces from hub to tip that cannot be treated independently. Computational methods that solve pitch-wise averaged laws of fluid motion within this axisymmetric plane are commonly referred to as *through-flow* methods and constitute the main topic of the present work.

2.2 Features of through-flow models

The through-flow model is primarily used during the early stages of turbomachinery design, when rapid assessments of aerodynamic performance under nominal operating conditions are needed. It provides a simplified yet sufficiently accurate approach that efficiently captures global aerodynamic trends from an axisymmetric representation of the flow field before resorting to more detailed simulations. One of its key advantages is its ability to simulate the entire turbomachine in a single computation, enabling the inclusion of stage-to-stage interactions at the scale of the full machine. This allows designers to explore the impact of various geometric and operating parameters with low computational cost, and to determine the machine's main characteristics so that it meets the constraints imposed by the thermodynamic cycle of the turbojet engine. Compared to 3D CFD simulations, the through-flow analysis runs two or three orders of magnitude faster [44] and it can operate in two distinct modes: a design mode, where flow quantities such as total quantities and the pitch-wise velocity are prescribed to compute the resulting flow angles; and an analysis mode, where the flow is solved based on a known geometry to predict machine performance during optimization phases.

Through-flow models also serve a range of other purposes. For instance, they can be used to interpret experimental data by reconstructing the flow field from limited measurements, such as total quantities at blade leading and trailing edges, and static pressures at annulus endwalls. This capability is particularly valuable when only a few aerodynamic quantities are known from tests and only at a limited number of locations. Additionally, TF models can provide boundary conditions for 3D single row calculations, which in turn supply flow angles and loss coefficients back to the TF model in order to validate the stage matching and, consequently the entire multi-stage turbomachinery design [9]. TF models therefore remain an integral part of modern multi-fidelity design frameworks [143] for modern compressors and turbines [95], continuing to be refined and corrected as needed.

In exchange for computational efficiency, through-flow methods are not without limitations. The azimuthal averaging approach can be expressed in a generalized form as

$$\mathrm{D}_t\mathbf{u}(r,\theta,x,t) = \mathbf{S}(\mathbf{u},r,\theta,x,t) \quad \Longrightarrow \quad \mathrm{D}_t\overline{\mathbf{u}}(r,x) = \overline{\mathbf{S}}(\mathbf{u},r,x)\,, \tag{2.1}$$

where the left-hand side represents the governing equations written as a total derivative of the conserved variables $\mathbf{u}$. Akin to RANS models, the averaging operation introduces additional unclosed terms in the source term $\overline{\mathbf{S}}$ on the right-hand side of Eq. 2.1, which require closure through empirical models. Indeed, the source term still depends nonlinearly on the full, unaveraged flow quantities $\mathbf{u}$, which are not directly computed from the averaged system, thereby making closure essential to complete the formulation. These closure models are typically calibrated using experimental data or high-fidelity simulations. This limits their applicability for unconventional designs or off-design operating conditions. Furthermore, the axisymmetric nature of through-flow methods means that certain three-dimensional flow phenomena, such as secondary flows and endwall effects, are not explicitly captured and must be indirectly accounted for. Therefore, there exists a wide variety of through-flow models, each of which based on specific modeling choices adapted to the needs and constraints of the intended application. Over the years, so many variants have emerged that their distinctions are not always clear. The similarities in assumptions and numerical strategies often make it difficult to grasp the true differences between methods [38]. Additionally, similar approaches are sometimes published under different names and conversely.

2.3 Adamczyk's cascade

Given the diversity of governing equations and closure models across through-flow formulations, it is important for users and developers to know the underlying assumptions in order to characterize the associated modeling error and the level of empiricism. In this context, Adamczyk [1] proposed a systematic approach to derive the hierarchy of modeling levels for simulating the flow in turbomachines. This approach is often referred to as the Adamczyk's averaging cascade. This classification provides a clear overview of the different levels of CFD modeling encountered in numerical simulations and their inherent assumptions and simplifications. As illustrated in Fig. 2.3, Adamczyk's averaging cascade relies on a succession of four averages that successively link the three-dimensional unsteady turbulent flow to a stationary axisymmetric meridional flow. Specifically, it consists of an ensemble averaging, a time-averaging, a passage-to-passage averaging and a circumferential averaging.

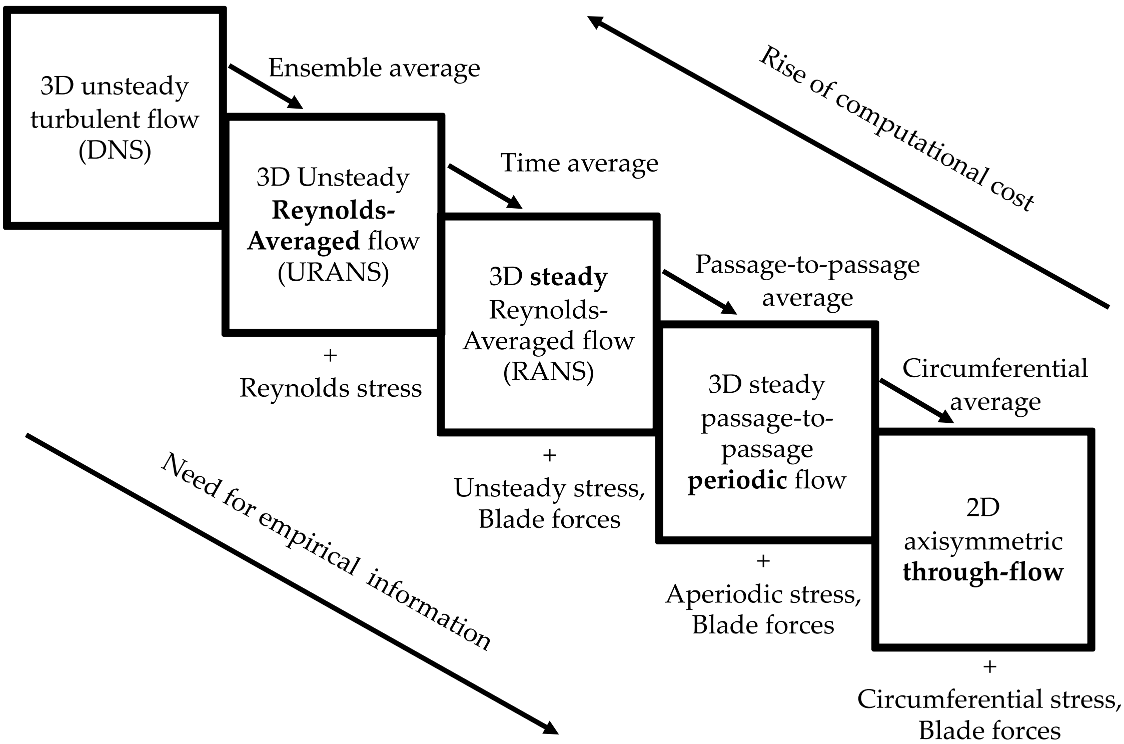

Figure 2.3: Adamczyk's cascade: levels of modeling used to simulate turbomachine flows (adapted from Adamczyk [2]).

Apart from the continuum hypothesis and thermal equilibrium, the unsteady compressible Navier-Stokes (NS) equations, and related equations of state, are the most accurate and general description of the behavior of a fluid within a compressor or turbine, but not in the combustion chamber. The equations that are obtained for the averaged quantities are thus mathematically exact. The resulting system of equations can be used to derive various reduced forms and to identify the sources of errors in existing models through comparison. It also helps identifying the unclosed source terms that arise from the averaging process, which are crucial for accurately predicting the performance of turbomachines. These source terms can be divided into two categories.

On the one hand, *stresses* appear due to the non-linearity of the Navier-Stokes equations. To illustrate this, consider the general definition of the Reynolds ($\overline{\cdot}$) and Favre ($\widetilde{\cdot}$) averages for compressible flows, i.e. weighted by the density ρ, of a flow quantity Q over a given interval Φ, respectively

$$\overline{Q} = \frac{\int_\Phi Q \,\mathrm{d}\Phi}{\int_\Phi \mathrm{d}\Phi} \quad \text{and} \quad \widetilde{Q} = \frac{\int_\Phi \rho Q \,\mathrm{d}\Phi}{\int_\Phi \rho \,\mathrm{d}\Phi} = \frac{\overline{\rho Q}}{\overline{\rho}}, \tag{2.2}$$

along with their associated definition of the fluctuations Q' and Q'',

$$Q' = Q - \overline{Q} \quad \text{and} \quad Q'' = Q - \widetilde{Q}. \tag{2.3}$$

The averaging of a product, as in the convective flux terms of the Navier-Stokes equations, reveals additional terms beyond the mean components:

$$\overline{\rho Q_1 Q_2} = \overline{\rho}\widetilde{Q_1}\widetilde{Q_2} + \overline{\rho Q_1'' Q_2''}\,. \tag{2.4}$$

The shape of the Reynolds stress, obtained by applying the ensemble averaging to the NS equations, can be clearly identified in the second term on the right-hand side of Eq. 2.4. Similarly, the unsteady, aperiodic and circumferential stresses are obtained for the three subsequent averages of the Adamczyk's cascade. These terms represent the mean effects of the flow features that are eliminated by the averaging in the whole meridional plane.

On the other hand, *blade forces* and their respective *energy source terms* explicitly appear in the throughflow equations as the result of the last averaging process, except for the ensemble averaging. For the other three averaging operators used in the Adamczyk's cascade, a gate function g, equal to one at a location inside the flow field and equal to zero inside a blade, must be introduced in Eq. 2.2 to account for the blade thickness in the channel [168], so that

$$\overline{Q} = \frac{\int_\Phi g Q \,\mathrm{d}\Phi}{\int_\Phi g \,\mathrm{d}\Phi} \quad \text{and} \quad \widetilde{Q} = \frac{\int_\Phi g \rho Q \,\mathrm{d}\Phi}{\int_\Phi g \rho \,\mathrm{d}\Phi}, \tag{2.5}$$

Indeed, the unsteady, passage-to-passage, and circumferential averages progressively remove blade rows from the computational domain. For instance, the time averaging of a turbine stage in the absolute frame of reference removes the rotor row because it is a source of unsteadiness. As illustrated in Fig. 2.4, this blade row no longer appears as a physical solid boundary, but rather as an actuator duct whose influence is distributed throughout the mean flow field and represented by body forces. A given location of the stationary mean flow lying in the rotor domain corresponds to the average of the instantaneous flow state at that spatial location over time. However, due to the relative motion of the rotor, this point may lie within the fluid domain at some instants and within the solid blade at others. This variation causes the averaging and differentiation operators to no longer commute. Similarly to

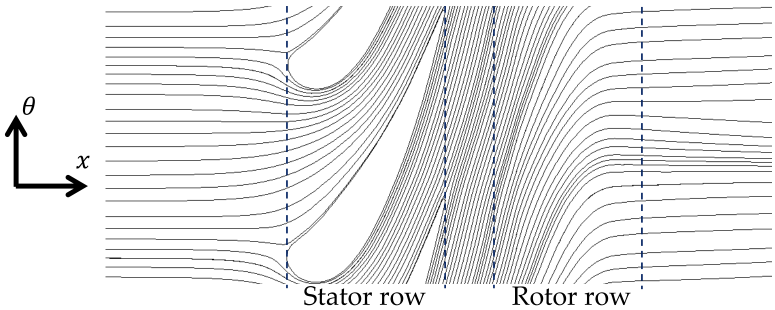

Figure 2.4: Time-averaged flow field of a turbine stage in the absolute frame of reference (adapted from Simon [168]).

Leibniz's integration rule, this yields

$$\overline{\frac{\partial Q}{\partial j}} = \frac{1}{b}\frac{\partial b\overline{Q}}{\partial j} - \frac{1}{2\pi b}\sum_{N}\left(Q_{B_2}\frac{\partial \theta_{B_2}}{\partial j} - Q_{B_1}\frac{\partial \theta_{B_1}}{\partial j}\right), \quad j = x, r, \theta, \tag{2.6}$$

where N is the number of blades per row, B_1, B_2 the two blade sides numbered in the order of the circumferential coordinates so that $\theta_{B_1} < \theta_{B_2}$, as shown in Fig. 2.5, and

$$b(x,r) = \frac{1}{\Phi}\int_{\Phi} g \mathrm{d}\Phi \tag{2.7}$$

is the tangential blade blockage factor, defined as the ratio of the portion of the annular circumference occupied by fluid to the total circumference. It can thus be expressed as

$$b = \frac{\Delta\theta}{2\pi/N} = \frac{(\theta_{B_2} - \theta_{B_1})}{2\pi/N} = 1 - \frac{\theta_b}{2\pi/N}, \tag{2.8}$$

where θ_b is the circumferential sector of the blade thickness $t_b = \theta_b r$. The second term on the right-hand side of Eq. 2.6 represents the blade forces exerted by the implicit presence of the blade in the mean flow field. Physically, the blade forces and energy source terms account for the interactions with the blade surface, namely the pressure loading (inviscid contribution), the shear stress (viscous contribution), and thermal effects such as the wall heat fluxes. Therefore, they are only present in the region of the domain corresponding to the fictitious presence of the blade in the flow field.

Each averaging operation in Adamczyk's cascade can be expressed using the unified mathematical framework introduced above. The first step is the classical ensemble averaging, which consists in averaging over a multitude of realizations of the flow. In turbomachinery, however, it is more practical to replace this with a phase-locked averaging, which considers multiple revolution periods from a single realization, under the assumption of ergodicity. This substitution is valid if the flow does not exhibit global instabilities such as rotating stall or surge. This assumption is justified, as a steady,

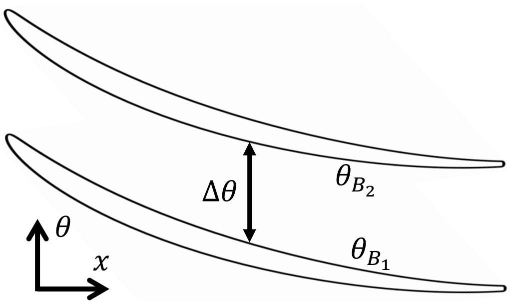

Figure 2.5: Circumferential averaging notation

axisymmetric representation like the one ultimately targeted by TF modeling, would not be meaningful in the presence of such phenomena. The goal of this first averaging step is to filter out stochastic unsteadiness. Formally, the averaging operators defined in Eq. 2.2 or Eq. 2.5 become a discrete summation over rotation periods. The continuous integration can only be rigorously defined if the underlying probability density function is known. In this context, the gate function g introduced in Eq. 2.5 equals one everywhere in the domain, since each point lies in the fluid at every instant of the averaging interval. This procedure filters out turbulent fluctuations and leads to the unsteady RANS equations, which describe a time-dependent mean flow influenced by turbulence effects.

The second step involves time-averaging the RANS equations to remove the remaining unsteadiness that is mainly associated with the change of relative position between successive blade rows. The temporal dependence of flow variables is thereby removed, and the resulting equations describe a steady mean flow. In this case, the averaging interval Φ corresponds to a single rotation period of the shaft, over which the unsteady fluctuations are filtered. As mentioned in the example above, the gate function g must be considered for rotating blade rows, since a given spatial point may lie within the blade at certain times and in the fluid at others due to rotor motion.

The third step is passage-to-passage averaging, introduced specifically for multistage turbomachinery. In such configurations, the mean flow obtained from the time-averaged equations is generally not periodic from one blade passage to the next within the same row. This is due to aperiodic effects, such as blade indexing: when the blade counts are not integral multiples, the circumferential misalignment between adjacent blade rows causes features like wakes from upstream blades to impinge differently on each downstream passage. This averaging step results in a spatially periodic mean flow over the pitch, including the mean influence of aperiodicity on the global flow field of a reference blade row. Consequently, the geometry of neighboring rows present in the flow field appears smeared in the frame of the row of reference. Formally, the averaging operator again corresponds to a discrete summation, here over blade passages of the row of interest. Importantly, for blade rows that are eliminated in this process, the gate function g must be introduced: since the averaging is performed over the azimuthal domain, a given spatial point may lie within the fluid or inside a blade solid depending on the angular position. The resulting flow field can be represented using a single passage and the azimuthal coordinate θ can be expressed as $\theta = \theta^* + 2\pi k/N$, with $k \in \mathbb{Z}$ and $\theta^* \in [0, 2\pi/N]$.

Finally, a circumferential averaging is performed to obtain the TF equations, which describe the steady axisymmetric mean flow in the meridional plane. Here, the averaging interval Φ spans a full blade pitch, $2\pi/N$, and the gate function is again required to account for the blade blockage, similarly to the previous step. This averaging removes any remaining θ-dependence from the flow.

The application of the complete averaging process to the Navier-Stokes equations in the absolute frame of reference results in the through-flow conservation of mass, momentum and energy,

$$
\begin{aligned}
&\frac{1}{b}\frac{\partial b\overline{\rho}\widetilde{V_x}}{\partial x} + \frac{1}{rb}\frac{\partial rb\overline{\rho}\widetilde{V_r}}{\partial r} = 0\,, \\
&\frac{1}{b}\frac{\partial b\left(\overline{\rho}\widetilde{V_j}\widetilde{V_x} + \overline{p}\delta_{xj}\right)}{\partial x} + \frac{1}{rb}\frac{\partial rb\left(\overline{\rho}\widetilde{V_j}\widetilde{V_r} + \overline{p}\delta_{rj}\right)}{\partial r} = \frac{1}{b}\frac{\partial b\overline{\tau_{jx}}}{\partial x} + \frac{1}{rb}\frac{\partial rb\overline{\tau_{jr}}}{\partial r} \\
&\qquad + \frac{\overline{\tau_{\theta r}} - \overline{\rho}\widetilde{V_\theta}\widetilde{V_r}}{r}\delta_{\theta j} + \frac{\overline{\rho}\widetilde{V_\theta}\widetilde{V_\theta} + \overline{p} - \overline{\tau_{\theta\theta}}}{r}\delta_{rj} \\
&\qquad - \frac{1}{b}\frac{\partial b\overline{\rho V_j'' V_x''}}{\partial x} - \frac{1}{rb}\frac{\partial rb\overline{\rho V_i'' V_r''}}{\partial r} + f_{b,j} + f_{v,j} \\
&\qquad - \frac{\overline{\rho V_\theta'' V_r''}}{r}\delta_{\theta j} + \frac{\overline{\rho V_\theta'' V_\theta''}}{r}\delta_{rj}\,, \\
&\frac{1}{b}\frac{\partial b\overline{\rho}\widetilde{V_x}\widetilde{H_t}}{\partial x} + \frac{1}{rb}\frac{\partial rb\overline{\rho}\widetilde{V_r}\widetilde{H_t}}{\partial r} = \frac{1}{b}\frac{\partial b\left(\overline{\tau_{xj}}\widetilde{V_j} - \overline{q_x}\right)}{\partial x} + \frac{1}{rb}\frac{\partial rb\left(\overline{\tau_{rj}}\widetilde{V_j} - \overline{q_r}\right)}{\partial r} \\
&\qquad - \frac{1}{b}\frac{\partial b\overline{\rho V_x'' H_t''}}{\partial x} + \frac{1}{rb}\frac{\partial rb\overline{\rho V_r'' H_t''}}{\partial r} + e_b + e_v \\
&\qquad + \frac{1}{b}\frac{\partial b\overline{\tau_{xj} V_j''}}{\partial x} - \frac{1}{rb}\frac{\partial rb\overline{\tau_{rj} V_j''}}{\partial r}\,,
\end{aligned}
\tag{2.9}
$$

where V is the velocity, p the static pressure, δ_{ij} the Kronecker delta, τ_{ij} the viscous stress, H_t the total enthalpy, q_j the heat flux modelled using Fourier's law, $f_{b,j}$ the inviscid blade force, $f_{v,j}$ the viscous blade force, e_b the inviscid energy source term and e_v the viscous energy source term. Note that summation is implied for repeated index $j = x$, r and θ. The complete set of equations associated with this approach, including the mathematical expressions of the unclosed source terms resulting from the first three averaging operations, is presented in Adamczyk's work [1]. The inclusion of the fourth, circumferential averaging step and its associated terms were later introduced and formalized by Simon [168]. For clarity, the cumbersome notation associated with the four averages is omitted in Eq. 2.9 but the flow variables presented above should be understood as flow quantities averaged four times. Moreover, the stresses are actually a summation of four contributions from the averaging cascade, such that

$$
\begin{aligned}
\overline{\rho Q_1'' Q_2''} &= \overline{\overline{\overline{\overline{\rho Q_1''^e Q_2''^e}^e}^t}^a}^c + \overline{\overline{\overline{\overline{\rho}^e Q_1''^t Q_2''^t}^t}^a}^c + \overline{\overline{\overline{\overline{\rho}^e}^t Q_1''^a Q_2''^a}^a}^c + \overline{\overline{\overline{\overline{\rho}^e}^t}^a Q_1''^c Q_2''^c}^c\,, \\
\overline{Q_1 Q_2''} &= \overline{\overline{\overline{\overline{Q_1 Q_2''^e}^e}^t}^a}^c + \overline{\overline{\overline{\overline{Q_1}^e Q_2''^t}^t}^a}^c + \overline{\overline{\overline{\overline{Q_1}^e}^t Q_2''^a}^a}^c + \overline{\overline{\overline{\overline{Q_1}^e}^t}^a Q_2''^c}^c\,,
\end{aligned}
\tag{2.10}
$$

where e, t, a, and c denote the ensemble, time, passage-to-passage, and circumferential averages, respectively.

Because mass is conserved, the continuity equation of the system 2.9 contains no source terms. In the momentum and energy equations, however, several contributions appear on the right-hand side.

The first line of each right-hand side contains diffusive fluxes, representing the divergence of viscous stresses and conductive heat fluxes. The second line of the momentum equation includes terms specific to the cylindrical coordinate system. The remaining lines group unclosed terms, including

- stresses due to the averaging operations,
- inviscid and viscous blade forces acting on the flow,
- energy source terms associated with blade interaction.

As explained by Adamczyk et al. [3], this system of equations provides a complete and unique description of the mean axisymmetric flow field. However, several conceptual paths can be followed to derive the meridional flow equations from the original NS equations, depending on the chosen reference frame and the arrangement of blade rows. Both the absolute and rotating frames of reference have their own time-averaged flow field. In each case, blade rows that are in relative motion with respect to one another are smeared within the flow field. Additionally, there exists one distinct average-passage flow description associated with each steady blade row in the frame of interest, reflecting its influence on the periodic mean flow. However, there is only one consistent axisymmetric representation of the mean flow field in a multistage configuration. This axisymmetric representation corresponds to the solution obtained by solving the averaged set of equations, and it should match the flow field that would be obtained by applying a posteriori averaging to the solution of the original, non-averaged Navier–Stokes equations. Therefore, axisymmetry is not an assumption imposed on the model, but rather an inherent property of the TF representation. Historically, earlier meaningful analysis of multistage turbomachinery required the simplifying assumption that each blade row had an infinite number of blades [132]. Provided that the inlet and outlet flows are both axisymmetric and steady, this idealization leads to an axisymmetric mean flow throughout the machine.

It is also important to note that the system of equations 2.9 is equivalent in form to the system obtained by applying a circumferential average directly to the steady Navier–Stokes equations. Consequently, a numerical solver cannot distinguish how the conservative quantities were averaged, whether through a cascade of operations or a single circumferential averaging step. Therefore, what differentiates one modeling approach from another are the source terms, which are closely linked to the nature of the averaging procedure used to compute them. The source terms appearing in these equations should be viewed as generic representations of the effects revealed by the full sequence of four successive averaging operations. Neglecting or approximating these contributions too coarsely inevitably introduces modeling errors into the predicted mean flow field. Thus, the fidelity of a through-flow model largely depends on how its source terms are treated. Additionally, choosing different governing equations than the full NS formulation can significantly impact the accuracy and applicability of the TF model to various turbomachinery configurations and operating conditions.

Finally, it is important to mention that nonlinearities in the equations of state that complement the Navier-Stokes equations can also lead to additional unclosed terms. For instance, the unknown pressure in Eq. 2.9 can be computed through

$$\overline{p} = (\gamma - 1)\overline{\rho}\left(\widetilde{E}_t - \frac{1}{2}\widetilde{V}_j\widetilde{V}_j - \frac{1}{2}\frac{\overline{\rho V_j'' V_j''}}{\overline{\rho}}\right), \tag{2.11}$$

where γ is the ratio of the heat capacities. The total enthalpy contained in the fluxes is given by:

$$\widetilde{H_t} = \widetilde{E_t} + \frac{\overline{p}}{\overline{\rho}}. \tag{2.12}$$

Similarly, the Favre-averaged Mach number is defined as

$$\widetilde{\mathrm{M}} = \frac{\widetilde{V}}{\widetilde{a}} - \frac{\overline{\rho a'' \mathrm{M}''}}{\overline{\rho}\widetilde{a}}, \tag{2.13}$$

which in turn depends on the speed of sound. The latter is obtained from

$$\widetilde{a} = \sqrt{\gamma r_{gas} \widetilde{T} - \frac{\overline{\rho a'' a''}}{\overline{\rho}}}, \tag{2.14}$$

where the temperature T is computed from

$$\widetilde{T} = \frac{\overline{p}}{\overline{\rho} r_{gas}}, \tag{2.15}$$

and r_{gas} is the gas constant. This shows that one cannot simply apply the standard equations of state to averaged variables. The rigorous and correct approach is to apply the averaging operator directly to the state equation itself. This is why the computation of the source terms stemming from the governing equations cannot simply be coupled to an existing solver without modification: the solver must allow the inclusion of the additional terms in the equations of state to avoid errors that would otherwise inevitably be introduced into the solution. However, if the flow under consideration is characterized by a low level of kinetic energy in the fluctuations, the difference between the two approaches should remain negligible.

This also means that there is only one consistent way to proceed when averaging the solution for comparison or computing the exact source terms. The quantities to be averaged that define the averaged state must be the conserved variables. The appropriate average for the velocity components and the total energy is the Favre formulation, while the density must be averaged using the Reynolds averaging. All other derived variables, such as pressure and temperature, must be computed according to Eqs. 2.11-2.12, which explicitly account for the additional stress terms. Any other averaging approach or procedure would lead to inconsistencies and, consequently, to additional sources of error.

In practice, some information is inevitably discarded because it is often not possible to access all the information required. Over the years, various averaging techniques [39, 74], such as mixed-out average, mass average, and other choices of variables for the averaged state have been developed for turbomachinery applications. The choice of averaging method must be guided by the decision to conserve the most important quantities for the case at hand, ensuring that the averaged flow field is physically consistent with the intended analysis or design objective and providing meaningful insight into turbomachinery performance and behavior. However, past practices often appear arbitrary, since different averaging schemes have been adopted mainly by convention or convenience.

2.4 Preliminary one-dimensional analysis of through-flow equations

The goal of this section is to present a preliminary analysis of through-flow models prior to addressing their classification and closure modeling. This analysis involves averaging a two-dimensional flow spatially to obtain a one-dimensional set of equations for the mean flow. The test case includes blockage factors, forces, and stresses analogous to the circumferential-averaging TF equations. This approach provides a more accessible means of understanding the underlying principles of Adamczyk's averaging procedure. Additionally, this analysis highlights the main properties of the through-flow equations, enabling the introduction of certain fundamental concepts in a clear and intuitive manner.

2.4.1 Test case: supersonic flow over a wedge

The test case consists of a supersonic, inviscid, compressible flow over a wedge, as illustrated in Fig. 2.6. The computational domain is bounded by two walls, with slip boundary conditions applied due to the inviscid assumption. It is divided into two blocks: the upstream section is a channel of constant-height y_1, while in the downstream section the channel height is reduced by the profile of the wedge $y_0(x)$. This wedge generates an oblique shock that separates two regions of uniform flow. Note that the region downstream of the shock reflection at the upper wall is not considered. The flow is assumed steady, calorically perfect and isentropic, i.e., adiabatic and reversible, everywhere except across the shock. As a result, the exact solution is known through the Rankine-Hugoniot relations [7], derived from the one-dimensional Euler equations (see Appendix A). The upstream flow and geometrical parameters used in the present configuration are summarized in Table 2.1.

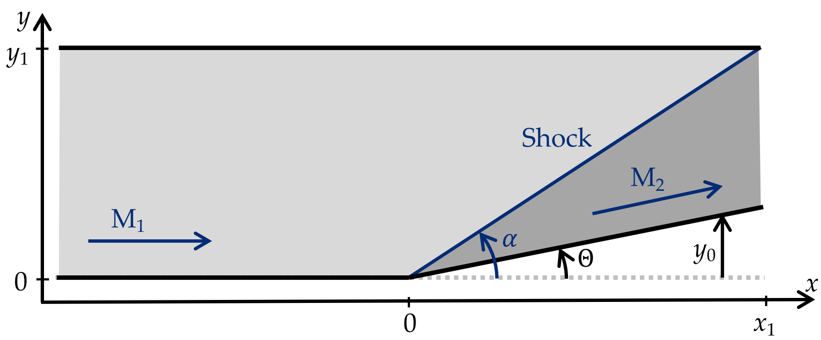

Figure 2.6: Flow over a wedge: problem definition in Cartesian coordinate system (x, y). The wedge angle is denoted by Θ and the shock angle by α.

Parameters	**Values**	
Mach number	$M_1 = 2.5$	$M_2 = 1.87$
Pressure	$P_1 = 101\,325$ Pa	$P_2 = 250\,019$ Pa
Temperature	$T_1 = 288.15$ K	$T_2 = 396.59$ K
Shock angle	$\alpha = 36.94°$	
Wedge angle	$\Theta = 15°$	
Non-dimensional wedge length	$x_1/y_1 = 1.33$	

Table 2.1: Flow and geometrical parameters of the test case.

2.4.2 Averaging procedure for the governing equations

The inviscid flow is fully described by the steady two-dimensional Euler equations defined as

$$
\begin{aligned}
\frac{\partial \rho V_x}{\partial x} + \frac{\partial \rho V_y}{\partial y} &= 0\,, \\
\frac{\partial\left(\rho V_x V_x + p\right)}{\partial x} + \frac{\partial \rho V_x V_y}{\partial y} &= 0\,, \\
\frac{\partial \rho V_y V_x}{\partial x} + \frac{\partial\left(\rho V_y V_y + p\right)}{\partial y} &= 0\,, \\
\frac{\partial \rho H_t V_x}{\partial x} + \frac{\partial \rho H_t V_y}{\partial y} &= 0\,,
\end{aligned}
\tag{2.16}
$$

This set of equations is spatially averaged in the y-direction and the Reynolds averaging operator from Eq. 2.5 is specified for a quantity Q as

$$
\overline{Q} = \frac{\int_\Phi g Q \,\mathrm{d}\Phi}{\int_\Phi g \,\mathrm{d}\Phi} = \frac{1}{b}\int_{y_0}^{y_1} Q dy\,,
\tag{2.17}
$$

where the blockage factor $b(x)$ is, in this case, the height of the computational domain $\Delta y = y_1 - y_0(x)$. The quantity Q is thus decomposed in a mean part and a fluctuating part using the Reynolds decomposition:

$$
Q = \overline{Q} + Q' \quad \text{so that} \quad \overline{Q'} = 0.
\tag{2.18}
$$

Similarly, the Favre averaging operator is also introduced since it simplifies the mathematical treatment of the density for compressible flows:

$$
\widetilde{Q} = \frac{1}{b\overline{\rho}}\int_{y_0}^{y_1} \rho Q dy = \frac{\overline{\rho Q}}{\overline{\rho}} \quad \text{and} \quad Q = \widetilde{Q} + Q'' \quad \text{so that} \quad \overline{\rho Q''} = 0.
\tag{2.19}
$$

The 1-D averaged equations are then obtained by averaging the equations. For the x-derivative, the Leibnitz integral rule stated in Eq. 2.6 is used so that

$$
\begin{aligned}
\overline{\frac{\partial Q}{\partial x}} &= \frac{1}{b}\int_{y_0}^{y_1} \frac{\partial Q}{\partial x} dy \\
&= \frac{1}{b}\left[\frac{\partial}{\partial x}\int_{y_0}^{y_1} Q dy - \left(0 - Q(y_0)\frac{\partial y_0}{\partial x}\right)\right] \\
&= \frac{1}{b}\frac{\partial(\Delta y \overline{Q})}{\partial x} + \frac{Q\left(y_0\right)}{b}\frac{\partial y_0}{\partial x}\,,
\end{aligned}
\tag{2.20}
$$

and averaging the y-derivative yields

$$
\overline{\frac{\partial Q}{\partial y}} = \frac{1}{b}\int_{y_0}^{y_1} \frac{\partial Q}{\partial y} dy = \frac{1}{b}(Q(y_1) - Q(y_0)) = \frac{1}{b}[Q]_{y_0}^{y_1}\,.
\tag{2.21}
$$

This procedure leads to the following set of equations for the one-dimensional mean flow:

$$
\begin{aligned}
\frac{1}{b}\frac{\partial}{\partial x}\left(b\overline{\rho}\widetilde{V_x}\right) &= -\frac{1}{b}\rho V_x\bigg|_{y_0}\frac{\partial y_0}{\partial x} - \frac{1}{b}[\rho V_y]_{y_0}^{y_1}\,, \\
\frac{1}{b}\frac{\partial}{\partial x}\left[b\left(\overline{\rho}\widetilde{V_x}\widetilde{V_x} + \overline{p}\right)\right] &= -\frac{1}{b}\left(\rho V_x V_x + p\right)\bigg|_{y_0}\frac{\partial y_0}{\partial x} - \frac{1}{b}[\rho V_x V_y]_{y_0}^{y_1} - \frac{1}{b}\frac{\partial}{\partial x}\left(b\overline{\rho V_x'' V_x''}\right)\,, \\
\frac{1}{b}\frac{\partial}{\partial x}\left[b\left(\overline{\rho}\widetilde{V_y}\widetilde{V_x}\right)\right] &= -\frac{1}{b}\left(\rho V_y V_x\right)\bigg|_{y_0}\frac{\partial y_0}{\partial x} - \frac{1}{b}[\rho V_y V_y + p]_{y_0}^{y_1} - \frac{1}{b}\frac{\partial}{\partial x}\left(b\overline{\rho V_y'' V_x''}\right)\,, \\
\frac{1}{b}\frac{\partial}{\partial x}\left[b\left(\overline{\rho}\widetilde{H_t}\widetilde{V_x}\right)\right] &= -\frac{1}{b}\left(\rho H_t V_x\right)\bigg|_{y_0}\frac{\partial y_0}{\partial x} - \frac{1}{b}[\rho H_t V_y]_{y_0}^{y_1} - \frac{1}{b}\frac{\partial}{\partial x}\left(b\overline{\rho H_t'' V_x''}\right)\,.
\end{aligned}
\tag{2.22}
$$

A strong analogy can be drawn between these equations and the general TF equations: the circumferential average has been replaced by a spatial average along the y-axis. Similarly to the θ-fluxes in the TF equations, the y-fluxes vanish. The height of the computational domain Δy acts as a blockage factor in the equations. Furthermore, additional terms appear in the set of equations. They can be divided into:

- wall forces and their associated energy source terms: $\frac{1}{b}[Q]_{y_0}^{y_1}$ and $\frac{1}{b}Q\Big|_{y_0}\frac{\partial y_0}{\partial x}$. These source terms stem from the averaging procedure of derivatives with a non-constant domain. They represent the force acting on the flow due to the presence of the wedge. These terms are only non-zero in the shock region, i.e., for $x > 0$. They are analogous to the inviscid blade force in the TF equations, which account for the interaction between the flow and the blade surface.
- Spatial stress: $\overline{\rho V_x'' V_x''}$, $\overline{\rho V_x'' V_y''}$ and $\overline{\rho V_x'' H_t''}$. These source terms originate from the average procedure of the non-linear convective fluxes, similarly to those of the TF equations. They represent the mean effect of the spatial fluctuations on the mean flow. Formally, the stresses are defined throughout the overall computational domain. However, for the case considered here, they vanish upstream of the shock region, i.e., $x < 0$, where the flow is uniform.

Note that the present analysis only considers terms analogous to the circumferential closure terms, excluding Reynolds stress, deterministic stress and aperiodic stress. Although the selected test case does not reproduce all the features of the TF equations, it still provides meaningful insight.

The exact values of these terms can be directly computed from the known analytical 2D flow field and geometry parameters. Mathematically, it can be demonstrated that in this case the wall forces containing the quantities ρ, V_j and H_t, cancel each other out, since

$$y_0 = x\tan\theta \quad \text{for} \quad x > 0 \tag{2.23}$$

and thus its derivative is

$$\frac{\partial y_0}{\partial x} = \tan\theta = \frac{V_y}{V_x}\bigg|_{y_0}\,. \tag{2.24}$$

Finally, for this specific case, $V_y = 0$ at the upper wall, i.e. for $y = y_1$. Introducing these simplifications into the governing equations leads to the aforementioned cancellations. For instance, the source terms in the continuity equation of Eqs. 2.22 result in

$$-\frac{1}{b}\rho V_x\bigg|_{y_0}\frac{\partial y_0}{\partial x}-\frac{1}{b}[\rho V_y]_{y_0}^{y_1}=-\frac{1}{b}\rho \cancel{V_x}\bigg|_{y_0}\frac{V_y}{\cancel{V_x}}\bigg|_{y_0}-\underbrace{\cancel{\frac{1}{b}\rho V_y\bigg|_{y_1}}}_{=0}+\frac{1}{b}\rho V_y\bigg|_{y_0}=0\,. \tag{2.25}$$

The results analysis show that these cancellations indeed hold when the averaging procedure is applied to the exact two-dimensional solution. Nevertheless, in the viscous case where the Navier–Stokes equations are averaged, the same terms also vanish, since the velocity components are equals to 0 at walls.

2.4.3 One-dimensional solver for the averaged equations

Considering the time-derivative of the conserved variables, the set of equations can be rewritten as

$$\frac{\partial \overline{\mathbf{u}}}{\partial t}+\frac{1}{b}\frac{\partial b\overline{\mathbf{F}}}{\partial x}=\overline{\mathbf{S_w}}+\overline{\mathbf{S_s}}\,, \tag{2.26}$$

where the vector of conserved variables, the inviscid fluxes, the wall forces and the spatial stresses are respectively defined as

$$\overline{\mathbf{u}}=\begin{bmatrix}\overline{\rho}\\ \overline{\rho}\widetilde{V_x}\\ \overline{\rho}\widetilde{V_y}\\ \overline{\rho}\widetilde{E_t}\end{bmatrix},\quad \overline{\mathbf{F}}=\begin{bmatrix}\overline{\rho}\widetilde{V_x}\\ \overline{\rho}\widetilde{V_x}\widetilde{V_x}+\overline{p}\\ \overline{\rho}\widetilde{V_y}\widetilde{V_x}\\ \overline{\rho}\widetilde{H_t}\widetilde{V_x}\end{bmatrix},\quad \overline{\mathbf{S_w}}=-\frac{1}{b}\begin{bmatrix}0\\ p\Big|_{y_0}\frac{\partial y_0}{\partial x}\\ [p]_{y_0}^{y_1}\\ 0\end{bmatrix},\quad \overline{\mathbf{S_s}}=-\frac{1}{b}\begin{bmatrix}0\\ \frac{\partial}{\partial x}\left(b\overline{\rho V_x''V_x''}\right)\\ \frac{\partial}{\partial x}\left(b\overline{\rho V_y''V_x''}\right)\\ \frac{\partial}{\partial x}\left(b\overline{\rho H_t''V_x''}\right)\end{bmatrix}. \tag{2.27}$$

Finally, the system of equations above is closed with the equations of state (EoS), Eqs. 2.11-2.15.

This system is solved in the x-direction using a finite-volume discretization [88] combined with a time-marching method. The computational domain is discretized into a one-dimensional mesh, and the equations are integrated over each control volume. The computational mesh is composed of 44 elements. Around $x = 0$, six elements are distributed on each side with a geometric progression ratio of 1.2, ensuring sufficient clustering in the region of strong gradients. The remaining elements are uniformly spaced. The fluxes at the boundaries of each control volume are computed using the Van-Leer numerical scheme [193]. The time integration to steady-state is performed using an explicit Euler method with a Courant–Friedrichs–Lewy (CFL) number of 0.3. The exact value of the source terms is obtained from the analytical solution. All details regarding the 1-D solver implementation, the evaluation of the exact source terms, as well as the governing equations are provided in Appendix B.

2.4.4 Comparison of the averaged flows

This section presents a comparison between the averaged solution obtained from the reference exact analytical two-dimensional solution and the numerical solution of the corresponding averaged equations using the exact values for the unclosed stresses and wall forces. To prioritize the source terms, each contribution extracted from the 2D flow field can be selectively activated or deactivated in the solver. By assessing the resulting variations in the 1-D averaged flow field, it is possible to evaluate their individual impacts and identify the dominant terms, as shown in Fig. 2.7. First, it can be observed that when no source terms are included, the solution corresponds expectedly to a constant, uniform flow in a channel. When only the wall forces are considered, the resulting solution is already close to the exact averaged solution, as these forces produce the main modifications in the flow. The spatial stress terms have a smaller influence. When all source terms are included, the 1-D solver reproduces the averaged flow field almost perfectly, demonstrating that the approach is exact when numerical errors are negligible. Another important conclusion is that there is no discontinuity within the shock region: only a shock parallel to the y-direction could have been observed. Similarly, a meridional model can only capture axisymmetric shocks, i.e., shocks parallel to the azimuthal direction.

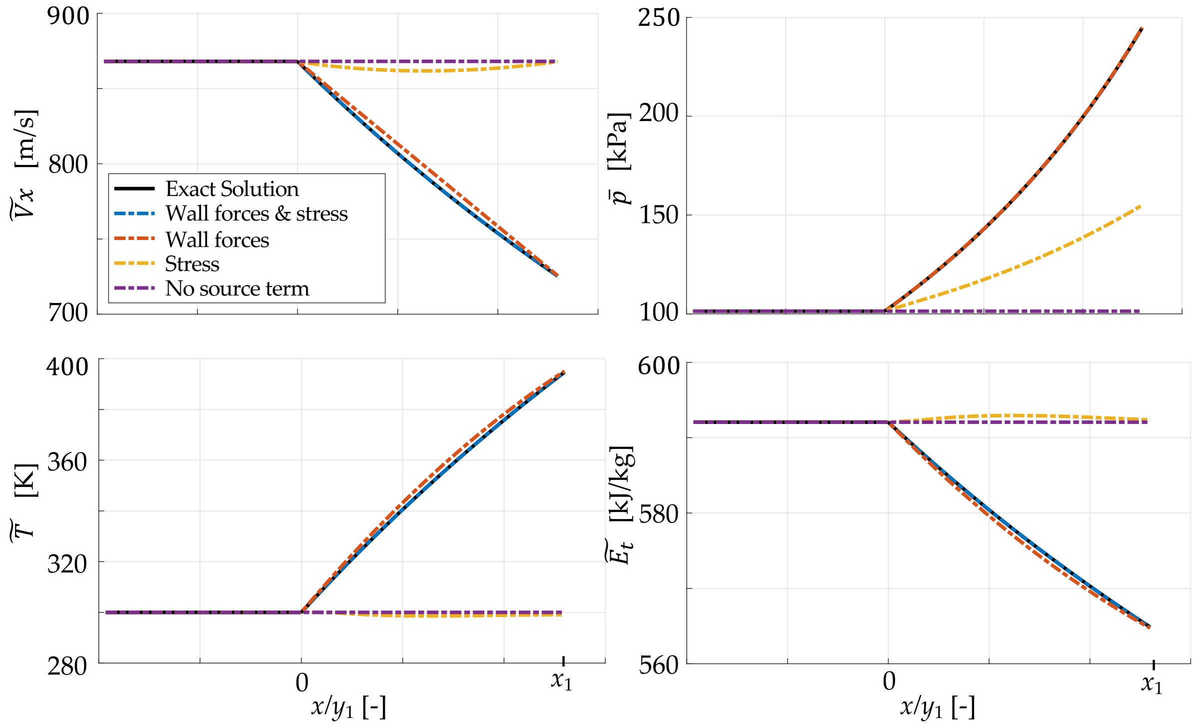

Figure 2.7: Comparison of the exact averaged solution and 1D-solver simulations fed with exact source terms from the analytical solution. The solution is shown for the velocity, pressure, temperature and total energy. The source terms are activated one by one to assess their influence on the averaged flow field.

The importance of the choice of averaging operator is highlighted in Fig. 2.8, which shows the significant differences between Favre and Reynolds averages. The Reynolds average is a meaningful formulation and it is easy to interpret. However, it is not adequate for the problem considered here because the solved set of equations is based on the density-weighted (Favre) average. The differences between the two approaches are most pronounced in regions where the spatial stress terms reach their peak values. Thus, the discrepancy between mass-averaged and density-averaged quantities increases with the non-uniformity of the flow. Conversely, the two averages coincide when the flow is uniform upstream of a shock. Extrapolating this observation to the circumferential average in a turbomachinery configuration suggests that, sufficiently far from the inlet and outlet of a blade row or a compressor, where the flow becomes circumferentially uniform, the two averages should exhibit only minor differences. Furthermore, Fig. 2.9 illustrates the impact of including the additional stress terms in the equations of state. The solution computed without these terms exhibits a non-negligible level of error, confirming that their omission leads to noticeable discrepancies in the averaged flow prediction.

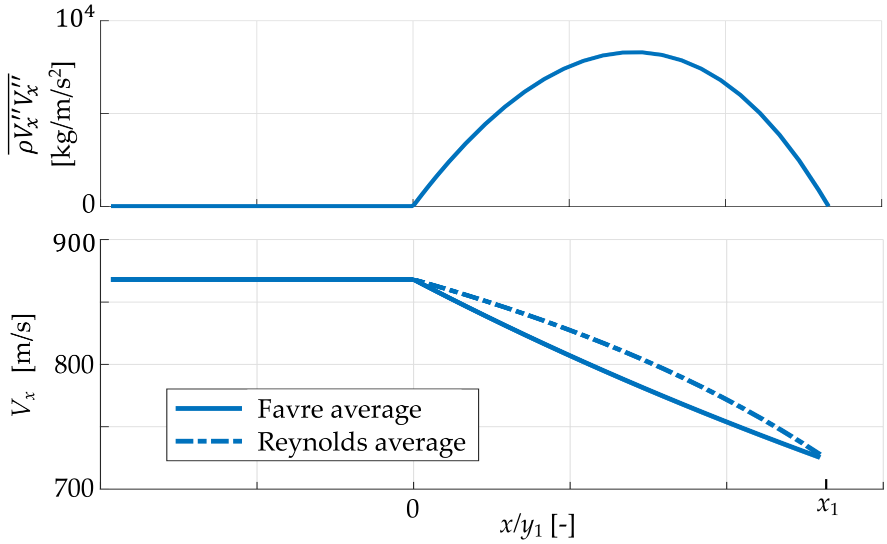

Figure 2.8: Spatial stress of the x-momemtum equation (top) and comparison of Favre and Reynolds averaging (bottom).

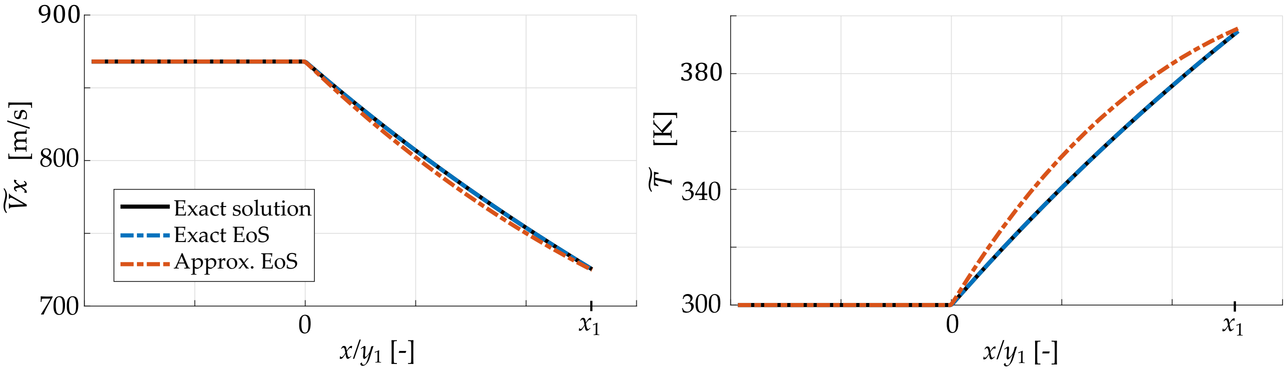

Figure 2.9: Comparison of the exact averaged solution and 1-D solver simulations fed with exact source terms from the analytical solution. Results are shown for velocity and temperature. The source terms in the equations of state (EoS) are alternately activated and deactivated to assess their influence on the averaged flow field.

Although the selected test case does not capture all the features of turbomachinery flows, it provides several important insights. In particular, it highlights key aspects of the averaging process, the relative importance of the various source terms and the significant influence that the choice of averaging method can have on the resulting solution. Moreover, this case is somewhat more extreme than the compressor configurations considered later in this work, since no shock waves will appear in those test cases. Nevertheless, it remains highly relevant for situations involving transonic blades. Importantly, this configuration demonstrates that the averaged solution can be accurately reproduced when the exact source terms are provided. The major challenge, however, lies in developing reliable models for these source terms, especially in the presence of shocks, whose accurate representation remains a particularly demanding aspect of through-flow modeling.

2.5 Classification of through-flow methods

The through-flow methods can be classified into several main categories based on the governing equations they solve and the modeling assumptions they make. In this section, we focus on the inherent choices made for the left-hand side of Eq. (2.1), i.e., the governing flow equations. An initial classification was proposed as early as the 1980s by Hirsch and Denton [89], and remains partly relevant today. The following discussion expands and updates this classification in light of more recent developments. The choice of governing equations can, to a large extent, be treated independently from the closure models selected to account for unresolved physics. These latter choices, which concern the right-hand side of Eq. (2.1) related to the closure problem, will be discussed in later sections.

2.5.1 Pitch-line analysis

The history of meridional flow models began with the rise of computational methods in turbomachinery design at the end of the 1960s. Prior to that, simpler analytical approaches convenient for hand calculations, such as *pitch-line analysis*, were used to support very first design iterations. Also referred to as *mean-line analysis*, this method predates axisymmetric through-flow modeling. The method is based on the assumption that the flow can be approximated by a one-dimensional flow along a pitch line, which is typically defined as the mean radius of the machine [92]. This approach simplifies the analysis by reducing the problem to a single streamline, which forms the basis for a more complete design. This allows for easier calculations based on basic thermodynamic relations accompanied by empirical correlations. Nevertheless, although this method is simple and computationally inexpensive, it remains indirectly costly due to its strong dependence on large empirical databases. These databases, which encapsulate decades of experimental measurements and industrial feedback, require continuous maintenance [2].

The pitch-line model assumes that the flow is uniform across the span of the blade, which is a reasonable approximation for many turbomachinery applications, especially when the blade height is small compared to the mean radius. Therefore, this one-dimensional approach lies conceptually below the last level of fidelity in the Adamczyk's averaging cascade illustrated in Fig. 2.3, representing a further simplification beyond two-dimensional through-flow models. The pitch-line model aims to provide a first-order estimate of key design and performance parameters early in the preliminary design phase [99]. It is particularly useful for rapidly determining:

- the number of stages required to achieve a target compression ratio,
- the axial evolution of flow area in order to maintain a nearly constant axial velocity despite of the changing gas density,
- and the general operating characteristics of the machine, including rough estimation of performance.

Pitch-line analysis can be used in both design mode, for estimating geometric evolution and stage count under design conditions, and in analysis mode, to approximate off-design behavior and performance trends [29]. When the hub and shroud radii are close, i.e. the blade height is small compared to the mean radius, radial variations are minimal, making the pitch-line assumption relatively accurate. In more general configurations, however, the method still used nowadays [195] may be extended by applying the analysis to several radial locations and coupling them through compatibility relations.

2.5.2 Isentropic simplified radial equilibrium

The simplest form of compatibility relations is known as the *Isentropic Simplified Radial Equilibrium* (ISRE). This simplified relation is derived from the radial momentum equation of the averaged system 2.9 under the assumptions of a steady, axisymmetric, inviscid and isentropic flow, sufficiently far from any blade row. Additionally, the annulus is assumed to be axial with negligible radial velocity components between blade rows, i.e., $\widetilde{V_r} = 0$ and and zero streamwise streamline curvature. Under these conditions, neglecting the stresses and assuming that the work is constant over the radius, the radial momentum equation simplifies to the classical radial equilibrium relation:

$$\frac{1}{\overline{\rho}} \frac{\partial \overline{p}}{\partial r} = \frac{\widetilde{V_\theta}^2}{r}. \tag{2.28}$$

This equation expresses a balance between the radial pressure gradient and the centrifugal effect resulting from the swirl velocity $\widetilde{V_\theta}$, which is the dominant effect in the radial momentum equation for most axial compressors [173].

Historically, radial equilibrium theory gained widespread use in the 1950s and remains relevant today in simplified preliminary design approaches [38]. Eq. 2.28, combined with a prescribed swirl distribution [92], enables the estimation of radial variations in the flow field and thus defines the spanwise structure of a compressor or turbine stage. The equation can be integrated to determine the pressure distribution across the annulus.

As illustrated in Fig. 2.10, this approach assumes that stream surfaces remain approximately at constant radius and that variations in radius and gas properties occur primarily within the blade passages, as well as viscous effects. However, it is important to note that the flow within the blade rows is not explicitly modeled by ISRE. Instead, a work input representing the energy exchange across the blade row,

$$\Delta \widetilde{H_t} = \Omega r_{\mathrm{TE}} \widetilde{V_{\theta,\mathrm{TE}}} - \Omega r_{\mathrm{LE}} \widetilde{V_{\theta,\mathrm{LE}}}\,, \tag{2.29}$$

where Ω is the blade rotation speed, can be introduced in the analysis mode to compute the downstream migration of the streamlines. This work input can be calculated solely from the leading edge and trailing edge pitch-wise velocity or equivalently, the flow angle. The axial velocity profile is eventually obtained from the relation

$$\widetilde{V_x} \frac{\partial \widetilde{V_x}}{\partial r} + \frac{\widetilde{V_\theta}}{r} \frac{\partial}{\partial r}\left(r \widetilde{V_\theta}\right) = 0, \tag{2.30}$$

stemming from the constancy of the enthalpy and entropy outside blade rows.

To account for total pressure loss, empirical corrections can be introduced, which enables first-order performance estimates of turbomachine stages. While simplified, this framework captures key aerodynamic trends even in complex or curved annulus geometries [173]. Therefore, the ISRE relation is still commonly used in space-marching through-flow solvers or as an outlet boundary condition in

RANS simulations. In these applications, it provides a consistent and physically motivated spanwise pressure profile for design conditions.

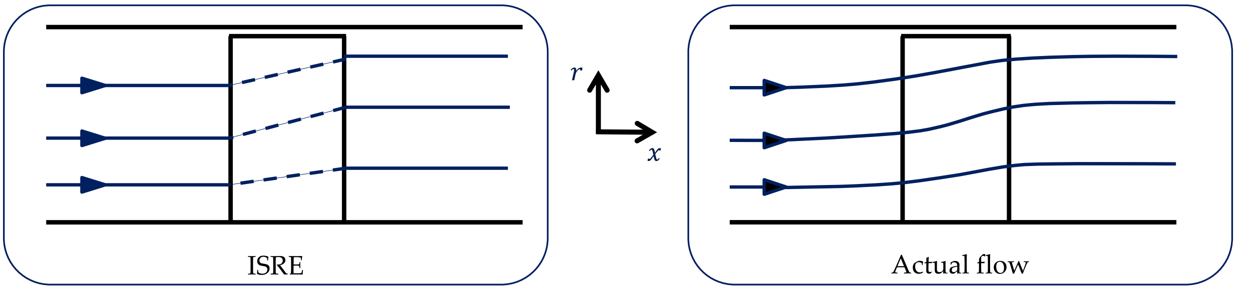

Figure 2.10: Schematic of the flow modeled by ISRE compared to the actual flow for the meridional streamlines (adapted from Cumpsty [38]).

2.5.3 Streamline curvature (SLC) method

Advances in computer technology have led to the development of iterative approaches that avoid the restrictive assumptions of earlier analytical methods. Based on the conceptual foundations of the meridional plane introduced by Wu [204] in 1952, the *streamline curvature method* emerged in the late 1960s as a natural extension of earlier approaches. The SLC method is one of the most historically significant and widely adopted numerical approaches in through-flow modeling [38], having been among the first to be implemented in software for industrial turbomachinery design. It remains in use today [30], particularly during early design phases requiring fast turnaround and reliable prediction. The SLC method thus marked one of the earliest practical applications of Computational Fluid Dynamics in turbomachinery design. Based on the radial equilibrium relation applied to successive axial stations, this method incorporates the curvature of streamlines c_m and the effects of flow turning within blade rows.

Considering a steady, axisymmetric, inviscid and adiabatic flow, the radial momentum equation that is usually solved for pressure takes the following form:

$$\frac{1}{\overline{\rho}}\frac{\partial \overline{p}}{\partial r} = \frac{\widetilde{V_\theta}^2}{r} - \widetilde{V_m}\frac{\partial \widetilde{V_m}}{\partial m}\sin\phi + \frac{\widetilde{V_m}^2}{r_m}\cos\phi + \overline{S}, \tag{2.31}$$

where

$$\widetilde{V_m} = \sqrt{\widetilde{V_x}^2 + \widetilde{V_r}^2} \tag{2.32}$$

is the meridional velocity and

$$\phi = \tan\frac{\widetilde{V_r}}{\widetilde{V_x}} \tag{2.33}$$

is the meridional flow angle so that

$$c_m = -\frac{\partial \phi}{\partial m} \quad \text{and} \quad \widetilde{V_m}\frac{\partial}{\partial m} = \widetilde{V_x}\frac{\partial}{\partial x} + \widetilde{V_r}\frac{\partial}{\partial r}. \tag{2.34}$$

The source term $\overline{S}$ includes empirical contributions accounting for inviscid and viscous blade effects [102]. If the last three terms on the right-hand side of Eq. 2.31 are neglected, the equation simplifies to the ISRE relation [173]. In the SLC method, the terms containing the meridional velocity are closed by using the continuity equation [142, 144, 173], including the blade blockage factor. Due to the adiabatic flow assumption, the energy equation simplifies considerably and can be reduced to a form that facilitates the derivation of the final system of governing equations. The circumferential momentum equation is solved to obtain the pitch-wise component of the blade force stemming from Eq. 2.31.

Computationally, the SLC method operates by assuming an initial set of streamlines and adjusting them iteratively to satisfy mass conservation, momentum balance, and empirical closure laws. The process continues until convergence of the streamline configuration is reached for specified inlet conditions, rotational speed, and mass flow rate. Discrete computational nodes are defined at the intersections between streamlines and predefined radial control surfaces, including blade row inlets and outlets. Intermediate stations are introduced within blade rows as well, enhancing the spatial resolution of the predictions. At each iteration, the updated streamline configuration leads to a new computational grid, and convergence is monitored by evaluating the deviation between successive streamline positions. In most cases, the governing equations are discretized using finite difference techniques, leading to a nonlinear system that is solved iteratively. Once convergence is achieved, flow properties and velocity components are evaluated at each control station along the streamlines, providing a detailed reconstruction of the meridional flow field. These methods are highly flexible, as they allow not only the design of multi-stage flow path geometries, from which simplified blade geometries and velocity triangles can be derived based on specified overall performance targets, but also operation in the analysis mode.

Although this method has proven effective and remains widely used in industry [75], it is important to highlight the underlying simplifications and modeling assumptions that limit its predictive capabilities in certain flow regimes. The axial momentum equation is not explicitly solved, meaning that the method inherently lacks the ability to capture shocks and the mass flow rate must be imposed by users. The flow is treated as inviscid, with slip boundary conditions applied along the annulus endwalls. There is no explicit stress closure; instead, losses and endwall effects are introduced through empirical correlations. As a result, no loss mechanism is predicted unless modeled empirically, highlighting the method's reliance on calibrated data rather than first-principles physics. Nevertheless, research efforts have focused on improving the modeling of additional viscous loss terms [64], with the aim of enhancing compressor performance predictions.

2.5.4 Matrix method

Another notable approach for analyzing meridional flow in turbomachinery, conceptually similar to the SLC method in terms of underlying flow assumptions, but differing in its mathematical formulation, is the so-called *matrix method* [41, 133, 203]. This technique relies on the use of a streamfunction formulation to describe the flow field by expressing the meridional velocity components as functions of a streamfunction ψ so that

$$\begin{aligned}\frac{\partial \psi}{\partial r} &= r b \overline{\rho} \widetilde{V_x} \,, \\ \frac{\partial \psi}{\partial x} &= -r b \overline{\rho} \widetilde{V_r} \,.\end{aligned} \tag{2.35}$$

Incorporating these relations in the radial momentum equation of motion, an equation for the streamfunction is obtained as

$$\frac{\partial^2 \psi}{\partial x^2} + \frac{\partial^2 \psi}{\partial r^2} = \overline{S} \,, \tag{2.36}$$

where $\overline{S}$ includes the effects of the blade forces [152]. The streamfunction formulation provides a simpler representation of the flow field because Eq. 2.36 inherently have solutions that satisfiy the continuity equation, the circumferential momentum equation and the customary form of the energy equation for adiabatic flow. However, the axial momentum equation is not explicitly solved, meaning that the mass flow rate is not predicted by the model but must be prescribed by the user.

The matrix method provides an alternative framework for solving the radial equilibrium equation in meridional flow analysis. While it shares the same core physical assumptions as the SLC method, it adopts a distinct numerical approach. By reformulating the problem in terms of a streamfunction, the governing equations can be expressed as a single partial differential equation. This equation, once discretized over the meridional plane using finite-difference schemes and a structured grid, is solved iteratively using matrix inversion techniques.

Despite its theoretical equivalence to SLC in terms of resolved physics, the matrix method has not gained the same level of popularity in industrial design workflows. As highlighted by Cumpsty [38], the physical interpretation of the SLC equations is more intuitive, making the method more accessible for engineers. Additionally, the SLC method tends to be more robust in the presence of high local Mach numbers. Because it solves the flow along individual streamlines rather than solving the entire system at once, it can accommodate local supersonic regions without destabilizing the solution procedure. In contrast, the matrix method's global solution strategy is more sensitive to such flow features, particularly when shocks are present. Nonetheless, both methods rely on similar modeling assumptions and suffer from the same limitations, such as the need for empirical closure to account for viscous effects and losses.

2.5.5 Euler through-flow method

The limitations of the SLC and matrix methods, particularly their inability to capture shocks and predict mass flow rates, and the continued growth of computational resources in the 1980's have motivated the development of more advanced through-flow models that solve more comprehensive laws of fluid motion, namely the Euler and the Navier-Stokes equations. These newer CFD-based approaches differ fundamentally in their numerical foundations. Early methods often relied on the finite difference method (FDM) for their simplicity. However, FDM is inherently limited to structured grids and does not guarantee the conservation of mass, momentum, or energy. In contrast, the finite volume method (FVM) became the preferred choice due to its direct discretization of the integral form of conservation laws. This formulation offers better physical consistency, particularly in the presence of discontinuities such as shock waves, and enables application on unstructured meshes for handling real geometries [88]. On the other hand, the finite element method (FEM), which was originally developed for diffusive structural mechanics problems, has not been adopted as widely in CFD as the FVM, though its use is steadily increasing. Only few through-flow solvers have been developed based on FEM formulations [91, 152]. Furthermore, hybrid approaches like the Discontinuous Galerkin method, combining features of FEM and FVM, are under active development and show promising capabilities for future applications [85]. However, to the best of the author's knowledge, no TF model has been developed based on the Discontinuous Galerkin method yet. One possible reason is that high-order accuracy is of limited interest in through-flow modeling, since the dominant errors already stem from the strong physical modeling assumptions rather than from the spatial discretization. Finally, it should also be noted that meridional simulations based on the finite element or finite volume method mainly rely on a fixed mesh of the fluid domain, as opposed to earlier streamline-based approaches where the computational grid evolves iteratively with the flow solution.

Another major advancement in through-flow modeling came with the introduction of time-marching methods. First proposed by Spurr [175], the method gradually gained traction throughout the 1990's and has since evolved, with further refinements appearing in later studies for Euler through-flow solvers [13, 47, 140, 181]. Time-marching formulations are based on the pseudo-unsteady resolution of the governing equations. In this method, the transient flow is advanced in artificial time until a steady-state solution is reached. This capability represents a clear advantage over earlier streamline-based and matrix approaches, which are fundamentally limited by their inability to robustly handle the transition in the governing equations from elliptic to hyperbolic type as the flow passes from the subsonic to the supersonic regime [40]. With time-marching, there is thus no particular restriction on the flow Mach number or the flow regime. Furthermore, this formulation also enables a more flexible and consistent treatment of blade force modeling. In many earlier TF methods, the circumferential momentum equation is not explicitly solved, but rather, it is used to compute the magnitude of the blade force, which is thus defined by its tangential component. This simplification can lead to convergence difficulties, particularly in configurations with high flow deflection or in the presence of temporary backflow in the blade channels [181]. In contrast, time-dependent formulations solve all three momentum equations throughout the domain. This allows for a more general and robust specification of the blade force magnitude, and helps stabilize computations across a wider range of flow conditions.

The *Euler through-flow methods* are based on the circumferentially averaged Euler equations, which govern the motion of a compressible fluid without viscosity. Removing the diffusive fluxes from the general through-flow equations 2.9 and considering the time-derivative of the conserved variables yields

$$\frac{\partial \overline{\mathbf{u}}}{\partial t} + \frac{1}{b}\frac{\partial b\overline{\mathbf{F}}}{\partial x} + \frac{1}{rb}\frac{\partial rb\overline{\mathbf{G}}}{\partial r} = \overline{\mathbf{S}}. \tag{2.37}$$

In this equation the vector of conserved variables is

$$\overline{\mathbf{u}} = \left[\begin{array}{ccccc} \overline{\rho}, & \overline{\rho}\widetilde{V_x}, & \overline{\rho}\widetilde{V_r}, & \overline{\rho}\widetilde{V_\theta}, & \overline{\rho}\widetilde{E_t} \end{array} \right]^T, \tag{2.38}$$

where ^{T} corresponds to the transpose and E_t the total energy. The inviscid fluxes are

$$\begin{aligned}\overline{\mathbf{F}} &= \left[\ \overline{\rho}\widetilde{V_x},\ \ \overline{\rho}\widetilde{V_x}\widetilde{V_x}+\overline{p},\ \ \overline{\rho}\widetilde{V_x}\widetilde{V_r},\ \ \overline{\rho}\widetilde{V_x}\widetilde{V_\theta},\ \ \overline{\rho}\widetilde{V_x}\widetilde{H_t}\ \right]^T, \\ \overline{\mathbf{G}} &= \left[\ \overline{\rho}\widetilde{V_r},\ \ \overline{\rho}\widetilde{V_r}\widetilde{V_x},\ \ \rho\widetilde{V_r}\widetilde{V_r}+\overline{p},\ \ \overline{\rho}\widetilde{V_r}\widetilde{V_\theta},\ \ \overline{\rho}\widetilde{V_r}\widetilde{H_t}\ \right]^T.\end{aligned} \tag{2.39}$$

The source term on the right-hand side of Eq. 2.37 has several contributions:

$$\overline{\mathbf{S}} = \overline{\mathbf{S_c}} + \mathbf{S_{bi}} + \overline{\mathbf{S_s}}. \tag{2.40}$$

The first term,

$$\overline{\mathbf{S_c}} = \frac{1}{r}\left[\ 0,\ \ 0,\ \ \overline{\rho}\widetilde{V_\theta}\widetilde{V_\theta}+\overline{p},\ \ -\overline{\rho}\widetilde{V_r}\widetilde{V_\theta},\ \ 0\ \right]^T, \tag{2.41}$$

stems from the evaluation of the flux divergence in cylindrical coordinates. The next term represents the effects of the inviscid blade force and is defined as

$$\mathbf{S_{bi}} = \left[\ 0,\ \ f_{b,x},\ \ f_{b,r},\ \ f_{b,\theta},\ \ e_b\ \right]^T. \tag{2.42}$$

Formally, this term contains the three components of the inviscid blade force as well as the energy source term associated with the work done by this force on the flow. The same naming convention will be used for all other blade force contributions, including their viscous component. Finally, the last contribution $\overline{\mathbf{S_s}}$ represents the unclosed stresses introduced by the averaging process.

One advantage of the Euler-based through-flow approach over the older methods is that it solves the axial momentum equation. This feature enables the prediction of both the mass flow rate and shock waves within the meridional plane, as well as the ability to capture two-dimensional recirculation zones. While such recirculations are, in theory, not visible in an azimuthally averaged flow unless they are dominant in the mean field, Liu et al. [127] notably demonstrated that these features can be captured by TF models. In terms of shock representation, several studies [13, 182] have shown that the Euler through-flow equations exhibit different shock-capturing performance in the analysis mode, where the blade force formulation uses a specified camberline, or in design mode, where the tangential momentum distribution rV_θ is prescribed. Moreover, the quality of the predicted shocks must still be interpreted with caution because they are only axisymmetric by nature, whereas the actual shocks are usually not, which should in theory result in a distributed rather than abrupt flow variation. As the impact of the shock on the flow depends on its orientation, a significant error can be expected. Dedicated shock-capturing techniques have thus been developed [115, 147, 166]. A detailed overview of the numerical aspects of Euler through-flow modeling is provided by Sturmayr [181].

Overall, Euler through-flow methods offer improved accuracy and predictive capabilities compared to earlier models and are thus still widely used and actively developed [143, 160]. However, the Euler formulation remains inviscid. In particular, it inherently neglects viscous effects, turbulence, or the associated blade friction forces. These physical phenomena must be introduced through empirical models. In practice, viscous blade forces can be reintroduced as additional source terms to the Navier-Stokes formulation, as if the blade force was contained within the averaged Euler equations.

One another notable limitation shared by streamline curvature and Euler-based through-flow models lies in their inviscid treatment of the annulus endwalls, where a slip boundary condition is typically assumed. This simplification is widely recognized as a major shortcoming of such models. To address this, a common practice involves introducing an aerodynamic blockage factor, which adjusts the effective flow area to better reflect the impact of boundary layers near the hub and casing. This factor is estimated using the boundary layer theory and serves as an approximation of the displacement thickness caused by wall-bounded viscous effects [38]. However, it is highly sensitive to empirical calibration and often ill-suited for capturing the endwall flow behavior [95]. As a results, inaccuracies in estimating aerodynamic blockage can result in stage mismatches, where some compressor stages fail to operate at their intended design conditions, ultimately degrading overall performance prediction.

2.5.6 Navier-Stokes through-flow method

These challenges have driven the development of through-flow methods that directly solve the Navier–Stokes equations, allowing for more realistic modeling of viscous effects, including those near endwalls. The *Navier-Stokes through-flow* equations can be directly obtained from Eq. 2.9 and read

$$\frac{\partial \overline{\mathbf{u}}}{\partial t} + \frac{1}{b}\frac{\partial b\left(\overline{\mathbf{F}} - \overline{\mathbf{F_v}}\right)}{\partial x} + \frac{1}{rb}\frac{\partial rb\left(\overline{\mathbf{G}} - \overline{\mathbf{G_v}}\right)}{\partial r} = \overline{\mathbf{S}}, \tag{2.43}$$

where the inviscid fluxes are also given by Eq. 2.39 and the viscous fluxes are

$$\begin{aligned}
\overline{\mathbf{F_v}} &= \left[\begin{array}{ccccc} 0, & \overline{\tau_{xx}}, & \overline{\tau_{xr}}, & \overline{\tau_{x\theta}}, & \overline{\tau_{xj}}\widetilde{V_j} - \overline{q_x} \end{array}\right]^T, \\
\overline{\mathbf{G_v}} &= \left[\begin{array}{ccccc} 0, & \overline{\tau_{xr}}, & \overline{\tau_{rr}}, & \overline{\tau_{r\theta}}, & \overline{\tau_{rj}}\widetilde{V_j} - \overline{q_r} \end{array}\right]^T.
\end{aligned} \tag{2.44}$$

Compared to the Euler through-flow equations, the source term $\overline{\mathbf{S}}$ also contains additional terms, including

$$\overline{\mathbf{S_{cv}}} = \frac{1}{r}\left[\begin{array}{ccccc} 0, & 0, & -\overline{\tau_{\theta\theta}}, & \overline{\tau_{r\theta}}, & 0 \end{array}\right]^T, \tag{2.45}$$

from the evaluation of the flux divergence in cylindrical coordinates, and the contribution of the viscous blade force defined as

$$\mathbf{S_{bv}} = \left[\begin{array}{ccccc} 0, & f_{v,x}, & f_{v,r}, & f_{r,\theta}, & e_v \end{array}\right]^T. \tag{2.46}$$

Finally, the stress $\overline{\mathbf{S_s}}$ contains additional components in the energy equation stemming from the average of the product $\tau_{jk}V_j$.

NS through-flow solvers include the capabilities of Euler-based methods, while capturing the axisymmetric boundary layer at the endwalls. Therefore, a more realistic prediction of the variation of flow variables across the span can be achieved. Numerical implementations typically rely on finite volume schemes with mesh refinement in the endwall regions to accurately compute the boundary layer while enforcing no-slip conditions at the endwalls. Similarly to Euler methods, the mesh is clustered at the blade leading and trailing edge to accurately capture the strong gradients there.

Navier-Stokes-based through-flow models have been proposed occasionally. Among the notable contributions, Fay et al. [60] pioneered their use on a single stator row. Later, Simon [168] developed a full solver based on a finite volume discretization and tested multiple turbulence models to close the Reynolds stress. Simon also provided detailed numerical methods involved in his TF models. Further developments have remained relatively isolated [105, 185] and most industrial applications still rely on less comprehensive models.

To mitigate the limitations of earlier approaches, researchers have progressively introduced corrective terms to mimic viscous behavior. For example, Howard and Gallimore [97] extended a classical streamline curvature model by incorporating turbulent diffusion and endwall shear stress effects. Their adjustments included a no-slip condition at the endwall to better emulate the physics captured by a full viscous formulation. These enhancements bring traditional methods closer to the accuracy of Navier–Stokes solvers by decreasing the need for empirical information.

Nevertheless, Navier–Stokes-based TF models are not without shortcomings. While they offer improved wall modeling, they still struggle with capturing three-dimensional endwall losses arising from non-axisymmetric secondary flows. Furthermore, circumferential, unsteady and aperiodic stresses are typically not resolved or are modeled in a very rudimentary way. The dependence on turbulence models to close the Reynolds stress also introduces a level of empiricism that impacts the generality and reliability of predictions. In summary, the reliability of the through-flow results depends on the accuracy and the relevance of the chosen closure models.

2.6 State-of-the-art of closure modeling

One of the most important results in the context of TF modeling was demonstrated by Simon [168] and others [14, 102, 185]: when the full Adamczyk's formulation is implemented and the exact value of source terms extracted from corresponding higher-fidelity 3D computations is used, the resulting TF solution shows a quasi-perfect match[1] with the azimuthally averaged 3D reference. This demonstrates that, in principle, the TF framework is capable of fully capturing the dominant aerodynamic features governing turbomachinery performance, provided that the correct source terms are supplied.

However, these exact values are often elusive because the unclosed terms depend on quantities that are not resolved by the through-flow solver. This introduces what is commonly known as the closure problem, i.e. the challenge of approximating the effects of unresolved physics in a low-fidelity modeling environment. In most practical applications, these source terms are either modeled using empirical or semi-empirical laws, or sometimes simply neglected, both of which introduce uncertainties into the solution. The next sections are devoted to this key issue. The origin and impact of unclosed terms arising from the azimuthal averaging process are reviewed and a classification of the different modeling approaches developed to represent them are discussed. These sections aim to clarify how the treatment of closure terms fundamentally affects the robustness and the accuracy of TF simulations by identifying the types of errors they introduce and by discussing their respective domains of validity. The literature review presented here focuses on the main representative methods, while deliberately not citing every single publication: referencing all works in the field would be a colossal and ultimately unhelpful task, as many methods are repeatedly reused, adapted, or renamed by different authors.

[1]The remaining differences are primarily attributed to small inconsistencies between the two types of simulations, as well as minor modeling and numerical errors.

2.6.1 Relative importance of source terms

An important preliminary step before focusing on modeling, as done in the study of Section 2.4, is to assess the relative importance of each unclosed source term in the TF equations. This prioritization helps determine which unknown terms require accurate modeling efforts and which ones could be reasonably neglected without significantly degrading the quality of the results. This need for prioritization was already recognized in early studies [2, 103, 173] and later explored in detail by Simon [168]. His analysis identified that the most critical contributions for accurately reproducing the flow physics are

- the inviscid and the viscous blade forces,
- the Reynolds stress, especially for the endwall flows,
- and the circumferential stress, stemming from the fourth averaging in the Adamczyk's cascade.

The inclusion of blade forces in through-flow modeling is a relatively straightforward requirement, as their absence would reduce the system to a simple channel flow without any interaction between the fluid and the blade geometry. While the necessity of inviscid blade forces has long been acknowledged, the same cannot be said for viscous blade forces. The widespread use of inviscid through-flow models in the literature suggests that viscous effects have often been either simplified or neglected in favor of other terms. However, in the vicinity of the annulus endwalls, it becomes clear that shear stress plays a significant role and cannot be disregarded. Moreover, Simon has shown that incorporating viscous blade forces is essential, particularly in low-speed compressor cases, to correctly reproduce the observed levels of aerodynamic losses. This finding stands in contrast with earlier results of the litterature [15, 158]. Contrary to the blade walls, the annulus endwalls are still present in the averaged flow and the contribution of the turbulence effects is important in these regions. The Reynolds stress is thus significant.

The circumferential stress has a lower importance but it can have a non-negligible contribution in regions of high flow non-uniformities: it plays a key role in shaping the radial distribution of losses and should not be overlooked when accurate performance predictions are required [102]. When unsteadiness is considered, the deterministic stress has a non-negligible contribution, although its influence is of lesser importance compared to the circumferential stress. The aperiodic stress accounting for flow aperiodicity between blade row passages is often neglected if the operating conditions are stable. On the other hand, it should be included if mistuning ought to be analysed.

The relative importance of these terms can nonetheless vary depending on the flow location, the specific flow conditions and the design of the turbomachinery component being analyzed. The following sections will review how these terms are typically modeled and highlight the associated error compared to the exact source terms.

2.6.2 Closure of blade forces

Blade forces explicitly appear during the averaging process because the integration bounds of the averaging are not constant over the domain. These terms represent the forces exerted on the flow by the implicit presence of the blade in the two-dimensional meridional flow.

2.6.2.1 Blade force contributions

The contributions of the inviscid and viscous blade forces, $\mathbf{S_{bi}}$ and $\mathbf{S_{bv}}$ respectively, are mathematically defined as

$$\mathbf{S_{bi}} = \frac{1}{2\pi b}\sum_N \begin{bmatrix} 0 \\ -\left[p\frac{\partial\theta}{\partial x}\right]_{B_1}^{B_2} \\ -\left[p\frac{\partial\theta}{\partial r}\right]_{B_1}^{B_2} \\ \left[\frac{p}{r}\right]_{B_1}^{B_2} \\ \left[\frac{p}{r}\right]_{B_1}^{B_2}\Omega r \end{bmatrix}, \quad \mathbf{S_{bv}} = \frac{1}{2\pi b}\sum_N \begin{bmatrix} 0 \\ \left[\tau_{xj}\frac{\partial\theta}{\partial j}\right]_{B_1}^{B_2} \\ \left[\tau_{rj}\frac{\partial\theta}{\partial j}\right]_{B_1}^{B_2} \\ \left[\tau_{\theta j}\frac{\partial\theta}{\partial j}\right]_{B_1}^{B_2} \\ \left[\tau_{\theta j}\frac{\partial\theta}{\partial j}\right]_{B_1}^{B_2}\Omega r - \left[q_j\frac{\partial\theta}{\partial j}\right]_{B_1}^{B_2} \end{bmatrix}, \tag{2.47}$$

where Ω is equal to the rotation speed of the shaft, $\Omega_{\mathbb{R}}$, for a rotor blade or 0 for a stator blade, and

$$\left[Q\frac{\partial\theta}{\partial x}\right]_{B_1}^{B_2} = Q_{B_2}\frac{\partial\theta_{B_2}}{\partial x} - Q_{B_1}\frac{\partial\theta_{B_1}}{\partial x}. \tag{2.48}$$

These contributions require the knowledge of both pressure and shear stress on both sides of the blade, which are unfortunately unknown due to the circumferential averaging. Therefore, the blade forces have to be approximated from known averaged quantities. To do so, the modeling is often based on the decomposition of the blade force into distinct physical phenomena. In the case of the inviscid blade force, for example, the two main physical effects, i.e. the deflection and the confinement of the flow, can be identified mathematically by expressing the upper and lower surfaces of the blade as a function of the camber line cl and blade blockage factor b [102], $\theta_{B_{1,2}} = \theta_{cl} \pm \frac{\pi b}{N}$, so that

$$\begin{aligned} \left(\frac{\partial\theta}{\partial j}\right)_{B_1} &= \left(\frac{\partial\theta}{\partial j}\right)_{cl} + \frac{\pi}{N}\frac{\partial b}{\partial j}, \\ \left(\frac{\partial\theta}{\partial j}\right)_{B_2} &= \left(\frac{\partial\theta}{\partial j}\right)_{cl} - \frac{\pi}{N}\frac{\partial b}{\partial j}. \end{aligned} \tag{2.49}$$

Introducing these expressions into the inviscid blade force $\mathbf{S_{bi}}$, the two contributions to the inviscid blade forces are found to be

$$\mathbf{S_{bi_1}} = \frac{1}{N}\sum_N \begin{bmatrix} 0 \\ \frac{p_{B1}+p_{B2}}{2b}\frac{\partial b}{\partial x} \\ \frac{p_{B1}+p_{B2}}{2b}\frac{\partial b}{\partial r} \\ 0 \\ 0 \end{bmatrix}, \quad \mathbf{S_{bi_2}} = \frac{1}{2\pi b}\sum_N \begin{bmatrix} 0 \\ -\left[p\right]_{B_1}^{B_2}\left(\frac{\partial\theta}{\partial x}\right)_{cl} \\ -\left[p\right]_{B_1}^{B_2}\left(\frac{\partial\theta}{\partial r}\right)_{cl} \\ \left[\frac{p}{r}\right]_{B_1}^{B_2} \\ \left[\frac{p}{r}\right]_{B_1}^{B_2}\Omega r \end{bmatrix}. \tag{2.50}$$

The resulting term $\mathbf{S_{bi_1}}$ represents the effect of the blade blockage, i.e. the contraction of the flow inside the blade passage due to the blade thickness. This blockage force is aligned with the gradient of the blockage factor. The second term $\mathbf{S_{bi_2}}$ represents the flow deflection in the blade row passage. The deflection force is oriented perpendicular to the blade camber surface. Finally, the viscous term $\mathbf{S_{bv}}$ represents loss generation due to shear stress acting on the blade walls. It is related to the boundary layers around the blade walls, and thus referred to as 2D profile loss.

Depending on the application, the blade forces can either be extracted a posteriori from blade-resolved CFD by different circumferential averaging techniques [109, 111, 168, 185], or they can be prescribed via closure models that express the forces in terms of local flow variables, geometry, and calibrated correlations. The approach used to close the blade force terms depends on the nature of the problem being addressed. In *analysis* or *direct* problems, the blade geometry, such as the camber line, is specified in advance and the objective is to determine the resulting flow field and performance. Conversely, in *design-type* or *inverse* problems, however, the desired aerodynamic performance is prescribed, such as a target distribution of circumferential velocity, and the corresponding blade geometry is sought. This study primarily focuses on the analysis framework, although certain aspects related to design-oriented formulations are also discussed. It is worth noting that the analysis and design approaches are not strictly exclusive: design formulations can be applied to analysis problems, and vice versa, depending on the context and modeling strategy. In practice, however, the analysis mode is more widely documented and developed in the literature.

2.6.2.2 Actuator disk method

A first method, known as the *actuator disk theory* or the Rankine-Froude theory, for modeling blade rows consists in replacing the blades by an equivalent discontinuity surface positioned at fixed axial locations, across which the flow experiences a sudden change due to surface forces. This approach, as presented by Horlock [94], has been introduced to enhance blade row representation in radial equilibrium analysis, and it continues to be employed today in turbomachinery studies [135]. The actuator disk model is based on the assumption that there is no interaction between the blades. As shown in Fig. 2.11, the flow is considered to be continuous except at the disk, where a discontinuity in pressure and velocity occurs. Discontinuities in stagnation pressure, enthalpy, and flow deviation are prescribed to mimic blade row effects. An extension of this approach is the *Blade Element Theory* (BET) [67], which accounts for radial variations in blade loading. At each radius, localized blade forces are evaluated from airfoil section data, either through lift and drag polars or CFD extractions.

Although originally developed for propellers and helicopter rotors, both methodologies have been applied to turbomachinery, notably to fan configurations [68, 77]. However, they do not model the detailed flow phenomena occurring within the blade rows. Actuator disk models neglect mass flow redistribution by the blades, blockage, swirl effects, or shock phenomena within blade passages, and their accuracy depends strongly on the quality of the prescribed jumps of total quantities [108]. At high pressure ratios, they may encounter convergence issues and spurious wave reflections at the discontinuity plane. Similarly, BET relies on isolated blade section data and thus cannot capture 3D effects such as blade row interactions. These effects are relatively limited when the number of blades is small, as in the case of propellers, but they become much more significant in compressors or turbines.

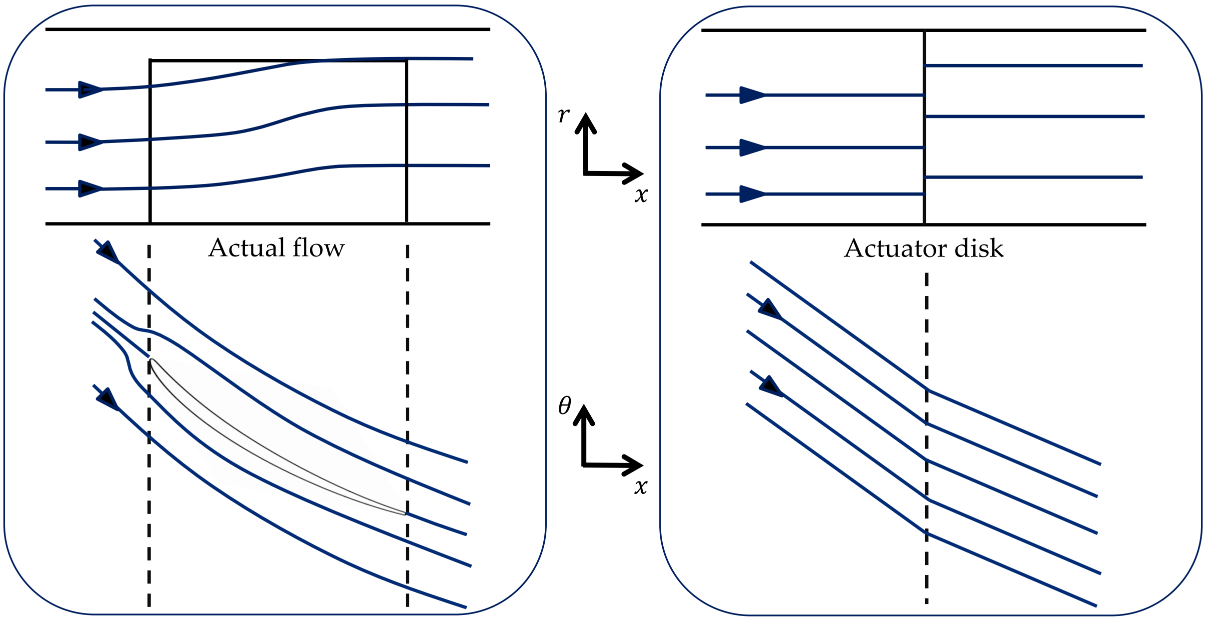

Figure 2.11: Schematic of the flow modeled by actuator disk compared to the actual flow for the meridional and blade-to-blade streamlines.

2.6.2.3 Body force approach

A more widespread methodology is the *Body Force Modeling* (BFM) approach. While actuator disk models represent blades as discontinuity surfaces, the body force approach distributes equivalent forces throughout the entire volume swept by the blades. In other words, instead of imposing a surface discontinuity, the blade row is replaced by an axisymmetric region where volumetric forces are distributed in the blade passage and applied to reproduce flow turning, blockage, and losses in finite-volume solvers. This formulation arises directly from the circumferential averaging of the Navier–Stokes or Euler equations, which naturally introduces additional body force terms interpretable as blade forces. Several studies have shown that this volumetric formulation offers clear advantages over the actuator disk model [68]. Since the source terms are active throughout the blade row region rather than on a single discontinuity plane, the body force approach can capture phenomena within the blade passage. This makes it particularly well suited for modeling turbomachinery blade rows, where the number of blades is large and three-dimensional flow interactions play a significant role. Its relevance becomes even greater when the aspect ratio is low and when substantial changes in the throughflow area occur across the blades, as is the case for highly loaded blade rows.

The concept of a distributed body-force field was first introduced by Marble [132], who represented a blade row as an axisymmetric region with an infinite number of blades and replaced their effect on the flow by external volumetric forces added to the equations of motion. These forces impose the streamwise distribution of the blade loading while being circumferentially averaged. As shown in Fig. 2.12, the blade forces are decomposed into two contributions: a component normal to the mean-flow path, $\mathbf{f_n} = \left[f_{n,x}\,,\quad f_{n,r}\,,\quad f_{n,\theta}\right]^T$, and a loss component, $\mathbf{f_p} = \left[f_{p,x}\,,\quad f_{p,r}\,,\quad f_{p,\theta}\right]^T$, aligned with the relative velocity. Using this representation, Marble derived relations linking thermodynamic quantities to these forces in order to produce the same net turning and entropy increase to the flow as

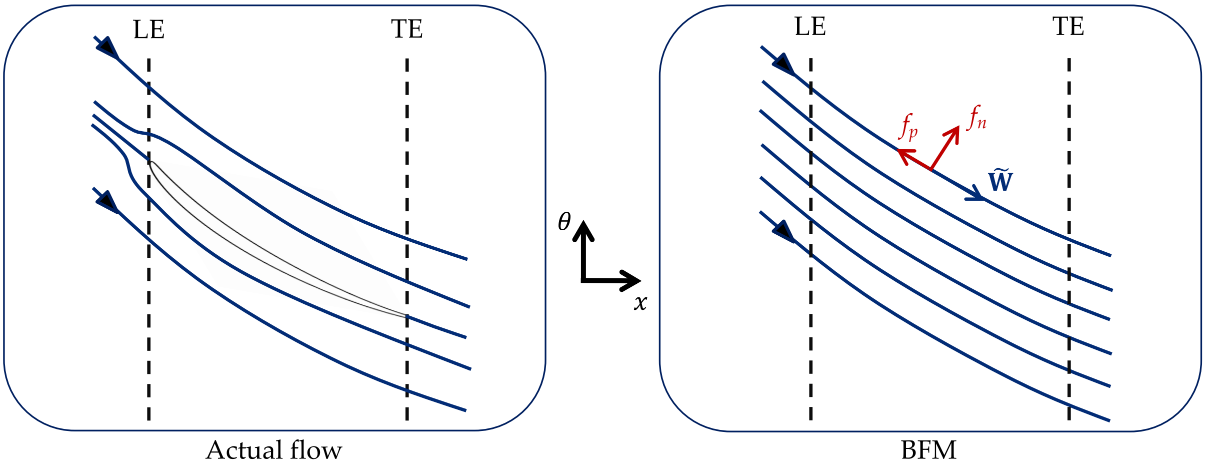

Figure 2.12: Meridional flow schematic: actual blade-resolved flow versus body-force model (BFM). The BFM replaces the blade row with a volumetric force field that reproduces an equivalent meridional streamline pattern; the body force is decomposed into a normal (turning) component $\mathbf{f_n}$ and a parallel (loss) component $\mathbf{f_p}$ aligned with the local velocity $\widetilde{\mathbf{W}}$.

the real blade row. Specifically, variations in tangential momentum, entropy and total enthalpy along a streamline are related to body force components through

$$
\begin{aligned}
\widetilde{V_m}\frac{\partial r\widetilde{V_\theta}}{\partial m} &= r f_{n,\theta} \,, \\
\widetilde{V_m}\frac{\partial \widetilde{s}}{\partial m} &= -\frac{\widetilde{W}}{\overline{\rho}\widetilde{T}} f_p \,, \\
\widetilde{V_m}\frac{\partial \widetilde{H_t}}{\partial m} &= \Omega r \left(f_{n,\theta} + f_{p,\theta} \right) \,,
\end{aligned}
\tag{2.51}
$$

where s is the entropy and $\widetilde{W}$ is the velocity expressed in the frame of reference of the considered blade row. The body forces are designed to ensure that only parallel forces $\mathbf{f_p}$ account for entropy generation and, consequently, losses. By contrast, the normal force $\mathbf{f_n}$, which governs the turning and associated pressure rise, deflects the flow without generating losses. Moreover, across a stator, i.e. a stationary blade row in the inertial frame, $\Omega = 0$ and the stagnation enthalpy remains constant. Thus, $\mathbf{f_n}$ and $\mathbf{f_p}$ are akin, respectively, to the deflection force defined in $\mathbf{S}_{\mathrm{bi}_2}$ and the viscous force in $\mathbf{S}_{\mathrm{bv}}$.

This approach was subsequently widely used in though-flow models, particularly for the SLC and Matrix method [46, 90, 102, 133] and then for finite volume TF models based on the Euler and the Navier-Stokes equations [13, 41, 168]. Several body-force formulations have since been developed. Despite methodological refinements, the central idea has changed little since its introduction. These approaches are presented hereafter.

Blockage force modeling

A key limitation of Marble's original formulation is that it does not natively represent blockage resulting from the finite blade thickness. This omission becomes critical in high-subsonic/transonic regimes, where the effective throat area controls choking and thus the maximum mass-flow rate through a blade row [186]. Accordingly, the blockage factor $b(x, r)$ must be explicitly reintroduced in the TF equations as in Eqs. 2.9. At the source-term level, the blockage contribution $\mathbf{S_{bi_1}}$, i.e. the first component of the inviscid blade-force split, must be retained explicitly, as defined in Eq. 2.50. The most common approach [12, 168] to close this source term is to assume that the average of the lower and upper blade surface pressure coming into play in the force expression is equal to the averaged pressure p computed by the through-flow solver, leading to

$$\mathbf{S_{bi1}} = \left[0\,, \frac{p}{b}\frac{\partial b}{\partial x}\,, \frac{p}{b}\frac{\partial b}{\partial r}\,, 0\,, 0\right]^T . \tag{2.52}$$

Deflection force modeling

The second contribution of the inviscid blade force is most often modelled through a force normal to the relative velocity, so that

$$\mathbf{S_{bi2}} = \left[0\,,\quad f_{n,x}\,,\quad f_{n,r}\,,\quad f_{n,\theta}\,,\quad f_{n,\theta}\Omega r\right]^T . \tag{2.53}$$

Strickly speaking, the deflection force f_{bi_2} defined in Eq. 2.50 is perpendicular to the blade camber surface. In the absence of losses and in the limit of an infinite number of thin blades per row [132], the averaged relative velocity is locally tangent to the blade camber surface, i.e. the blade mean surface. Therefore, in these conditions, the normal blade force, f_n, is also perpendicular to the camber surface. However, in real flows the boundary layer that develops on the blade surfaces causes the mean stream surface to deviate from the camber surface, so this does not hold anymore. If the orthogonality condition to the camber surface were enforced, the deflection force would have a component that is parallel to the velocity, which would generate entropy. However, loss generation should result exclusively from the parallel blade force. The blade deflection force is therefore assumed to be perpendicular to the mean-flow surface by imposing the orthogonality condition

$$\mathbf{f_n} \cdot \widetilde{\mathbf{W}} = \mathbf{f_n} \cdot \left(\widetilde{\mathbf{V}} - \Omega r \mathbf{e}_\theta\right) = 0 \tag{2.54}$$

where $\mathbf{e}_\theta$ is the unit vector in the circumferential direction. This condition prevents a generation of loss in the relative frame of reference and, thus, a generation of entropy. The direction of this force is thus known from Eq. 2.54.

Regarding the computation of the modulus of the deflection force, there are two main types of approaches in the literature. The first type of approach consists in *imposing the local direction of the flow* to reproduce the azimuthally-averaged flow. The second type of approach consists in defining the local force f_n by analogy to the *lift force around isolated airfoils*. These two approaches are detailed below.

The former can be formulated either in analysis mode or in design mode. In the analysis formulation, the flow is assumed to follow the mean flow path given by the camber surface modified by some deviation angle $\delta(x, r)$. This deviation angle accounts for the fact that the actual flow does not exactly follow the camber line because of the presence of the blade boundary layer, as stated above. It is formally defined as the local difference between the mean tangential flow angle $\beta(x, r)$, which is defined in the frame of reference of the considered blade, and the blade (camber line) angle κ so that

$$\delta = \beta - \kappa\,, \tag{2.55}$$

and has to be computed from empirical correlations obtained from cascade flow theory or experimental measurements. In practice, the deviation angle is most often defined at the trailing edge and must then be redistributed along the streamline in order to obtain a streamwise distribution suitable for force modeling.

A first analysis-based formulation, which is widely used in the SLC models [42, 64, 102, 191] but also in Euler TF [143, 160], *explicitly* computes the circumferential component of the force $f_{n,\theta}$ from the circumferential momentum which is not solved anymore in the blade domain. It yields, for each streamtube,

$$f_{n,\theta} = \frac{\dot{m}_m}{r}\frac{\partial\left(r\widetilde{V_\theta}\right)}{\partial m}\,, \tag{2.56}$$

where $\dot{m}_m$ is the mass-flow rate of the streamtube. The circumferential velocity can be obtained from the meridional speed through

$$\widetilde{V_\theta} = \widetilde{V_m}\tan\beta + \Omega r\,, \tag{2.57}$$

and the mean flow angle β is prescribed using Eq. 2.55 and a empirical correlation for δ. The axial and radial components, $f_{n,x}$ and $f_{n,r}$, are then expressed as functions of $f_{n,\theta}$ by enforcing the orthogonality condition on the blade mean surface so that

$$f_{n,x} = -r\frac{\partial\theta_{cl}}{\partial x}\cdot f_{n,\theta} \quad \text{and} \quad f_{n,r} = -r\frac{\partial\theta_{cl}}{\partial r}\cdot f_{n,\theta}\,. \tag{2.58}$$

The two coefficients correspond to the tangent functions of the dihedral angle and the lean angle, respectively [102]. Furthermore, the radial component $f_{n,r}$ has often been neglected for older prismatic blades. For modern blades with strongly three-dimensional profiles, its contribution is non-negligible [168]. In classical SLC formulations, where only the leading-edge and trailing-edge conditions across a blade row are required, Eq. 2.56 is approximated as $\frac{\dot{m}}{r}\left[(r\widetilde{V_\theta})_{\mathrm{TE}} - (r\widetilde{V_\theta})_{\mathrm{LE}}\right]$. Later refinements introduced a prescribed load distribution along the streamline, thereby allowing the computation of a distributed force.

A second analysis, but *implicit*, formulation consists in computing the modulus of the blade force by using a time-marching procedure [168] to enforce the slip condition, Eq. 2.54, through

$$\frac{\partial f_n}{\partial t^*} = -C\left(\widetilde{V_x}n_x + \widetilde{V_r}n_r + \left(\widetilde{V_\theta} - \Omega r\right)n_\theta\right)\,, \tag{2.59}$$

where n_x, n_r and n_θ are the components of the vector normal to the mean flow path, t^* is a pseudo-time and C is a coefficient to control the convergence process. The blade force modulus is thus modified by a restoring force proportional to the orthogonality error between the blade force itself and the actual computed flow direction. Finally, the components of the force are obtained by projecting the modulus onto the normal components of the meridional stream surface. At convergence, the orthogonality condition of Eq. 2.54 is satisfied since the meridional stream surface coincides with the mean flow path. As a result, the flow is constrained to the prescribed deviation angle.

This methodology was first applied by Baralon et al. [13] and Pacciani et al. [143] to the circumferential component of the force and the radial and axial components were then recovered from the relations of Eq. 2.58. It has been shown by Simon [168] that applying it rather to the modulus of the overall blade force leads to a more robust iterative process.

Another implicit methodology, based on a design formulation [182], consists in imposing the circumferential velocity $V_\theta{}^*$ while solving the circumferential momentum equation. The circumferential velocity at the trailing edge is typically derived from the known flow angle using Eq. 2.57. At the leading edge, V_θ is determined by the incoming flow, and the circumferential velocity distribution within the passage is constructed by interpolating between the LE and TE values. A time-marching procedure is then applied to the blade force modulus:

$$\frac{\partial f_n}{\partial t^*} = C\left(\widetilde{V_\theta}^* - \widetilde{V_\theta}\right) . \tag{2.60}$$

As in Eq. 2.59, the blade force modulus is modified by a quantity proportional to the difference between the prescribed velocity, $\widetilde{V_\theta}^*$, and the computed one, $\widetilde{V_\theta}$, until convergence, i.e. $\widetilde{V_\theta} = \widetilde{V_\theta}^*$. Finally, the radial and axial components are recovered from Eq. 2.58. These implicit approaches are thus based on a time differential equation that imposes a restoring force cast as a proportional–integral–derivative (PID) controller and drives the error between the instantaneous and prescribed flow directions to 0. The quality of the solution of both implicit and explicit approaches depends on the accuracy of the empirical correlations and on the axial distributions of the deviation angle or the prescribed circumferential velocity.

Lift-based approaches rely on explicit analysis formulation. The blade force modulus is thus given by algebraic relations that depend on the local flow state and geometry so that the force field responds instantaneously. The deviation angle is computed locally with respect to the blade camber surface and becomes a result of the computation rather than a prescribed value. The components of the force are then obtained by projecting the modulus onto the normal components of the meridional stream surface to enforce the orthogonality condition, Eq. 2.54.

A first model was proposed by Gong [69] and later refined by Peters [150]. By analogy with a compressible flow in a staggered channel, the normal component of the body force is modeled as

$$f_n = \frac{\partial \overline{p}}{\partial x}\frac{\sin(\kappa)}{\cos^2(\kappa)} + \frac{1}{2}\overline{\rho}\frac{K_n}{s_\sigma}\sin(2\delta)\widetilde{W}^2 , \tag{2.61}$$

where

$$s_\sigma = \frac{2\pi r\sqrt{\sigma}\cos\kappa}{N} , \tag{2.62}$$

is the blade-to-blade staggered spacing, σ is the solidity and $K_n(x, r)$ is a model coefficient that has to be calibrated using empirical correlations or higher-fidelity data (e.g., RANS or experiments). The model is thus sensitive to operating conditions. Moreover, the pressure-gradient contribution has proved to add numerical stiffness [187].

Hall [78] then proposed a calibration-free model by analogy with the inviscid incompressible flow around a isolated flat-plate airfoil. Thollet [185] showed that, for high-subsonic and supersonic regimes, a compressibility correction is required and introduced the metal blockage. The normal force is expressed as

$$f_n = \tfrac{1}{2}\overline{\rho}\frac{K_{\text{Mach}}}{s_b b n_{\kappa,\theta}} 2\pi\,\delta \widetilde{W}^2\,, \tag{2.63}$$

where s_b is the blade pitch, $n_{\kappa,\theta}$ is the tangential component of the vector normal to the blade mean surface and K_{Mach} is the Prandtl-Glauert correction factor [7] given by

$$K_{\text{Mach}} = \begin{cases} \min\left(\frac{1}{\sqrt{1-\widetilde{\text{M}}_W^2}}, 3\right), & \text{if } \widetilde{\text{M}}_W < 1 \\ \min\left(\frac{4}{2\pi\sqrt{\widetilde{\text{M}}_W^2-1}}, 3\right), & \text{if } \widetilde{\text{M}}_W > 1 \end{cases} \tag{2.64}$$

with $\widetilde{\text{M}}_W = \widetilde{W}/\widetilde{a}$ the local mach number. Lately, Crea et al. [36] introduced a calibration factor K_c to scale the ideal lift of a flat plate toward the actual flow response.

Thollet also proposed his own model based on the thin airfoil theory to address some limitations of Gong's formulation. In his lift analogy, the normal component is written as

$$f_n = \overline{\rho}\frac{\sigma}{s_\sigma} 2\pi\left(\beta - K(x)\beta_0\right)\widetilde{W}^2, \tag{2.65}$$

where β_0 is a local zero-lift relative angle and

$$K(x) = \max\left\{1 + K_0\left(1 - 2\frac{x - x_{\text{LE}}}{x_{\text{TE}} - x_{\text{LE}}}\right), 1\right\} \tag{2.66}$$

is an offsets function that improves the prediction of the choke mass–flow rate. K_0 is a calibration constant. The main limitation is thus the need for manual calibration, which impacts reproducibility and robustness.

Another model worth mentioning is based on the local centripetal acceleration of the relative flow due to the local curvature. For instance [20, 161], a model for the normal force reads

$$f_n = \frac{1 - \widetilde{M}_x^2}{\left(1 - \widetilde{M}^2\right)\cos^2(\kappa)} \frac{\overline{\rho}\widetilde{W}_{cl}^2}{r_m}\,, \tag{2.67}$$

where $\widetilde{W}_{cl}$ is the velocity tangent to the camber line. Other authors [27, 129, 208] have also relied on a centripetal acceleration, but introduced different multiplicative factors or corrective terms.

Finally, some analytical models have also been developed, such as the one proposed by Pazireh [147], which is free of any calibration. In this formulation, the normal force is written as

$$f_n = \frac{N}{4\pi r} \frac{\overline{\rho}\left(W_{B_1}^2 - W_{B_2}^2\right)}{n_\theta}\,, \tag{2.68}$$

where the relative velocities on the suction side and the pressure side, respectively, are computed from cascade analytical laws.

Viscous force modeling

The viscous blade force is modelled through a parallel force that is not only tangential to the camber surface but parallel with the relative flow velocity so that

$$\mathbf{S_{bv}} = \left[0\,,\quad f_{p,x}\,,\quad f_{p,r}\,,\quad f_{p,\theta}\,,\quad f_{p,\theta}\Omega r\right]^T. \tag{2.69}$$

This assumption on the force direction is appropriate when losses arise predominantly from skin friction. It is nevertheless an idealization, since boundary-layer crossflow can introduce a small transverse component that axisymmetric through-flow theory does not rigorously capture.

Two principal strategies are commonly used to determine the modulus of the parallel force. The first *prescribes losses* through a *distributed loss model*. Using Marble's loss equation from Eq. 2.51 or, equivalently the Gibbs relation incorporated into the Euler equations [19, 48, 93], the entropy production is related to the dissipative force as

$$f_p = \overline{\rho}\widetilde{T}\frac{\widetilde{V_m}}{\widetilde{W}}\frac{\partial \widetilde{s}}{\partial m}\,, \tag{2.70}$$

where $\widetilde{s}$ is the entropy. This equation is formally valid for an inviscid flow but it can be extended to viscous flow keeping the modeling error small [168]. In the regions of large gradients at the casing and hub, the relation introduces an incorrect level of entropy rise since the losses are already partly accounted for by the viscous and turbulent stresses in the endwall flows. However, this error is rather small because the relative contribution of $\frac{\partial \widetilde{s}}{\partial m}$ to the global entropy production is the lowest in these regions. Equivalently, the magnitude of the friction force can be recast as

$$f_p = \cos(\kappa)\,\frac{\overline{p}}{\overline{p}^{\Omega}_{t,W}}\frac{\partial \overline{p}^{\Omega}_{t,W}}{\partial m}\,, \tag{2.71}$$

where $\overline{p}^{\Omega}_{t,W} = \overline{p}\left(\frac{\widetilde{T}^{\Omega}_{t,W}}{T}\right)^{\gamma/(\gamma-1)}$ is the rotary total pressure, $\widetilde{T}^{\Omega}_{t,W} = \widetilde{T}_{t,W} - \frac{(\Omega r)^2}{2c_p} = \widetilde{T} + \frac{\widetilde{W}^2}{2c_p} - \frac{(\Omega r)^2}{2c_p}$ is the rotary total temperature et c_p is the heat capacity at constant pressure. In the litterature, this model is usually simplified by neglecting the curvature term $\cos(\kappa)$ [161, 182], and likewise by approximating the pressure ratio as $\frac{\overline{p}}{\overline{p}^{\Omega}_{t,W}} \approx 1$ [147].

The terms $\frac{\partial \widetilde{s}}{\partial m}$ and $\frac{\partial \overline{p}^{\Omega}_{t,W}}{\partial m}$ are often linearized in the axial direction, so that they are approximated, respectively, by

$$\frac{\partial \widetilde{s}}{\partial m} \approx \frac{\Delta \widetilde{s}}{c_m} \quad \text{and} \quad \frac{\partial \overline{p}^{\Omega}_{t,W}}{\partial m} \approx \frac{\Delta \overline{p}^{\Omega}_{t,W}}{c_m}\,, \tag{2.72}$$

where c_m is the length of the streamline. The entropy rise Δs_m and the total pressure jump $\Delta \overline{p}^{\Omega}_{t,W}$ are prescribed either directly [142] or using a loss coefficient ω [48, 173]. This loss coefficient is computed from empirical correlations. Its definition may vary across authors, and the differences will be discussed hereafter. In some works, the loss coefficient $\omega(r)$ is redistributed axially using a weight function to obtain a streamwise profile to improve predictive accuracy [143, 161]. Finally, the entropy variation has also been computed using a local machine efficiency [48, 133], as an alternative to the use of a loss coefficient.

In addition, Pazireh [147] proposed another formulation based on the trailing-edge momentum thickness for directly linking the parallel force to boundary-layer characteristics. This approach builds on the loss determination method of Drela and Youngren [54]. The trailing-edge momentum thickness is prescribed from 2D cascade correlations or from `MISES` computations.

The second methodology to model the parallel force is based on a *drag analogy* of isolated airfoils, as proposed by Howell [98]. Gong [69] then relates loss to drag through

$$f_p = \frac{\overline{\rho}}{s_\sigma} C_D \widetilde{W}^2 \,, \tag{2.73}$$

where C_D is a drag coefficient. This global coefficient was calibrated by Gong using empirical correlations and by Cao using CFD [27], and reported values typically lie in the range $C_D \approx 0.04$–0.05. Some authors [160, 206] have also adopted the generic aerodynamic formulation of the drag force. Most of these approaches rely on the assumption of small incidence angles and are therefore valid primarily in the vicinity of nominal operating conditions. Subsequent developments have thus focused primarily on refining the functional form of C_D. For instance, Peters [150] made C_D depend on the relative Mach number at the inlet via a quadratic polynomial to partially capture off-design behavior. Thollet [185] proposed a similar idea but using the local relative Mach number:

$$C_D = K_{p1} \widetilde{M}_W^2 + K_{p2} \widetilde{M}_W + K_{p3} \,, \tag{2.74}$$

with the coefficients K_{p1}, K_{p2}, K_{p3} calibrated from CFD. A remaining limitation of such forms is the need to recalibrate per speed line, since $\widetilde{M}_W$ varies significantly with rotational speed. To mitigate this sensitivity, Thollet suggested expressing C_D in terms of the local flow coefficient

$$\Phi = \frac{\widetilde{W}_m}{\Omega r} \,, \tag{2.75}$$

instead of the Mach number.

Thollet also proposed a dedicated expression for the drag coefficient to capture the off-design effects, introducing a quadratic dependence on the deviation from the best-efficiency angle so that

$$C_D = C_D^{\eta_{\max}} + 2\pi\sigma \left(\beta - \beta^{\eta_{\max}}\right)^2 \,, \tag{2.76}$$

where $C_D^{\eta_{\max}}$ and $\beta^{\eta_{\max}}$ are, respectively, the local drag coefficient and the relative flow angle at the point of maximum efficiency η. This calibration is robust and requires only a single operating point without re-tuning across speed lines.

Hall [78] developed a similar formulation, based on the maximum-efficiency operating point, that was then extended to compressible regimes through the inclusion of the Mach number correction factor K_{Mach}. The drag coefficient is then written as

$$C_D = 2C_f + 2\pi K_{\text{Mach}} \left(\delta - \delta^{\eta_{\max}}\right)^2 \,, \tag{2.77}$$

where C_f is the flat-plate skin-friction coefficient obtained from a correlation, and $\delta^{\eta_{\max}}$ is the deviation angle at maximum efficiency. It yields

$$f_p = \frac{1}{2}\frac{\overline{\rho}}{s b n_{\kappa,\theta}} C_D \widetilde{W}^2. \tag{2.78}$$

This formulation does not require additional calibration beyond the empirical correlation for C_f.

More recently, Crea et al. [36] modified Hall's expression for C_D by introducing additional calibrated coefficients to tune the model response and compensate for the discrepancy between the simplified flat-plate analogy and the actual blade flow. This approach uses a relatively simple formulation as a basis, while relying on calibration against higher-fidelity data to emulate more complex models. The resulting method improves the prediction of off-design losses compared with the original formulation.

Cao et al. [27] also proposed an additional contribution to the parralel force f_p to account for losses associated with the adverse pressure gradient. The additionel term to Eq. 2.73 is expressed as

$$C_{D,2}\frac{\partial \overline{p}}{\partial x}\frac{\left(\Omega r_{\text{tip}}\right)^2 \widetilde{W}}{\widetilde{V}^3} \tag{2.79}$$

where $C_{D,2}$ is a function of the incidence angle and is calibrated from empirical correlations.

Finally, analytical formulations have also been proposed, such as the model of Pazireh [147], in which the parallel force is expressed as the sum of the volumetric contributions from the suction and pressure sides so that

$$f_p = \frac{\overline{\rho}}{\widetilde{W} n_\theta}\frac{N}{2\pi r}\left(C_{D,B_1}\widetilde{W}^3_{B_1} + C_{D,B_2}\widetilde{W}^3_{B_2}\right). \tag{2.80}$$

Akin to the normal force model, the relative velocities on the suction and pressure sides are obtained from cascade analytical laws but the drag coefficients must be computed from empirical correlations or higher-fidelity data.

2.6.2.4 Alternative approaches

Besides the above formulations, a number of alternative approaches have been proposed that do not fit neatly into any previous BFM category but are rather based on the concept of equivalent volumetric forces. First, a variant of the actuator disk, known as the *actuator duct* or *actuator zone* concept [73], has been proposed where the lift and drag forces derived from airfoil polars are not applied on a discontinuous surface but are axially distributed over the blade row domain in a body-force alike manner. The distribution, however, is largely arbitrary and not necessarily tied to the actual blade geometry, so these models suffer from limitations similar to those of the original actuator disk formulation. As a result, these low-order approaches still require minimal engine information and are mainly suited for preliminary design.

Moreover, *quasi-3D* formulations, influenced by Wu's early work [204], numerically couple axisymmetric TF with cascade flow solvers, enabling a better representation of blade-passage physics than blade-force models. The foundations of this approach were laid by Jennions and Stow [103], who outlined the coupling of an axisymmetric solver providing the stream surfaces with a cascade solver delivering the corresponding blade-force distribution. Building on this concept, Spurr [175] combined a time-marching Euler TF solver with a blade-to-blade method, and demonstrated good agreement with full 3D Euler computations. More recently, Kravtsoff [112] revisited this line of work for axial compressor applications, aiming to reduce empiricism. Blade forces are obtained by solving the incompressible flow in periodic cascade streamsurfaces using the Hess & Smith potential method [84], with viscous effects added through the Von Kármán integral boundary-layer approach [198].

Another method, specific to the modeling of the normal force and referred to as *Immersed Boundary with Smeared Geometry* (IBMSG) method [27, 149] computes the blade force at each iteration to force streamlines to follow the mean flow path by enforcing the slip condition given in Eq. 2.54. This approach is conceptually close to the implicit analysis formulation described earlier, since it also relies on prescribing the blade force direction. However, it differs by being explicit, with the normal force expressed in the form of a penalty law such that

$$f_n = -C\mathbf{W} \cdot \mathbf{n} \,. \tag{2.81}$$

This method remains strongly dependent on the actual blade geometry and the empirical correlations to predict the flow deviation angle. It is referred to as an immersed method because, similarly to early immersed boundary techniques, the boundary condition is imposed through an explicit forcing term added to the governing equations.

Finally, some approaches aim to model the blade forces using either a *surrogate model* or a *interpolated blade-force fields* extracted from database of higher-fidelity simulations. The general idea is to relate the body forces to local flow variables (e.g., relative Mach number, flow coefficient, incidence) and construct response surfaces or interpolation tables. Early efforts [109] interpolated body-force distributions using low-order polynomials. More recently, López de Vega et al. [130] proposed a machine-learning strategy, training separate neural networks for normal and parallel force components of each blade row, validated against blade-resolved data. Such data-driven approaches have been applied not only to the BFM framework discussed above [128, 186], but also to BET methods [145], where lift and drag data for isolated blade sections are interpolated from polar databases as a function of the locally induced velocity. Kiffer et al. [108], on the other hand, used an adaptive geometrical adjustment by defining a distribution of virtual blade gometry from prescribed performance targets stemming from URANS simulations. The main advantage of these methods is that they allow force prediction without direct dependence on blade geometry. However, their accuracy is strongly tied to the quality and completeness of the database: large sets of operating points are needed and the method remains limited by the accuracy of the force extraction procedure itself. Extraction procedures of body forces from high-fidelity data has been discussed by Kiwada [109], Simon [168] and Thollet [185].

2.6.3 Closure of the stress terms

Stresses appear due to the non-linearity of the Navier–Stokes equations. These terms represent the mean influence of the flow fluctuations that are eliminated by the averaging in the meridional plane. These are effects that are not accounted for in the steady axisymmetric throughflow equations. Unlike blade forces, which are logically confined to the blade-row region, stresses are present throughout the entire computational domain, as illustrated in Fig. 2.13.

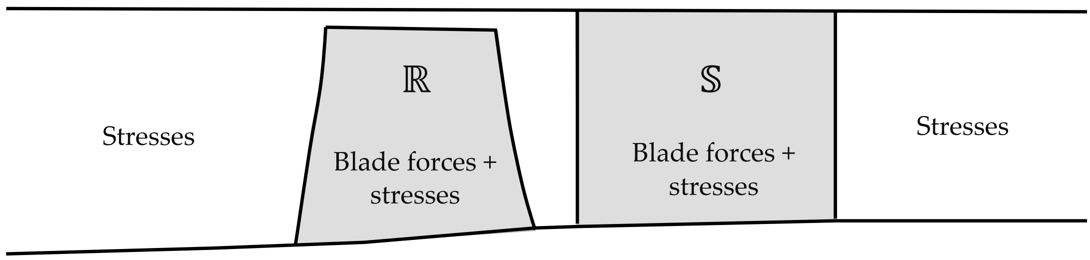

Figure 2.13: Spatial distribution of source terms in the meridional plane of a compressor stage. Blade forces are confined to the blade-row regions, while stresses act throughout the entire domain.

2.6.3.1 Physical interpretation

Compared to blade forces, the stresses are also harder to interpret directly from their algebraic form. Furthermore, it is difficult to attribute a specific physical effect to each stress component because they interact with blade forces and with each other in several mechanisms, as illustrated in Fig. 2.14. A comprehensive introduction to the flow physics underlying stresses is given by Adamczyk [2]. Broadly speaking, stresses are responsible for all unsteady and non-axisymmetric phenomena outside the blade-row regions. The tip-gap flow, in particular, develops consistently outside the blade passages and is therefore entirely represented through the stress terms. These phenomena also include leakage flows, hub and tip boundary layers, and blade wakes. They are also related to additional mechanisms that superimpose with blade forces within the passages, such as secondary flows. For instance, the interaction of individual blades with hub and tip boundary layers is particularly significant and it may challenge the common assumption that viscous forces are limited to simple skin friction aligned with the relative velocity. In reality, loss generation mechanisms arise not only from shear stresses acting along the blade surfaces, but also from stress components that contribute to the overall dissipation. Stresses are also related to key mechanisms such as radial mixing, shock-induced loss, and aerodynamic blockage.

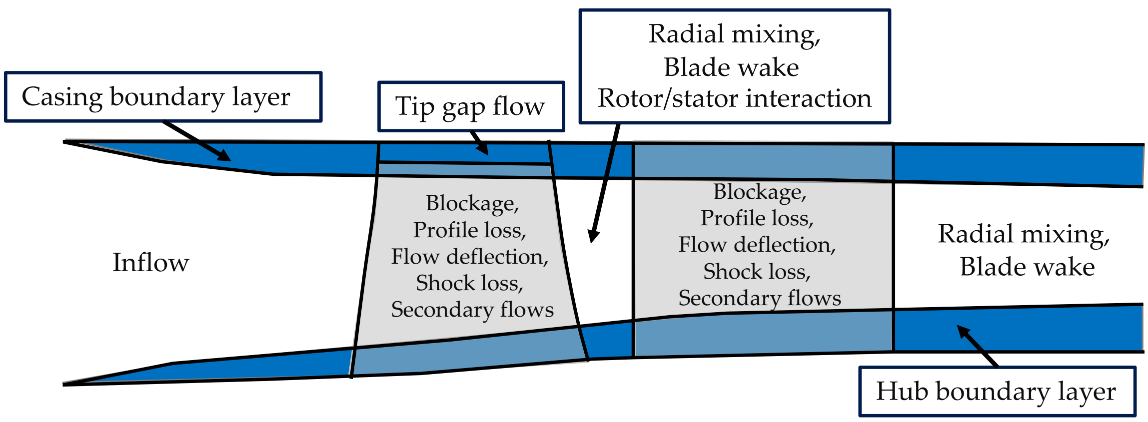

Figure 2.14: Schematic of the main physical mechanisms in a compressor stage contributing to source terms in the meridional plane.

It is however well established that the Reynolds stress accounts for the turbulent effects that are important within the boundary layers and in regions of strong gradients. The characteristics of turbulence have long been studied in general fluid mechanics and also specifically in turbomachinery. These studies highlighted the contribution of the Reynolds stress in wake diffusion and shear-layer mixing. By contrast, the other types of stress have received far less attention, and their physical interpretation remains more elusive.

Simon [168] demonstrated that the circumferential stress primarily includes the effects responsible for radial mixing, i.e. the spanwise redistribution of loss that reduces the gradients close to the endwalls, as well as the aerodynamic blockage. These effects, such as secondary flows, tip leakage or shock-induced loss, are at first order steady. Therefore, they mostly result in contributions to the circumferential stress. For instance, the blockage of the flow close to the hub caused by corner stall was also represented almost entirely by circumferential stress. Moreover, the entropy generation associated with the viscous blade force is in practice inseparable from the contribution of endwall secondary flows represented by the circumferential stress.

The unsteady stress is generally less significant than circumferential stress but becomes non-negligible in high-speed or transonic regimes, where unsteadiness is strong. Physically, its origin in the absolute frame of reference can be decomposed into a spatial contribution, steady in the rotating frame but appearing unsteady in the considered frame of reference, and a purely temporal contribution that remains unsteady in both frames. The first contribution represents the periodic content of the flow tied to rotor–stator interactions. The second contribution of the unsteady stress, which is related to unstable modes such as the rotating stall, was first supposed negligible [3] but it has been shown later that the purely unsteady part of the deterministic stresses can play a significant role [15]. The unsteady stress must thus be included to correctly capture radial mixing and spanwise redistribution in zones of strong blade-row interactions. An example is the interaction of a blade row with an upstream-generated flow distortion: as the radial migration of stator wakes enters a rotor, the centrifugal balance with the radial pressure gradient is weakened compared to the core flow because the wake has lower swirl, causing the wake to drift toward the hub. This downward migration accumulates low-energy fluid and produces a pulsating passage vortex, strongly modulating entropy and secondary-flow structures.

The aperiodic stress has been even less studied than the circumferential or deterministic stress. This stress appears as contributions from surrounding blade rows on the same shaft with circumferential variations at scales unrelated to the pitch of the row of interest, i.e. the blade indexing. Overall, aperiodic stresses are generally neglected because the effect of indexing in axial flow compressors has proved to be small. This is however not the case for turbines [2]. It should also be included if mistuning or inlet flow distortion ought to be analysed.

2.6.3.2 Modeling approach

Different closure techniques have been proposed to evaluate the stresses at a much lower cost than extracting them from 3D simulations including all blade passages [12, 102, 158, 168]. A first class of closure models is directly derived from the mathematical expressions of the stresses in Adamczyk's cascade, aiming to reduce the level of empiricism. Through-flow solvers incorporating such closures are commonly referred to as *high-order through-flow* models, as they explicitly access and exploit higher-order information from the governing equations.

Reynolds stresses are commonly closed by turbulance models. In Navier-Stokes TF solvers, turbulence models are already implemented to account for turbulence effects. Numerous turbulence models have been proposed in the literature [57], ranging from algebraic formulations to two-equation transport models based on the Boussinesq hypothesis, as well as more advanced closures such as second-moment models or nonlinear eddy viscosity models. In practice, it has been shown that a two-equation turbulence model is sufficient to capture the relevant flow features in through-flow computations [168], so no specific adaptation beyond what is used for channel-flow simulations is required. Nevertheless, these models are not without deficiencies: for instance, the Boussinesq approximation assumes turbulence isotropy of the normal stresses, a simplification that is known to introduce modeling errors and remains an active subject of research [58].

Several strategies have been developed to account for the unsteady stress in a steady through-flow framework. One approach consists in treating this stress analogously to turbulence modeling: it is assumed to be transported by the mean flow, and additional transport equations are solved for each stress component [33, 178, 192]. An alternative is the *harmonic balance* method, originally proposed by He and Ning [81]. In this formulation, the flow is decomposed into a steady mean part and a set of harmonic perturbations. The governing equations for the perturbations are solved in the frequency domain, with as many systems of equations as twice the number of harmonics retained. The number of harmonics required depends on the flow features and the complexity of the phenomena to be represented. In practice, three harmonics are often sufficient to converge the steady solution, although more may be needed to accurately reproduce the instantaneous unsteady features. The method has been successfully applied to multistage compressors and turbines [34, 79, 196, 199]. Comparisons against transport-based models have shown that the harmonic method seems to provide superior accuracy [180]. Note also that Hall et al. [79] proposed a closure model based on an analytic approach describing the wake development inside a downstream blade row.

In the same line, a harmonic closure has also been implemented by Thomas [188] to close the circumferential stress. In this formulation, a non-intrusive coupling with a through-flow solver allows the circumferential stresses to be consistently introduced into a meridional computation, requiring only about five Fourier modes. By contrast, to the author's knowledge, no dedicated closure model has yet been proposed for the aperiodic stress. Nevertheless, both circumferential and aperiodic stresses share a common origin in circumferential averaging: the former result from averaging within each blade pitch, while the latter arise from averaging across the entire annulus. This suggests that, at least conceptually, both could be treated within a unified modeling framework.

High-order methods are generally more recent and have seen less widespread use, largely due to their higher complexity, additional implementation requirements, and increased computational cost. It is even common to simply neglect stresses altogether or, instead, to rely on approximate low-order closures to estimate their effects. Low-order strategies typically complement or modify the blade-force representation by corrections applied to the deviation angle and the loss coefficients, or through empirical calibrations embedded in body-force formulations.

2.6.4 Empirical information

The blade-force and stress closure models described above often include empirical correlations or calibration constants to enhance their predictive accuracy. These correlations and coefficients are typically derived from experimental data or high-fidelity simulations. However, their applicability is always constrained by the operating range and the calibration datasets on which they are built. This section provides an overview of the most commonly used empirical correlations and calibration techniques in throughflow modeling.

2.6.4.1 Calibration

The use of calibration constants is particularly relevant for explicit formulations based on lift and drag analogies. In such approaches, it has been shown that calibration is generally required to adjust on-design performance predictions, while reliable off-design predictions demand further calibration strategies. Early formulations [136, 150, 206], such as Gong's model [69], required multi-point calibration from various operating conditions. Others, like Thollet's formulation [185], by contrast, only require a single-point calibration. Most studies have explored calibration with RANS simulations but Tucker [189] reviewed strategies where large eddy simulations (LES) were used to provide calibration data for body-force models. In parallel, empirical correlations, that are described hereafter, typically rely on calibration coefficients that must be adjusted to experimental or numerical data. These correlations have thus also undergone continuous refinement through calibration against such datasets.

2.6.4.2 Correlations

In body-force modeling approaches where blade losses and flow deviation are imposed, two local quantities play a central role: the deviation angle, denoted $\delta(x, r)$, and the entropy rise, often expressed through a loss coefficient $\omega(x, r)$. Accurate prediction of δ and ω is essential, since they directly determine both the turning imparted to the flow and the associated dissipative effects. Purely analytical cascade methods, while useful for design exploration, are not sufficient for routine axial-compressor design because of their limited accuracy and restricted applicability [10].

An alternative approach is to rely on databases of blade-resolved simulations. For instance, Chima [35] used radial profiles of deviation and entropy within each blade row, calibrated with normalized characteristic maps to extend predictions to off-design conditions, thereby effectively bypassing explicit geometry-based closures. These databases may also be used to extrapolate empirical loss correlations [104], to scale existing empirical coefficients or to construct surrogate meta-models of profile losses [148]. However, the predictive capability of these models remained limited when applied to inlet conditions different from those used in the calibration set.

In practice, the flow deviation and the losses are typically computed using empirical correlations, derived from experiments or, to a lesser extent, from high-fidelity computations. An important advantage of such correlations is that they usually require only blade leading-edge and trailing-edge information to estimate both the deviation angle and the loss coefficients. These parameters are generally available at the preliminary design stage, even when detailed blade geometry is not yet defined, which makes correlation-based methods particularly attractive in early compressor design.

For the deviation, it is the trailing-edge deviation angle, $\delta_{TE}(r)$, that is generally measured. For the losses, Aungier [10] emphasized that a consistent definition of the loss coefficient is essential. Observations show that the total pressure loss is broadly proportional to the kinetic energy of the flow.

A classical definition for compressors is therefore

$$\omega(r) = \frac{\overline{p}_{t,\mathrm{W,LE}} - \overline{p}_{t,\mathrm{W,TE}}}{\frac{1}{2}\overline{\rho}\widetilde{W}^2_{\mathrm{LE}}}, \tag{2.82}$$

but a more robust formulation uses the dynamic pressure as reference,

$$\omega(r) = \frac{\overline{p}_{t,\mathrm{W,LE}} - \overline{p}_{t,\mathrm{W,TE}}}{\overline{p}_{t,\mathrm{W,LE}} - \overline{p}_{\mathrm{LE}}}, \tag{2.83}$$

which is found to be much less sensitive to changes in Mach number. This distinction is minor in low-speed test-cases, where the flow can be regarded as incompressible, but becomes critical when empirical correlations derived from such tests are applied to predict losses in high-Mach-number blade rows. These definitions of the loss coefficient implicitly assume constant total enthalpy across the blade row. This is a reasonable approximation for axial stators but also for rotors if the relative total enthalpy is considered. Although radial migration of streamlines violates this condition, the effect is negligible in axial compressors. A more rigorous formulation was thus introduced by Aungier [10] and Çetin et al. [32], who defined the loss coefficient as

$$\omega(r) = \frac{\overline{p}_{t,is,\mathrm{W,TE}} - \overline{p}_{t,\mathrm{W,TE}}}{\overline{p}_{t,\mathrm{W,LE}} - \overline{p}_{\mathrm{LE}}}, \tag{2.84}$$

where

$$\overline{p}_{t,is,\mathrm{W,TE}} = \overline{p}_{t,\mathrm{W,LE}} \left(1 + \frac{\gamma - 1}{2} \frac{(\Omega r_{\mathrm{TE}})^2}{\gamma r_{gas} \widetilde{T}_{t,\mathrm{W,LE}}} \left(1 - \left(\frac{r_{\mathrm{LE}}}{r_{\mathrm{TE}}}\right)^2\right)\right)^{\frac{\gamma}{\gamma-1}} \tag{2.85}$$

denotes the relative isentropic total pressure.

The deviation angle $\delta_{TE}(r)$ and the global loss coefficient $\omega(r)$ must subsequently be redistributed along the streamline to obtain an axial distribution of these parameter fields, $\delta(x,r)$ and $\omega(x,r)$ respectively. The distribution of the deviation angle is usually linear while the loss coefficient is kept constant along a streamline but some authors have imposed a non-linear distribution to better match experimental data [143, 161, 182].

A further consideration concerns the way experimental data or high-fidelity computations are averaged to define inlet and outlet conditions of a blade row. When only sparse instrumentation is available, crude area-averages of probe data are often the only practical choice. Despite their limitations, they nonetheless perform reasonably well in many cases compared to more rigorous definitions if the flow does not contain major separations. Moreover, outside the blade rows the flow tends to recover rapidly toward axisymmetry, so that different averaging procedures become largely equivalent for through-flow analyses. It is also true that the empiricim of the cascade correlations often represent a larger source of uncertainty. Another source of ambiguity lies in the axial location of the measurement planes, which is not always clearly defined and may not correspond exactly to the blade leading or trailing edges, potentially leading to inconsistencies in the extracted correlations.

Finally, the use of empirical correlations for δ_{TE} and ω is based on the simplifying assumption that the different physical mechanisms in a turbomachine, as introduced by Denton [48], can be decomposed and treated independently, with their contributions assumed to add linearly. The phenomena are often decomposed into three categories: two-dimensional flow mechanisms in the blade-to-blade plane referred to as profile loss, three-dimensional and non-axisymmetric mechanisms associated with the endwalls, like endwall boundary layers, secondary flows or shocks, and the interactions between these mechanisms. This last contribution is thus either neglected or implicitly embedded within the correlations for the first two categories. Based on this view, the total deviation angle and loss coefficient can be written as a summation of the corresponding contributions,

$$\omega = \sum_K \omega_{K,2D} + \sum_K \omega_{K,3D}, \quad \text{and} \quad \delta_{TE} = \sum_K \delta_{K,2D} + \sum_K \delta_{K,3D}. \tag{2.86}$$

This approach is widely adopted, as it allows correlations to be constructed separately for deviation and for losses, before combining them. In reality, however, the flow physics is more complex and involves strong couplings between mechanisms, making their separation somewhat arbitrary. Such approximations may introduce inconsistencies, since compensating errors in one contribution often affect others [39]. The challenge of loss decomposition and extraction has been further addressed in an interesting recent study by Raina et al. [156]. The complexity of the three-dimensional flow fields through a compressor blade row can be qualitatively appreciated from Fig. 2.15. Basic flow features of secondary flows are shown but the final flow topology is largely determined by the interactions of these features and their relative strength, which strongly depends on the passage geometry and loading. The correlations for each of these contributions are detailed hereafter.

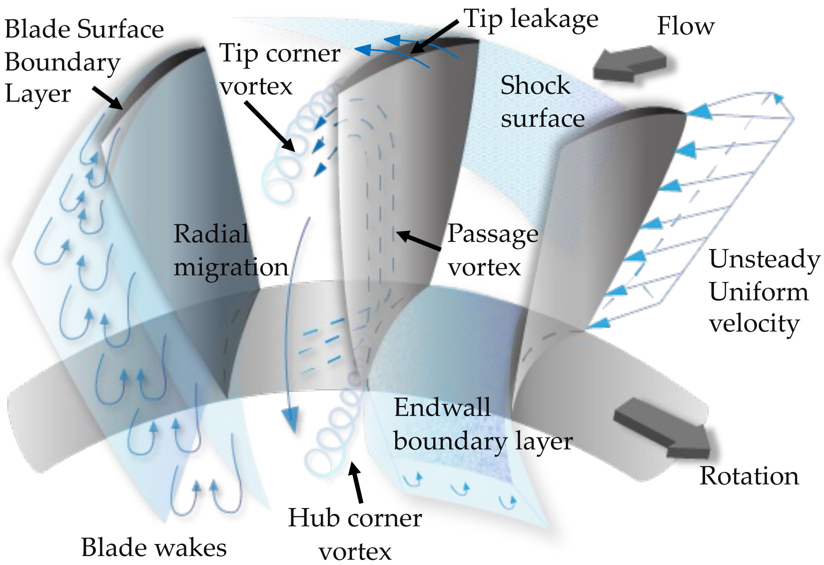

Figure 2.15: Illustration of the flow structures within an axial-flow compressor rotor (adapted from Wisler [201]).

Profile loss

In compressor aerodynamics, profile loss refers to the loss generated by the boundary layers that form on blade surfaces in an idealized two-dimensional flow. This loss would exist even in the absence of secondary or endwall effects and have traditionally been quantified through cascade experiments. These experiments provide the foundation for correlations that predict total pressure loss and fluid turning, though the deviation angle δ is not strictly speaking a loss-generating mechanism, under fairly general operating conditions. Howell [98] was among the first to estimate the profile loss by relating it to lift and drag coefficients familiar from aircraft analysis, separating profile drag from annulus drag and secondary losses. This approach was overtaken by the famous work of Lieblein [125, 126], who used a diffusion factor to establish a connection between profile losses and the boundary-layer momentum thickness. In practice, Lieblein's approach also highlighted that the deviation angle δ_{2D} and the loss coefficient ω_{2D} should be decomposed into a design contribution, defined at a reference incidence i^*, and an off-design contribution, often expressed in a quadratic form, that increases with the actual incidence angle i. Importantly, he also proposed a correlation for estimating the optimal incidence at which the minimum-loss condition is achieved, thus providing a consistent framework for both on-design and off-design predictions. His correlations, derived from NACA low-speed cascade tests on standard profiles (e.g., C4, NACA 65), became widely used and served as the basis for subsequent developments [37, 106, 110]. For more advanced airfoil designs, such as controlled-diffusion blades, the same principles are generally adapted to capture the improved aerodynamic characteristics of these profiles.

These works were later reviewed and consolidated by Çetin et al. [32], and more recently revisited by Banjac et al. [11] and Petrovic et al. [152], who examined their applicability, in addition to some correlations that will be discussed hereafter. Note that Pfitzinger et al. [153] proposed to use blade-to-blade computations from `MISES` intead of empirical correlations to predict the parameters δ and ω. The same idea but relying on a singularity method was also suggested by König et al. [114]. Another noticeable approach was proposed by Papailiou [146], who employed an inverse integral boundary-layer method in design mode for highly loaded compressor blades. Based on prescribed inlet and outlet conditions (i.e., the diffusion), his procedure converged to a blade geometry that achieved the target diffusion with minimum loss generation.

Mach number effects

The original correlations of Lieblein were derived from low-speed, quasi-incompressible cascade tests. When applied to high-subsonic or transonic conditions, additional effects related to compressibility must be taken into account. Aguirre et al. [5] emphasized the need for accurate inclusion of transonic effects in streamline curvature methods, showing that neglecting shock and compressibility phenomena leads to systematic under-prediction of losses. Several authors have thus proposed modifications for higher Mach numbers [37, 76, 110, 183]. Later, Çetin et al. [32] performed a comprehensive review of the correlations available up to that time. König et al. [114] and Schobeiri [167], and then Manfredi and Fontaneto [131], further advanced this line of work by explicitly developing correlations for both subsonic and supersonic inlet conditions, with particular attention to more modern blade designs. Finally, Baralon et al. [13] demonstrated that defining the blockage normal to the flow path, rather than aligned with the circumferential direction, leads to predictions that, although formally inconsistent with the averaged equations, agree more closely with experimental measurements of transonic cases. However, Thollet [185] showed that such a modification was not required when using blade force models based on the lift–drag analogy. In his approach, the predicted choke mass flow rate was already consistent with experiments when employing the standard circumferential blockage definition. He argued that this difference most likely stems from the formulation adopted by Baralon, who enforced a flow tangency condition on the mean flowpath to impose the velocity direction.

Endwall losses

The annulus endwalls and the flow that develops there are among the most complex and least understood regions of a turbomachine. Several mechanisms are active in this region, including the development of endwall boundary layers and secondary flows such as tip leakage flows, and passage vortices, all of which contribute to additional loss generation and flow deviation. In throughflow modeling, the most common way of accounting for endwall effects has been to couple the throughflow solver with separate boundary-layer models, sometimes supplemented by secondary-flow correlations [56, 96]. However, such methods face intrinsic limitations: as highlighted by Cumpsty [38], boundary-layer theory was originally devised for external aerodynamics with well-behaved flows, and its assumptions are not well satisfied near the endwalls of compressors, where the separation between boundary layer and core flow is unclear. In Navier–Stokes throughflow formulations, turbulence models are instead employed to represent these effects more consistently [168].

When endwall boundary layers are not modeled, their influence is often partly and crudely approximated through an additional aerodynamic blockage. Some formulations introduce it as a correction to the blade forces, while others represent it as an effective reduction in the annulus flow area [13]. Related to this, the Axial Velocity Density Ratio (AVDR) correction [155, 176] is commonly applied in cascade-based correlations, effectively correcting the deviation predicted from cascade data. In a similar spirit, Kravtsoff [112] proposed an implementation in which the aerodynamic blockage of blade boundary layers and wakes is treated as an additional contribution to the geometric blockage.

The endwall boundary layers also interact with blade boundary layers near the endwalls, giving rise to secondary flows such as tip leakage flows, corner vortices, and passage vortices. These inherently three-dimensional mechanisms cannot be explicitly captured by the axisymmetry nature of classical throughflow models. They produce flow blockage, add to the overall loss level, and modify the local velocity triangles, thereby reducing compressor performance. Despite their complexity and the challenges in quantifying them [38, 48], several attempts have been made to model their impact. Mellor and Wood [134] proposed a system of equations based on integral boundary-layer theory, including the effects of the blade-to-blade pressure gradient and turbulence. Hirsch [86] extended this approach to a single-stage compressor and concluded that the boundary-layer shape factor should be variable rather than constant. Aungier [10] later introduced a model for the deviation angle based on the tangential force deficit, building on the insights of Koch and Smith [110]. More recently, Pacciani et al. [143] proposed a novel approach in which the secondary flow within the passage is represented by a transverse velocity field modeled as a Lamb–Oseen vortex. This allowed them to capture deviation velocities in low-momentum regions with reduced reliance on empiricism. Alternative strategies include the use of experimental correlations to directly introduce three-dimensional loss and deviation increments. Roberts et al. [162, 163] developed such correlations, which have been widely implemented in throughflow solvers, including the work of Simon and Léonard [169]. Gallimore [64] proposed a physics-based approach that modifies the circumferential component of the blade force in the endwall regions. This approach is based on experimental observations showing that the blade force distribution near the endwalls should vary smoothly across the span rather than abruptly changing.

The rotor tip flow also deserves particular attention. Vorticity-based approaches [116] treat the leakage flow as a vortex and estimate its losses from circulation and vortex core growth. Blockage-based approaches [110] link the leakage to casing boundary-layer thickening and tangential force deficits. Jet-based approaches[179] consider the leakage as a jet in crossflow, while Denton [48] proposed a thermodynamic mixing model based on entropy generation from two mixing streams. More recent throughflow implementations often adopt Denton's formulation [11, 143], whereas Simon [168] used Roberts' correlations to include additional deviation due to leakage.

Finally, leakage flow under stator are often neglected in throughflow simulations, although their impact can be significant. Banjac et al. [11] extended the turbine leakage correlation of Morris and Hoare [139] to compressors, and proposed a simple model linking entropy rise to the leakage mass flow rate through the seals. These losses were then added to the other endwall secondary losses. In principle, such effects could also be modeled more directly by introducing an axisymmetric cavity and coupling it with the main annulus flow using, for example, a chimera approach [31].

Wake and Radial mixing

Blade boundary layers generate wakes that are convected downstream and interact with subsequent blade rows, increasing turbulence and losses. Various models have been proposed to represent wake transport and decay in inter-row regions [117, 174]. The subsequent redistribution of loss in the spanwise direction is commonly referred to as radial or spanwise mixing. Without accounting for it, the loss distribution may appear unrealistic, with values that are underestimated near the endwalls and overestimated around midspan. Two main interpretations of the mechanism have been proposed in the correlations. Adkins and Smith [4] attributed radial mixing to convective transport driven by secondary flows, whereas Gallimore [63] described it in terms of turbulent diffusion. Later studies, such as Wisler et al. [202], confirmed experimentally that both effects coexist. Lewis [122] then proposed a combined formulation including both diffusion and convection, and it has been employed in modern compressor studies by Casey and Robinson [30] and Ricci et al. [159].

2.7 Concluding remarks

This chapter has reviewed the foundations and state-of-the-art of through-flow modeling. A wide variety of TF methods exist, ranging from early pitch-line and streamline curvature approaches to more advanced Euler and Navier–Stokes formulations. Their differences lie not only in the governing equations but also in the way closure terms are introduced, in particular the modeling of blade forces and stresses. The main sources of modeling error thus stem from the choice of equations, the treatment of closure terms, and the empiricism of the correlations or the calibration, whose validity is often limited to specific geometries or operating ranges. This inevitably introduces uncertainties that must be carefully assessed. The formulation of the TF model implemented in this work, together with the specific choices of closure strategies, are described in detail in the next chapter.

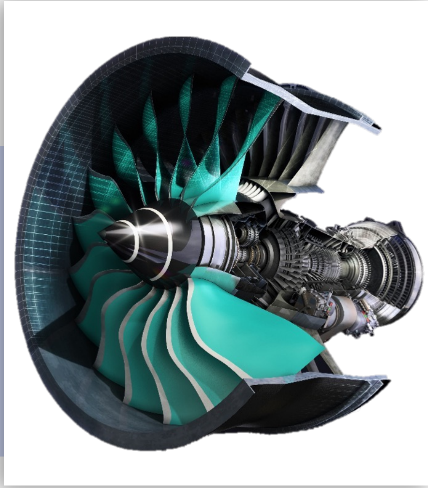

Chapter 3

Numerical implementation

This chapter introduces the through-flow framework used in this thesis. First, the choice of a viscous TF solver is motivated and the governing equations are summarized. Then, the software architecture is described, followed by the computational setup. The closure models are detailed next, with emphasis on blade body-force representations and on the adopted turbulence model. The baseline empirical correlations used for deviation, losses, and optimal incidence, are subsquently presented. Finally, the incidence correction at the leading edge is introduced.

3.1 Viscous through-flow model equations

In this thesis, a *time-marching Navier–Stokes based viscous through-flow solver* has been chosen as the baseline modeling strategy to analyze compressor test cases. The motivation behind this choice was the desire to reduce empiricism by capturing near-wall viscous effects directly. Inviscid through-flow models, whether based on the SLC method or on an Euler formulation, indeed treat the annulus endwalls as inviscid boundaries, with a slip condition along the walls. This simplification is recognized as one of the major drawbacks of inviscid through-flow modeling [97, 168]. Strategies discussed in the previous chapter to compensate for the missing physics have proved to be inadequate for such complex internal flows, or highly empirical [38, 95]. On the other hand, the viscous through-flow method predicts realistic velocity profiles near the annulus walls, thereby eliminating the need for empirical blockage factors or independent endwall boundary-layer calculations. The associated increase in incidence caused by near-wall velocity deficits is also naturally captured. Moreover, time-marching CFD-based formulations have also demonstrated improved numerical robustness compared to classical formulations, while retaining a low computational cost compared to full three-dimensional simulations. For these reasons, the viscous TF solver is based on Eq. 2.43.

Rather than developing a dedicated through-flow solver, it is common to adapt an existing 3D Navier-Stokes code [112, 185, 207] to solve the through-flow equations. This is also the approach taken here, where the solver `elsA` from ONERA [26] is used as base solver. In order to limit the modifications required in `elsA`, the viscous through-flow equation, Eq. 2.43, need to be recast in a different form. In particular, the presence of the blockage factor $b(x, r)$ and the use of cylindrical coordinates on the left-hand side of Eq. 2.43 need to be addressed. After some manipulations the through-flow equation can be rewritten as

$$\frac{\partial \overline{\mathbf{u}}}{\partial t} + \frac{\partial(\overline{\mathbf{F}} - \overline{\mathbf{F_v}})}{\partial x} + \frac{\partial(\overline{\mathbf{G}} - \overline{\mathbf{G_v}})}{\partial r} = \overline{\mathbf{S}} - \frac{(\overline{\mathbf{F}} - \overline{\mathbf{F_v}})}{b}\frac{\partial b}{\partial x} - \frac{(\overline{\mathbf{G}} - \overline{\mathbf{G_v}})}{b}\frac{\partial b}{\partial r}, \tag{3.1}$$

where the source term $\overline{\mathbf{S}} = \overline{\mathbf{S_c}} + \overline{\mathbf{S_{cv}}} + \mathbf{S_{bi_1}} + \mathbf{S_{bi_2}} + \mathbf{S_{bv}} + \overline{\mathbf{S_s}}$ has the same generic form as previously, but with the definition of $\overline{\mathbf{S_c}}$ and $\overline{\mathbf{S_{cv}}}$ in Eqs. 2.41 and 2.45 replaced by

$$\begin{aligned}
\overline{\mathbf{S_c}} &= \frac{1}{r}\left[\; -\overline{\rho}\widetilde{V_r} \quad , -\overline{\rho}\widetilde{V_x}\widetilde{V_r} \quad , \overline{\rho}\widetilde{V_\theta}\widetilde{V_\theta} - \overline{\rho}\widetilde{V_r}\widetilde{V_r} \quad , -2\overline{\rho}\widetilde{V_r}\widetilde{V_\theta} \quad , -\overline{\rho}\widetilde{V_r}\widetilde{H_t} \;\right]^T, \\
\overline{\mathbf{S_{cv}}} &= \frac{1}{r}\left[\; 0 \quad , \overline{\tau_{xr}} \quad , \overline{\tau_{rr}} - \overline{\tau_{\theta\theta}} \quad , 2\overline{\tau_{r\theta}} \quad , \overline{\tau_{rj}}\widetilde{V_j} - \overline{q_r} \;\right]^T.
\end{aligned} \tag{3.2}$$

Equation 3.1 thus preserves the traditional form of the left-hand side used in Cartesian Navier-Stokes solvers, and only the additional sources terms related to the blockage factor, to the through-flow closure models and to the cylindrical coordinates originally used, need to be specifically adapted.

The drawback of this formulation is that it is not conservative, since these terms are no longer expressed in a divergence form. While conservative and non-conservative formulations are mathematically equivalent, their discretized form on a finite size grid is not: a non-conservative formulation may introduce unphysical numerical errors, such as an artificial creation of mass stemming from the truncation error. As a consequence, strict mass-flow conservation between inlet and outlet is not guaranteed. Nonetheless, the possible mass-flow rate imbalance can be kept below an acceptable small tolerance, e.g. 0.1%, through a mesh refinement process, especially in the blade LE/TE regions where the gradients of the blockage factor are the strongest. This effect can thus be neglected, but conservative schemes are generally more accurate and robust, particularly in the presence of large gradients or discontinuities such as shock waves [88].

The present implementation of the through-flow model explicitly includes the blade forces $\mathbf{S_{bi_1}}, \mathbf{S_{bi_2}}, \mathbf{S_{bv}}$ (Eqs. 2.52, 2.53 and 2.69). Their corresponding closure models are detailed in the following section. On the other hand, the aperiodic, unsteady and circumferential stresses are neglected, so that $\overline{\mathbf{S_s}}$ only includes the Reynolds stress. This Reynolds stress is directly computed by the base solver elsA through a standard turbulence model (see later). Note that in Chapter 4, improvements of some correlations used in blade forces are introduced as an attempt to include the effects of some specific flow features (e.g., blade tip flow) that would otherwise be modeled by the circumferential and unsteady stresses.

Finally, the working fluid, air, is assumed to be a calorically perfect gas with Newtonian behavior. Consequently, the specific heats are constant and the equations of state are given by Eqs. 2.11-2.12. Furthermore, the dependence of the dynamic viscosity μ on the temperature is modeled through Sutherland's law (Appendix A) and the heat flux in Eq. 2.43 through Fourier's law with a constant Prandtl number. It is important to mention that in all nonlinear constitutive relationships, the additional unclosed terms (e.g., $\overline{\rho V_j'' V_j''}$ in Eq. 2.11) are neglected. As illustrated by the oblique shock example in Sec. 2.4, this approximation induces an error, but in light of all other approximations and uncertainties in the calculation of the closure models, this error is considered acceptable.

3.2 CFD solver

The system of governing equations described in the previous section is solved using a coupling methodology that relies on the combination of two computational codes. The solution of the transport equation, Eq. 3.1, is computed by the axisymmetric version of Onera's CFD solver `elsA` [26] using a finite-volume approach on structured meshes[1]. This also includes the calculation of the axisymmetric source terms $\overline{\mathbf{S_c}}$ and $\overline{\mathbf{S_{cv}}}$, the Reynolds stress in $\overline{\mathbf{S_s}}$ and the corresponding transport equations for the turbulence model. On the other hand, the computation of the actual blade body forces and blockage source terms is done separately by the code `ASTEC` (Aerodynamic Source Terms for Efficient Computations), developed by Safran Tech with contributions from the present author. This software is used as an add-on to `elsA`, providing it with the complementary source terms necessary for solving the meridional flow. In the present work, the through-flow solver is employed in analysis mode, where the compressor performance is sought for a prescribed geometry.

3.2.1 Coupling strategy

The coupling between `elsA` and `ASTEC` is realized within the python environment of `ASTEC`, as described in Fig. 3.1. Arrays storing the flow variables and the source terms at the cell centers are shared in memory. After each CFD iteration, `elsA` provides the flow field, which is then processed by `ASTEC` routines to compute the blade force and blockage source terms. These are returned to `elsA` and applied at the following iteration until convergence is reached.

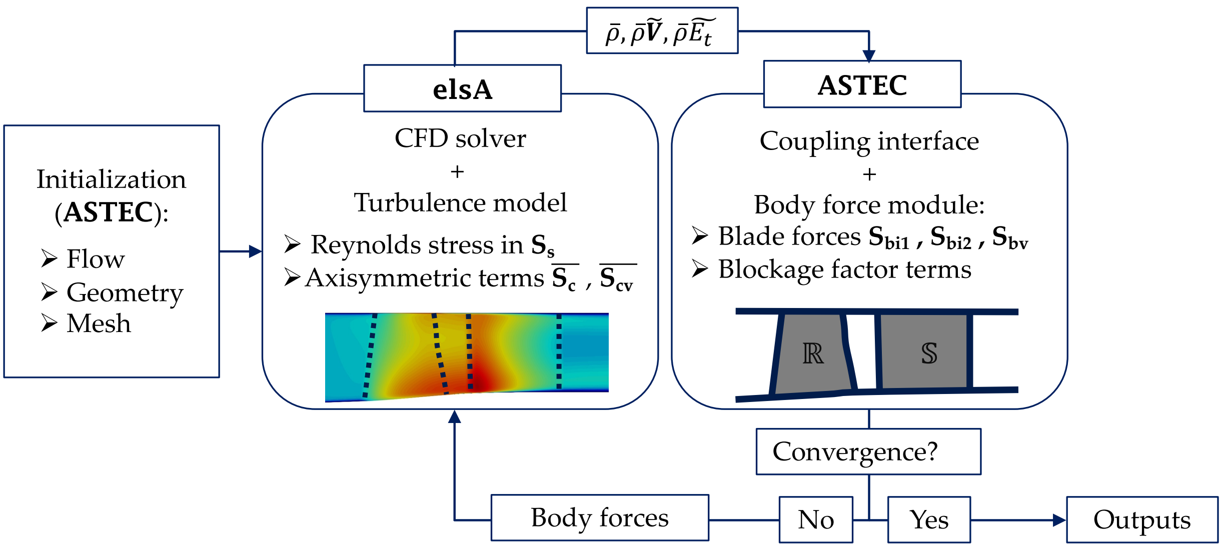

Figure 3.1: Coupling chart between the `elsA` solver and `ASTEC` routines.

During the initialization phase, the geometric information required by the closure models, i.e. the camber line coordinates and the blade thickness distribution, is interpolated on the CFD mesh for the calculation of the source terms. The interpolation procedure used to perform this mapping

[1]The FVM has become the state-of-the-art discretization technique in CFD and is extensively documented in the literature (see for example [88]). As such, its principles are not recalled here.

ensures consistency between the geometrical input data and the discretized computational grid. The interpolated quantities are then combined with the flow field to evaluate the additional source terms.

A key property of this non-intrusive strategy is that the CFD solver itself cannot distinguish the nature of the variables it computes: whether they are averaged over the circumferential direction or obtained through a different filtering process is irrelevant to the left-hand side operator. What differentiates one through-flow formulation from another lies entirely in the source terms. In this sense, `ASTEC` specializes the `elsA` solver for meridional modeling by supplying the appropriate source terms consistent with the averaging procedure described earlier. This framework is thus flexible and it facilitates multidisciplinary extensions stemming from future advances.

3.2.2 Computational grid

In the present through-flow configuration, a multi-block structured 3D mesh with a single cell in the circumferential direction is used to discretize the flow domain and periodic boundary conditions are imposed in the azimuthal direction, i.e. on the front and back sides. This setup enforces the computation of a circumferentially averaged flow on a axisymmetric planar domain. Experience from previous studies [168] on axial turbomachines has shown that the discretization error decreases as the number of cells along the blade chord increases, with a stronger sensitivity when the inlet flow angle is high. In particular, for a moderate inlet flow angle, i.e. lower than 65°, a uniform distribution of roughly 30 to 40 cells in the axial direction of the blade passage generally provides sufficient accuracy. For higher blade angles, or at elevated Mach numbers, a denser grid becomes necessary in order to properly capture the source terms associated with flow turning.

Moreover, the grid is clustered in the endwall regions to resolve boundary layers, and refined at the blade leading and trailing edges to capture strong gradients there. Note that both the leading and trailing edges, as well as the rotor tip, are aligned with mesh lines. A mesh convergence study has been carried out to refine the grid near the endwalls and at the blade leading and trailing edges until the inlet and outlet mass-flow rates converge. In addition, the dimensionless wall distance y^+ should be adjusted consistently with the selected turbulence model. An example of the computational mesh for a compressor stage is shown in Fig. 3.2.

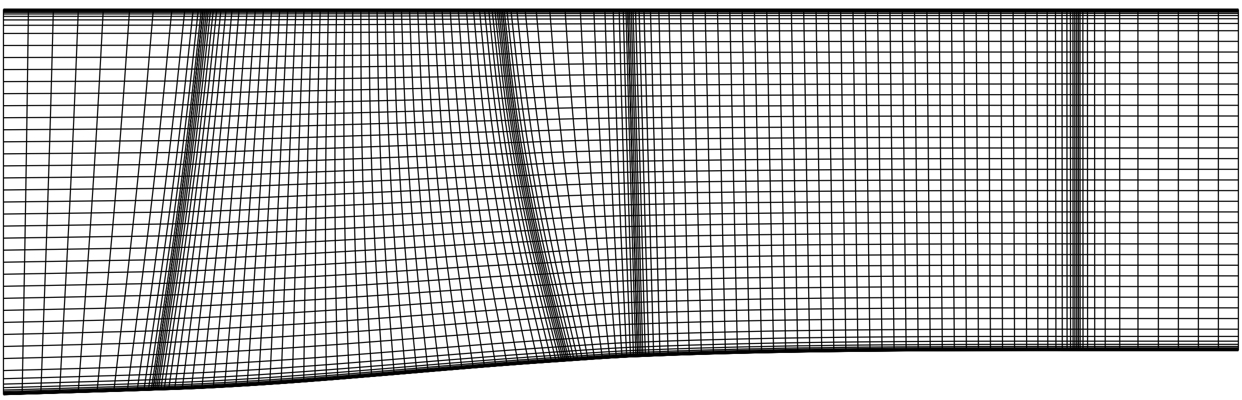

Figure 3.2: Illustration of the meridional mesh for a compressor stage (61x141= 8601 cells).

3.2.3 Boundary conditions

At the subsonic inlet, the span-wise distributions of total pressure, total temperature, and the circumferential and radial flow angles are imposed as physical boundary conditions. It is assumed that there is no upstream prewhirl so that the upstream quantities are conserved when varying the operating point. Regarding the turbulent quantities, a turbulence intensity of $I_{\text{turb}} = 2\%$ and a turbulent-to-laminar viscosity ratio of $\mu_t/\mu = 100$ are prescribed, which are representative of internal flows at a Reynolds number of the order of 5×10^5. These turbulent conditions are then converted into the corresponding transported turbulent variables of the selected turbulence model.

At the subsonic outlet, the static pressure is prescribed at a reference radius, and the radial equilibrium equation, Eq. 2.28, is used to compute a consistent radial distribution. The reference static pressure p_{ref} is imposed by a valve law to control the operating point, and thus the mass-flow rate. The outlet static pressure is then updated iteratively according to

$$p^{K+1} = p^K + C_{\mathcal{V}} \left(p_{\text{ref}} \frac{\dot{m}^K}{\dot{m}_{\text{ref}}} - p^K \right), \tag{3.3}$$

where the superscript K denotes the solver iteration, $\dot{m}_{\text{ref}}$ is the reference mass-flow rate and $C_{\mathcal{V}}$ is a relaxation constant that controls the response of the valve law. At convergence, $p^\infty/\dot{m}^\infty = p_{\text{ref}}/\dot{m}_{\text{ref}}$.

Endwall boundary conditions follow the classical treatment of the Navier–Stokes equations. At both hub and casing, impermeability and no-slip conditions are enforced, and the walls are considered adiabatic. It should be noted that the rotor hub rotates at the rotation speed of the shaft, whereas the casing and the stator hub are fixed. Finally, as mentionned above, periodic boundary conditions are imposed on front and back surfaces of the single pitch-wise mesh cells due to the axisymmetric flow assumption.

3.2.4 Numerical parameters

The through-flow solver inherits its numerical scheme from the CFD software `elsA`. A backward Euler implicit scheme with relaxation is used for the time discretization, while the convective fluxes are discretized using the classical Jameson scheme [101]. This scheme is based on a second-order central difference, complemented by a second-order artificial dissipation term. The computation of viscous fluxes relies on the Monotonic Upstream-Centered Scheme for Conservation Laws of van Leer to reconstruct the primitive variables at the cell-edge centers, while their first derivatives are evaluated using the diamond-path scheme, which provides second-order accuracy for viscous contributions on structured meshes. A CFL number of 30 is used, with a linear ramp from 1 to 30 during the first 100 iterations to improve numerical stability in the startup phase. Finally, a multigrid approach is employed to speed up convergence to the steady state solution.

3.3 Closure models

This section presents the closure strategies adopted for the terms included in the through-flow solver. The various models are discussed, and the reasons for their selection are explained.

3.3.1 Turbulence model

The Reynolds stress is closed by the k-l Smith model [171], based on the Boussinesq hypothesis in which turbulence is modeled by introducing a scalar turbulent viscosity μ_{turb}. It is commonly used for turbomachine computations in industry, especially because of its aptitude to better take into account the compressibility effects than standard k-ε type models. Moreover, it has low sensitivity to the distribution of the grid points close to the wall [172]. Strictly speaking, turbulence models should be consistently averaged in time, between passages, and circumferentially, e.g. in the sense of Adamczyk's cascade framework. However, given the strong assumptions already underlying RANS closures, the direct use of the model "as is" provides sufficiently accurate results in practice. This through-flow solver is thus able to capture the two-dimensional endwall flow features, such as the flow blockage and the level of losses near the endwalls.

The components of the viscous stress tensor then read:

$$\begin{aligned}
\overline{\tau_{xx}} &= \tfrac{2}{3}\left(\mu_{\text{turb}}+\mu\right)\left(2\frac{\partial \widetilde{V_x}}{\partial x}-\frac{\partial \widetilde{V_r}}{\partial r}-\frac{\widetilde{V_r}}{r}\right), & \overline{\tau_{xr}} &= \left(\mu_{\text{turb}}+\mu\right)\left(\frac{\partial \widetilde{V_r}}{\partial x}+\frac{\partial \widetilde{V_x}}{\partial r}\right),\\
\overline{\tau_{rr}} &= \tfrac{2}{3}\left(\mu_{\text{turb}}+\mu\right)\left(2\frac{\partial \widetilde{V_r}}{\partial r}-\frac{\partial \widetilde{V_x}}{\partial x}-\frac{\widetilde{V_r}}{r}\right), & \overline{\tau_{x\theta}} &= \left(\mu_{\text{turb}}+\mu\right)\frac{\partial \widetilde{V_\theta}}{\partial x},\\
\overline{\tau_{\theta\theta}} &= \tfrac{2}{3}\left(\mu_{\text{turb}}+\mu\right)\left(2\frac{\widetilde{V_r}}{r}-\frac{\partial \widetilde{V_x}}{\partial x}-\frac{\partial V_r}{\partial r}\right), & \overline{\tau_{r\theta}} &= \left(\mu_{\text{turb}}+\mu\right)\left(\frac{\partial \widetilde{V_\theta}}{\partial r}-\frac{\widetilde{V_\theta}}{r}\right),
\end{aligned} \tag{3.4}$$

where μ is the molecular viscosity. Similarly, Fourier's law is extended to include turbulent heat transfer so that

$$\overline{q_x} = -(k+k_{\text{turb}})\frac{\partial \widetilde{T}}{\partial x}, \qquad \overline{q_r} = -(k+k_{\text{turb}})\frac{\partial \widetilde{T}}{\partial r}, \tag{3.5}$$

where k is the thermal conductivity and k_{turb} its turbulent counterpart. A constant molecular Prandtl number $\text{Pr} = 0.72$ is assumed, while a turbulent Prandtl number $\text{Pr}_{\text{turb}} = 0.9$ is used for the evaluation of the thermal conductivities.

3.3.2 Blade forces

The representation of blade effects within the through-flow solver is based on the body-force approach. This choice follows naturally from the CFD framework employed, since the underlying solver is readily modified to include additional source terms in the governing equations. As recalled in the previous chapter, two main methodologies exist for modeling blade forces. The first one prescribes directly the deviation and loss distributions to reproduce the azimuthally-averaged flow, while the second introduces equivalent lift and drag forces whose magnitudes depend on local flow variables. The latter is based on blade element momentum method and has been widely used for propeller or fan modeling.

Both strategies, however, suffer from reproducibility issues. In lift–drag formulations, the force coefficients are usually inferred from empirical correlations or from higher-fidelity datasets, and they often require re-tuning when changing operating points or geometries. Similarly, deviation and loss models rely on empirical relations. As a result, both approaches are characterized by a significant degree of empiricism and limited predictive robustness. As emphasized by Cumpsty [38], the prevailing and more physically consistent viewpoint is to consider the blades as forming passages rather than as isolated aerofoils. This interpretation motivates the choice of body-force strategies based on the circumferential averaged passage.

Blockage force

The blockage force $\mathbf{S}_{\mathbf{bi}_1}$ is modeled according to Eq. 2.52, which assumes that the mean of the pressure-side and suction-side pressures can be approximated by the circumferentially averaged static pressure. Coupling the blockage force with the blockage source terms in Eq. 3.1 leads to the cancellation of the pressure contribution, resulting in the following expression:

$$\underbrace{\left[0\,,\frac{p}{b}\frac{\partial b}{\partial x}\,,\frac{p}{b}\frac{\partial b}{\partial r}\,,0\,,0\right]^T}_{=\mathbf{S}_{\mathbf{bi}_1}} - \underbrace{\left(\frac{(\overline{\mathbf{F}}-\overline{\mathbf{F}_\mathbf{v}})}{b}\frac{\partial b}{\partial x} + \frac{(\overline{\mathbf{G}}-\overline{\mathbf{G}_\mathbf{v}})}{b}\frac{\partial b}{\partial r}\right)}_{=\text{ blockage terms}} = \underbrace{\frac{1}{b}\left(\overline{\mathbf{F}_\mathbf{v}}\frac{\partial b}{\partial x} + \overline{\mathbf{G}_\mathbf{v}}\frac{\partial b}{\partial r}\right)}_{=\text{ viscous terms}} - \underbrace{\frac{1}{b}(\rho\widetilde{\mathbf{V}}\cdot\nabla\mathbf{b})\widetilde{\mathbf{Z}}}_{=\text{ inviscid terms}}\,, \tag{3.6}$$

where $\nabla\mathbf{b} = \left[\frac{\partial b}{\partial x}, \frac{\partial b}{\partial r}, 0\right]^T$ and $\widetilde{\mathbf{Z}} = \left[1, \widetilde{V_x}, \widetilde{V_r}, \widetilde{V_\theta}, \widetilde{H_t}\right]^T$.

Viscous contributions to the blockage terms are often neglected in practice [112, 185]. In the present implementation, these terms are nevertheless included for completeness, but they have been shown to be negligible compared to the inviscid blockage contribution. Finally, it is crucial to compute the gradient of the blockage factor consistently at each cell center to avoid spurious numerical errors.

Deflection force

The implicit analysis formulation, in which the modulus of the blade force is computed using the pseudo-time dependent equation 2.59,

$$\frac{\partial f_n}{\partial t^*} = -C\left(\widetilde{W_x}n_x + \widetilde{W_r}n_r + \widetilde{W_\theta}n_\theta\right)\,, \tag{3.7}$$

is used for the deflection force because it is more robust than others and because the present study deals with analysis problems. The variable t^* corresponds to the pseudo-time used by `elsA`, meaning that at each solver iteration, the force magnitude is incremented by a term proportional to the residual of the scalar product in Eq. 2.59. This residual represents the normal component of the relative velocity at the blade surface—that is, the component of the local flow velocity that is not aligned with the mean flow path. Consequently, the force changes as long as the flow is not aligned with the local camber, corrected for the distributed deviation angle δ. Simon [168] demonstrated that applying this formulation to the modulus of the overall blade force, rather than directly to its circumferential component, results in a more robust iterative process.

The relaxation constant C in Eq. 2.59 plays a crucial role in the convergence process. If C is chosen too large, the solution may diverge, whereas a too small value results in slow convergence. Baralon et al. [13] showed that the optimal scaling of C is linked to the inverse of the pseudo-time step Δt^*, with a dependency of the form

$$C \sim \frac{\overline{\rho}}{\Delta t^{*2}} \sim \overline{\rho}\frac{\left(\widetilde{V_m}+\widetilde{a}\right)^2}{\Delta x^2}\,, \tag{3.8}$$

where Δx is a typical cell size. In practice, Persico and Rebay [149] recommended a value of

$C = 10^4$ kg m^{-3} s^{-2}, which provides a good compromise between stability and convergence rate. However, this value is highly case-dependent and likely tied to the specific operating conditions, flow regime, and numerical setup considered in that study. Therefore, it should not be regarded as a universal recommendation. In the present implementation, a similar approach is followed, with C increasing linearly during the initial iterations to avoid premature divergence while still achieving fast convergence once the solution stabilizes.

A practical difficulty arises from the orthogonality requirement between the blade force and the local flow direction. During the convergence process, the direction of the blade force tends to oscillate, which may lead to unphysical fluctuations and spurious perturbations propagating upstream and downstream. To overcome this issue, the force is imposed to be perpendicular to the mean flow path rather than to the actual flow direction, as proposed by Simon [168]. The normal components of the mean flow path used to project the blade force modulus, are obtained by rotating the blade normal vector $\mathbf{n}_b$ through the Euler–Rodrigues formula:

$$\mathbf{n} = \mathbf{n}_b \cos\delta + \mathbf{e} \wedge \mathbf{n}_b \sin\delta + (1 - \cos\delta)\,(\mathbf{e} \cdot \mathbf{n}_b)\,\mathbf{e}\,, \tag{3.9}$$

where the rotation axis $\mathbf{e}$ corresponds to the unit meridional velocity vector,

$$\mathbf{e} = \left[-\frac{V_x}{V_m}, \frac{V_r}{V_m}, 0\right]^T, \tag{3.10}$$

and the rotation angle is the local deviation angle $\delta(x, r)$. This angle is usually defined at the blade trailing edge but it is used here for the entire blade surface to account for the boundary layer on the blade wall. To obtain the deviation angle field $\delta(x, r)$ everywhere in the blade, it is linearly interpolated along the chord position from $\delta = 0$ at the LE to its (radially distributed) value δ_{TE} at the TE.

At convergence the mean flow path coincides with the streamsurface, as illustrated in Fig. 3.3, and no entropy is generated. This improvement is illustrated in Fig. 3.4, where the oscillatory behavior obtained with the classical formulation is compared to the stabilized solution obtained with the fixed-direction approach.

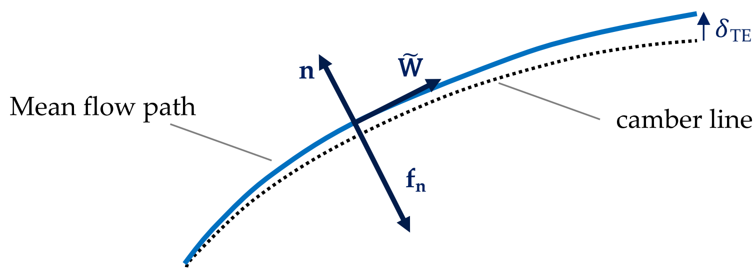

Figure 3.3: Configuration of the mean flow path at convergence.

At this stage, the method still requires an empirical correlation for the trailing-edge deviation angle δ_{TE}. This correlation, which determines the spanwise distribution of δ_{TE} is introduced in Section 3.3.3.

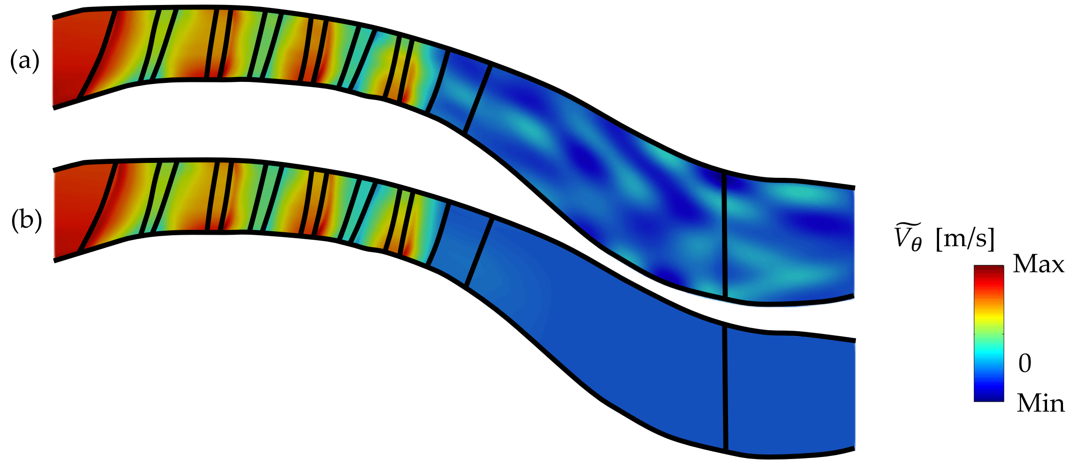

Figure 3.4: Contour of the tangential velocity of a low-pressure compressor with (a) a standard approach vs (b) a deflection force imposed normal to the mean flow path.

Viscous force

The modeling of the viscous force follows the distributed loss model defined in Eq. 2.70, which stems from the work on a moving particle along the streamline. Moreover, the entropy rise is assumed linearly distributed along the blad chord so that

$$f_p = \overline{\rho}\widetilde{T}\frac{\widetilde{V_m}}{\widetilde{W}}\frac{\Delta\widetilde{s}}{c_m}, \tag{3.11}$$

where

$$\Delta\widetilde{s} = c_p \log\frac{\widetilde{T}_{t,\mathrm{W,TE}}}{\widetilde{T}_{t,\mathrm{W,LE}}} - r_{gas}\log\frac{\overline{p}_{t,\mathrm{W,TE}}}{\overline{p}_{t,\mathrm{LE}}}, \tag{3.12}$$

and c_p is the specific heat coefficient at constant pressure. The total temperature ratio is computed from the rothalpy conservation so that

$$\frac{\widetilde{T}_{t,\mathrm{W,TE}}}{\widetilde{T}_{t,\mathrm{W,LE}}} = 1 - \frac{(\Omega r_{\mathrm{LE}})^2 - (\Omega r_{\mathrm{TE}})^2}{2c_p\widetilde{T}_{t,\mathrm{W,LE}}}, \tag{3.13}$$

while the total pressure ratio is expressed using the definition of the loss coefficient $\omega(r)$, Eq. 2.84, as

$$\frac{\overline{p}_{t,\mathrm{W,TE}}}{\overline{p}_{t,\mathrm{W,LE}}} = \frac{\overline{p}_{t,is,\mathrm{W,TE}}}{\overline{p}_{t,\mathrm{W,LE}}} - \omega\left(1 - \frac{\overline{p}_{\mathrm{LE}}}{\overline{p}_{t,\mathrm{W,LE}}}\right). \tag{3.14}$$

This loss coefficient must be obtained from correlations. Consistently with the linearization of the entropy rise along the chord, the loss coefficient is assumed constant along streamlines, being evaluated only from the blade LE and TE positions. The specific correlation used for $\omega(r)$ is presented in Section 3.3.3.

3.3.3 Baseline correlations

The radial distributions of the deviation angle δ_{TE} and loss coefficient ω, used in the computation of the deflection force and the viscous force respectively, are usually unknown, and are therefore obtained from empirical correlations. In the context of a multifidelity approach, where TF and 3D RANS are combined, loss correlations could be learned from the RANS simulations. However, correlations adapted for modern engine designs, i.e., with highly loaded three-dimensional blades, are often kept confidential. As a consequence, the span-wise profiles of δ_{TE} and ω are here computed using empirical correlations originally developed by Lieblein [126] and reported by Aungier [10], with additional contributions from Carter [28], Johnsen and Bullock [106], and Pollard and Gostelow [155]. Further improvements and additions to the baseline correlations are presented in Chapter 4.

These correlations are decomposed into two contributions: a *design* part and an *off-design* part. The design value corresponds to a reference performance at the optimal incidence angle i^* which minimizes the loss coefficient. The off-design contribution is therefore computed as a function of the difference between the actual incidence i and the optimal incidence i^*. However, the near-optimum incidence angle is a priori not known. A correlation characterizing the design incidence angle i^* is thus needed in addition to the deviation angle and loss coefficient correlations.

The correlations for i^*, δ_{TE} and ω rely only on geometric and aerodynamic quantities evaluated at the leading and trailing edges, and are mostly validated for standard blade profiles such as NACA families at low-speed. In the case of high-speed flow conditions and advanced blade designs, such as the controlled diffusion airfoils designed for a prescribed velocity distribution, some modification of the models may be necessary to take into account the improved performance achieved by modern blades. Moreover, the aforementioned correlations are derived from experimental data of two-dimensional cascades. As a result, they only account for two-dimensional profile loss generated in a blade-to-blade plane. However, actual compressor cascades are annular and their successive blade rows are closely spaced, leading to significant interaction in the flowfield. In other words, the three-dimensional losses and radial mixing induced by these interactions are not included in the correlations. Losses related to the growth of the boundary layer on the endwalls are already captured by the Navier-Stokes equations and the turbulence model. The ones stemming from the blade-endwall interaction cannot be captured by an axisymmetric model and may require complementary correlations or stress models.

The following subsections describe in detail the correlations used in the present solver for the optimal incidence angle, the deviation angle and the loss coefficient. The main quantities involved are recalled in Fig. 3.5. Note that all the angles are expressed in degrees. Although some correlations in the literature are expressed in terms of the angle of attack A,

$$A = \beta_{\mathrm{LE}} - \lambda \,, \tag{3.15}$$

where λ is the stagger angle, most, and in particular the ones used here, are based on the incidence angle

$$i = \beta_{\mathrm{LE}} - \kappa_{\mathrm{LE}} \,. \tag{3.16}$$

Finally, one should note that the empirical correlations are applicable to positive camber angles, i.e. compressor stator blades as defined by the author's convention (see Fig. 3.5). For negative camber

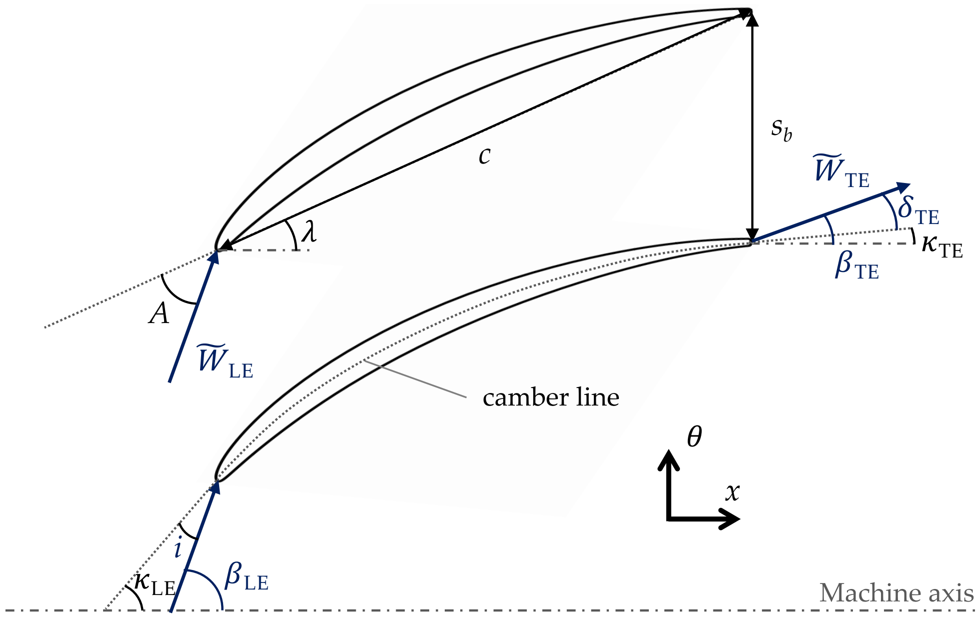

Figure 3.5: Cascade nomenclature in the local frame of reference. The flow angles shown are, by convention, defined as positive in the orientation indicated in the figure.

angle cascades, i.e. compressor rotor blades, the sign of the camber angle must be reversed. After applying the correlations, the sign of the output angles must be again changed to be consistent with the sign convention.

Optimal incidence angle

As mentioned above, the contributions at design conditions in the correlations for δ_{TE} and ω depend on the optimal incidence angle i^*, which must also be approximated. Lieblein [126] proposed a correlation of the form

$$i^* = K_{sh} K_{t,i} \, (i_0^*)_{10} + n \, (\kappa_{\mathrm{LE}} - \kappa_{\mathrm{TE}}) \, , \tag{3.17}$$

where the design incidence angle varies linearly with the total camber. The slope parameter is expressed as

$$n = 0.025\sigma - 0.06 - \frac{\left(\frac{\beta^*_{\mathrm{LE}}}{90}\right)^{(1+1.2\sigma)}}{1.5 + 0.43\sigma} \, , \tag{3.18}$$

with β^*_{LE} the design inlet flow angle and $\sigma = c/s_b$ the solidity. The blade pitch is computed as $s_b = \frac{2\pi\overline{r}}{N}$ where $\overline{r}$ is the man radius of the blade section undr consideration.

The first term in Eq. 3.17 represents the zero-camber incidence angle i_0^*, which accounts for blade-thickness blockage effects. At zero camber, the minimum-loss incidence angle would theoretically vanish, with the stagnation point located at the leading edge. However, staggered blades in a cascade create a blockage normal to the incoming flow, especially along the blade's lower surface. This causes the velocity on the lower side to exceed that on the upper side. A small positive incidence angle is therefore required to shift the stagnation point and reduce the lower-surface velocity. Minimum loss is obtained when this positive incidence yields a circulation around the blade, Γ, equal to zero. The zero-camber incidence angle for 10% thick NACA-65 profiles is given by

$$(i_0^*)_{10} = \frac{(\beta_{\mathrm{LE}}^*)^u}{5 + 46\mathrm{e}^{-2.3\sigma}} - 0.1\sigma^3 \mathrm{e}^{\frac{\beta_{\mathrm{LE}}^* - 70}{4}} , \qquad u = 0.914 + \frac{\sigma^3}{160} . \tag{3.19}$$

Although this correlation was derived from NACA-65 blades with 10% thickness, it can be extended to other blade types by applying correction factors to $(i_0^*)_{10}$. The blade-shape factor K_{sh} accounts for variations in leading-edge geometry: $K_{sh} = 1$ for NACA-65 profiles, $K_{sh} = 1.1$ for C4-series blades, and $K_{sh} = 0.7$ for double-circular-arc blades. The thickness correction factor is defined as

$$K_{t,i} = \left(\frac{10 t_b}{c}\right)^q , \qquad q = \frac{0.28}{0.1 + \left(\frac{t_b}{c}\right)^{0.3}} . \tag{3.20}$$

Finally, it is worth mentioning that the design incidence correlation is implicit because the design inlet flow angle is directly related to the incidence by $\beta_{\mathrm{LE}}^* = i^* + \kappa_{\mathrm{LE}}$, and thus unknown a priori. The correlation must therefore be solved iteratively, typically using a Newton–Raphson method.

Deviation angle

The deviation angle at the trailing edge required to compute the deflection force $\mathbf{f_n}$ is obtained from the correlation

$$\delta_{\mathrm{TE}}(r) = \delta_{\mathrm{TE}}^* + \left[\frac{\partial \delta}{\partial i}\right]^* (i - i^*) + 10 \left(1 - \frac{\widetilde{W}_{m,\mathrm{TE}}}{\widetilde{W}_{m,\mathrm{LE}}}\right) , \tag{3.21}$$

which combines the contribution at design conditions, off-design corrections, and a term accounting for the axial velocity–density ratio (AVDR).

The first term on the right-hand side of Eq. 3.21 corresponds to the contribution at design conditions. It is obtained using a methodology similar to Lieblein's design incidence correlation, derived from low-speed cascade data:

$$\delta_{\mathrm{LE}}^* = K_{sh} K_{t,\delta} (\delta_0^*)_{10} + m \left(\kappa_{\mathrm{LE}} - \kappa_{\mathrm{TE}}\right) , \tag{3.22}$$

where

$$K_{t,\delta} = 6.25 \left(\frac{t_b}{c}\right) + 37.5 \left(\frac{t_b}{c}\right)^2 , \tag{3.23}$$

and K_{sh} is the same as in Eq. 3.18.

The first contribution, $(\delta_0^*)_{10}$, is the zero-camber deviation angle. As discussed previously, for a zero-camber blade at zero incidence, the velocity on the lower surface exceeds that on the upper surface, which induces a positive deviation angle. Applying a small positive incidence compensates this imbalance, and the deviation increases until it reaches a finite positive value at the minimum-loss incidence condition. This base zero-camber deviation angle, derived by Johnsen and Bullock [106], reads

$$(\delta_0^*)_{10} = 0.01\sigma\beta_{\mathrm{LE}}^* + \left(0.74\sigma^{1.9} + 3\sigma\right) \left(\frac{\beta_{\mathrm{LE}}^*}{90}\right)^{1.67 + 1.09\sigma} . \tag{3.24}$$

The second term in Eq. 3.22 introduces a modification of Carter's rule [28], reformulated by Lieblein for improved accuracy. The slope parameter m is expressed as

$$m = \frac{m_{1.0}}{\sigma^d}, \qquad d = 0.9625 - 0.17\frac{\beta^*_{\mathrm{LE}}}{100} - 0.85\left(\frac{\beta^*_{\mathrm{LE}}}{100}\right)^3, \tag{3.25}$$

with

$$m_{1.0} = \begin{cases} 0.17 - 0.0333\frac{\beta^*_{\mathrm{LE}}}{100} + 0.333\left(\frac{\beta^*_{\mathrm{LE}}}{100}\right)^2, & \text{for NACA-65 profiles,} \\ 0.249 + 0.074\frac{\beta^*_{\mathrm{LE}}}{100} - 0.132\left(\frac{\beta^*_{\mathrm{LE}}}{100}\right)^2 + 0.316\left(\frac{\beta^*_{\mathrm{LE}}}{100}\right)^3, & \text{for circular-arc profiles.} \end{cases} \tag{3.26}$$

The second term of Eq. 3.21 represents the off-design contribution. Following Johnsen and Bullock [106], it assumes a linear variation of deviation with incidence with

$$\left[\frac{\partial \delta}{\partial i}\right]^* = \frac{1 + \left(\sigma + 0.25\sigma^4\right)\left(\frac{\beta^*_{\mathrm{LE}}}{53}\right)^{2.5}}{\mathrm{e}^{3.1\sigma}}. \tag{3.27}$$

As sketched in Fig. 3.6, this linear behavior is indeed observed over a broad range of incidence around the design point in many cascade experiments [10, 38, 126].

Finally, the last term in Eq. 3.21 accounts for the influence of the axial velocity–density ratio (AVDR), $\frac{\overline{\rho}_{\mathrm{TE}}\widetilde{W}_{m,\mathrm{TE}}}{\overline{\rho}_{\mathrm{LE}}\widetilde{W}_{m,\mathrm{LE}}}$. In the original NACA tests, the AVDR was kept close to 1 through suction of the endwall boundary layers, thereby reducing blockage, delaying stall, and lowering midspan losses. In real compressors, however, the AVDR generally deviates from unity due to design choices or blockage effects, and corrections to δ_{TE} and ω must be introduced, as proposed by Pollard and Gostelow [155]. In particular, the deviation angle decreases if the axial flow is accelerated (AVDR > 1), since the deceleration along the blade surfaces is reduced. The numerical factor 10 in the correlation is empirical and may vary from about 8 for low stagger angles to about 20 for high stagger angles [38].

Loss coefficient

The profile loss coefficient $\omega_{2\mathrm{D}}$ is required to calculate the viscous blade force $\mathbf{f_p}$ in $\mathbf{S_{bv}}$. The correlation developed by Lieblein [126] for $\omega_{2\mathrm{D}}$ is based on the assumption that boundary-layer growth is mainly governed by the blade loadingand more importantly, by the velocity distribution on the blade suction side. As a result, the profile loss can be related to the properties of the wake[2]. Under design conditions and assuming that $\widetilde{W}_{m,\mathrm{LE}} = \widetilde{W}_{m,\mathrm{TE}}$, which is typically done in classical designs, the loss coefficient is

[2]The exact relation, assuming incompressible two-dimensional cascade flow with uniform inlet conditions, is given by

$$\omega_{2\mathrm{D}} = 2\frac{\theta_w}{c}\frac{\sigma}{\cos\beta_{\mathrm{TE}}}\left(\frac{\cos\beta_{\mathrm{LE}}}{\cos\beta_{\mathrm{TE}}}\right)^2\left[1 - \frac{\theta_w}{c}\frac{\sigma H}{\cos\beta_{\mathrm{TE}}}\right]^{-3}\left(\frac{2H}{3H-1}\right). \tag{3.28}$$

It is obtained from the conservation of the mass-flow rate and total pressure in the clean part of the flow, and the first three wake-moment thicknesses

$$\int_0^\infty \left(\frac{u}{U_e}\right)^j \left(1 - \frac{u}{U_e}\right) \mathrm{d}y, \quad j = 0, 1, 2, \tag{3.29}$$

corresponding respectively to the displacement δ_w ($j = 0$), momentum loss θ_w ($j = 1$), and energy loss thickness ($j = 2$). The wake shape factor $H = \delta_w/\theta_w$ is close to unity (≃1.08 according to Lieblein [124]) at typical wake measuring stations and thus, the last two factors are often neglected for turbulent attached flows.

approximately proportional to the wake momentum thickness, expressed as

$$\omega_{2D}(r) = 2\frac{\theta_w}{c}\frac{\sigma}{\cos\beta_{TE}}\left(\frac{\widetilde{W}_{TE}}{\widetilde{W}_{LE}}\right)^2 , \tag{3.30}$$

where θ_w is the momentum thickness of the wake.

For conventional velocity distributions, Lieblein showed that the momentum diffusion process can be expressed as the ratio between the maximum suction-side velocity W_{max} and the outlet velocity W_{TE}. Several diffusion factors were derived from these parameters and used as correlating quantities for the loss coefficient. Early correlations, however, were valid only at design incidence and did not account for off-design conditions. To generalize the model, Lieblein introduced the equivalent diffusion factor D_{eq}, which explicitly includes incidence effects. The wake momentum thickness is then correlated to D_{eq} as

$$\frac{\theta_w}{c} = K_1\left[K_2 + 3.1\,(D_{eq}-1)^2 + 0.4\,(D_{eq}-1)^8\right], \tag{3.31}$$

with $K_1 = 0.004$ and $K_2 = 1$. This correlation is valid for a wide range of blade configurations provided that $D_{eq} < 2$, the so-called *diffusion limit*. For $D_{eq} > 2$, the flow conditions lead to an abrupt rise in losses and wake momentum thickness, as shown in Fig. 3.6.

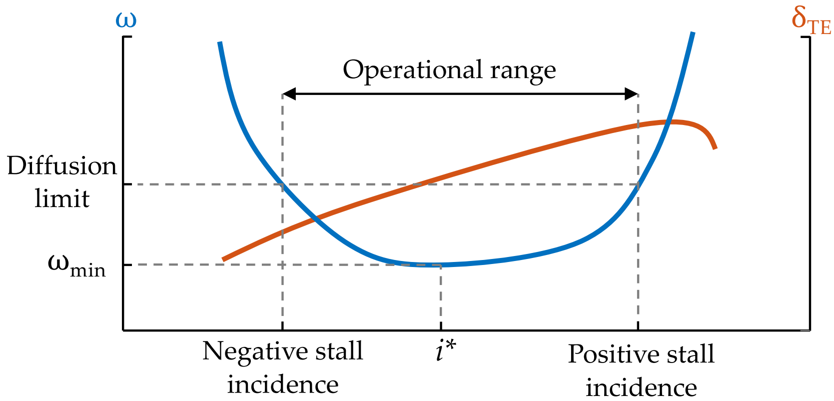

Figure 3.6: Qualitative behavior of the key parameters δ_{TE} and ω laws with respect to the incidence i.

The equivalent diffusion factor is defined as

$$D_{eq} = \left(\frac{W_{max}}{W_{LE}}\right)\frac{\widetilde{W}_{LE}}{\widetilde{W}_{TE}} \approx \left(1.12 + 0.61\underbrace{\frac{\cos^2\beta_{LE}}{\sigma}\left[\frac{r_{LE}\widetilde{V}_{\theta,LE} - r_{TE}\widetilde{V}_{\theta,TE}}{r_{LE}\widetilde{W}_{m,LE}}\right]}_{=\Gamma'} + a\,|i-i^*|^{1.43}\right)\frac{\cos\beta_{TE}}{\cos\beta_{LE}}\frac{\widetilde{W}_{m,LE}}{\widetilde{W}_{m,TE}} , \tag{3.32}$$

where $a = 0.0117$ for NACA-65 blades and $a = 0.007$ for C4 circular-arc blades for instance. In the present work, the former value is retained. This relation is valid from design incidence up to positive stall. To extend its applicability to negative stall conditions, the incidence term is expressed with an absolute value.

The second term in the parenthesis in Eq. 3.32 is related to the incompressible circulation parameter

Γ', defined as[3]

$$\Gamma' = \frac{\cos^2 \beta_{\mathrm{LE}}}{\sigma} \left(\tan \beta_{\mathrm{LE}} - \tan \beta_{\mathrm{TE}}\right) = \frac{\cos^2 \beta_{\mathrm{LE}}}{\sigma} \frac{\left(\widetilde{V}_{\theta,\mathrm{LE}} - \widetilde{V}_{\theta,\mathrm{TE}}\right)}{\widetilde{W}_{m,\mathrm{LE}}}, \tag{3.35}$$

where $\widetilde{W}_{m,\mathrm{LE}} = \widetilde{W}_{m,\mathrm{TE}}$. For annular cascades where the streamline radius and axial velocity vary, a more general expression is used:

$$\Gamma' = \frac{\cos^2 \beta_{\mathrm{LE}}}{\sigma} \left(\tan \beta_{\mathrm{LE}} - \frac{r_{\mathrm{TE}} \widetilde{W}_{m,\mathrm{TE}}}{r_{\mathrm{LE}} \widetilde{W}_{m,\mathrm{LE}}} \tan \beta_{\mathrm{TE}}\right) = \frac{\cos^2 \beta_{\mathrm{LE}}}{\sigma} \frac{\left(r_{\mathrm{LE}} \widetilde{V}_{\theta,\mathrm{LE}} - r_{\mathrm{TE}} \widetilde{V}_{\theta,\mathrm{TE}}\right)}{r_{\mathrm{LE}} \widetilde{W}_{m,\mathrm{LE}}}. \tag{3.36}$$

Finally, it should be emphasized that the model does not explicitly account for the velocity distribution on the pressure side, which can significantly affect the wake momentum thickness. Indeed, W_{max} refers to the maximum velocity on the suction side, and thus no information from the pressure side is used in the formulation. Moreover, these correlations, like the correlation for the deviation angle, were originally developed for incompressible flow and 10% thick profiles. In reality, compressibility increases both losses and diffusion at high Mach numbers, while Reynolds number effects also influence boundary-layer growth and wake properties. A practical way to account for these additional effects is to tune the correlations constants by comparison with performance data from a range of compressors. These adjustments are presented in Chapter 4.

3.3.4 Incidence correction

For a given flow incidence, the flow direction at the blade row inlet does not follow the camber line at the leading edge. However, the flow angle in the bladed region is imposed by the blade flow deflection force. Consequently, an angle discontinuity occurs at the leading edge, as illustrated in Fig. 3.7. This discontinuity leads to a sudden and non-physical increase of entropy and a spurious generation of losses, whose magnitude increases with the absolute value of the incidence angle.

The issue of incidence discontinuity arises specifically in analysis-type models, where the flow angle is prescribed rather than results from the solution. A numerical treatment is thus adopted to remove the flow discontinuity. A common methodology [13, 123, 149, 168] consists in linearly modifying the mean-flow-path angle in the blade leading edge regions so that it adapts to the incident flow, in a manner similar to the imposition of the deviation angle at the trailing edge. As shown in Fig. 3.8, the fix is applied so that the stream surface modification due to incidence affects the first few percents of the blade chord. The blade geometry, and thus the mean flow path, are thus locally modified by this numerical artifact. However, the actual geometric parameters of the blade remain the inputs to the correlations used in the solver.

[3] The circulation parameter is related to the circulation Γ around the airfoil through

$$\Gamma' = \frac{s_b \cos^2 \beta_{\mathrm{LE}}}{\sigma} \frac{\Gamma}{W_{\mathrm{LE}}}. \tag{3.33}$$

Using a contour integral around the airfoil,

$$\Gamma = \oint W \, dl = \frac{V_x}{s_b} \left(\tan \beta_{\mathrm{LE}} - \tan \beta_{\mathrm{TE}}\right). \tag{3.34}$$

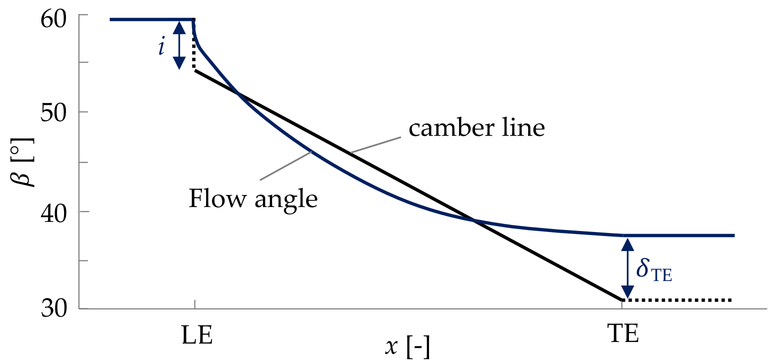

Figure 3.7: Local flow angle distribution in a cambered NACA 65-009 cascade. Comparison between the potential flow solution and the camber-line driven approach at an incidence of 5° [112].

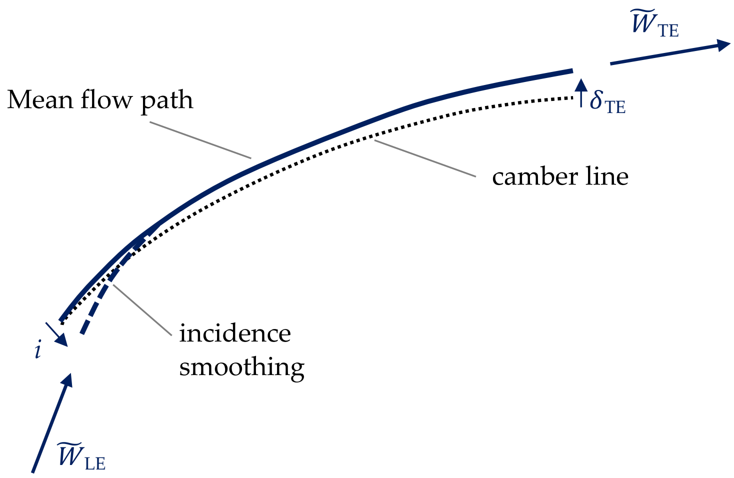

Figure 3.8: Sketch of the smoothed blade geometry at positive incidence.

This artifice can be seen as a non-physical modification of the blade loading distribution since the mean camber surface is changed. Nonetheless, the assumption that the flow follows the mean camber surface at the leading edge is anyway a crude one since the flow is highly non-axisymmetric in that region. As emphasized by Baralon [12], comparisons with tangentially averaged 3D data confirm that a flow turning occurs within the first 20–30% of the chord, consistently with the chosen correction strategy. At positive incidence, for instance, the leading edge region exhibits a redistribution of momentum, with acceleration on the suction side and deceleration on the pressure side. The resulting gradient progressively turns the flow so that the tangentially averaged flow angle does not follow the blade angle within the first percents of chord. While this justification holds for subsonic and transonic regimes, its extension to supersonic incidence is less straightforward due to the interplay of shocks and expansion waves. Furthermore, some blade definitions do not possess a well-defined metal angle. For instance, the camber line of the NACA 65 series presents an infinite slope at both the leading and trailing edges, making the definition of a geometric blade angle ambiguous. As a result, cascade test data for these profiles were usually reported in terms of angle of attack and flow turning, rather than incidence and deviation angles. To overcome this limitation, it has become common practice to define effective inlet and outlet blade angles based on an equivalent circular-arc camber line. This reference camber line is constructed as the circular arc passing through the two end points of the profile and the point of maximum camber located at mid-chord, following the approach originally described by Johnsen and Bullock [106].

Baralon [12] originally applied this technique to about 20 to 30% of the chord, showing that the severity of the discontinuity is weaker in subsonic cases. In addition, he proposed an alternative approach based on modifying the momentum equations with supplementary source terms to directly control both entropy production and the flow angle at the leading edge. However, such a formulation requires changes to the discretization scheme and the use of ghost cells, making it intrusive and numerically less robust; it is therefore not retained in the present work. The analysis of the spurious entropy generation confirms that a smoothing on the first 30% of the chord is adequate. Smoothing over a smaller portion of the chord leads to entropy generation and performance prediction error, while a longer portion impacts the geometry in a too large proportion, as shown in Fig. 3.9. Smoothing over 30% of the chord is thus used in the following, unless otherwise specified.

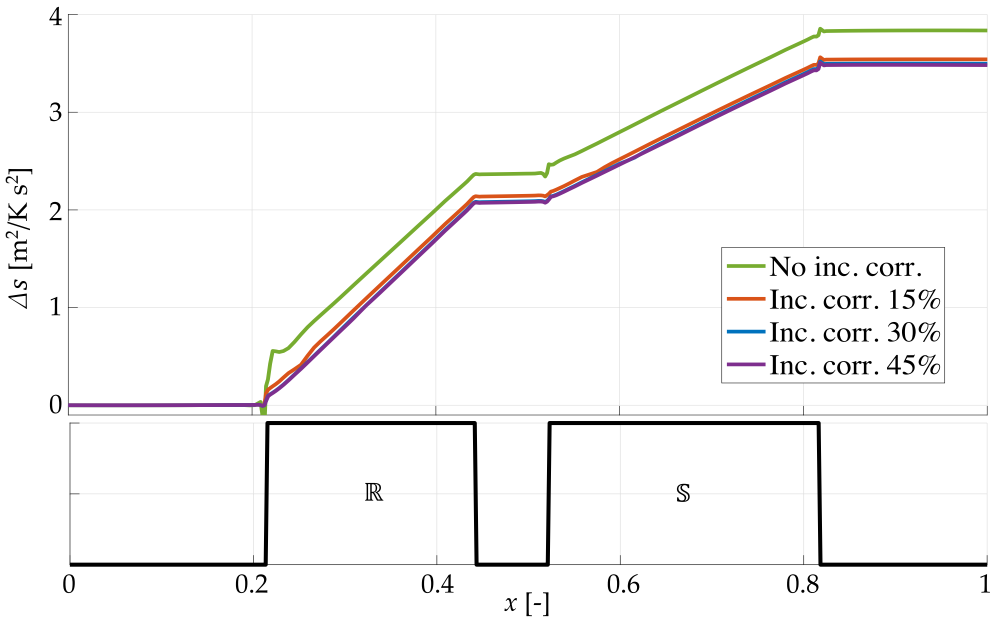

Figure 3.9: Entropy generation along a mid-span streamline for different extents of the incidence smoothing in a compressor stage.

3.4 Concluding remarks

In summary, the through-flow framework presented in this chapter relies on a viscous, time-marching Navier–Stokes formulation adapted from a 3D CFD solver. The governing equations are recast in a non-intrusive form, enabling a coupling between `elsA` and the dedicated `ASTEC` routines for the computation of blade body forces and blockage source terms. A turbulence closure is provided by the k–l Smith model while the closure of the blade forces requires empirical correlations for the deviation angle δ_{TE} and the loss coefficient ω. The predictive capability of the through-flow solver is assessed in Chapter 4, where the accuracy of the baseline correlations is quantified and possible improvements or extensions are proposed.

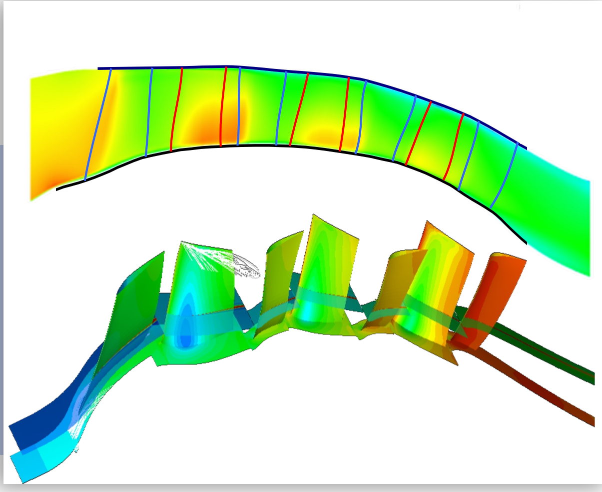

Chapter 4

Model Analysis

This chapter describes the evaluation of the through-flow model introduced in Chapter 3 on two axial compressor test cases to assess the applicability of the method. The test cases are first introduced, after which TF simulations are compared to steady, pitchwise-periodic 3D RANS computations employing a mixing-plane approach at the rotor–stator interfaces. On the one hand, the model error arising from solver approximations and closure assumptions is assessed. On the other hand, the predictive accuracy relative to the baseline correlations is quantified. Finally, modifications to existing correlations are proposed to enhance fidelity, including recalibration where appropriate and the introduction of new correlations when necessary. The overarching goal of this chapter is to address the question: *How accurate is the through-flow approach compared to higher-fidelity methods such as RANS simulations?*

4.1 Axial compressor test cases

This section presents the two configurations choses as test cases: the CME2 compressor stage and a modern subsonic axial low-pressure compressor. To provide the background necessary for interpreting the results and analyses discussed in the following sections, the fundamental theoretical concepts of axial-flow compressors are first reviewed. The reference numerical simulations used for validation are also briefly discussed.

4.1.1 Background on axial-flow compressors

Compressors in aeronautical propulsion systems belong to the family of *dynamic* compressors, as they generate a pressure rise by transferring kintic energy to a flowing fluid stream. Within the overall transformation sequence undergone by the air in a gas turbine engine, which is described by the Brayton cycle, the fundamental role of the compressor is to increase the stagnation pressure and the stagnation enthalpy of the working fluid before it enters the combustion chamber and then expands in the turbine. A higher enthalpy rise leads to greater temperature and pressure levels at the combustor outlet, which in turn improves the efficiency and specific thrust of the engine.

The energy transfer results from fundamental mechanical principles. According to Newton's second law, the torque exerted by a rotating blade row is equal to the rate of change of the flow angular momentum about the rotation axis. For an adiabatic flow, this principle leads directly to the *Euler* *turbomachinery equation*, which relates the change in stagnation enthalpy across the blade row to the variation in tangential momentum:

$$\Delta\widetilde{H_t} = \Omega\left(r_{\mathrm{TE}}\widetilde{V_{\theta,\mathrm{TE}}} - r_{\mathrm{LE}}\widetilde{V_{\theta,\mathrm{LE}}}\right) . \tag{4.1}$$

From this relationship, two main ways of increasing the stagnation enthalpy can be identified: by enlarging the radius of the streamtube, thereby increasing the blade speed, or by deflecting the flow to modify its swirl component. These two mechanisms correspond to the two major compressor families: *centrifugal compressors*, which rely on the radial acceleration of the flow, and *axial compressors*, which increase energy mainly through flow deflection within successive blade rows. In general, centrifugal compressors can achieve higher pressure ratios per stage because of their larger energy transfer capability due to the increased radius. However, axial compressors offer superior efficiency by distributing the total compression work over a greater number of stages, while maintaining a higher mass-flow rate. In modern engines, this concept is further extended by dividing the compression system into a *low-pressure compressor* and a *high-pressure compressor*, each mechanically coupled to its corresponding low- and high-pressure turbine through a dedicated shaft. This architecture allows a better distribution of the aerodynamic work and enables each shaft to operate at its own optimal rotational speed, thereby improving the compacity. Note that *mixed-flow compressors* can combine features of both concepts to balance performance and compactness.

In the present work, the focus is placed on axial compressors, which are predominant in modern aero-engine architectures. As stated above, axial compressors operate through multiple stages, each composed of a rotating blade row (the rotors) followed by a stationary blade row (the stators). Only the rotor can exchange mechanical work with the fluid: it accelerates the flow tangentially, thereby increasing its swirl and transferring kinetic energy from the shaft to the fluid. The downstream stator then decelerates this swirling motion, converting a portion of the acquired kinetic energy into static pressure while redirecting the flow toward the proper incidence for the row of the next stage. This alternating mechanism is shown in Fig. 4.1.

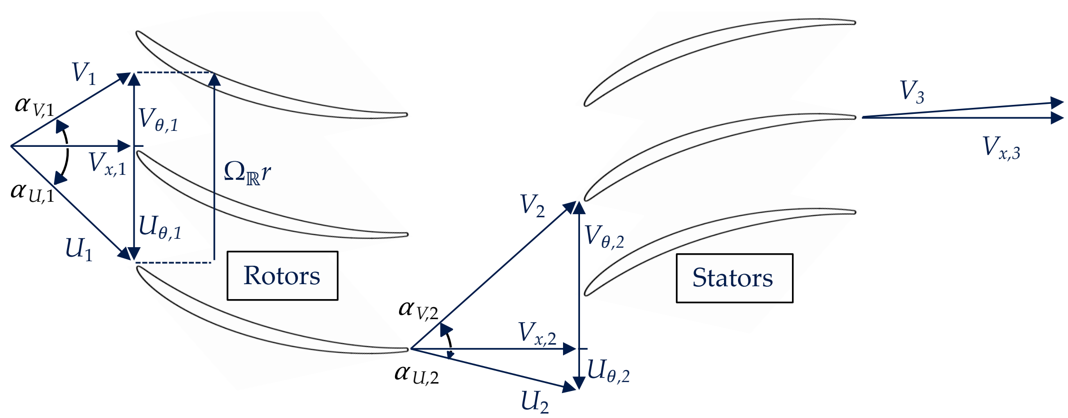

Figure 4.1: Velocity triangles of an axial compressor stage on a cascade streamsurface at constant radius. α is the tangential flow angle expressed either in the absolute frame of reference (α_V) or in the rotating frame of reference (α_U). U is the relative velocity.

Since only the rotors can perform mechanical work on the fluid, the total enthalpy remains constant across the stator rows. In the rotating frame of reference, however, it is the quantity known as the rothalpy I that is conserved along a streamline in rotor rows. The rothalpy is defined as

$$\widetilde{I} = \widetilde{H}_{t,U} - \frac{1}{2}(\Omega_{\mathbb{R}} r)^2 , \tag{4.2}$$

where $H_{t,U}$ is the stagnation enthalpy in the relative frame of reference. The conservation of rothalpy can be derived from Eq. 4.1 together with the definition of the relative velocity U [38].

The key performance parameters of a compressor are usually measured by the *isentropic efficiency* η_{is} and the *total pressure ratio* Π. The total pressure ratio Π is defined based on the total pressure evaluated between the inlet of the first blade row and the outlet of the last blade row as

$$\Pi = \frac{\overline{p}_{t,\text{out}}}{\overline{p}_{t,\text{in}}} . \tag{4.3}$$

The isentropic efficiency η_{is} is given by the ratio between the ideal (isentropic) work required to drive the compressor and the actual work input. A higher efficiency indicates that a larger portion of the work produced by the turbine can be converted into useful work output rather than being consumed to drive the compressor shaft. It can be expressed as

$$\eta_{\text{is}} = \frac{\widetilde{H}_{t,\text{out,is}} - \widetilde{H}_{t,\text{in}}}{\widetilde{H}_{t,\text{out}} - \widetilde{H}_{t,\text{in}}} = \frac{\Pi^{\frac{\gamma-1}{\gamma}} - 1}{\frac{\widetilde{T}_{t,\text{out}}}{\widetilde{T}_{t,\text{in}}} - 1} . \tag{4.4}$$

The performance of axial compressors is commonly represented using compressor maps, which plot the total pressure ratio and isentropic efficiency as functions of the mass-flow rate for a given rotational speed of the shaft, as illustrated in Fig. 4.2. Each iso-speed line is bounded by two physical limits: the *surge* limit at low mass-flow rates and the *choke* limit at high mass-flow rates.

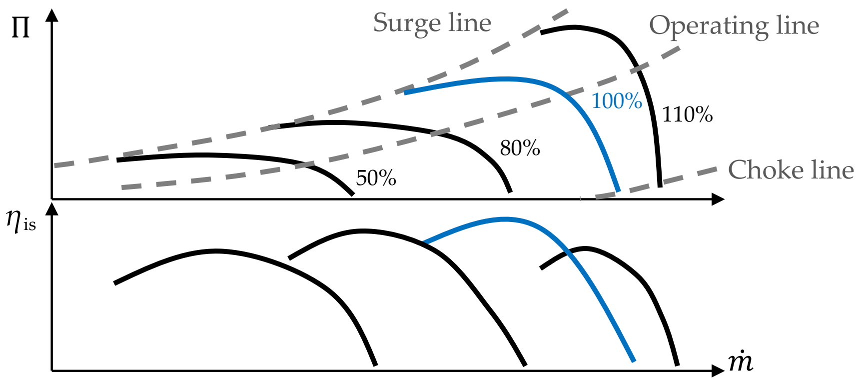

Figure 4.2: Compressor performance map. The iso-speed lines are indicated as fractions of the nominal rotational speed, $\Omega_{\mathbb{R}}$ (blue line).

At low flow rates, the incidence on the blades rises, reaching loading limits and causing boundary-layer separation, which results in a degradation of aerodynamic performance. When this process intensifies, the compressor may reach the stall or even the surge condition, characterized by large-amplitude, low-frequency oscillations of the flow rate and pressure ratio. Under these conditions, portions of the flow can locally reverse direction, and in severe cases, the entire compressor may experience alternating forward and backward flow. Such unstable phenomena are highly detrimental and can lead to mechanical failure if sustained. To prevent the onset of such instabilities, compressors must operate at a safe distance from the surge line. This distance is quantified by the *surge margin*, K_{stall}, which represents the acceptable range between the flow conditions at the design point and those at which surge occurs. The surge margin may be expressed in terms of either the mass-flow rate or the pressure ratio between the design operating point and the conditions at which surge occurs [10]. A high surge margin indicates a more stable compressor. In practice, Π_{surge} is often set to the maximum pressure ratio Π_{max}, as this is the point where the increase in aerodynamic loss compensates the additional energy imparted by the compressor [138]. With this definition, the surge margin can reach up to about 20% in the case of axial compressors used in turbofan engines [71].

At the opposite end of the operating range, when the downstream pressure decreases, the mass-flow rate increases until sonic conditions are reached in one or more blade passages. Beyond this point, the flow becomes *choked*: no further increase in mass flow is possible for the given geometry, and the compressor efficiency rapidly drops. For these reasons, both the stall and choke boundaries must be avoided during operation. In practice, the complete engine is designed to operate the compressor slightly below the surge pressure ratio, along what is known as the *operating line* on the compressor map. The nominal design point is therefore selected between these two extremes, near the peak efficiency. These performance curves can also be plotted for each individual stage of the compressor to achieve the *stage matching*. In this case, the objective is to ensure that every stage operates under its optimal conditions, namely at high efficiency and high pressure ratio.

4.1.2 Test case 1: the CME2 compressor stage

The first test case considered in this study is the well-documented CME2 research compressor, designed by Safran Aircraft Engines [43, 72]. The CME2 is a single-stage, low-speed axial compressor that has been extensively used in the literature. This configuration was notably used by Simon [168] to compute the exact source terms of the circumferentially averaged TF equations. Figure 4.3 shows a meridional view of the compressor flow path and its 3D geometry. The compressor stage is almost purely axial, with only a slight radial variation of the hub line along the meridional direction. The main operating

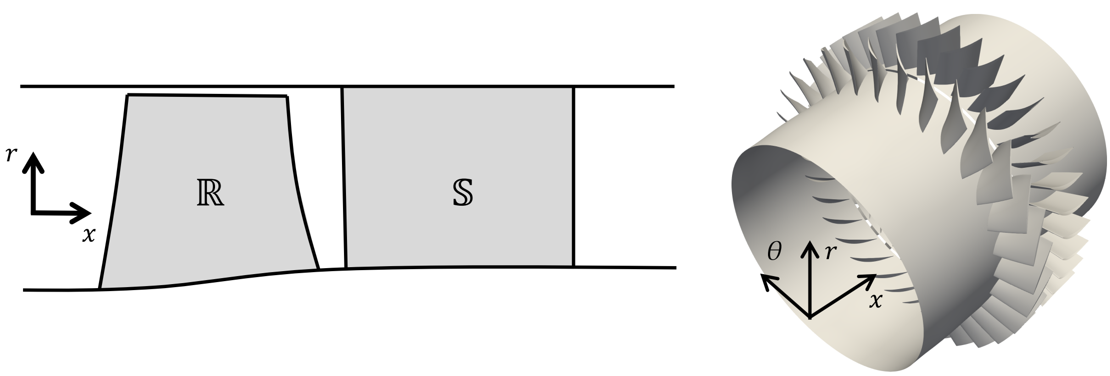

Figure 4.3: CME2 stage configuration: meridional view (left) with the rotor ($\mathbb{R}$) and stator ($\mathbb{S}$) blades and 3D view (right).

parameters are summarized in Table 4.1. The flow remains entirely subsonic throughout the stage, with a relative Mach number at rotor tip of about 0.55. The Reynolds number, based on the axial chord length, is approximately 3×10^5, corresponding to fully turbulent flow conditions. The stator is nearly prismatic, and both the rotor and stator blades feature controlled diffusion airfoil profiles. The corresponding blade geometries are shown in Fig. 4.4.

Parameters	**Values**
Rotor blade count	30
Stator blade count	40
Rotor tip-gap height	0.4 mm
Casing radius (inlet)	$r_{\text{casing}} = 0.275$ m
Hub radius (inlet)	$r_{\text{hub}} = 0.214$ m
Rotor/stator axial distance (mid-span)	20 mm
Nominal rotation speed	$\Omega_{\mathbb{R}}$ = 6300 RPM (105 Hz)
Nominal mass-flow rate	$\dot{m} = 10.5\,\mathrm{kg\,s^{-1}}$
Nominal pressure ratio	$\Pi = 1.15$
Nominal isentropic efficiency	$\eta_{\text{is}} = 0.92$

Table 4.1: Geometrical and flow parameters of the CME2 compressor stage.

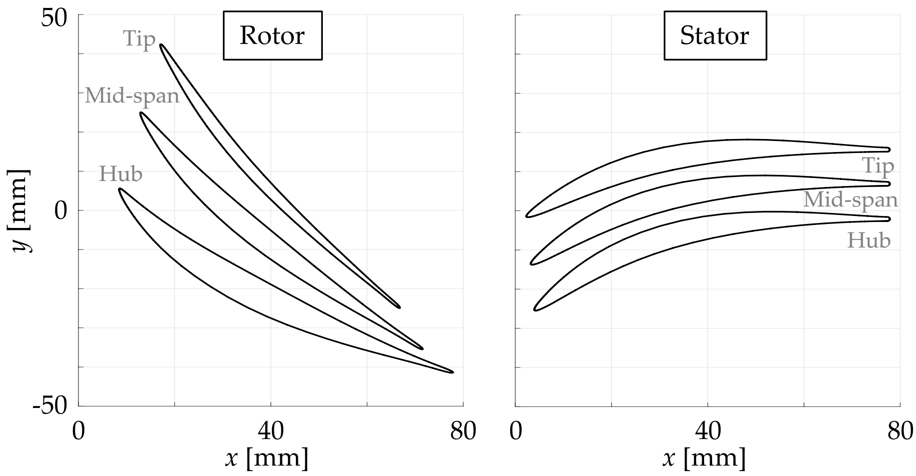

Figure 4.4: CME2 blade geometry at hub, mid-span and tip locations.

4.1.3 Test case 2: a modern axial low-pressure compressor

The second test case consists of a modern low-pressure compressor designed by Safran Aero Boosters, which is embedded in operating aircraft engines. In contrast to the CME2, this highly loaded compressor features a higher, though still subsonic, Mach number flow, a significantly higher mass-flow rate and its endwalls exhibit significant radius variations. It is composed of three stages of modern 3D blades between an inlet guide vane (IGV) and a strut, as depicted in Fig. 4.5. The three blade rows exhibit a higher aspect ratio and a lower solidity compared to the CME2 blades. For confidentiality reasons, the exact geometry of this configuration is deliberately not shown, and all results presented in the following sections are nondimensionalized.

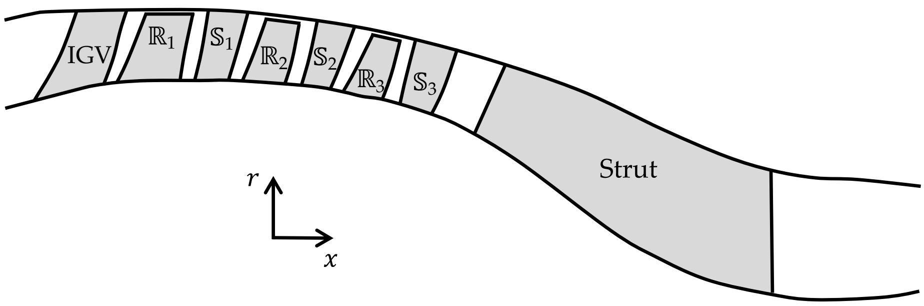

Figure 4.5: Meridional view of the low-pressure compressor test case where IGV represents the inlet guide vane, and $\mathbb{R}_i$ and $\mathbb{S}_i$ the rotor and stator of row i, respectively.

4.1.4 Reference simulations

To assess the solver, through-flow simulations of both test cases are compared against steady, pitchwise-periodic RANS computations performed with the `elsA` solver using the *mixing-plane* approach. The numerical setup of the RANS simulations and their boundary conditions are identical to those presented in Section 3.2.3 and 3.2.4. The computational meshes were generated with `Autogrid` from Numeca. Only one blade passage is modeled per blade row, assuming that the flow is periodic from passage to passage. The mixing-plane approach establishes a steady circumferentially averaged flow field at each rotor–stator interface. Each blade row is thus computed independently in a steady local frame, with periodic boundary conditions on front and back surfaces. This model is formally valid in the limit of large axial spacing between blade rows but remains widely used in the industry for its robustness and computational efficiency. A detailed review of the mixing-plane methodology and its various implementations in turbomachinery applications has been provided by Sturmayr [181].

The main differences between the TF and RANS formulations arise from the treatment of the blade forces and the modeling of circumferential stress. In the through-flow approach, the aerodynamic effects of the blades are represented by body-force source terms, whereas in RANS computations, these forces are directly produced by the physical blade surfaces immersed in the flow. The circumferential stress, which should in principle appear in the averaged equations, is neglected in the TF formulation. The Reynolds stress is modeled in both types of simulation through an identical turbulence model. However, in the TF solver it should be azimuthally averaged to remain consistent with the circumferentially averaged formulation.

RANS simulations actually represent the level of fidelity just above the TF model in the Adamczyk's cascade: they also neglect unsteady and aperiodic stresses but explicitly resolve the mean blade passage flow. The mixing-plane treatment introduces additional modeling errors at the rotor–stator interfaces that are not present in the through-flow computations. In addition, the well-known deficiencies and uncertainties associated with turbulence modeling also contribute to RANS modeling errors. This aspect is illustrated in Fig. 4.6, where the performance of the CME2 compressor stage is computed using two different turbulence models and compared to LES and experimental results. Noticeable discrepancies appear between the two predictions, and the difference tends to increase as the operating point moves away from the nominal conditions. For instance, near the stall limit, although the stall mechanism predicted by RANS appears broadly consistent with experimental evidence for the CME2 stage, the evolution of the flow differs markedly from one turbulence model to the other. In particular, the stall initiation in both simulations results from an interaction between the tip-leakage flow and a vortex-type separation forming on the stator suction side under high incidence (see Fig. 4.7). However, the two RANS models lead to different patterns of the deviation angle and loss coefficient, as shown in Fig. 4.8. These differences also alter the predicted location of the numerical stall limit, i.e. the last stable point before the simulation diverges or oscillates without reaching a steady periodic state. Fundamentally, turbulence models are not specifically calibrated for secondary flows and separation; consequently, neither model can be relied upon as is to robustly predict the mean stall inception mechanism. It is worth noting that the influence of the turbulence model is expected to be smaller in the TF simulations, since turbulence effects enter only through the modeling of viscous forces at the endwalls, whereas the blade loading is prescribed via body-force terms and is thus largely independent of the turbulence closure. However, the empirical correlations underlying the TF formulation are not expected to remain reliable in the vicinity of stall.

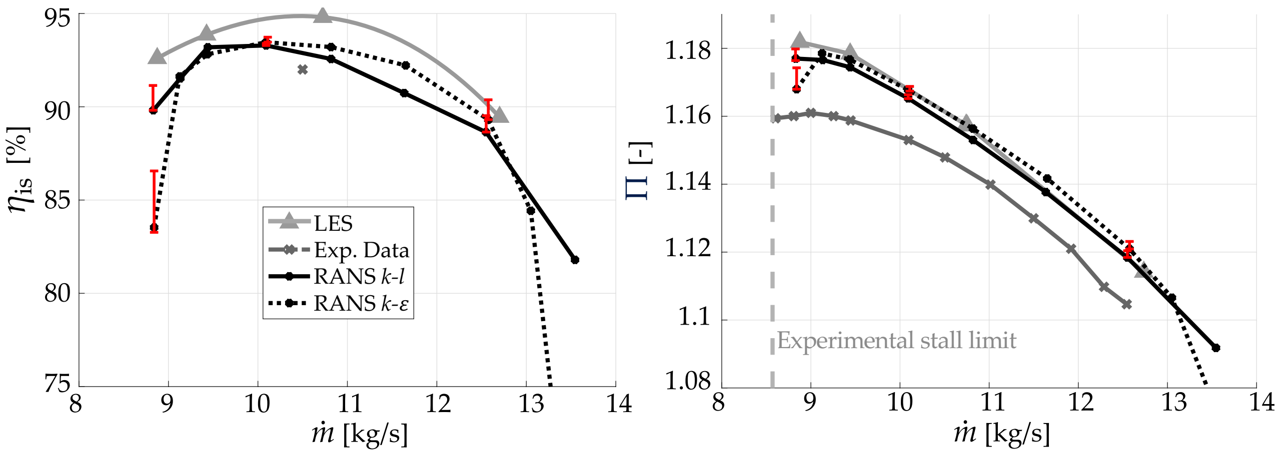

Figure 4.6: Isentropic efficiency η_{is} (left) and total pressure ratio Π (right) as a function of the mass-flow rate at the nominal rotational speed of the CME2 compressor stage. Comparison of experimental measurements [72], LES [72] and 3D RANS using the $k-l$ Smith turbulence model and the $k-\epsilon$ Launder–Sharma model. Error bars represent the differences between a classical Favre (area-weighted) average and a mass-weighted average.

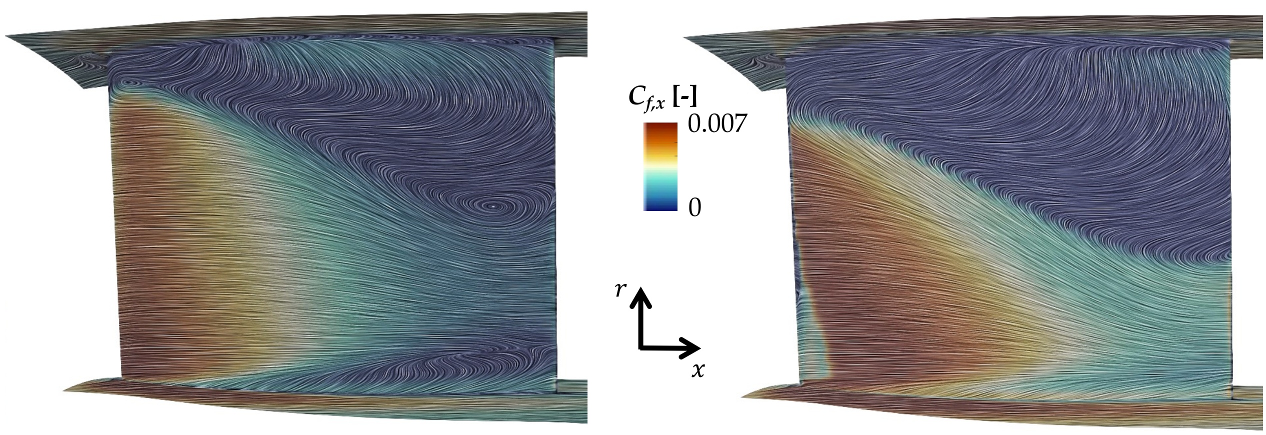

Figure 4.7: Distribution of the axial skin-friction coefficient on the stator suction surface of the CME2 stage close to stall limit: RANS simulations using the $k-l$ Smith turbulence model (left) and the $k-\epsilon$ Launder–Sharma model (right).

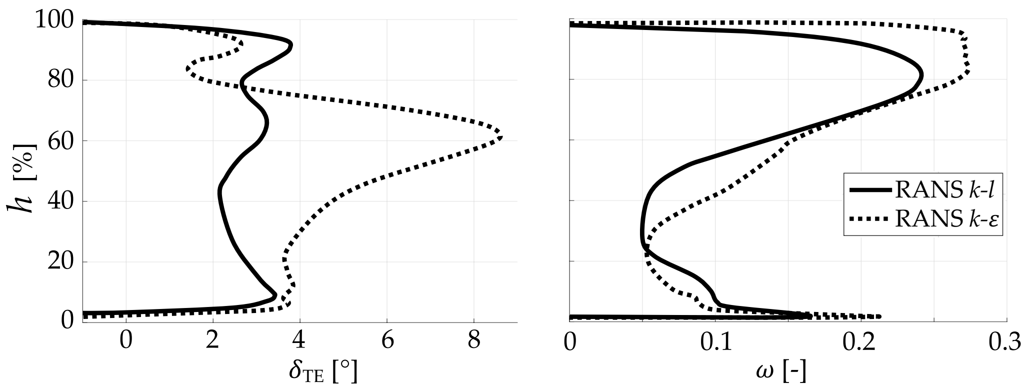

Figure 4.8: Comparison between pitch-wise averaged 3D RANS using the $k-l$ Smith turbulence model and the $k-\epsilon$ Launder–Sharma model close to stall limit: deviation angle δ at the trailing edge (left) and loss coefficient ω (right) along the stator blade span h.

The use of RANS for result comparison is thus questionable as the reliability is still low according to the Adamczyk's cascade. However, these simulations are widely used in the industry because higher levels of fidelity are almost inaccessible during the design process in view of their computational cost. It should also be emphasized that neither experimental measurements nor higher-fidelity numerical simulations are free of error. The experimental data reported by Gourdain [72], for instance, exhibit non-negligible uncertainties. The measurements were obtained using hot-wire and cross-film probes, the latter being intrusive and restricted to non-bladed regions in the present configuration. In addition, the averaging procedure and the specific measurement plane can also have a significant impact on the reported quantities. The error associated with the choice of averaging method is illustrated in Fig. 4.6 for RANS simulations using two different averaging approaches, where the discrepancy between the two increases as the operating point moves away from nominal conditions.

Similarly, the LES results presented in Gourdain [72] also display discrepancies. As noted by the author, LES predictions are significantly more sensitive than RANS to modeling "details," including boundary-condition specification, mesh resolution in shear layers, subgrid-scale parameter choices, and small geometric features. These sensitivities can introduce notable deviations in predicted performance and flow structures.

In the present context we do not need to outperform RANS and it is therefore more relevant to compare TF simulations to RANS rather than to more precise simulations such as LES. In this sense, the steady periodic RANS results serve as the primary target for assessing the predictive capability of the through-flow model. In future work, however, it will also be of interest to compare the TF approach against higher-fidelity simulations, such as URANS and LES, in order to further improve the model behavior in operating regimes such as near-stall conditions, where unsteadiness and aperiodic flow phenomena play a significant role.

Note that, in the present work, a reduced computational domain is employed compared to that used in Gourdain [72]. The original LES setup extends farther upstream and downstream, whereas a shorter domain is adopted here to limit computational cost. This approach also minimizes discrepancies between the 3D and through-flow solutions by reducing the impact of mismatched boundary-layer development upstream of the rotor. The reference simulations of the second test case have been calibrated to best fit the test bench experimental results at the design operating point. It should be noted, however, that when throttling the compressor using a valve law, the assumption of constant inlet total conditions may introduce slight deviations in the predicted performance curves compared to experimental measurements.

4.2 Through-flow solver assessment

As previously discussed, Simon [168] demonstrated that when the full Adamczyk formulation is used together with exact source terms extracted from 3D RANS computations, the through-flow solution can reproduce almost perfectly the azimuthally averaged 3D flow field, provided that the discretization schemes satisfy the requirements of stability and consistency and that the boundary conditions are consistently specified. This result confirms that, in principle, the TF framework is fully capable of recovering the averaged high-fidelity solution. However, these exact source terms are rarely available in practice, as the unclosed terms depend on flow quantities that are not directly resolved by the through-flow solver. The major challenge, therefore, lies in developing reliable models for these source terms, whose accurate representation remains one of the most demanding aspects of through-flow modeling. The objective of this section is thus to assess whether the TF model described in Chapter 3, when relying on its practical approximations and closure models instead of exact source terms, can achieve a comparable level of agreement with the reference RANS simulations. To do so, the results of the through-flow simulations for both test cases are presented and compared to the reference RANS results using the $k-l$ Smith turbulnce model. The analysis focuses on overall performance metrics as well as on detailed flow field comparisons.

The discrepancies between the through-flow and RANS results can be separated into two main sources in addition to the numerical errors, which are expected to remain negligible. The first corresponds to *model errors*, arising from the approximations and assumptions inherent to the governing equations and closure relations (e.g., expression of the blade forces in terms of deviation angle and loss coefficient) described in the previous chapter. The second source is related to the *empiricism* of the correlations and calibrations used within the blade force formulation.

4.2.1 Model error quantification

The first objective is to determine whether the through-flow model is capable of reproducing the 3D RANS results when the ideal correlation parameters are known. To this end, the TF simulations are supplied with the exact radial distributions of the key quantities δ_{TE} and ω, extracted from each corresponding high-fidelity computations. This approach allows the modeling error to be isolated from the uncertainty associated with the correlation empiricism.

CME2 compressor stage

The comparison of CME2 performance, evaluated with respect to the rotor row inlet and stator row outlet stations[1], is shown in Fig. 4.9. The performance of the CME2 compressor stage is well captured by the Navier-Stokes TF solvers. In particular, the shape of the curves is reproduced with good fidelity,

[1]In the case of the RANS and TF simulations, these stations are defined as locations slightly upstream of the rotor leading edge and slightly downstream of the stator trailing edge, with a small axial offset.

including the peak location and overall trend across the operating range, meaning that the flow turning and losses are accurately represented.

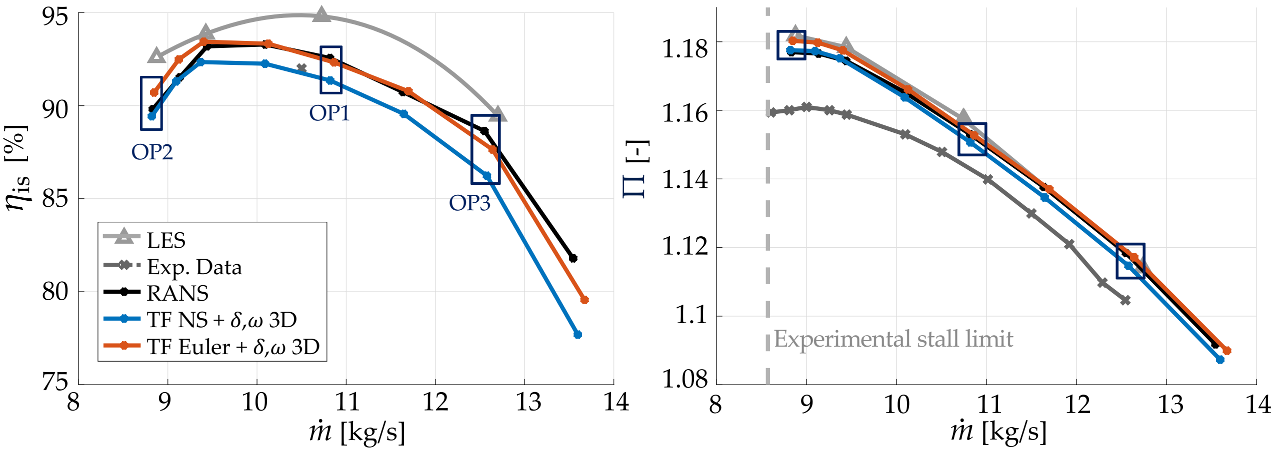

Figure 4.9: Isentropic efficiency η_{is} (left) and total pressure ratio Π (right) as a function of the mass-flow rate at the nominal rotational speed of the CME2 compressor stage. Comparison of experimental measurements [72], LES [72], RANS and through-flow simulations fed with exact correlation parameters from RANS computations.

Nevertheless, the viscous TF formulation tends to slightly underestimate the stage performance, especially in terms of isentropic efficiency. This bias originates from the fact that the radial profiles of deviation angle and loss coefficient already include all mechanisms responsible for deviation and loss, including viscous effects in the main stream and within the endwall boundary layers. These effects are therefore imposed twice in the viscous TF model: once through the prescribed δ_{TE} and ω profiles, and again through the Reynolds stresses introduced by the turbulence model. For illustration, the performance predicted by the Euler-based TF model is also shown in Fig. 4.9. In this case, the efficiency curve is noticeably improved, confirming that the double imposition of certain loss mechanisms was the primary source of error.

This raises the question of whether an inviscid approach might be more appropriate in such situations, as it would inherently avoid this issue. This question will be further discussed below, but it can already be stated that, if a model accounting for the full set of losses is available, an Euler-based formulation would provide a consistent framework to prevent double counting. However, in practice, this issue is expected to arise only in specific situations, namely when exact source terms are available, which is an uncommon case, or when additional endwall corrections are introduced. The latter are generally associated with a limited level of accuracy and generality in the literature. Moreover, previous studies, such as the work of Simon [168], have shown that combining a viscous formulation with secondary-flow correlations can yield satisfactory results, as these correlations are often not calibrated within the near-wall region, typically within the first few percent of the boundary layer, making them complementary to the viscous formulation. Therefore, this observation does not imply that an Euler-based TF solver should systematically be preferred over a NS-based formulation. Rather, it highlights that, for comparisons in which the loss and deviation profiles are directly extracted from viscous RANS simulations, an inviscid formulation constitutes a more consistent choice. Alternatively, when using a viscous TF solver, the δ_{TE} and ω distributions derived from RANS should in principle be modified to remove the contribution of viscous mechanisms already resolved by the turbulence model, thereby avoiding double counting. Although such a decomposition is not straightforward in practice, this result underlines the importance of ensuring consistency between the physical content of the correlations and that of the governing equations employed in the through-flow model.

The remaining discrepancies can be attributed to a combination of numerical and modeling errors. Numerical errors primarily arise from the interpolation procedures required to transfer the radial distributions of δ_{TE} and ω from the 3D RANS mesh onto the TF grid. Moreover, near the endwalls, the deviation angle is bounded to avoid predicting locally mean reversed flow if the interpolated or extracted RANS values are inaccurate. Although the TF solver is formally able to accommodate such behavior, doing so greatly stiffens the problem, especially since the physical relevance of the resulting separation becomes questionable. In addition, the loss coefficient is evaluated along the streamlines through Eq. 2.84. An inaccurate streamline reconstruction or interpolation error may occasionally lead to negative values of the loss coefficient, which are non-physical. For this reason, the loss coefficient is constrained to remain non-negative in the present implementation. The contribution of numerical errors is, however, expected to remain limited compared to that of modeling errors.

The modeling errors arise from the assumptions underlying the formulation of the through-flow model. In particular, the following limitations should be recalled:

- the blade forces are represented through simplified body-force models that only approximate the underlying physics;
- the deviation angle and the entropy gradient are assumed to vary linearly along the streamlines, which introduces an additional level of approximation;
- in the presence of a nonlinear equation of state, the additional unclosed terms that appear in the circumferentially averaged equations are systematically neglected;
- the circumferential stress is ignored outside the blade rows and only partially accounted for through the prescribed distributions of δ_{TE} and ω in the blade rows.

The last two sources of modeling error are likely to be most significant in regions where the flow exhibits strong non-uniformities. As illustrated in Fig. 4.10, such regions of strong non-uniformity are primarily located near the blade leading and trailing edges and in the endwall regions, as indicated by the high levels of kinetic energy associated with the circumferential stress in these areas. Around the leading edge, the incoming flow undergoes a rapid reorganization as it wraps around the blade, while at the trailing edge the abrupt disappearance of the blade induces further redistribution of momentum. Within the blade row itself, the kinetic energy varies because of the boundary-layer growth and the aerodynamic loading required to turn the flow. Nevertheless, despite these sources of epistemic uncertainty, the through-flow model still predicts the turbomachinery flow field with remarkably good accuracy.

A qualitative overview of the averaged streamsurface predicted by the TF model under nominal operating conditions (OP1) is presented in Fig. 4.11, which clearly illustrates the flow turning achieved by the blade forces in both blade rows. Moreover, the endwall boundary layers are well represented in the stream surface of the NS-based TF model, as such a viscous formulation, unlike inviscid

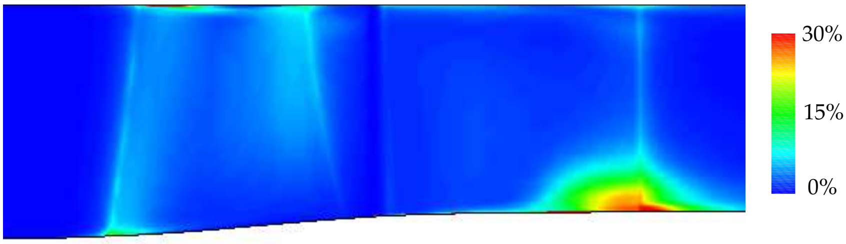

Figure 4.10: Percentage of total kinetic energy associated with circumferential stress contributions from RANS at nominal operating conditions of the CME2 compressor stage (adapted from Simon [168]).

through-flow models, allows resolving the boundary layers on the annulus endwalls. As can also be observed near the hub, the streamlines are deflected by the rotation of the hub due to the imposed no-slip condition. The combination of low kinetic energy within the viscous layers and the curvature induced by the blade passage results in boundary layers that become markedly skewed.

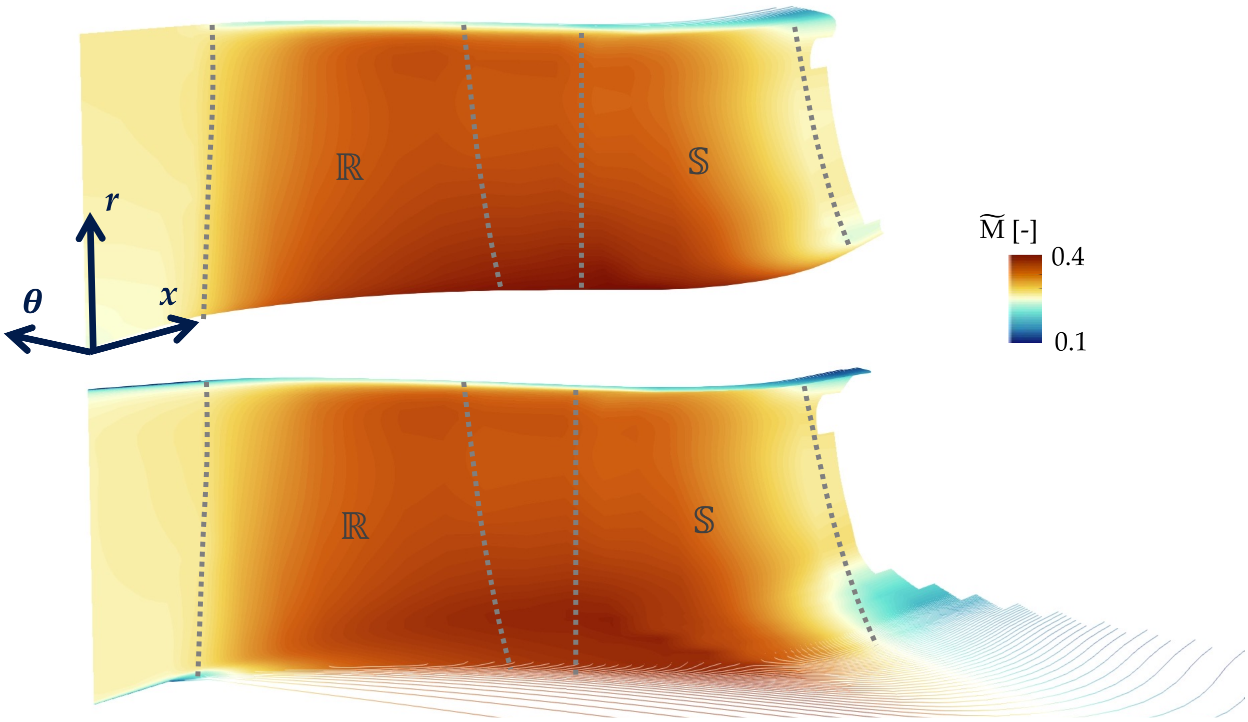

Figure 4.11: Axisymmetric averaged streamlines for the CME2 stage at the nominal operating point (OP1), from Euler-based (top) and NS-based (bottom) TF simulations, with Mach number contours and fictitious rotor (R) and stator (S) positions.

More quantitative insight is provided in Figs. 4.12–4.17, which present the radial distributions at the rotor and stator outlets for three operating conditions. The comparisons are performed at identical mass-flow rates, or within a very small tolerance when exact matching is not possible. Overall, the TF model supplemented with the 3D information extracted from the reference RANS solutions captures the spanwise evolution of the flow with very good accuracy, although the discrepancies become slightly more pronounced near the stall limit (OP2). It remains, however, difficult to clearly determine which source of error predominates in this regime.

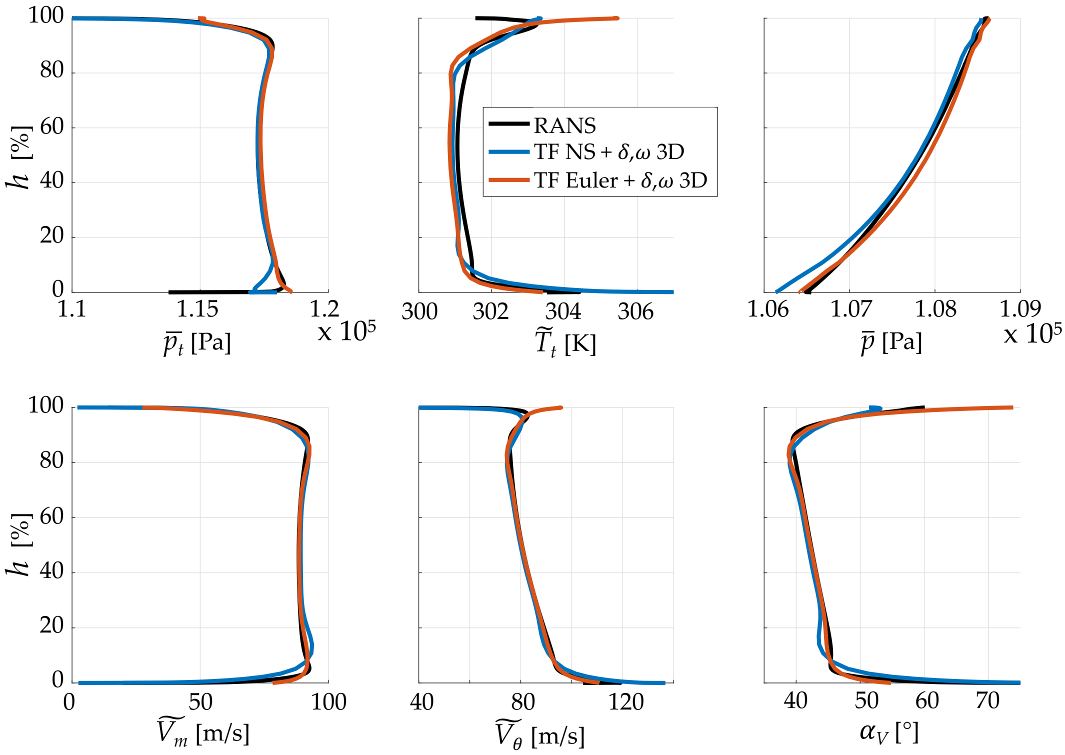

Figure 4.12: Comparison between TF and pitch-wise averaged 3D RANS simulations of the CME2 stage at nominal conditions (OP1): spanwise distributions of total pressure, total temperature, static pressure (top), axial and azimuthal velocities, and flow angle (bottom) at the rotor outlet.

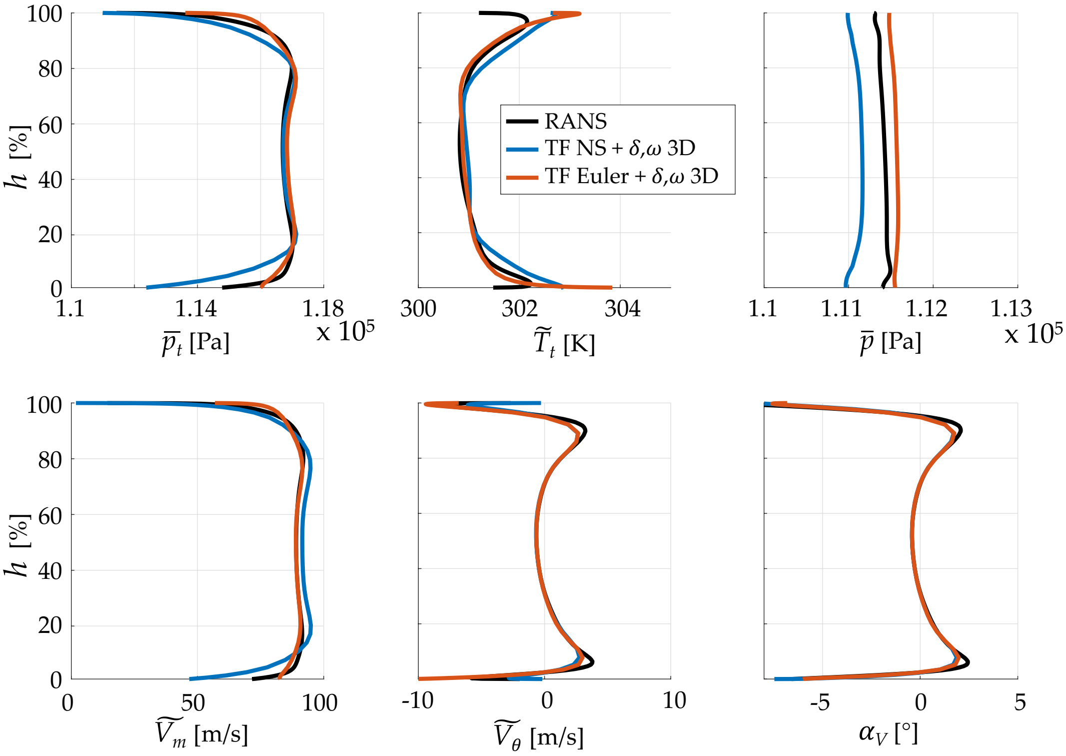

Figure 4.13: Comparison between TF and pitch-wise averaged 3D RANS simulations of the CME2 stage at nominal conditions (OP1): spanwise distributions of total pressure, total temperature, static pressure (top), axial and azimuthal velocities, and flow angle (bottom) at the stator outlet.

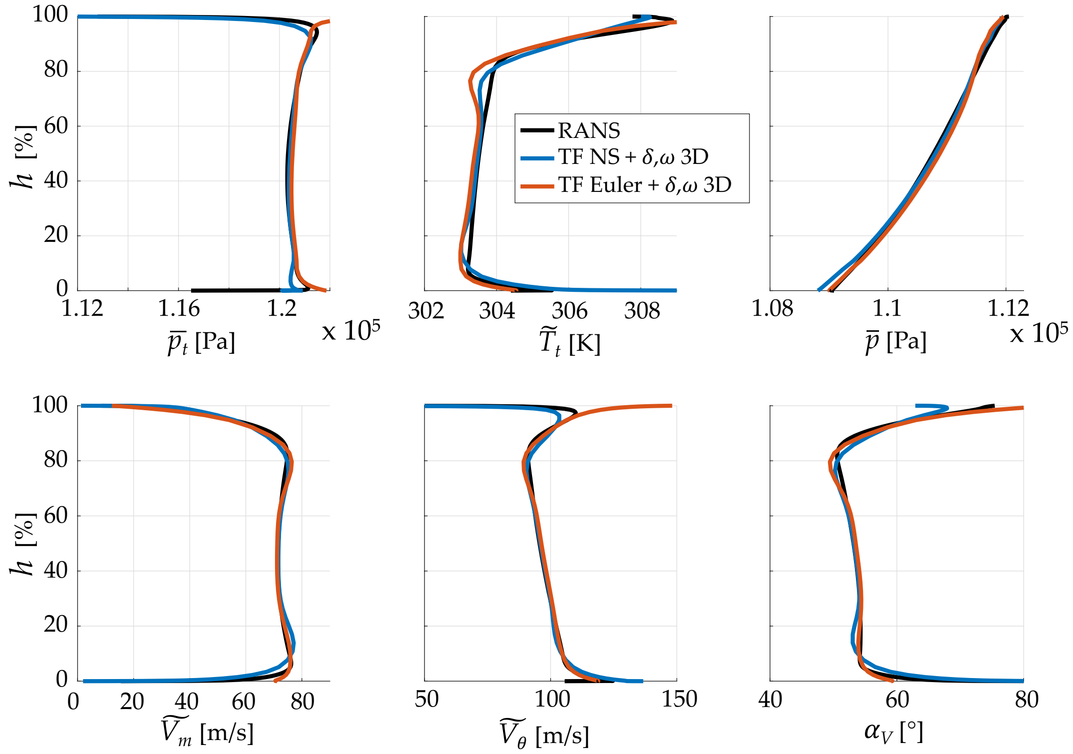

Figure 4.14: Comparison between TF and pitch-wise averaged 3D RANS simulations of the CME2 stage at peak pressure ratio (OP2): spanwise distributions of total pressure, total temperature, static pressure (top), axial and azimuthal velocities, and flow angle (bottom) at the rotor outlet.

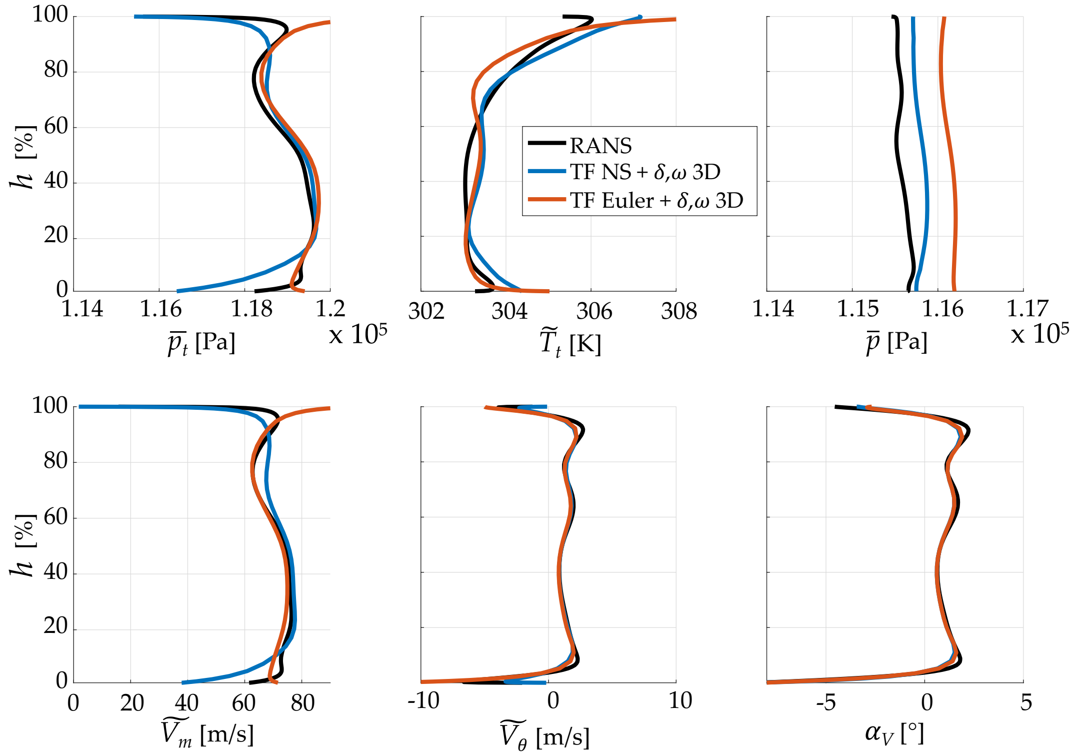

Figure 4.15: Comparison between TF and pitch-wise averaged 3D RANS simulations of the CME2 stage at peak pressure ratio (OP2): spanwise distributions of total pressure, total temperature, static pressure (top), axial and azimuthal velocities, and flow angle (bottom) at the stator outlet.

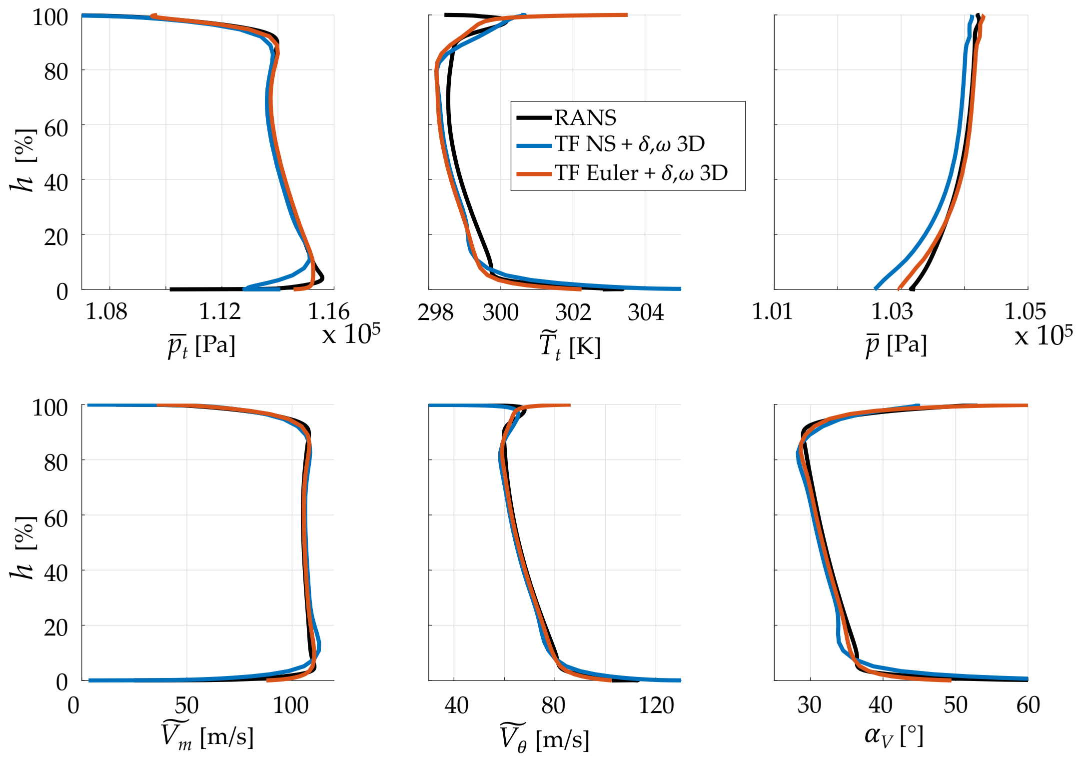

Figure 4.16: Comparison between TF and pitch-wise averaged 3D RANS simulations of the CME2 stage close to choke conditions (OP3): spanwise distributions of total pressure, total temperature, static pressure (top), axial and azimuthal velocities, and flow angle (bottom) at the rotor outlet.

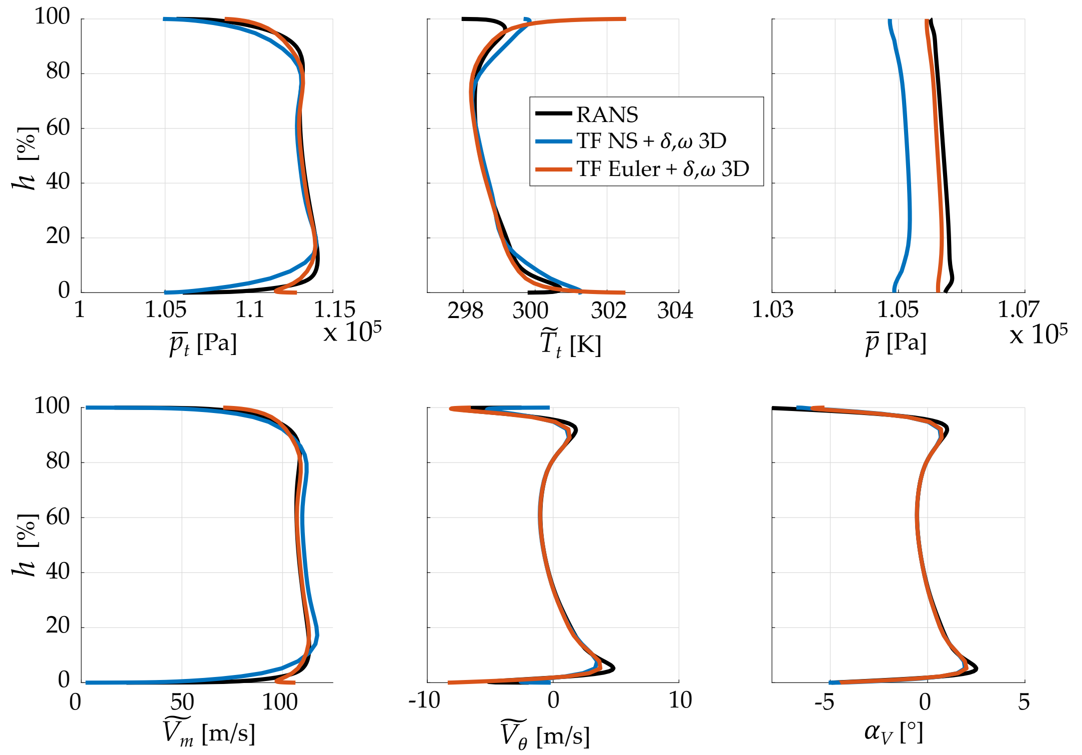

Figure 4.17: Comparison between TF and pitch-wise averaged 3D RANS simulations of the CME2 stage close to choke conditions (OP3): spanwise distributions of total pressure, total temperature, static pressure (top), axial and azimuthal velocities, and flow angle (bottom) at the stator outlet.

Some differences also persist most notably in the endwall regions. For the Navier–Stokes TF formulation, the endwall boundary layers tend to be overly thick. This is a direct consequence of the double imposition of loss mechanisms at the hub and shroud: the endwall blockage is partly contained in the prescribed δ_{TE} and ω distributions and is again introduced through the turbulence model. As a result, the meridional velocity in the core flow is slightly higher in the NS-based TF solution in order to satisfy the same mass-flow requirement. This additional loss also leads to a lower static pressure level for the same mass-flow rate. For the Euler-based TF model, these discrepancies are significantly reduced, as the viscous contributions are not reintroduced through the Reynolds stress.

Nevertheless, the mean level of total pressure is very well reproduced. The predictions of $\widetilde{V_\theta}$ and of the absolute flow angle α_V are also satisfactory, as expected given that the local flow-angle distribution is imposed. It should also be recalled that the radial profiles are extracted just downstream of the trailing edge. The discrepancies observed in $\widetilde{V_\theta}$ and α_V can therefore be partly explained by the fact that, once the flow exits the bladed region, the flow angle is no longer controlled by the body-force term. As discussed above, this region is characterized by significant circumferential stresses that are not represented in the present model. For instance, the discrepancies in the absolute flow angle α_V observed at the outlet of the rotor mainly arise from slight differences in the meridional velocity V_m, which adjusts to ensure consistency with the target mass flow rate. For an imposed relative flow angle α_U and rotational speed Ωr, these variations lead to small changes in the velocity triangle, and therefore in the resulting absolute flow angle α_V. In particular, the meridional velocity at the hub near the rotor outlet is lower in the NS-based TF predictions than in the RANS results, resulting in a larger absolute flow angle α_V, as illustrated in Fig. 4.18.

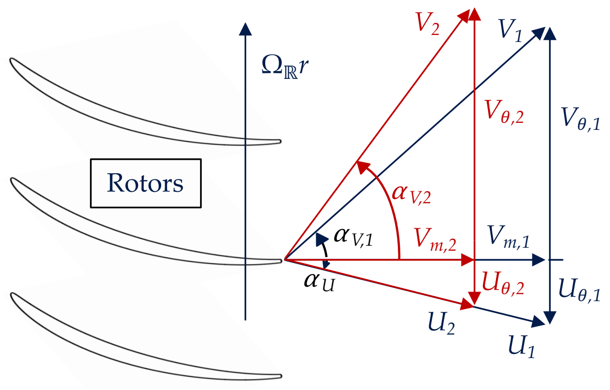

Figure 4.18: Velocity triangles of a streamsurface at the rotor outlet for two different meridional velocities, $V_{m,1}$ and $V_{m,2}$, while the relative outlet flow angle α_U is imposed.

The total-temperature distribution exhibits somewhat larger differences, as it depends on several flow variables. Indeed, from Eq. 4.1, the total temperature along a streamline in a rotor blade row can be expressed as

$$c_p \Delta \widetilde{T}_t = \Delta \left(\Omega_{\mathbb{R}} r \widetilde{V_x} \tan \alpha_W + (\Omega_{\mathbb{R}} r)^2 \right) . \tag{4.5}$$

In this case, for which the inlet flow is almost axial and the inlet total temperature is uniform, the total temperature at the rotor outlet is given by

$$\frac{\widetilde{T}_{t,\mathrm{TE}}}{\widetilde{T}_{t,\mathrm{LE}}} = 1 + \frac{\Omega_{\mathbb{R}} r_{\mathrm{TE}}}{c_p \widetilde{T}_{t,\mathrm{LE}}} \left(\tan \alpha_{W,\mathrm{TE}} \widetilde{V}_{x,\mathrm{TE}} + \Omega_{\mathbb{R}} r_{\mathrm{TE}} \right) . \tag{4.6}$$

Errors in the predicted flow angle, in the meridional velocity, or in the migration of the streamlines therefore have a direct impact on the total temperature level at the rotor outlet. For the stator, the total temperature level is directly inherited from the rotor exit flow. In addition, differences in the amount of losses captured by the TF model, either within the bladed regions or in the inter-row zones, lead to discrepancies in the predicted total temperature distribution through their influence on entropy generation. Double counting of losses is also particularly evident in the total temperature distribution near the hub and tip, where the NS-based TF model tends to overpredict the total temperature.

It should also be recalled that no blade force is applied within the rotor tip gap. In this region, the flow is governed solely by the solver rather than by prescribed body-force source terms, which explains why the discrepancies are generally larger there. The NS-based TF formulation captures the tip-gap behavior more accurately, owing to its ability to represent viscous effects and endwall shear more consistently than the Euler-based version. The high level of total temperature rise predicted by the Euler computation is due to an inaccurate estimation of the flow angle in this region.

Axial low-pressure compressor

The comparison of the low-pressure compressor performance, evaluated with respect to the first row inlet and last row outlet stations, is shown in Fig. 4.19. The results are non-dimensionalized by reference values related to the nominal operating conditions (OP1) for confidentiality reasons. The through-flow simulations give accurate results along the overall performance curves while such a model is usually used to predict only nominal conditions at early design iterations. As in the first test case, the agreement obtained here is also very good, confirming the robustness of the approach over a wide range of operating conditions. The mean epistemic error margin based on an L2 norm of the extrapolated performance curves is less than 1% for the total pressure ratio, and the run time of the throughflow simulation is at least two orders of magnitude shorter than that of the corresponding RANS simulation. The relative difference for the isentropic efficiency is slightly higher. This small disagreement between the performance predictions are mainly due to the circumferential stress that is intrinsically included in the RANS computations but neglected by the through-flow model. In addition to this, rotor tip clearance and leakage flow cavity are currently not represented in the through-flow path. Their impact is only partially included in the prescribed parameters distribution. Finally, a more realistic stream-wise distribution of the key parameters δ_{TE} and ω could also improve the prediction, as shown by Pacciani et al. [143].

At low mass-flow rate, the performance characteristics are limited by the non-convergence of both computational codes close to the same (numerical) stall-onset point: either limit-cycle oscillations appear or the simulation simply diverges. At high mass-flow rate, the choking condition is achieved for a slightly lower mass-flow rate than the RANS prediction. This discrepancy is primarily attributed to the double imposition of boundary-layer losses: they are introduced once through the prescribed δ_{TE} and ω distributions, and again through the turbulence model. This interpretation is supported by

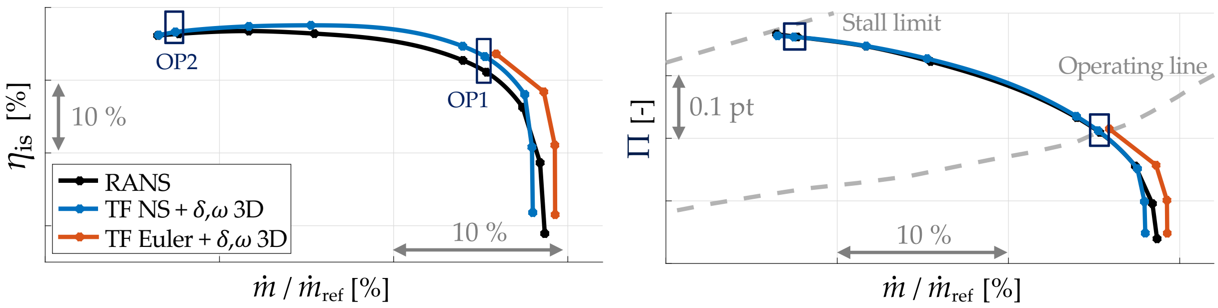

Figure 4.19: Isentropic efficiency η_{is} (left) and total pressure ratio Π (right) as a function of the normalized mass-flow rate of the low-pressure compressor. Comparison of RANS and through-flow simulations fed with exact correlation parameters from RANS computations.

the Euler-based TF simulations shown in Fig. 4.19, which slightly overestimate the choking mass-flow rate because all viscous losses and blockage mechanisms are underestimated. In addition, the flow turning at the blade leading edge is not directly imposed: it results from the incidence correction combined with the linear variation of the deviation along the streamlines. This treatment also affects the predicted choking mass-flow rate.

The corresponding radial distributions for two operating conditions are shown in Figs. 4.20–4.23 for the first stage. The results obtained for the other stages exhibit the same trends but, for the sake of conciseness and confidentiality, they are not presented here. Similarly, the Euler-based TF results are not shown, as they would not provide additional insight. As in the first test case, the radial distributions are very well captured by the through-flow model. The agreement obtained with the NS-based TF formulation is even slightly better for this test-case than with the Euler-based TF, because the double imposition of losses in the endwall region has a reduced impact when the aspect ratio is higher. Moreover, in multi-stage compressors, the endwall boundary layers generally are relatively thin due to the high blade span, thereby limiting their overall influence on the core flow [209]. Unlike the CME2 test case, whose RANS simulations did not include a stator undercasing cavity, the present RANS simulations feature such cavities, and their influence is clearly visible in the near-hub radial distributions. These effects are not explicitly modeled in the through-flow approach, which naturally leads to localized discrepancies. As expected, these differences increase further under off-design operating conditions.

As a conclusion, it has been shown that the viscous through-flow model is able to reproduce fairly well the 3D steady averaged flow field under the aforementioned assumptions provided that the key parameter distributions of δ_{TE} and ω are precisely known (e.g., from high-fidelity data).

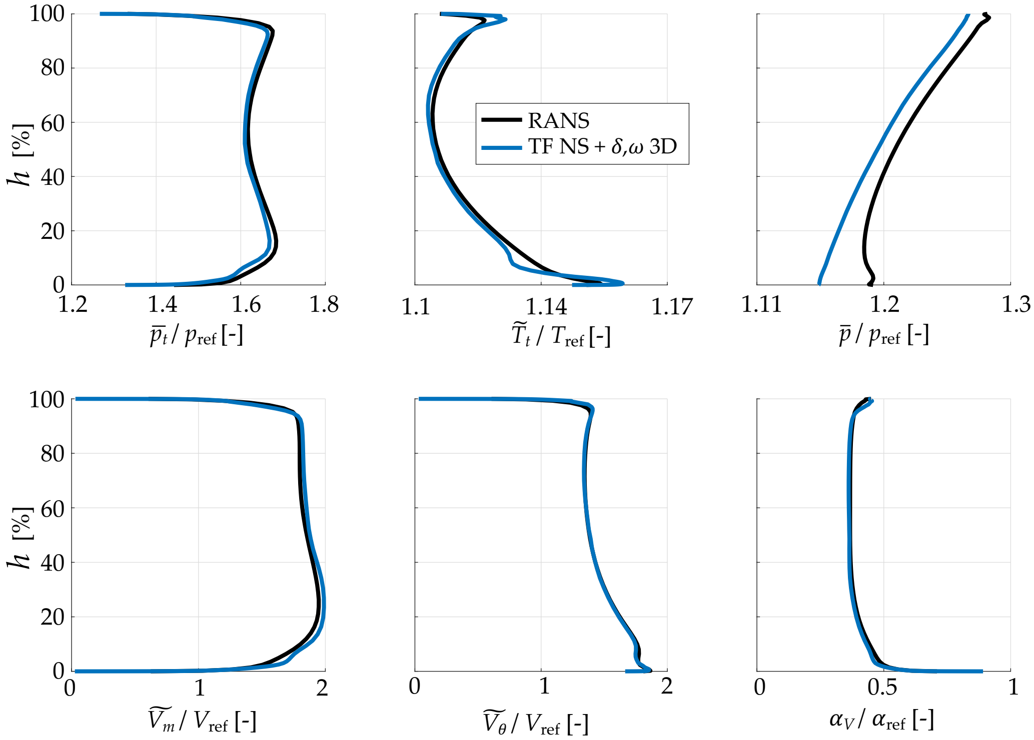

Figure 4.20: Comparison between TF and pitch-wise averaged 3D RANS simulations of the compressor at nominal conditions (OP1): spanwise distributions of total pressure and temperature, static pressure (top), axial and azimuthal velocities, and flow angle (bottom) at the $\mathbb{R}1$ outlet.

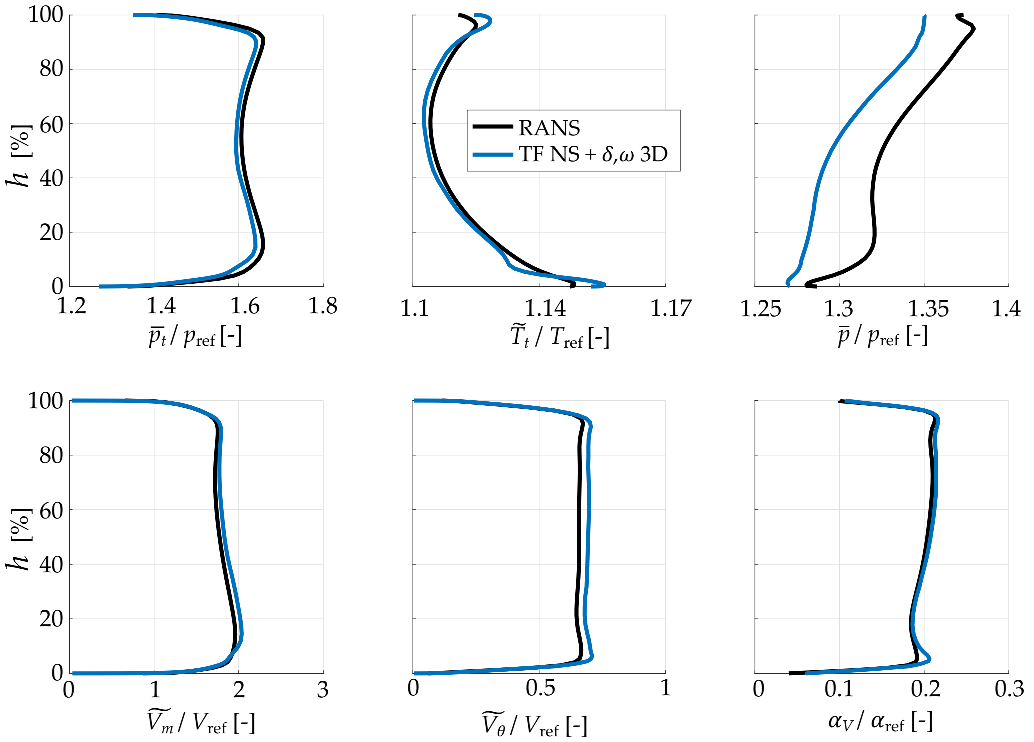

Figure 4.21: Comparison between TF and pitch-wise averaged 3D RANS simulations of the compressor at nominal conditions (OP1): spanwise distributions of total pressure and temperature, static pressure (top), axial and azimuthal velocities, and flow angle (bottom) at the $\mathbb{S}1$ outlet.

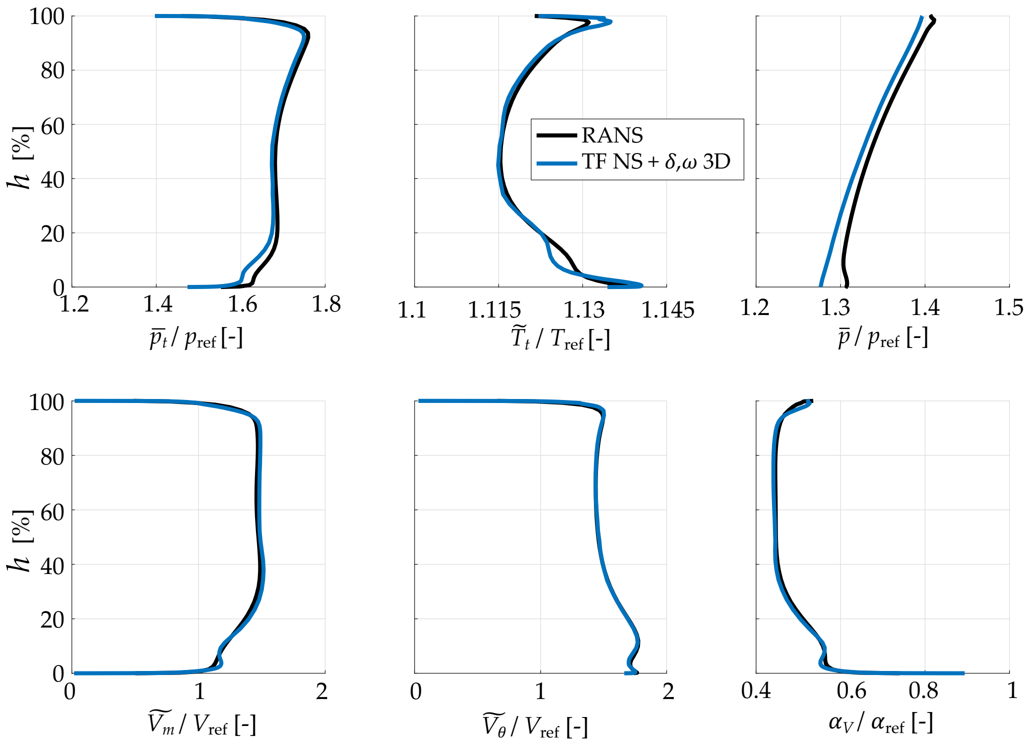

Figure 4.22: Comparison between TF and pitch-wise averaged 3D RANS simulations of the compressor close to stall conditions (OP2): spanwise distributions of total pressure and temperature, static pressure (top), axial and azimuthal velocities, and flow angle (bottom) at the $\mathbb{R}1$ outlet.

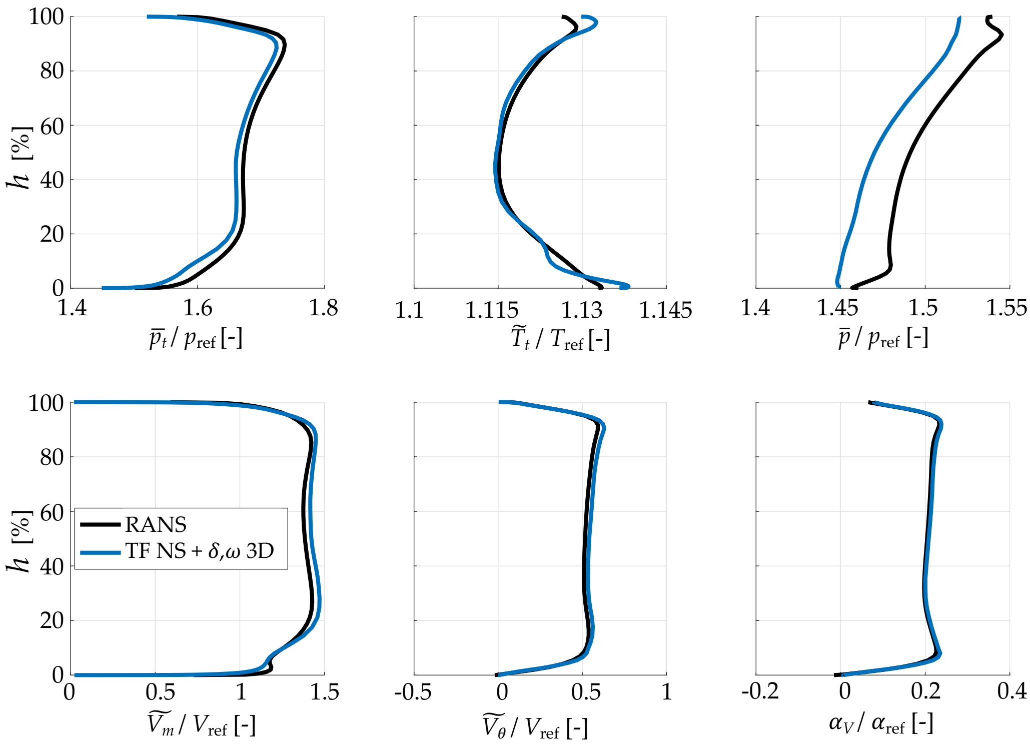

Figure 4.23: Comparison between TF and pitch-wise averaged 3D RANS simulations of the compressor close to stall conditions (OP2): spanwise distributions of total pressure and temperature, static pressure (top), axial and azimuthal velocities, and flow angle (bottom) at the $\mathbb{S}1$ outlet.

4.2.2 Extension of the blade force model to the rotor tip gap

As discussed in Section 2.6.3, the flow physics in the rotor tip gap are primarily included in the circumferential stress, since no blade-force term is mathematically defined in this region. Since this stress is not explicitly modeled in the present formulation, the flow phenomena generated within the tip gap are governed solely by the viscous terms and by the turbulence closure appearing in the through-flow equations. As a consequence, an axisymmetric tangential shear layer develops along the casing induced by the adverse axial pressure gradient.

Nevertheless, it is common practice in some through-flow implementations to extend the blade-force model into the tip-gap area in order to introduce additional deviation, loss, and blockage. However, when the radial distributions of deviation angle δ_{TE} and loss coefficient ω are prescribed from RANS simulations, these effects are already partially accounted for at and below the rotor tip. Although this extension concerns less than 1% of the blade span, it can noticeably modify the near-wall flow behaviour, as illustrated in Fig. 4.24. In the context of Euler-based TF simulations, adding the blade force terms in the tip-gap region improves the control of the local flow dynamics and leads to a better agreement with both RANS results and NS-based TF predictions. This improvement is especially visible on the radial distributions of total temperature and tangential velocity at the rotor outlet.

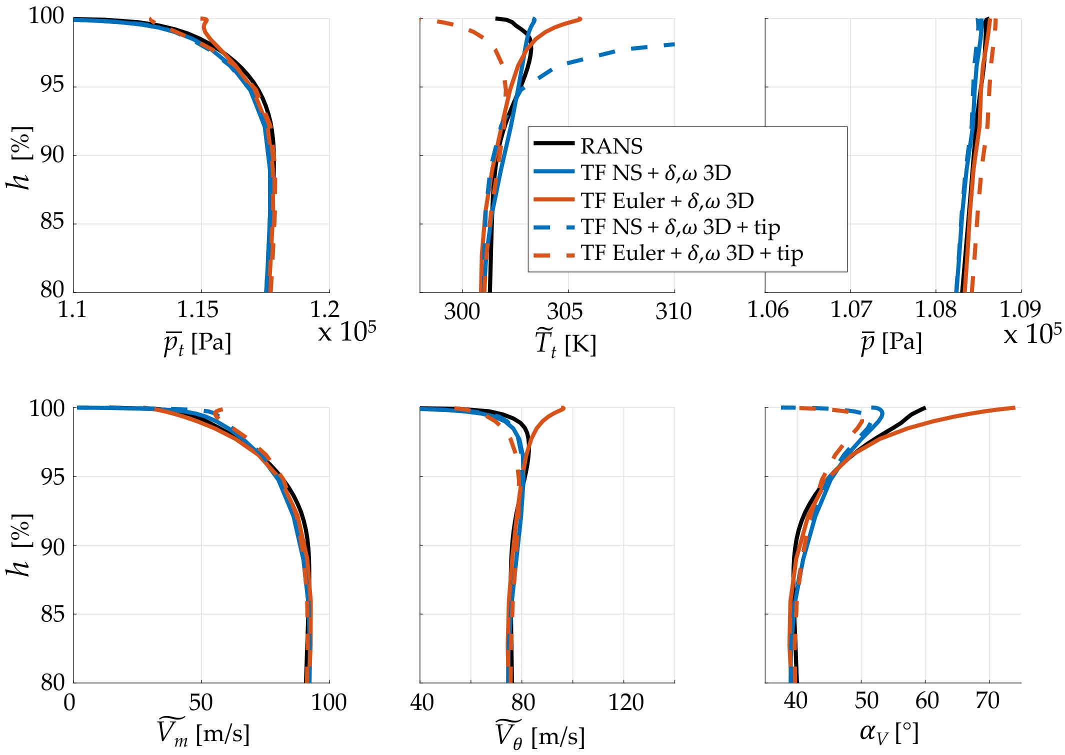

Figure 4.24: Comparison between TF (with and without a blade force extension in the tip gap region) and pitch-wise averaged 3D RANS simulations of the CME2 compressor stage at nominal conditions (OP1): spanwise distributions of total pressure and temperature, static pressure (top), axial and azimuthal velocities, and flow angle (bottom) at the rotor outlet.

For NS-based TF calculations, however, the effect of this extension is far more limited. Because viscous effects are already represented consistently through the no-slip condition applied at the casing, the additional blade forces bring no real benefit. Moreover, an overshoot of total temperature is observed when the extension is activated. This stems from an inconsistency between the no-slip condition at the wall, imposing zero velocity, and the blade-force formulation, which implicitly assumes a blade moving at the local tangential speed. This issue does not arise in Euler-based simulations, where only an impermeability condition is enforced at the casing. A more rigorous formulation would therefore be required to model aerodynamic effects in the tip-gap region, particularly for NS-based TF simulations. In practice, however, the extension of the blade force does not yield a significant improvement in the prediction of overall performance or spanwise gradients, given the very small size of the tip-gap region and the fact that its main effects are already partially captured by the imposed δ_{TE} and ω distributions near the rotor tip. Moreover, extending the blade definition into the tip gap amounts to reintroducing a metallic blockage term, but without its full aerodynamic counterpart. For these reasons, the tip gap is left free of any blade force in the remainder of this work.

4.2.3 Correlations accuracy

The radial distributions of the deviation angle δ_{TE} and loss coefficient ω are unknown in practice, and are obtained from empirical correlations. The second objective is therefore to assess the impact of the empiricism inherent to these correlations on the accuracy of the through-flow simulations.

4.2.3.1 Baseline correlations

The results of the through-flow simulations using the baseline correlations reported in Section 3.3.3 is shown in Fig. 4.25 for the CME2. The adequacy of these correlations is poor, even for the low-speed compressor stage, leading to significant underestimation of the total pressure ratio across the entire operating range compared to RANS. This phenomenon can be explained by the overestimation of the deviation angle at the blade trailing edge along the span, as highlighted in the top part of Fig. 4.26 where the deviation angle predicted by the baseline correlation is compared to that extracted from the RANS simulation at nominal operating conditions.

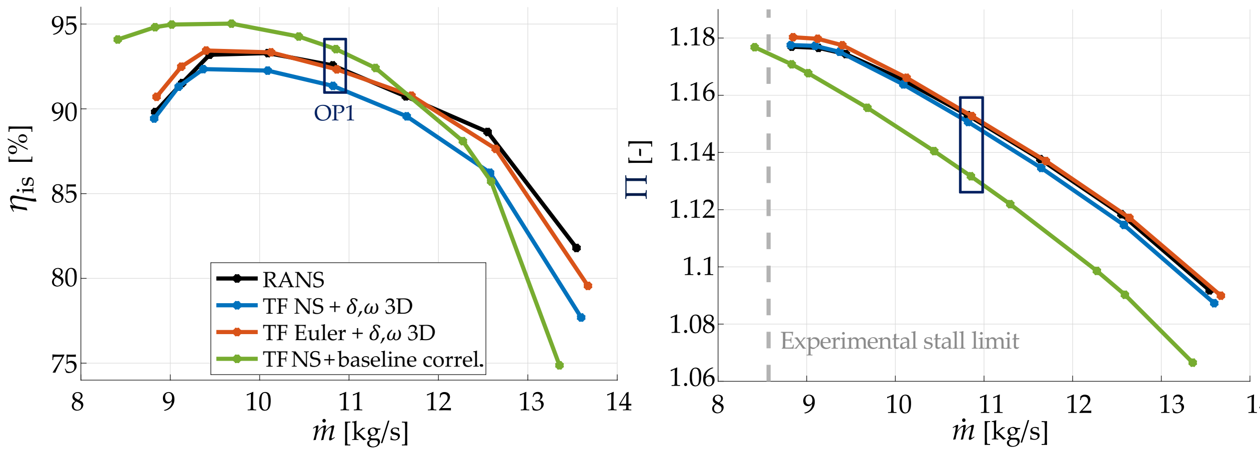

Figure 4.25: Isentropic efficiency η_{is} (left) and total pressure ratio Π (right) as a function of the mass-flow rate at the nominal rotational speed of the CME2 compressor stage. Comparison of RANS and through-flow simulations fed with exact correlation parameters from RANS computations and using baseline empirical correlations.

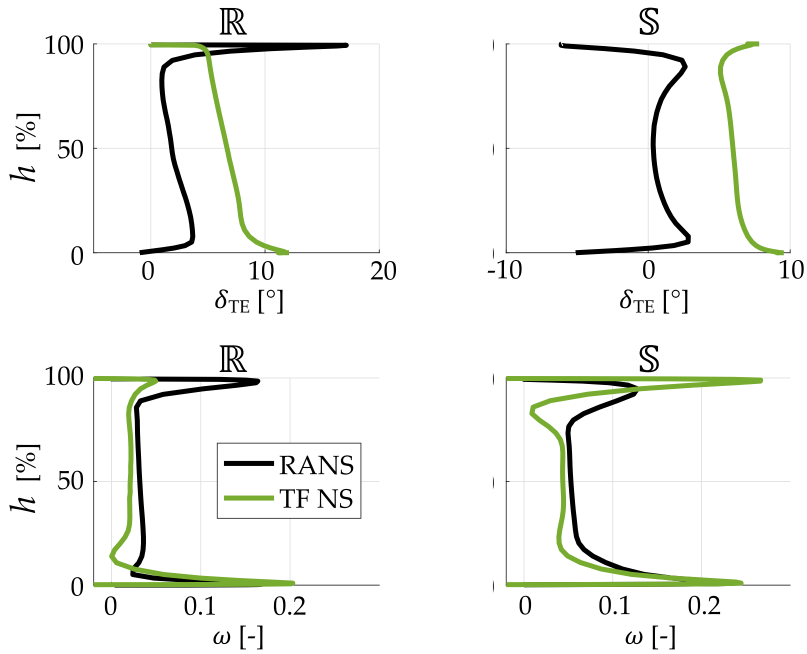

Figure 4.26: Comparison between TF simulations using the baseline correlations and pitch-wise averaged 3D RANS simulation of the CME2 compressor stage at nominal conditions (OP1). Deviation angle δ_{TE} at the blade trailing edge and blade loss coefficient ω along the blade height h of the rotor (left) and stator (right).

The loss prediction shows reasonably good agreement at nominal operating conditions in the mid-span region. The boundary layers generated by the viscous effects included in the NS-based TF formulation, together with the turbulence model, provide a representative level of endwall losses. Nevertheless, the isentropic efficiency predicted by the TF solver progressively departs from the RANS solution as the operating point moves away from nominal conditions. Improvements to the loss modeling are therefore required to obtain better accuracy, particularly at off-design conditions. This includes accounting for loss redistribution due to radial mixing and introducing a dedicated loss model for the rotor tip-gap region.

These differences are even more pronounced in the second test case, as shown in Fig. 4.27, where a significant underestimation of the total pressure ratio and an overestimation of the the isentropic efficiency is observed across the entire operating range. These discrepancies can again be attributed to inaccuracies in the predicted deviation angle and loss coefficient, as illustrated in Figs. 4.28 and 4.29, respectively. The deviation angle is noticeably overestimated across the entire blade span, leading to an underpumping. The loss coefficient is underestimated for most of the blade span, resulting in an overly optimistic prediction of the isentropic efficiency.

Modern blade geometries are no longer composed of profile sections chosen from blade families but are optimized using CFD. The empirical correlations employed in the present work are therefore not strictly applicable to such geometries. Most empirical deviation and loss models available in the literature were developed between the 1960s and the 1980s and were validated under flow conditions, and for blade families (NACA 65 series, C4 or Double-Circular-Arc profiles), that differ markedly from current industrial practice. In particular, the widely used Lieblein correlations originate from low-speed tests carried out on this conventional two-dimensional cascades. The overestimation of

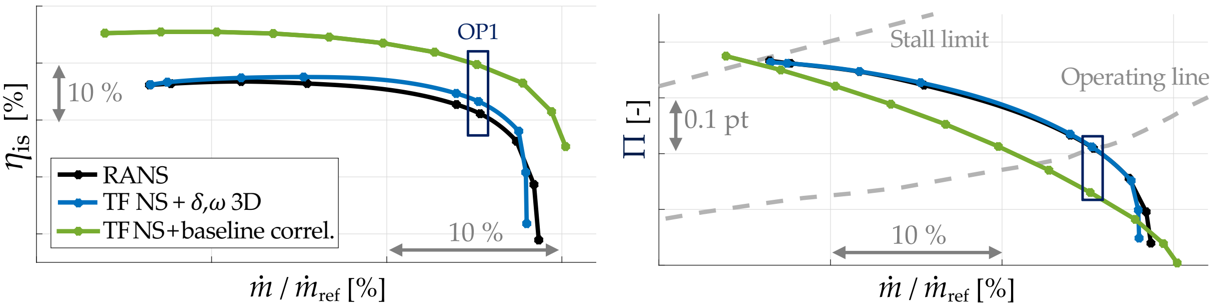

Figure 4.27: Isentropic efficiency η_{is} (left) and total pressure ratio Π (right) as a function of the normalized mass-flow rate of the low-pressure compressor. Comparison of RANS and through-flow simulations fed with exact correlation parameters from RANS computations and using baseline empirical correlations.

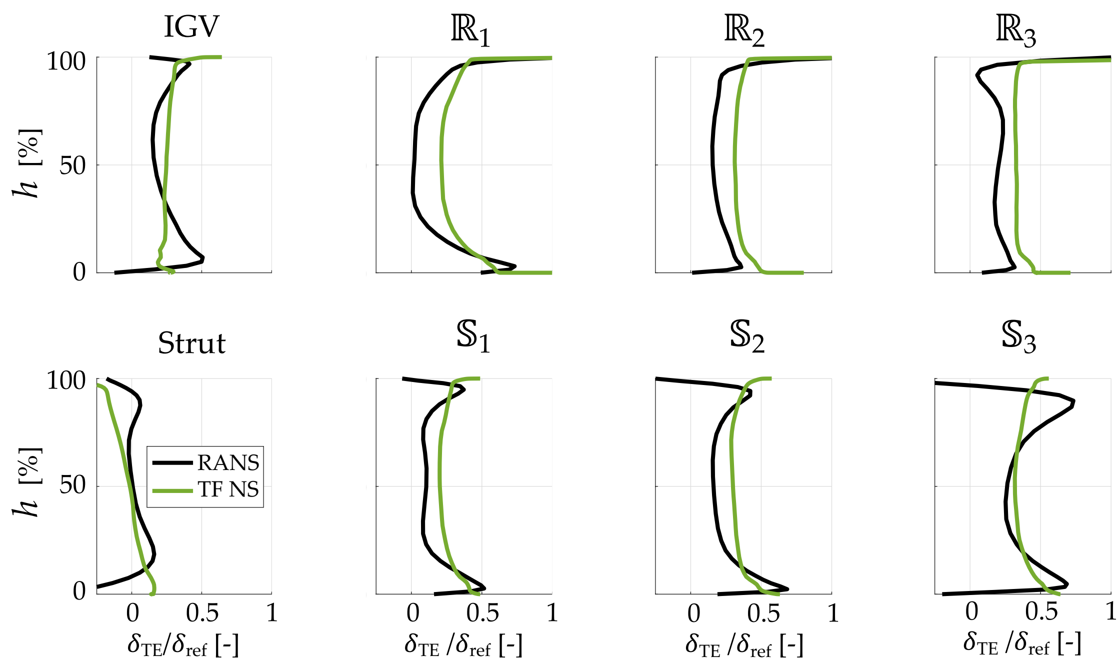

Figure 4.28: Comparison between TF simulations using the baseline correlations and pitch-wise averaged 3D RANS simulation of the low-pressure compressor at nominal conditions (OP1). Deviation angle δ_{TE} at the blade trailing edge along the blade height h.

deviation observed here is therefore a natural consequence of using correlations originally derived from earlier, less loaded compressor technology compared to controlled diffusion airfoils. Moreover, in contrast to the CME2 stage, the blades of the low-pressure compressor considered in this second test case are even more loaded, strongly three-dimensional, and operate at relatively higher, though still subsonic, Mach numbers. Therefore, improvements of these models for modern three-dimensional blades are needed to enhance their prediction accuracy and other types of losses should be included in the models (tip gap, radial mixing, ...) to achieve a more comprehensive representation of the flow physics.

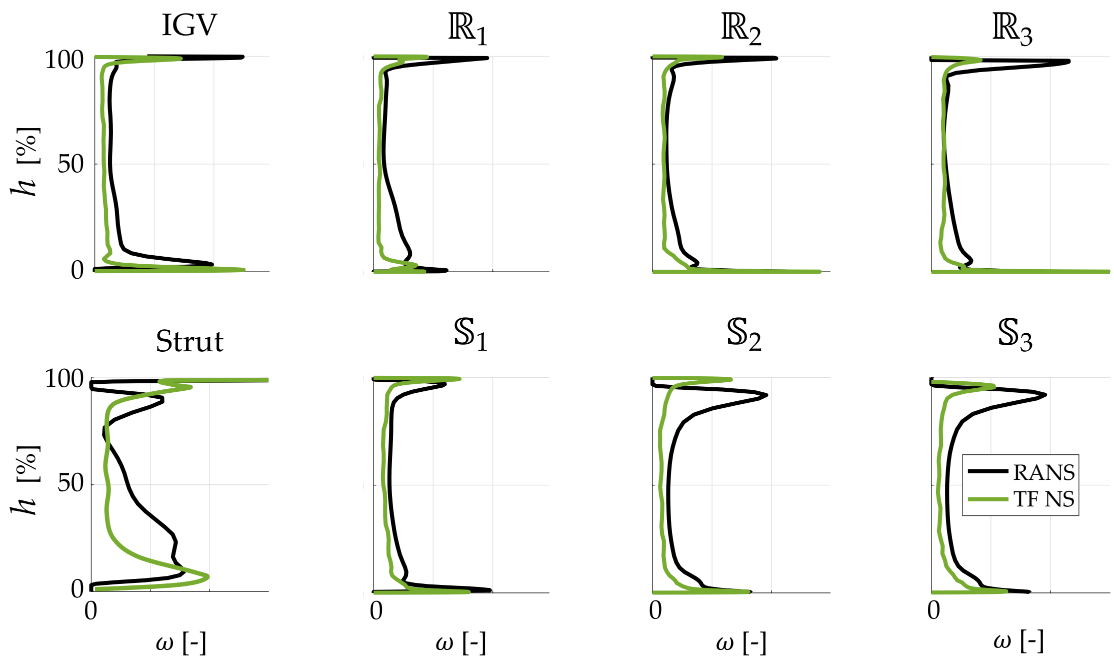

Figure 4.29: Comparison between TF simulations using the baseline correlations and pitch-wise averaged 3D RANS simulation of the low-pressure compressor at nominal conditions (OP1). Loss coefficient ω along the blade height h.

4.2.3.2 Modifications to baseline correlations

A database of cascade computations has been constructed and used to evaluate, compare, and refine the baseline correlations for profile loss introduced in Section 3.3.3. The dataset was generated using the 3D RANS solver `elsA` by performing a large number of blade-to-blade simulations in stream-tube configurations [55]. The considered cascades correspond to the blade rows of the case of interest, i.e., the low-pressure compressor stages. Note that the IGV and the strut are not included. Simulations were conducted at three spanwise locations: 10%, 50%, and 90% of the blade height. For each section, the cascade was computed over a wide range of inlet incidences in order to capture both near-design and off-design conditions. This dataset is not intended to support a general revision of the existing loss and deviation correlations. Indeed, it is limited to a relatively small number of blade profiles and does not encompass the full variety of geometries and operating regimes encountered in modern axial compressors. The modifications introduced in the following therefore aim primarily at improving the prediction accuracy for the specific second test case examined in this work, rather than providing a comprehensive overhaul of the current correlation framework.

As schematically illustrated in Fig. 4.30, the qualitative behaviour of the baseline correlations for the compressor blade rows is broadly similar: the minimum-loss level is systematically underestimated, and the predicted loss polar is noticeably too wide, a behaviour that is characteristic of correlations derived from low-speed cascade experiments. The deviation angle is generally overestimated across the range of incidence. The optimal incidence is reasonably well captured, although a slightly larger discrepancy is observed for the rotor blades.

A straightforward way to adjust the optimal incidence, as proposed in Petrovic et al. [152], is to introduce a correction term that shifts the original correlation, effectively translating the loss polar.

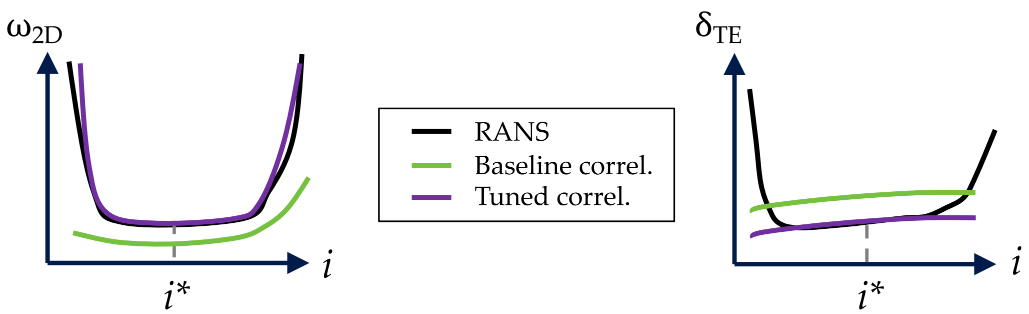

Figure 4.30: Qualitative behavior of the key parameters δ_{TE} and ω_{2D} laws with respect to the incidence i.

This approach generally performs well because the correlation only depends on the blade geometry. In the present work, however, no modification of the optimal-incidence correlation has been applied, as such an adjustment was not deemed necessary for the compressor configuration under consideration.

Regarding the deviation angle, no major advances have been proposed in the literature since Lieblein introduced his correlation in the mid-1950s. For this reason, a dedicated calibration of the existing deviation model has been carried out in the present work, using the cascade-based dataset described above. The analysis of the cascade database made it possible to identify the dominant terms in the δ_{TE} correlation. In the expression

$$\delta_{\mathrm{TE}} = \underbrace{\delta^*_{\mathrm{TE}}}_{[87\%-98\%]} + \underbrace{\left[\frac{\partial \delta}{\partial i}\right]^* (i - i^*)}_{[1\%-5\%]} + \underbrace{10\left(1 - \frac{\widetilde{W}_{m,\mathrm{TE}}}{\widetilde{W}_{m,\mathrm{LE}}}\right)}_{[1\%-7\%]}, \tag{4.7}$$

the design deviation angle δ^*_{TE} is by far the most influential contribution, typically accounting for nearly 90% of the total deviation. The two remaining terms play only a minor role. Moreover, the slope of the correlation with respect to incidence, represented by the $(i - i^*)$ term, was found to be consistent. Its relative magnitude is small since for a relatively high solidity the deviation angle is only weakly sensitive to variations in the incidence i [126].

A more detailed examination of the design value δ^*_{TE} shows that, in its standard formulation,

$$\delta = \underbrace{K_{sh} K_{t,\delta} (\delta^*_0)_{10}}_{[3\%-13\%]} + \underbrace{m\left(\kappa_{\mathrm{LE}} - \kappa_{\mathrm{TE}}\right)}_{[87\%-97\%]}, \tag{4.8}$$

the dominant contribution arises from the second term coming from the Carter's rule [28]. The two empirical factors involved in the slope parameter m, Eq. 3.25, have thus been modified according to

$$\begin{aligned} m_{1.0} &= a_1 + a_2\left(\frac{\beta^*_{\mathrm{TE}}}{100}\right) + a_3\left(\frac{\beta^*_{\mathrm{TE}}}{100}\right)^2, \\ b &= a_4 + a_5\left(\frac{\beta^*_{\mathrm{TE}}}{100}\right) + a_6\left(\frac{\beta^*_{\mathrm{TE}}}{100}\right)^3, \end{aligned} \tag{4.9}$$

where the coefficients a_j are new calibration constants. These constants were adjusted to minimise the discrepancy between the correlation predictions and the RANS results of the database. For confidentiality reasons, their values are not reported here. The calibration effort focused primarily on the mid-span location (50%), where traditional correlations are typically defined. Despite this targeted approach, the calibrated model provides reliable predictions of the deviation angle for all blade rows considered, including at 10% and 90% of the span, as illustrated in Fig. 4.30 (purple line). Naturally, the growth of deviation outside the diffusion-limited regime is not captured by the modified correlation, as expected from a model rooted in diffusion-limited cascade behaviour.

In contrast to deviation angle correlations, numerous improvements to the Lieblein profile loss model have been proposed over the years in an attempt to extend its validity beyond the limitations previously discussed. A notable contribution in this regard is the work of König [114], who significantly extends the applicability of the profile loss correlation to a broader variety of blade profiles and to high subsonic regimes by incorporating compressibility effects as well as streamtube contraction through the influence of the axial-velocity-density ratio

$$\mathrm{AVDR} = \frac{\overline{\rho}_{\mathrm{TE}}\widetilde{W}_{m,\mathrm{TE}}}{\overline{\rho}_{\mathrm{LE}}\widetilde{W}_{m,\mathrm{LE}}}\,. \tag{4.10}$$

It should be noted, however, that the AVDR was already included in the implementation of the Lieblein correlation used in the present work.

The updated expression of the profile loss coefficient proposed by König is given by

$$\omega(r)_{\mathrm{2D}} = 2\frac{\theta_w}{c}\frac{\sigma}{\cos\beta_{\mathrm{TE}}}\left(\frac{\widetilde{W}_{\mathrm{TE}}}{\widetilde{W}_{\mathrm{LE}}}\right)^2\frac{\overline{\rho}_{\mathrm{TE}}}{\overline{\rho}_{\mathrm{LE}}}\left(1+\frac{\gamma-1}{2}\widetilde{M}^2_{W,\mathrm{TE}}\right)^{\frac{1}{\gamma-1}}\,, \tag{4.11}$$

and, in order to better capture the behaviour at off-design incidence conditions, the equation for the momentum thickness, Eq. 3.31, is replaced by the formulation taken from Swan [183],

$$\left(\frac{\theta_w}{c}\right) = \left(\frac{\theta_w}{c}\right)^* + K_p\left(D_{\mathrm{eq,c}} - D^*_{\mathrm{eq,c}}\right)^2\,, \tag{4.12}$$

where $D_{\mathrm{eq,c}}$ is the equivalent diffusion ratio for compressible flows and the supercript * denotes the value at design conditions, i.e. at the optimal incidence angle. Moreover, the original Lieblein correlation is no longer valid for $D_{\mathrm{eq}} > 2$. To address this limitation, König proposed replacing it with two new expressions for the design momentum thickness $\left(\frac{\theta_w}{c}\right)^*$, validated for modern blade cascades, including a specific formulation for large design equivalent diffusion factors $D^*_{\mathrm{eq,c}}$:

$$\begin{aligned} \left(\tfrac{\theta_w}{c}\right)^* &= 0.0071D^*_{\mathrm{eq,c}} - 0.0029\,, && D^*_{\mathrm{eq,c}} \leq 2\,, \\ \left(\tfrac{\theta_w}{c}\right)^* &= 0.1786D^{*2}_{\mathrm{eq,c}} - 0.7071D^*_{\mathrm{eq,c}} + 0.7111\,, && D^*_{\mathrm{eq,c}} > 2\,. \end{aligned} \tag{4.13}$$

The parabolic factor K_p introduced in Swan's formulation accounts for the dependence of the loss polar with the inlet Mach number: as the Mach number rises, the slope of the parabolic variation of the momentum thickness becomes steeper, and the value of K_p must accordingly increase to reflect the stronger sensitivity of the wake momentum thickness to deviations from the minimum-loss diffusion level. To extend Swan's formulation to cascades of arbitrary blade geometry, König introduced an additional dependence of K_p on the blade shape itself, in addition to the inlet-flow Mach number. A single geometric parameter was sought and the most suitable choice was found to be the effective suction-side height $w_{s,\text{eff}}$, which measures the height at maximum camber of the suction side relative to the mean ordinate between its intersections with the LE and TE circles, as shown in Fig. 4.31. This parameter is representative of the flow turning capability on the suction side and has a strong impact on diffusion behaviour at off-design incidences. With these considerations, König proposed the following expressions for the parabolic factor:

$$\begin{aligned} K_p &= \max\left(0.032,\ 0.032\, e^{\,10.109\left(\widetilde{M}_{\text{W,LE}}-M_{\text{ref}}\right)}\right), \qquad D_{\text{eq,c}} - D^*_{\text{eq,c}} > 0\,, \\ K_p &= \max\left(0.016,\ 0.016\, e^{\,16.864\left(\widetilde{M}_{\text{W,LE}}-M_{\text{ref}}\right)}\right), \qquad D_{\text{eq,c}} - D^*_{\text{eq,c}} < 0\,, \end{aligned} \tag{4.14}$$

where the reference Mach number M_{ref} depends on the effective suction-side height $w_{s,\text{eff}}$ through

$$\begin{aligned} M_{\text{ref}} &= -1.464\sqrt{\frac{w_{s,\text{eff}}}{c}} + 1.198, \qquad D_{\text{eq,c}} - D^*_{\text{eq,c}} > 0\,, \\ M_{\text{ref}} &= -1.464\sqrt{\frac{w_{s,\text{eff}}}{c}} + 1.043, \qquad D_{\text{eq,c}} - D^*_{\text{eq,c}} < 0\,. \end{aligned} \tag{4.15}$$

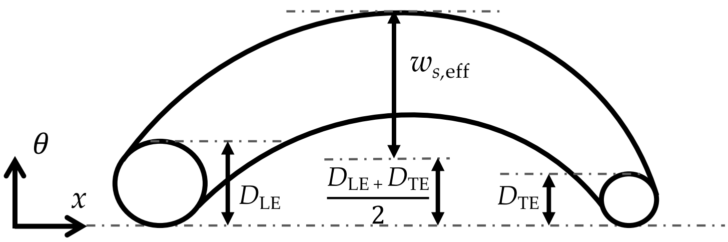

Figure 4.31: Effective suction side height $w_{s,\text{eff}}$ of an airfoil according to König et al. [114].

The compressible equivalent diffusion factor is obtained by applying the von Kármán-Tsien correction formula [197] to the incompressible equivalent diffusion factor D_{eq} through

$$D_{\text{eq,c}} = \frac{1-\chi}{1-\chi\left(D_{\text{eq}}\frac{\widetilde{W}_{\text{TE}}}{\widetilde{W}_{\text{LE}}}\right)^2} D_{\text{eq}}\,, \tag{4.16}$$

where

$$\chi = \left[\frac{\widetilde{W}_{\text{LE}}}{1+\sqrt{1-\widetilde{W}^2_{\text{LE}}}}\right]^2 . \tag{4.17}$$

As shown by König, the equivalent diffusion factor D_{eq} predicted by Lieblein's original relation (Eq. 3.32) remains applicable for cascades with strongly cambered blades so that

$$D_{\text{eq}} = \left(1.12 + 0.61\Gamma' + 0.0117\,|i-i^*|^{1.43}\right)\frac{\cos\beta_{\text{TE}}}{\cos\beta_{\text{LE}}}\frac{\widetilde{W}_{m,\text{LE}}}{\widetilde{W}_{m,\text{TE}}}\,, \qquad \Gamma' > 0.2\,. \tag{4.18}$$

However, for cascades with more moderate front-side camber on the suction surface like modern compressor blade designs, i.e. for which $\Gamma' \leq 0.2$, Lieblein's diffusion formulation becomes less accurate. For these geometries, König proposed the alternative expression:

$$D_{\mathrm{eq}} = \left(1 + 1.446\Gamma' - 1.180\Gamma'^2 + 0.0117\,|i - i^*|^{1.43}\right) \frac{\cos\beta_{\mathrm{TE}}}{\cos\beta_{\mathrm{LE}}} \frac{\widetilde{W}_{m,\mathrm{LE}}}{\widetilde{W}_{m,\mathrm{TE}}}\,, \qquad \Gamma' \leq 0.2\,. \tag{4.19}$$

The incompressible circulation parameter defined in Eq. 3.36 is evaluated from compressible flow data using the Prandtl–Glauert transformation:

$$\Gamma' = \sqrt{1 - M_{\mathrm{LE}}^2}\,\Gamma'_{\mathrm{c}}\,, \tag{4.20}$$

where Γ'_{c} is computed from compressible-flow quantities. Finally, the design value of the compressible equivalent diffusion factor, $D^*_{\mathrm{eq,c}}$, is obtained by evaluating $D_{\mathrm{eq,c}}$ at the optimal incidence i^*.

Finally, the term $(i - i^*)$ in Eqs. 4.18–4.19 was found to remain valid for all cascades investigated, regardless of the profile family. The same symmetry assumption as in the baseline correlations was therefore applied here by replacing $(i - i^*)$ with $|i - i^*|$. However, it should be noted that the model is not validated for incidences lower than the design value ($i < i^*$). In addition, the formulation does not explicitly account for the velocity distribution on the pressure side of the blade. For controlled-diffusion airfoils, however, this limitation is of lesser importance because the pressure-surface Mach number is designed to remain nearly constant and subsonic under nominal conditions. At negative incidence, this is no longer true: significant diffusion may develop on the pressure side, and the model would therefore require revision and dedicated validation in such operating conditions. Given the good performance demonstrated by König's correlation over a broad range of blade geometries, as schematically illustrated in Fig. 4.30, no further calibration of these profile loss correlations was introduced. Consequently, the model was used in its original form without further modification.

CME2 compressor stage

The updated correlations used in this study were not specifically tuned for the CME2 compressor stage: the deviation model was calibrated using data from the low-pressure compressor, and compressibility effects are expected to play a limited role here, as the relative Mach number remains below 0.6. Nevertheless, it is still of interest to examine whether the improvements introduced by König for the profile-loss correlation, together with the calibrated deviation model, lead to a better prediction of the stage performance and of the radial flow distributions in this configuration.

The performance curves obtained using the modified correlations for the CME2 compressor stage are presented in Fig. 4.32. A significant improvement in prediction accuracy is observed compared to the results obtained with the baseline correlations. The total pressure ratio is now more accurately captured across the entire operating range, and the isentropic efficiency shows a marked improvement over a large range of operating conditions. This enhancement can be attributed primarily to the refined deviation angle correlation, which provides a more accurate representation of the flow turning capability of the blades. In addition, since the deviation is only weakly sensitive to incidence variations up to the onset of blade stall, the calibrated model enables a reliable prediction of the performance over a wide range of mass-flow rates. The loss predictions also benefit from the incorporation of the revised diffusion factor, leading to a better estimation of losses at various operating points.

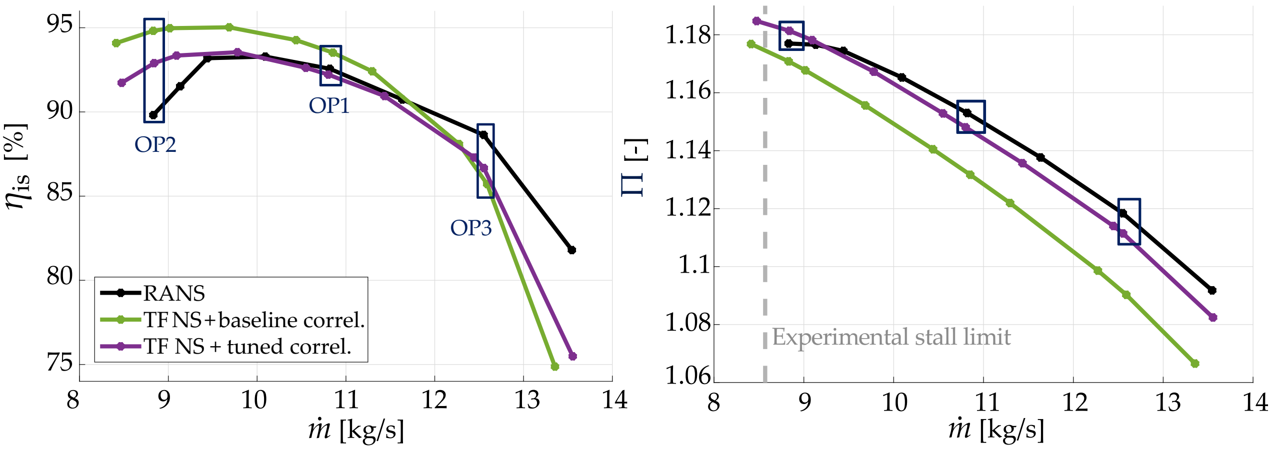

Figure 4.32: Isentropic efficiency η_{is} (left) and total pressure ratio Π (right) as a function of the mass-flow rate at the nominal rotational speed of the CME2 compressor stage. Comparison of RANS and through-flow simulations with baseline and tuned empirical correlations.

However, as shown in Figs. 4.33-4.35, the deviation angle remains slightly overestimated along the span, especially as the mass flow rate increases. This highlights the empiricism error of the calibration procedure, which makes it challenging to apply a given correlation uniformly from one compressor configuration to another. Nevertheless, the overall trend is correctly captured, and the loss predictions are also improved.

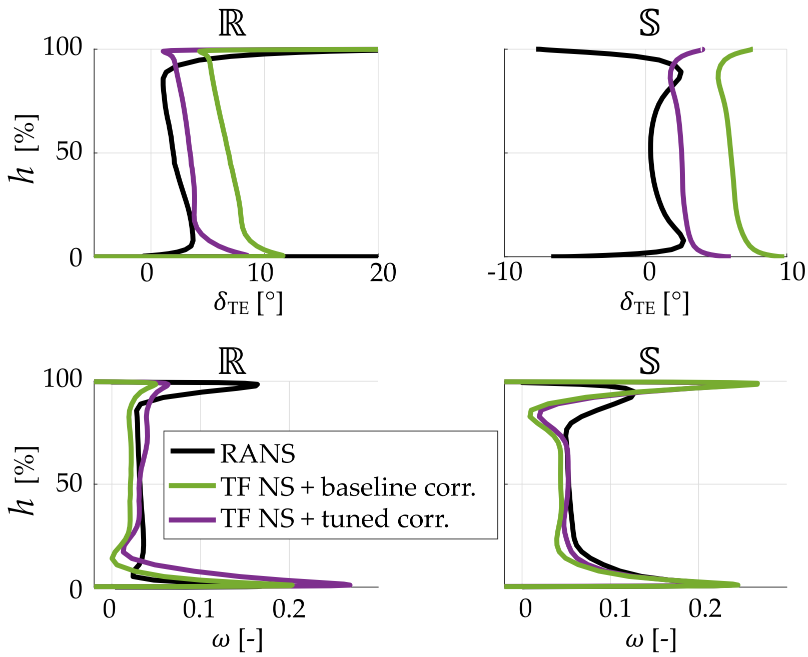

Figure 4.33: Comparison between TF simulations using the baseline or the tuned correlations and pitch-wise averaged 3D RANS simulation of the CME2 cmpressor stage at nominal conditions (OP1). Deviation angle δ_{TE} at the blade trailing edge and blade loss coefficient ω along the blade height h of the rotor (left) and stator (right).

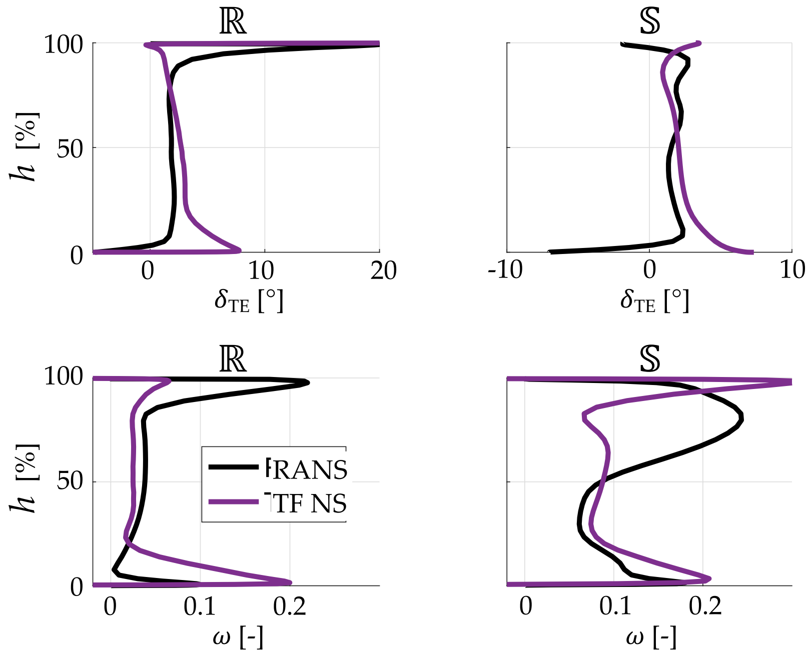

Figure 4.34: Comparison between TF simulations using the tuned correlations and pitch-wise averaged 3D RANS simulation of the CME2 cmpressor stage at peak pressure ratio (OP2). Deviation angle δ_{TE} at the blade trailing edge and blade loss coefficient ω along the blade height h of the rotor (left) and stator (right).

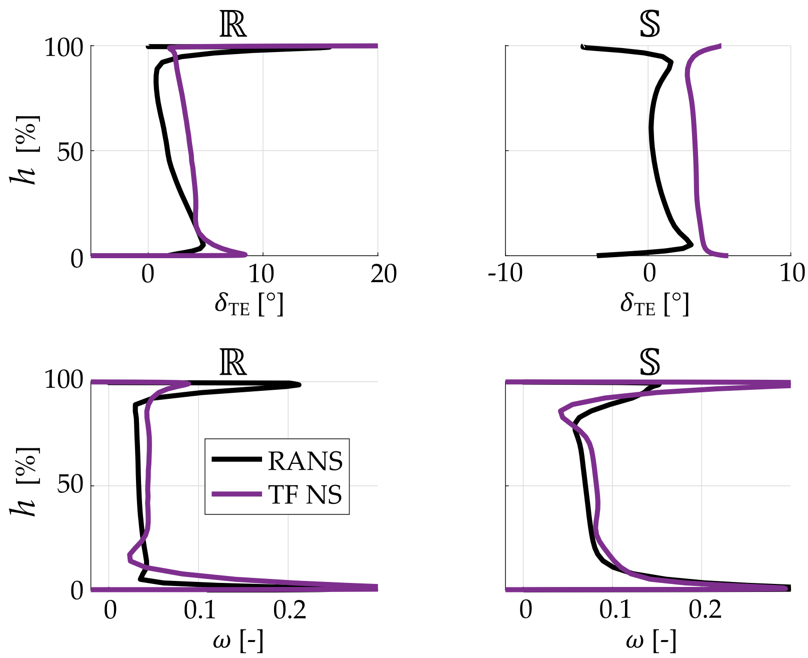

Figure 4.35: Comparison between TF simulations using the tuned correlations and pitch-wise averaged 3D RANS simulation of the CME2 cmpressor stage close to choke conditions (OP3). Deviation angle δ_{TE} at the blade trailing edge and blade loss coefficient ω along the blade height h of the rotor (left) and stator (right).

The discrepancies that persist at high and low mass-flow rates arise mainly from the modeling of secondary flows. Although the hub and casing boundary layers provide a reasonable estimate of the endwall entropy increase since the entropy production in these regions is largely governed by the development of the annulus boundary layers, the tip-gap loss remain unaccounted for. Furthermore, the radial redistribution of losses through mixing is not represented in the current through-flow formulation. The combination of profile losses with annulus-boundary-layer effects often leads to an overestimation of near-hub losses, especially on the rotor.

Moreover the deviation angle is not accurately predicted in the endwall regions. A more refined deviation model including secondary-flow contributions would, for instance, capture the prediction of the peak pressure ratio, as secondary-flow-induced turning is known to affect both the aerodynamic loading and the effective blockage. An inaccurate representation of these mechanisms directly affects the work input of the stage and modifies the mass-flow rates.

Finally, part of the discrepancies can also be attributed to the propagation of modeling errors from one blade row to the next. For instance, an inaccurate prediction of the rotor deviation angle modifies the incidence at the downstream stator inlet, which in turn alters the flow turning and the associated level of loss. Such cumulative effects across consecutive blade rows naturally degrade the overall agreement with the reference RANS solution.

Axial low-pressure compressor

The performance curves obtained using the modified correlations for the low-pressure compressor are presented in Fig. 4.36. The TF predictions are drastically improved, especially at design conditions (OP1). As shown in Figs. 4.37 and 4.38, the deviation angle is now much more accurately reproduced within the core flow, and the loss coefficient is also better captured, particularly in the mid-span region. This leads to a significantly improved agreement with the reference RANS results. Even for the strut, which features a very low aspect ratio and experiences strong radial and tangential variations of the flow, the predicted deviation and loss levels remain reasonably accurate within the core-flow region. This is noteworthy because the correlations are not, strictly speaking, suited for such a symmetric blade profile with small aspect ratio and significant chord-length variation along the radius.

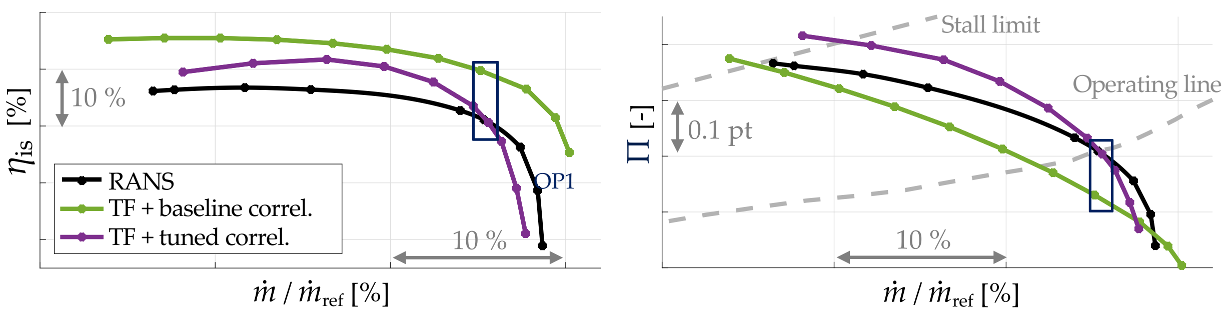

Figure 4.36: Isentropic efficiency η_{is} (left) and total pressure ratio Π (right) as a function of the normalized mass-flow rate of the low-pressure compressor. Comparison of RANS and through-flow simulations with baseline and tuned empirical correlations.

A qualitative overview of the solution is provided in Figs. 4.39 and 4.40, where the meridional velocity magnitude and static pressure fields are shown. The overall flow structure is correctly reproduced by the TF solver, although some discrepancies remain in the endwall regions. In particular, the tip-gap boundary layer tends to be underestimated, while the hub-side boundary layer is slightly overpredicted. These tendencies are also visible in the radial distributions of the loss coefficient ω: the underestimated tip-gap losses are effectively compensated by an overestimation of the hub losses, a behaviour already observed for the CME2 stage. Indeed, the 2D empirical relations introduced earlier are not valid in the vicinity of the endwalls, where the flow departs significantly from a two-dimensional behaviour. Despite these local deviations, the mean level of losses remains reasonably well captured. The metallic blockage, which accounts for the blade thickness distribution, contributes to an accurate prediction of the meridional velocity field inside the blade passages. The static pressure field is also in good agreement with the reference data, and the TF solver successfully reproduces the pressure rise across the compressor stage. The assumed linear variation of deviation angle and entropy along the streamlines leads to the correct qualitative pressure pattern within the blade passages. This approximation is particularly appropriate near the design operating point and around mid-span, where both entropy and deviation are known to vary almost linearly between leading and trailing edges.

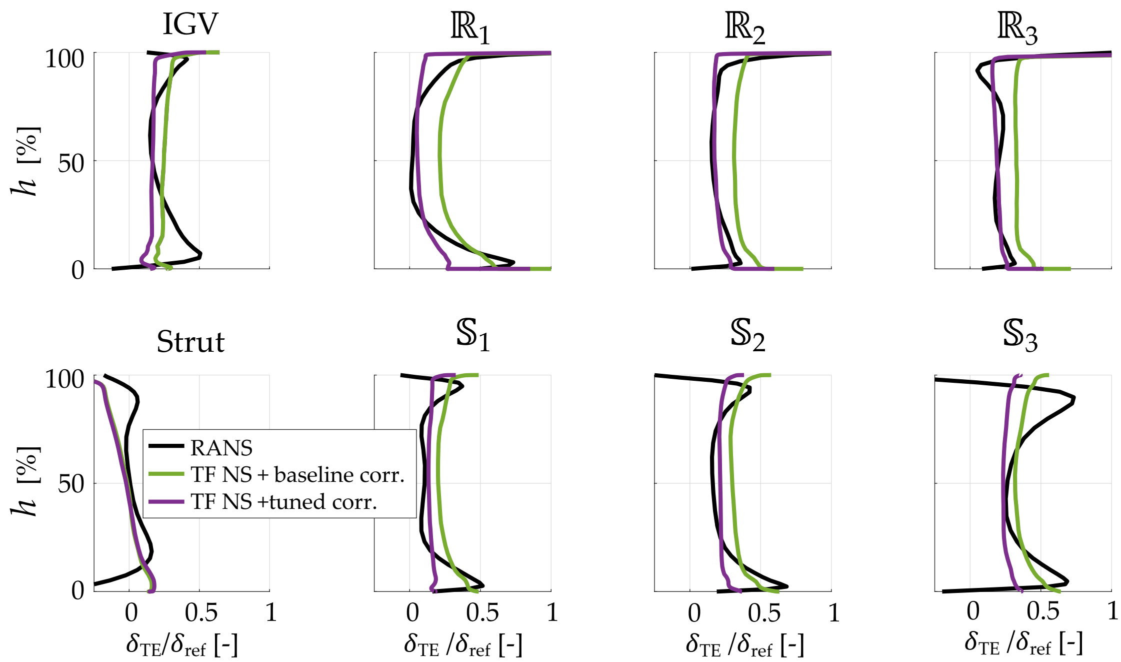

Figure 4.37: Comparison between TF simulations using the tuned correlations and pitch-wise averaged 3D RANS simulation of the low-pressure compressor at nominal conditions (OP1). Deviation angle δ_{TE} at the blade trailing edge along the blade height h.

Although the agreement at nominal operating conditions can be considered reasonable, the correlations should still be improved at off-design conditions. The linear law predicted by the deviation angle correlation reproduces fairly well the deviation angle behavior in a range relatively close to the optimal incidence angle i^*, i.e., the incidence angle that achieved minimal loss, but completely fails to predict off-design conditions beyond the diffusion limit.

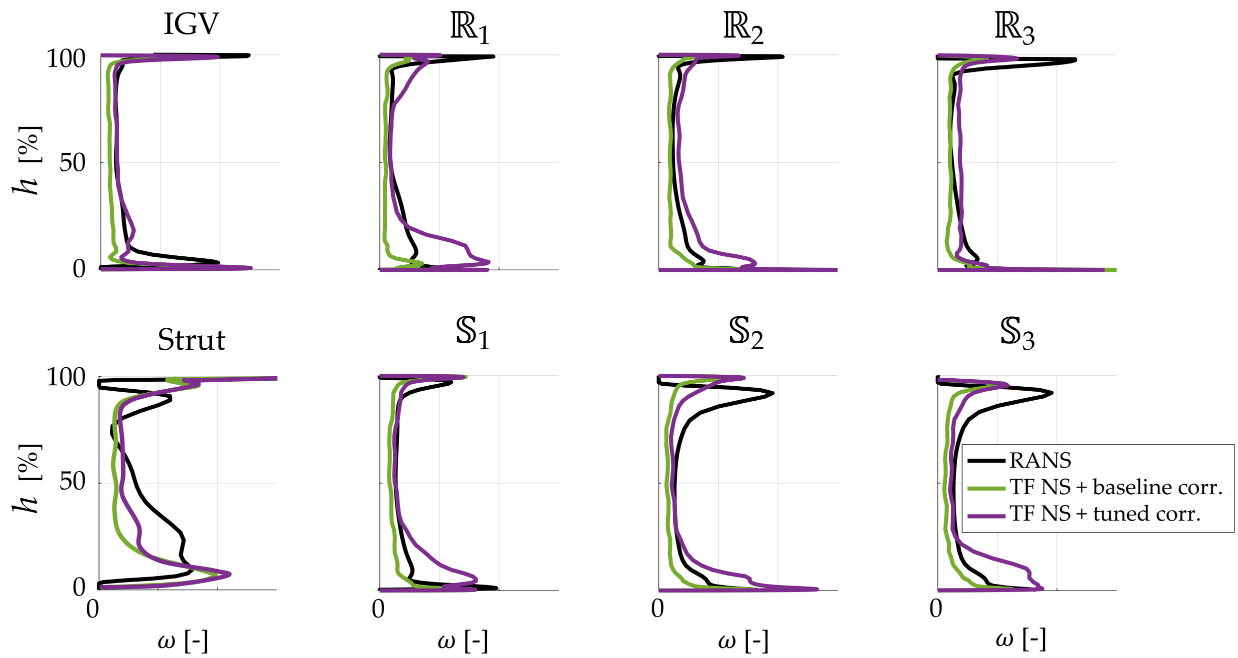

Figure 4.38: Comparison between TF simulations using the tuned correlations and pitch-wise averaged 3D RANS simulation of the low-pressure compressor at nominal conditions (OP1). Loss coefficient ω along the blade height h.

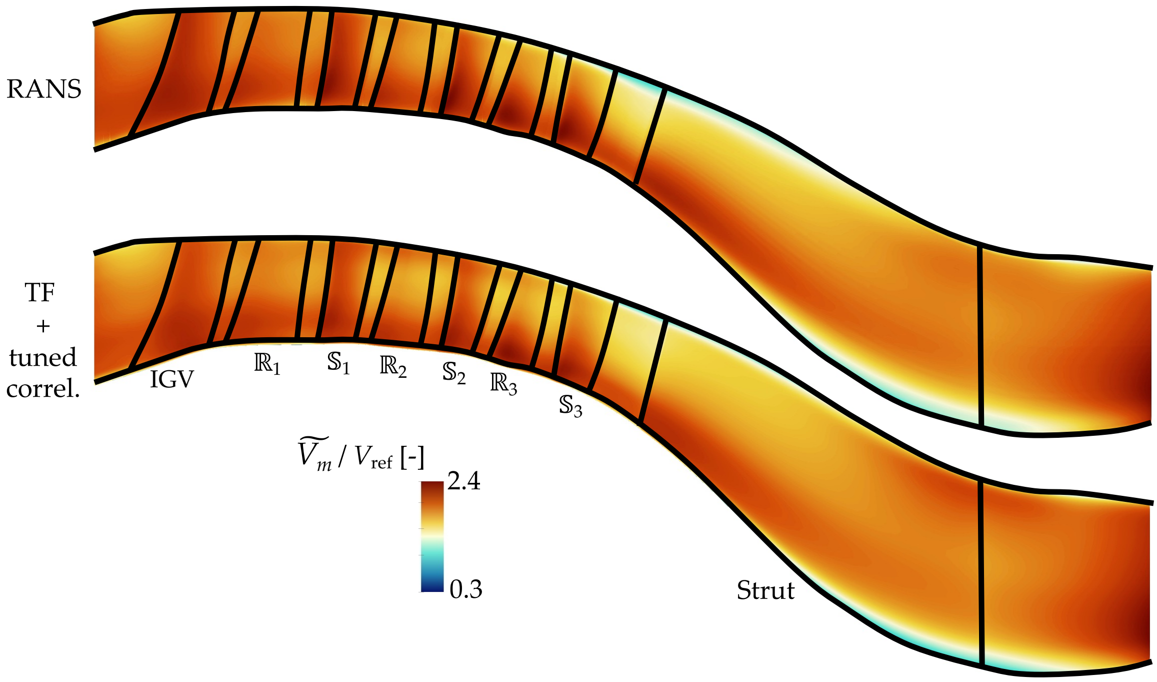

Figure 4.39: Contour of the meridional velocity for (top) the pitch-wise averaged 3D RANS and (bottom) TF simulations using the tuned correlations at nominal conditions (OP1).

Moreover, the profile-loss correlation shows an even stronger sensitivity to the $(i - i^*)$ term, as the loss polar tends to become narrower with increasing Mach number. As a consequence, the tolerance to the error related to the optimal incidence angle is reduced, and inaccuracies propagating from one blade row to the next, such as an error in the deviation angle leading to an incorrect incidence on the downstream blade row, have a more pronounced impact in a multistage turbomachine.

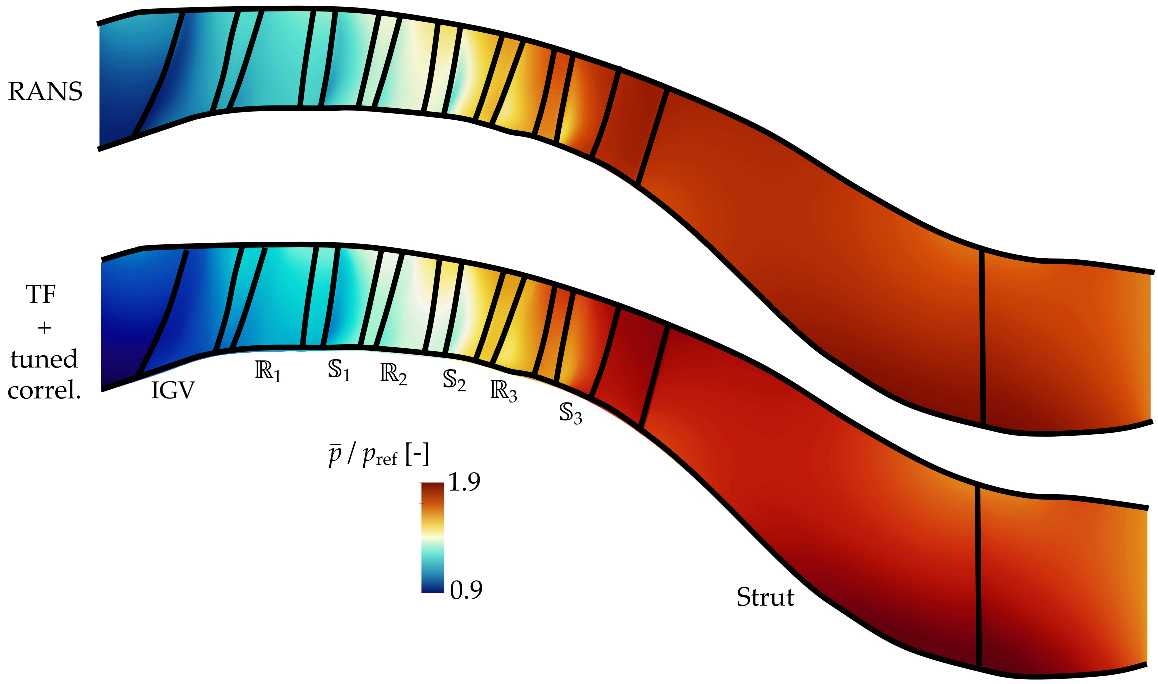

Figure 4.40: Contour of the pressure for (top) the pitch-wise averaged 3D RANS and (bottom) TF simulations using the tuned correlations at nominal conditions (OP1).

In addition, unlike the CME2 stage, the combination of endwall boundary-layer loss and profile loss is no longer sufficient to fairly reproduce the physics of the present low-pressure compressor stage over an extended operating range. Secondary flow intensity increases markedly with blade loading. The current implementation of the through-flow model does not incorporate these secondary-flow mechanisms in the formulation of either the deviation angle or the loss coefficient, nor does it include a radial-mixing model capable of redistributing losses such as those generated by tip-leakage flows. These missing physical contributions become increasingly important in off-design conditions and further limit the predictive capability of the model for heavily loaded, multi-stage configurations.

4.3 Concluding remarks

The analysis conducted in this chapter has shown that the through-flow model is capable of delivering accurate predictions of both the overall performance and the spanwise distributions of the key aerodynamic quantities in multi-stage axial compressors. This level of fidelity is maintained across the entire operating range, provided that sufficiently accurate estimates of the deviation angle and loss coefficient are supplied. In other words, when the inputs to blade-force model are reliably characterized, the TF solver can reproduce the essential features of the three-dimensional, pitchwise-averaged flow with a reliable precision, thereby demonstrating that the intrinsic model errors of the through-flow formulation itself remain comparatively small. These results also indicate that the TF approach is not limited to preliminary design at nominal operating conditions. On the contrary, it has the potential to support later stages of compressor development, including off-design performance assessments and optimization tasks. The model also exhibits the capability to capture the numerical stability limit of the turbomachine.

However, the accuracy of these predictions remains strongly dependent on the quality of the correlations used to model the deviation angle and the profile loss. While the calibration effort demonstrated in this chapter can yield highly accurate results for a given compressor configuration, its empirical nature prevents the approach from delivering uniformly reliable predictions across all blade geometries. This limitation becomes increasingly pronounced for modern blade generations, whose design philosophies have evolved far beyond the canonical airfoil families on which most historical correlations were built. Unlike in past decades, current industrial practice based on advanced 3D shaping and optimization strategies has not converged toward an universally applicable airfoil family.

Nevertheless, some degree of standardization does exist and the development of new or extended correlations is increasingly feasible. Historically, most loss models were derived from experimental data, which inherently limited the amount and resolution of accessible local flow information. Today, however, large databases of high-fidelity cascade CFD simulations can be generated at relatively low cost, enabling the systematic construction of new correlations based on broad parametric variations in blade geometry and operating conditions. Such approaches hold significant promise, though they must be pursued with care: the reliability of CFD-based datasets remains strongly tied to turbulence-model performance. As a result, experimental data remain essential and complementary.

In addition, incorporating correlations that account explicitly for secondary-flow effects is essential, particularly for off-design conditions where these mechanisms intensify. Such flows strongly influence both the effective turning and the loss production in the vicinity of the endwalls, and their impact becomes even more pronounced in low–aspect-ratio turbomachinery. Several empirical secondary-flow models have been proposed in the literature, like those by Roberts et al. [163]. However, the axisymmetric Navier–Stokes formulation already represents part of the endwall shear and heat-transfer effects through the resolution of the boundary layers, raising the question of how to consistently combine empirical secondary-flow correlations with the physics inherently captured by the solver. As measurements were usually not taken very close to the endwalls, these models do not fully capture the detailed loss mechanisms associated with near-wall regions and can be combined to NS-based TF solver [168]. Moreover, Manfredi [131] has identified a set of correlations that appears particularly promising for modern compressor configurations.

Furthermore, the breakdown of loss and deviation introduced in Eq. 2.86 is over-simplified, as it is difficult to assess to what extent each loss contribution is actually independent from the others [48]. Although such a linear decomposition can provide satisfactory predictions at design conditions and for relatively simple blade geometries [157], this simplification may lead to an overestimation of the total loss if the various empirical correlations are not jointly calibrated against higher-fidelity data.

In the context of a multifidelity approach, where TF and 3D RANS are combined, as described in the Section 1.2, the correlations for δ_{TE} and ω could also be learned from the RANS simulations. This would greatly improve the reliability of the performance prediction by the TF solver, or at least ensure a much better coherence with that obtained by RANS. Given that the target application of this work lies in the late design phases, where the geometry is already known and considerations such as manufacturing tolerances and variability come into play, leveraging data-driven models (e.g., regression-based surrogates, reduced-order tables, or machine-learning approaches) instead of purely empirical correlations appears not only feasible but also justified.

However, the present study has highlighted the risk of double counting the losses in the endwall regions when exact source terms derived from RANS or endwall loss corrections are directly imposed within the viscous TF formulation. Although this effect is relatively minor in multi-stage compressors, where the endwall boundary layers generally remain thin compared with the blade span, it may still lead to a slight overestimation of the losses close to the hub and casing. In practice, this issue is not encountered in standard TF modeling based on empirical correlations, as high-fidelity information is usually unavailable. In this context, a viscous formulation is advantageous over an Euler formulation because it naturally accounts for realistic velocity gradients and boundary-layer development near the annulus walls and between blade rows, thereby reducing the reliance on additional empirical modeling. The main challenge therefore lies in the availability of reliable correlations capable of consistently separating the different loss mechanisms. In this respect, RANS simulations could be used to decompose the total losses into profile losses, annular wall losses, and secondary-flow losses, for instance by modifying the wall boundary conditions in dedicated RANS computations, as proposed by Raina et al. [157].

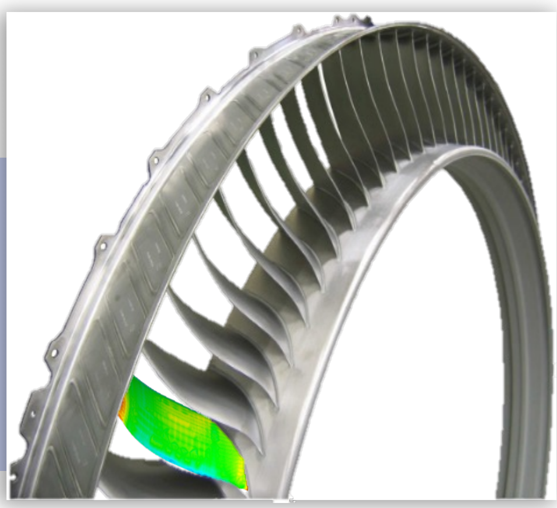

Chapter 5

Geometric Variability

This chapter presents the sensitivity analysis of the viscous through-flow model with respect to the propagation of geometric variabilities. The overall goal is thus to determine, through this sensitivity analysis, which types of geometric variations can be captured by the through-flow model and how the specific TF modelling features influence their propagation. The TF solver, based on the improved correlations introduced in Chapter 4, is used to quantify the relative variation of performance with respect to baseline conditions. The main quantities of interest (QOI) to assess design robustness with respect to manufacturing variabilities are the total pressure ratio and the isentropic efficiency as functions of the mass-flow rate. In the present preliminary analysis, the model ability to capture geometric variability effects is assessed only at nominal conditions, because the correlations still need to be improved at high incidence conditions, and additional dedicated modelling is needed to account for secondary-flow effects more accurately. Therefore, the stall margin and the choke mass-flow rate are not considered here as a QOI. It is important to recall that, because of the axisymmetric nature of the TF model and the assumed periodicity of the RANS reference simulations, geometric variabilities are intrinsically assumed to be identical on each blade of a given row. The test case considered in this chapter is exclusively the low-pressure compressor, which is the configuration of interest for manufacturing tolerances. The overarching goal of this chapter is to address the question: *Can a viscous through-flow solver capture key performance variations induced by geometric variabilities?* In doing so, this analysis serves as a proof of concept for the multi-fidelity strategy introduced in Chapter 1.

5.1 Sources of epistemic uncertainty

It is worth stressing out that correct boundary conditions, together with an accurate description of the geometry at the simulated operating point, are critical for predictive capability. As underlined by Adamczyk [2], these details cannot be overemphasized. If uncertainties remain, sensitivity studies are necessary to quantify their impact on the simulation results. Moreover, modern compressor blades are characterised by the three-dimensionality of their design. These so-called 3-D effects, namely the sweep, the lean, and the blade end twist, are introduced to enhance turbomachinery aerodynamic performance. In particular, they provide an effective means to influence and control secondary-flow development. Indeed, secondary flows are not solely driven by blade loading, they are also strongly affected by the three-dimensional shaping of the blade. By modifying the stacking line, one can alter secondary-flow behaviour without changing either the design velocity triangles or the blade airfoil profiles [51, 65]. In addition, endwall contouring is another widely used technique to improve the flow in the hub and tip regions [25]. Such geometric features are naturally resolved in 3-D RANS simulations, where the full blade geometry is explicitly represented.

In contrast, their representation in through-flow models is inherently more questionable, since the blade geometry is not directly present in the axisymmetric formulation. Nevertheless, the blade geometry is still embedded in the TF representation, albeit in a different form. In the body-force approach, the blade profiles are decomposed into a camber surface and an associated thickness distribution along the corresponding blade sections. This description stems directly from the averaging process of the RANS equations, as used for Eq. 2.49, where the camber surface is defined as

$$\theta_{cl}(x,r) = \frac{\theta_{B_1}(x,r) + \theta_{B_2}(x,r)}{2}\,. \tag{5.1}$$

An illustrative example of the camber surface and thickness distribution is shown in Fig. 5.1, represented as a stack of blade sections, analogous to the 3-D blade representation used in RANS. Provided that the discretization of these profiles is sufficiently refined, both in terms of the number of spanwise cuts and the point distribution, and that the interpolation onto the through-flow mesh is performed consistently, the three-dimensional geometry of the blade can be faithfully represented within this modelling framework. On the one hand, this geometric information is directly exploited by the body-force formulation: the normal and parallel forces are imposed perpendicular to and parallel to the camber line, respectively, though they are adjusted according to the local deviation angle. The thickness distribution, in turn, enters explicitly through the blockage terms, as it determines the local blockage factor appearing in the body-force source terms. On the other hand, additional geometric parameters required as inputs to the empirical correlations, such as the camber angle, the chord length, or the solidity, are also derived from this discretised geometry. These quantities are then used to evaluate the loss coefficients and the deviation angle prescribed by the correlation models.

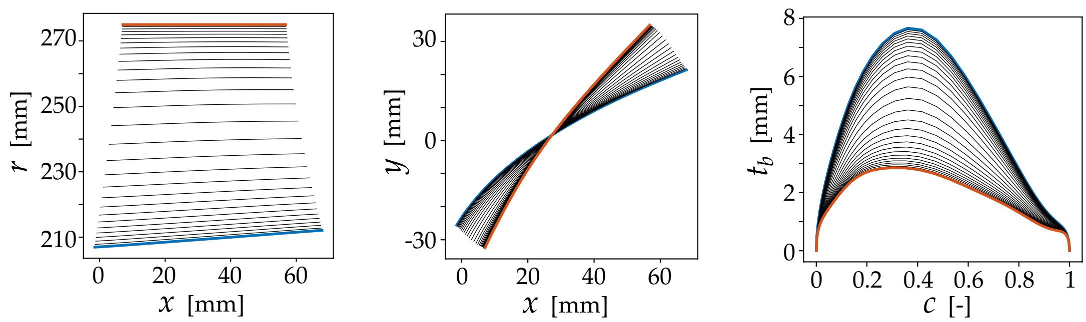

Figure 5.1: Discretization of the blade camber surface (middle) and thickness distributions t_b (right) along the corresponding camber lines (left) for the rotor of the CME2 compressor stage.

Some of these three-dimensional effects are axisymmetric in nature and are therefore fully captured by the TF solver. For example, blade lean, which corresponds to a non-radial stacking axis, is inherently embedded in the radial component of the blade forces and contributes to the spanwise redistribution of the mass-flow rate. Similarly, blade end twist, introduced to align the blade with the local flow and to mitigate high-incidence regions near the endwalls, can be partially accounted for: the Navier–Stokes

TF solver is able to predict the increase in incidence that naturally occurs close to the hub and shroud.

However, other three-dimensional effects are intrinsically non-axisymmetric and thus require dedicated modelling. For instance, although twist influences the local incidence, its impact on endwall losses must be complemented by empirical models that explicitly relate losses to off-design incidence in the endwall region. Likewise, lean is often designed to alleviate or suppress corner separation through unloading of the endwall sections. This effect cannot be captured at the TF level unless a specific model establishes a link between reduced blade loading and the corresponding decrease in corner vortex loss. Moreover, only axisymmetric endwall contouring could be consistently taken into account within a TF framework. As shown in Chapter 4, the influence of 3-D blade design on spanwise loss and deviation can be reproduced accurately when exact distributions of δ_{TE} and ω are available. When relying on correlations, however, several of these mechanisms are only partially represented.

In addition to these limitations, two further modelling aspects must be considered, as they may significantly affect how geometric variabilities are propagated, particularly near the blade LE. The first one is related to the incidence correction introduced in Section 3.3.4. In the present work, a smoothing on the first 30% of the chord is used. The blade geometry is thus locally modified by this numerical artifact. This smoothing, however, is necessary: using a shorter portion leads to excessive entropy generation, as shown in Fig. 5.2. Moreover, this correction has a non-negligible impact on the predicted performance at high mass-flow rate and particularly on the choking mass-flow rate. Without this correction or when using a significantly shorter smoothing length, the TF model severely underestimates the choking mass-flow. Indeed, the abrupt change in blade angle produces an unrealistically strong local loading, which in turn induces a significant fluid acceleration. At high freestream velocities, this excessive acceleration can drive the passage towards premature sonic blockage, thereby reducing the predicted choking mass-flow. Conversely, applying the smoothing over a longer chordwise extent alters the blade geometry over an excessively large region and provides no additional benefit. Even if this optimal choice introduces a low error in the global blade loading, this modification of the blade geometry can smooth any geometric variability in this region. A special attention should therefore be paid to this numerical artifact when propagating geometric uncertainties.

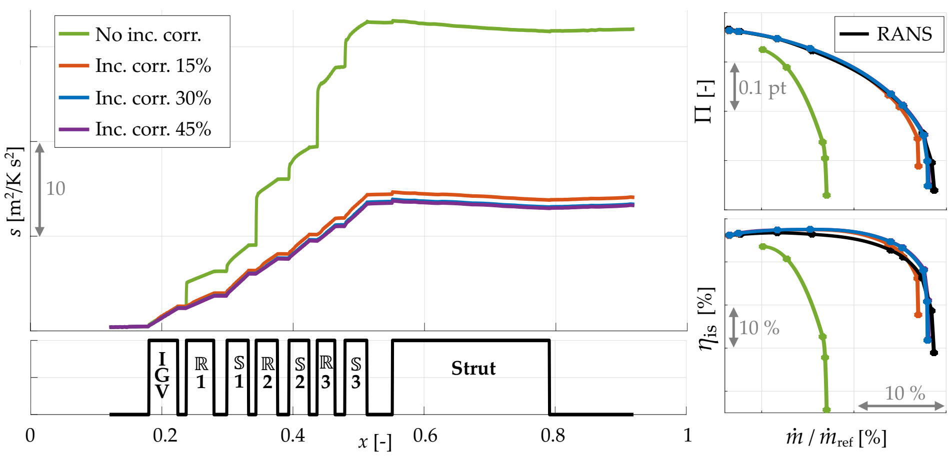

Figure 5.2: Entropy generation along a mid-span streamline for different extents of the incidence smoothing in the compressor (left). Corresponding total pressure ratio and isentropic efficiency of TF simulations fed with the exact correlation parameters from RANS computations (right).

The second aspect concerns the pre-processing of the blade geometry for TF simulations. Unlike NACA airfoils which are parameterized based on a known line of mean camber, modern optimized airfoils are directly defined by the position of the pressure and suction surface. However, most TF simulations require a blade definition in terms of a mean camber line and a tangential thickness distribution for the blade force computation. As a consequence, an additional reconstruction step is necessary to extract the camber surface. Several methods exist to generate such camber lines and generally allow a straightforward extraction from a given blade geometry. Nevertheless, in the vicinity of the leading edge, and trailing edge to a lesser extent, algorithms determining a mean camber line can be unreliable because the line of camber is no longer quasi-parallel with the section outline [118] and its definition is thereby not unique. The deviation of the reconstructed camber line over the first few percent of the chord may partly stem from a deliberate LE biasing introduced to enhance blade performance. In such cases, the apparent deviation of the camber line in this region is therefore only partially an artefact of the reconstruction process. The resulting blade angle κ can significantly vary close to the leading edge depending of the pre-processing tool. Although these tools are based on the same definition of the camber line, the LE treatment leads to dissimilar blade angle distributions, which may not be consistent with the blade loading distribution. Since this quantity is used by the correlations, any inaccuracy in its evaluation may distort the predicted loss and deviation angle. The impact of this epistemic uncertainty can therefore exceed geometric variability in the LE region.

In order to assess the model sensitivity with respect to this uncertainty, TF simulations have been run based on the blade geometric outputs from two available algorithms, one based on a barycentric computation (Algorithm 1), introduced in Eq. (5.1), and the other relying on an inscribed-circle method [205] (Algorithm 2), respectively. As shown in the left part of Fig. 5.3, the blade angle of each blade row computed by both algorithms exhibits abrupt variations in the LE region and may differ by up to 5 degrees with respect to each other in the immediate vicinity of the leading edge. As shown in the right part of Fig. 5.3, the direct impact of the blade angle distribution (blue lines) is low on the blade force if the correlation parameters δ_{TE} and ω are known, i.e., taken from the RANS simulations here. Since the incidence correction smears the LE uncertainty, and losses and deviation do not depend at all on incidence being directly taken from the 3D RANS, the predictions of the TF simulations are quite similar for the two blade angle distributions of Fig. 5.3 (left).

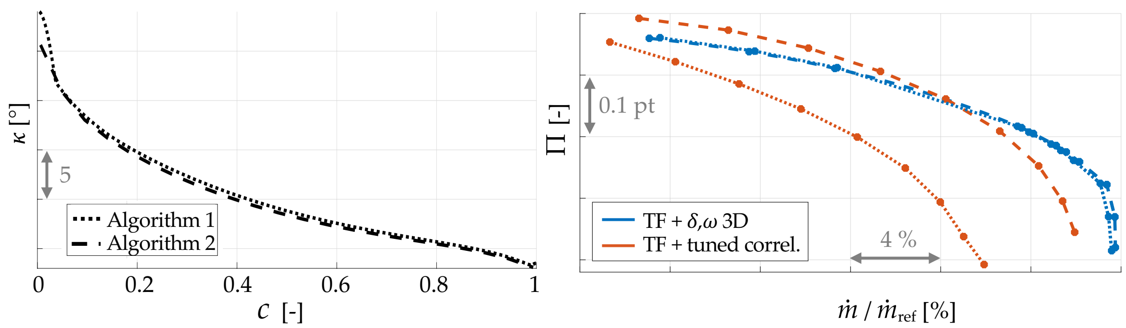

Figure 5.3: Example of blade angle distribution along the chord (left) and total pressure ratio as a function of the mass flow rate (right) at the nominal rotational speed of the compressor for two airfoil splitting algorithms (dotted and dashed lines). Comparison of RANS (black line) and through-flow simulations fed with exact correlation parameters from RANS computations (blue lines) and using tuned correlations (orange lines).

However, the empirical correlations for δ_{TE}, ω and, especially i^*, use the actual geometry as input and are highly sensitive to the LE and TE blade angle. Because these correlations rely solely on information at the blade LE and TE, any error in the reconstructed blade angle at these locations implicitly results in a blade that is interpreted by the correlations as having a total camber different from the real geometry. As a result, the blade angle uncertainty indirectly influences the blade forces through these correlations. It can be seen that, in this case, the TF model using empirical correlations (orange lines in Fig. 5.3 (right)) demonstrates a large variability in its prediction. The methodology adopted here to alleviate this uncertainty consists in extending the camber line monotonically, according to a linear law, over the first few percent of the blade chord. It should be noted that all results presented in Chapter 4 already rely on this methodology. Another methodology may consist in using the value of the blade angle outside the uncertainty region, i.e., at a few percents of the chord further downstream, as input for the calibrated correlations. Regardless of the chosen method, this artifice effectively removes the epistemic uncertainty arising from the camber-line reconstruction in the LE and TE region. However, any variation of the camber line induced by geometric variability within this same region is consequently filtered out as well.

5.2 Sensitivity analysis with respect to geometric variabilities

To assess the ability of the TF model to capture performance variations induced by geometric variabilities, a sensitivity analysis is conducted by comparing the performance variations predicted by the TF model with those obtained from reference RANS simulations. Since the baseline performance predicted by TF and RANS simulations differ due to modeling errors, the focus is here on the relative variation of performance with respect to nominal conditions predicted by the respective solvers so that their respective qualitative trends can be evaluated. The aforementioned nominal conditions are defined as the intersection points between the operating line and the iso-speed line computed by the respective solvers (OP1), as shown in Fig. 4.36. Geometric variations representative of manufacturing variability are propagated. These parameters, which are typically measured during industrial quality-control procedures, are presented in the next sections. In this study, the considered variations include perturbations of the blade leading angle, the blade thickness, the rotor tip-gap height, the three-dimensional position of undeformed blades, and, deformations of the hub and shroud geometry.

5.2.1 Position of undeformed blades and endwall deformation

5.2.1.1 Imposed geometric variations

Five types of geometric variations on blade rows have been chosen to assess the TF model predictions. First, three degrees of freedom are related to the three-dimensional position of the undeformed stator blades, namely the variation of the stagger angle $\Delta\lambda$, the stream-wise (Δx) and pitch-wise ($r\Delta\theta$) position keeping the blade geometry unchanged, as shown in Fig. 5.4. Both Δx and $r\Delta\theta$ are defined by two contacts points, similarly to a mechanical feeler during quality controls. In the case of the circumferential position ($r\Delta\theta$), only the relative position between contact points matters because of the row axisymmetry. The second set of degrees of freedom is related to linear endwall deformations, ΔE_h at the hub and ΔE_c at the casing, respectively. In particular, the axisymmetric endwalls, namely the hub and casing, are locally altered by displacing two control points on the walls in the vicinity of the blade leading and trailing edge. The control points are linearly connected to upstream and downstream reference points, as depicted in Fig. 5.4(b). The ranges of variability for the five degrees of freedom have been defined based on industrial tolerance limits and are summarized in Table 5.1. It should be emphasized that, among the 78 simulations, each geometric variation has been analyzed independently of the others: combined variations are not considered in the present work. Note that the set of hub contour variations ΔE_h only contains the deformation (2.85, −2.85) in the case of the $\mathbb{S}2$ and $\mathbb{S}3$ blades and the deformation (−2.85, +2.85) of the hub is not included for the $\mathbb{R}1$ blade [1].

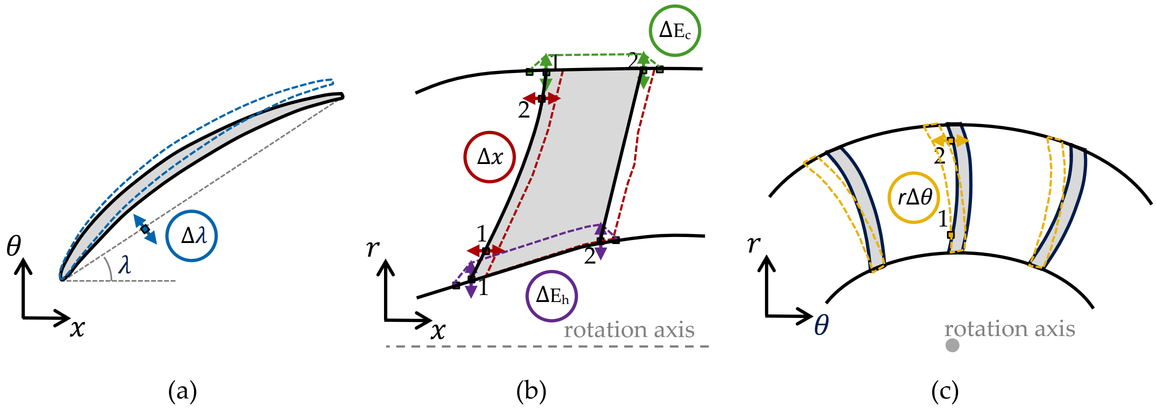

Figure 5.4: Sketch of the geometric DOE's in (a) the blade-to-blade, (b) meridional and (c) front planes: three dimensional blade rigid motions and linear endwall deformation. The dotted color lines illustrate the corresponding modified geometry for a positive deviation with respect to the baseline.

Table 5.1: Set of relative variations for each degree of freedom per considered blade row of the low-pressure compressor (IGV, $\mathbb{R}1$, $\mathbb{S}1$, $\mathbb{S}2$, $\mathbb{S}3$). The lengths and angles are non-dimensionalized by a mean chord $\overline{c}$ and a mean stagger angle $\overline{\lambda}$, respectively.

DOF's	Relative variations [%]
$\Delta\lambda/\overline{\lambda}$	−7.5; −3.75; 3.75
$(\Delta x_1,\ \Delta x_2)/\overline{c}$	(1.7, 1.7); (1.7, −1.7) (−1.7, 1.7); (−1.7, −1.7)
$(r_2\Delta\theta_2 - r_1\Delta\theta_1)/\overline{c}$	−4.3; −2.15; 2.15; 4.3
$(\Delta E_{c1},\ \Delta E_{c2})/\overline{c}$	(2.85, −2.85); (−2.85, 2.85)
$(\Delta E_{h1},\ \Delta E_{h2})/\overline{c}$	(2.85, 2.85); (2.85, −2.85) (−2.85, 2.85); (−2.85, −2.85)

These geometric variations impact both the blade forces and correlations. As shown in Fig. 5.5, the optimal incidence angle i^* only depends on geometric parameters, namely the leading and trailing edge blade angle κ, the thickness-to-chord ratio $\frac{t_{max}}{c}$ and the solidity σ, which are constant in the

[1]These data points are missing due to convergence issues encountered in RANS calculations. Moreover, the cases for the other rotors are not reported here for the sake of conciseness.

present case because the blade geometry itself remains unchanged. Therefore, i^* is not impacted by the variabilities considered here. Similarly, the input geometric parameters of the correlations for δ_{TE} and ω are independent of blade position variations, except for the radial coordinate that can slightly vary. As a result, both correlation outputs depend only indirectly on the geometric variations through the flow parameters, that is the optimal and actual incidence angle, the velocity components, the density and the Mach number. In addition to be influenced by potential correlation variations, the blade forces are directly impacted by the vector components normal and tangent to the blade camber surface. Specifically, the stream-wise variation Δx perturbs the blade sweep designed to reduce the leading edge loading and secondary flows. Moreover, the leading edge is slightly misaligned with respect to the incident streamlines. As a consequence, the incidence conditions are slightly altered, as well as the correlation outputs. As a consequence, the meridional variation of the blade row position is fully captured by a TF computation. Stagger angle variations mainly impact the localized blade twist and thereby, the blade span-wise alignment with the flow while the blade twist was precisely calibrated to reduce the high incidences in the endwall regions. These high incidence conditions can also be predicted in the endwall regions but the profile loss correlation should be complemented by a secondary loss model to take full advantage of this TF feature.

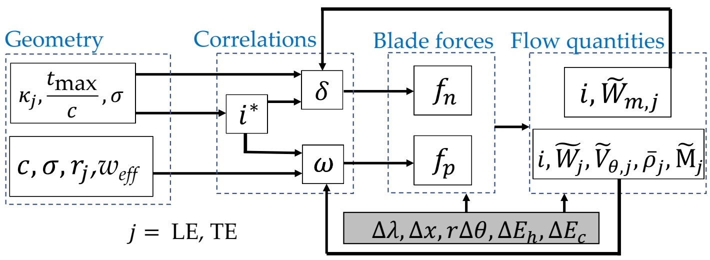

Figure 5.5: Dependencies of blade forces and correlation outputs with respect to geometric and flow quantities. The geometric variations imposed are indicated by the shaded box.

The pitch-wise perturbation impacts the blade lean, which changes the span-wise distribution of the stage reaction and the mass-flow rate through the radial pressure gradient and the streamline curvature. The circumferential and radial components of the blade force are thus impacted so that the pressure close to the endwalls is increased and the fluid is deflected toward mid-span sections. This effect is axisymmetric and fully captured by a through-flow computation. Finally, the endwall deformation is mainly felt by the boundary layer and thus the turbulence model. It also impacts the computation of the correlations through the variation of the flow conditions.

5.2.1.2 Variability analysis

The variation of the quantities of interest with respect to the imposed manufactured perturbations at nominal conditions is summarized for all cases in Figs. 5.6 and Fig. 5.7. Each variation is subsequently presented individually in Figures Figs. 5.8-5.10 for clarity. The results show a global good agreement between the trends predicted by RANS and TF models. The mean absolute difference between relative performance variation of both solvers is equal to 0.0065%, 0.0074% and 0.0017% for the mass flow rate, the total pressure ratio and the isentropic efficiency, respectively. The error for the efficiency variation seems lower but the variation range is three times lower than those of other quantities. Consequently, the relative errors are of the same order of magnitude.

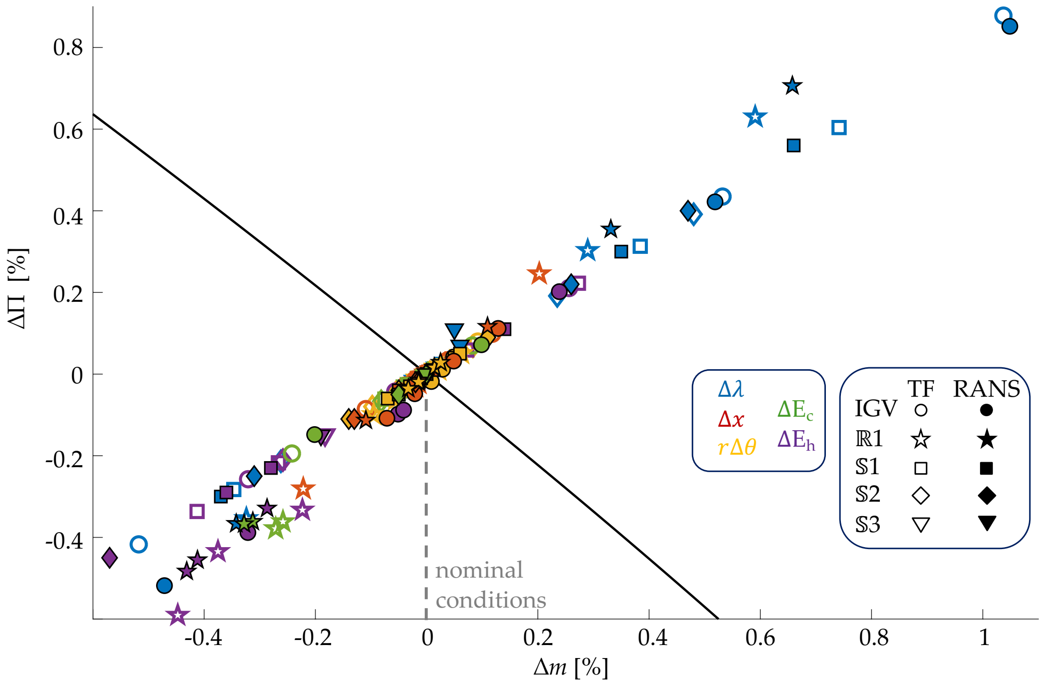

Figure 5.6: Relative pressure ratio and mass flow rate variations due to geometric variabilities at nominal operation conditions. Comparison of RANS (closed symbols) and though-flow (open symbols) simulations where only a parameter is modified per blade row and per simulation. The black lines are the iso-speed performance curves of reference.

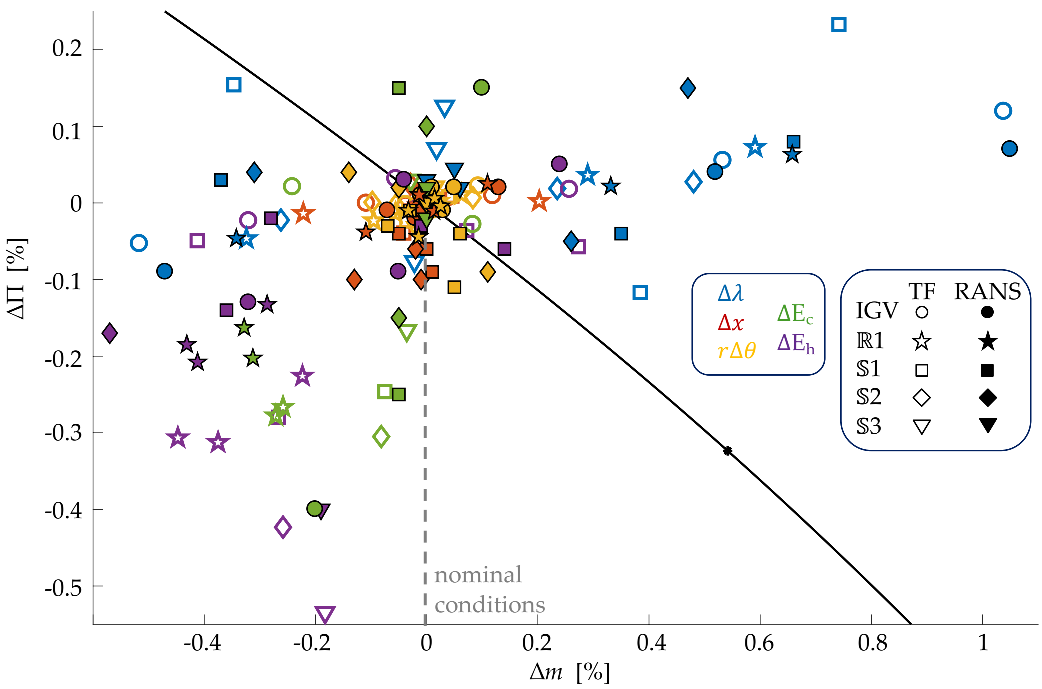

Figure 5.7: Relative isentropic efficiency and mass flow rate variations due to geometric variabilities at nominal operation conditions. Comparison of RANS (closed symbols) and though-flow (open symbols) simulations where only a parameter is modified per blade row and per simulation. The black lines are the iso-speed performance curves of reference.

While the variations of the isentropic efficiency appears scattered around its baseline value, the total pressure ratio mostly exhibits a linear variation with respect to the mass flow rate. This linear behavior can be explained by the boundary conditions used in both the RANS and TF simulations: at the outlet, the flow is smoothed as the symmetric strut mostly forces an axial flow at its trailing edge. Therefore, the radial equilibrium predicts a static pressure distribution which is almost uniform and imposed by the prescribed reference pressure. On the other hand, the mass-flow rate is proportional to the total-to-static pressure ratio at the outlet station. Therefore, the mass-flow rate and the total pressure ratio are a function of only the outlet total pressure as the total pressure is imposed at the inlet and the static pressure at the outlet station. As a result, for a given compression load, more efficient work leads to an increase in both $\dot{m}$ and Π. In the case of the isentropic efficiency, additional parameters related to loss mechanisms come into play.

With regard to the respective contributions of the variability parameters, the stagger angle seems to have the greatest impact, while the variations of the blade axial position seem to have the lowest importance. However, the relative importance of the impact of each geometric parameter can be misleading because their range of variation is different and their relative variation to the nominal value is also different. It is therefore more relevant to compare the impact of each geometric parameter separately, as shown in Figs. 5.8-5.10.

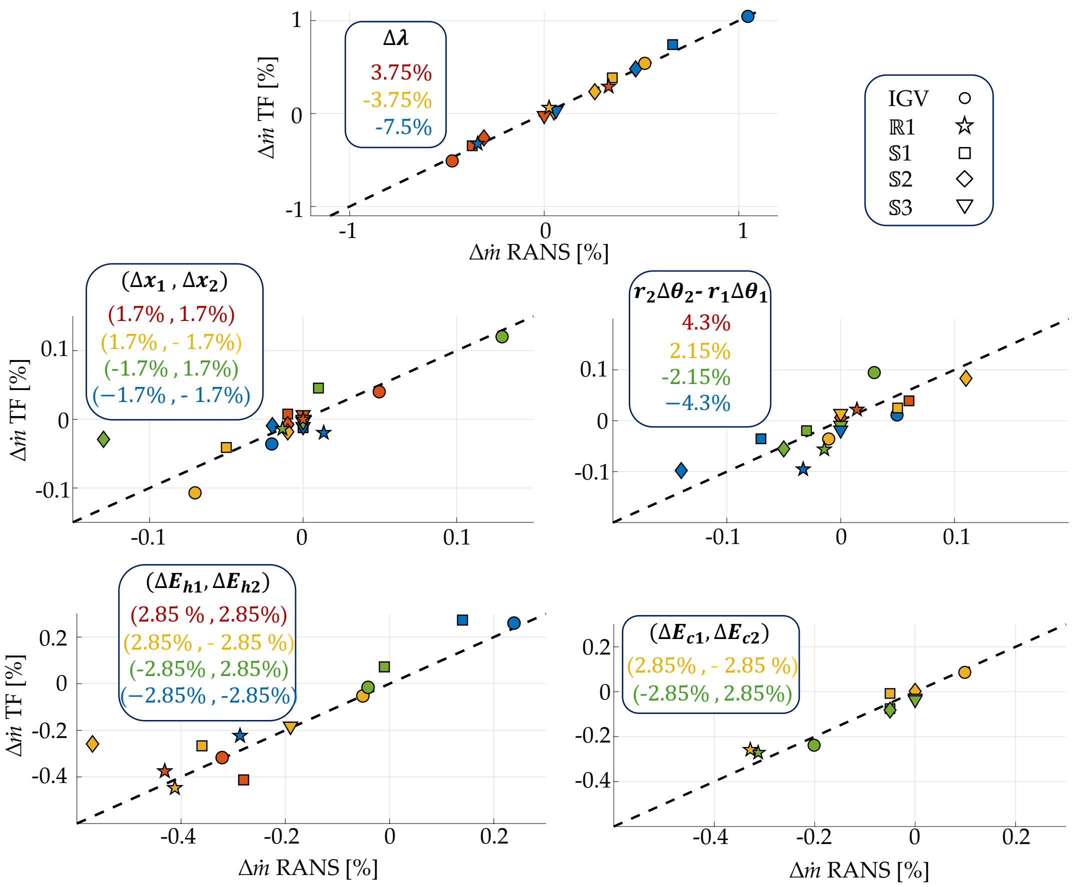

Figure 5.8: Relative mass-flow rate variations due to stagger angle variation (top), meridional displacement (centre left), pitch-wise displacement (centre right), hub and casing deformation at nominal operation conditions (bottom). Correlations between RANS and though-flow (TF) simulations where only a parameter is modified per blade row and per simulation.

A modification of the most upstream blade rows often has a higher impact on the performance because the resulting perturbed flow impacts all downstream blade rows in cascade and changes their incident flow conditions. Consequently, the performance of the downstream blade rows are also altered. The global trend is accurately captured by the TF model as the scatter points closely align with the linear correlation law. The accuracy of the isentropic efficiency variation is a bit lower, as the TF model does not include all sources of loss in its empirical correlations. Moreover, the deficiencies of turbulence models can also play a role in the endwall region.

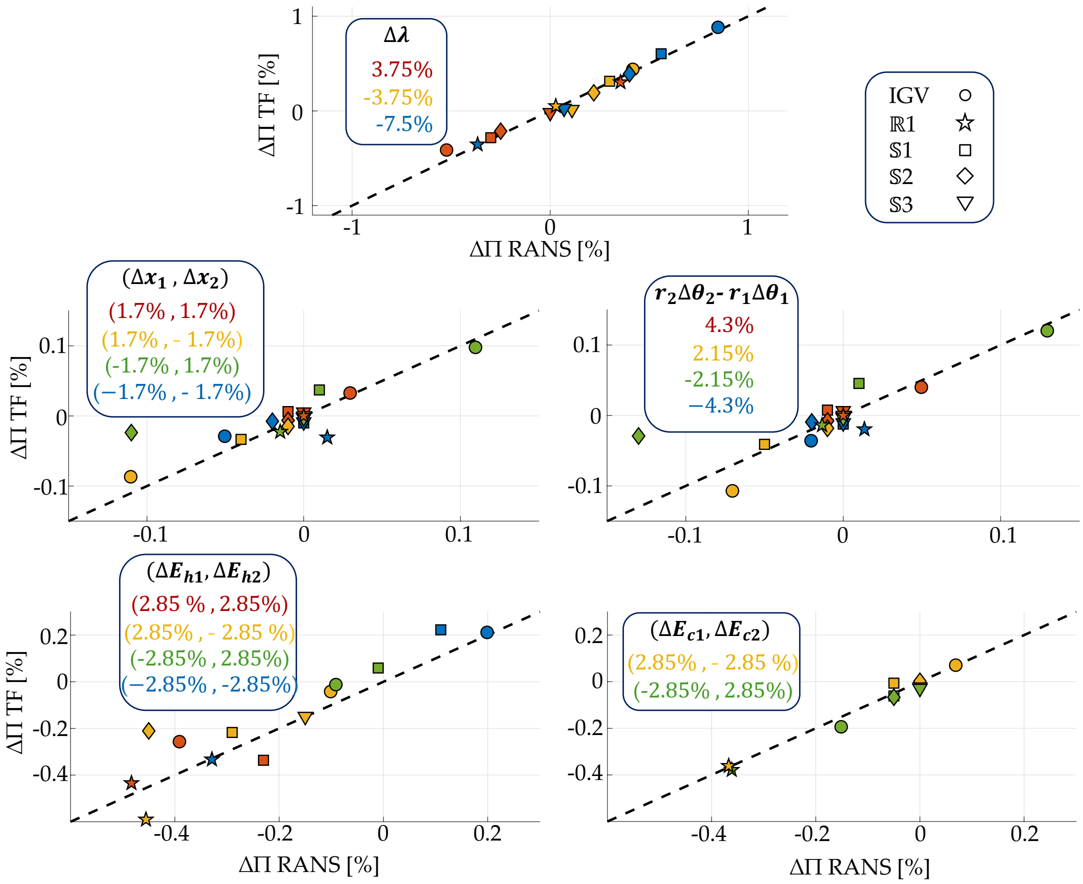

Figure 5.9: Relative pressure ratio variations due to stagger angle variation (top), meridional displacement (centre left), pitch-wise displacement (centre right), hub and casing deformation at nominal operation conditions (bottom). Correlations between RANS and though-flow (TF) simulations where only a parameter is modified per blade row and per simulation.

Finally, the variations of the correlation parameters δ_{TE} and $\omega_{2\mathrm{D}}$ of the S1 blade with respect to imposed geometric variability on the S1 blade are shown in Fig. 5.11. Moreover, the total loss coefficient ω, which includes the profile loss from correlations for ω and endwall loss from the turbulence model, is also presented. The individual plots indicate that the flow variance is essentially caused by the stagger angle and endwall perturbations. The impact of endwall deformations is consistently felt by the flow in a region close to the hub and casing. These effects are partly driven by the turbulence model in viscous TF equations. Due to the variation of the deviation angle, performance variations are mostly felt by the downstream blade rows which experience inlet flow variations.

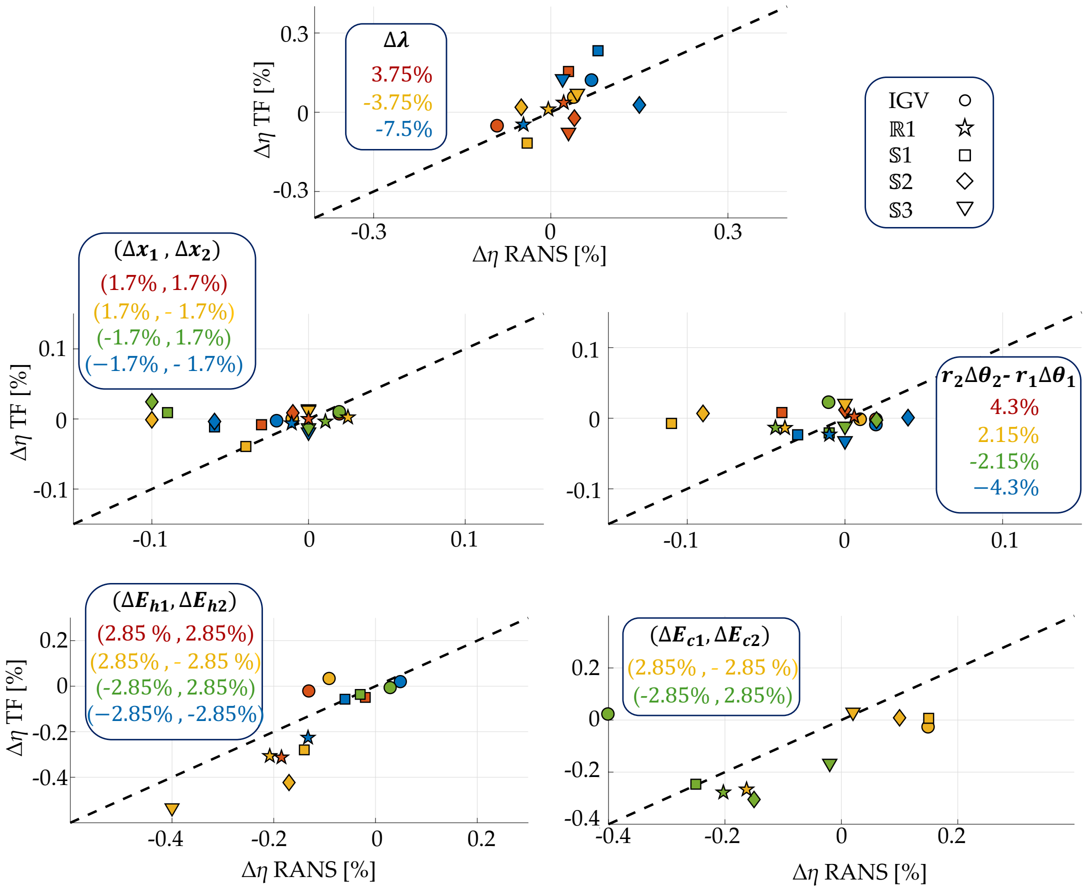

Figure 5.10: Relative isentropic efficiency variations due to stagger angle variation (top), meridional displacement (centre left), pitch-wise displacement (centre right), hub and casing deformation at nominal operation conditions (bottom). Correlations between RANS and though-flow (TF) simulations where only a parameter is modified per blade row and per simulation.

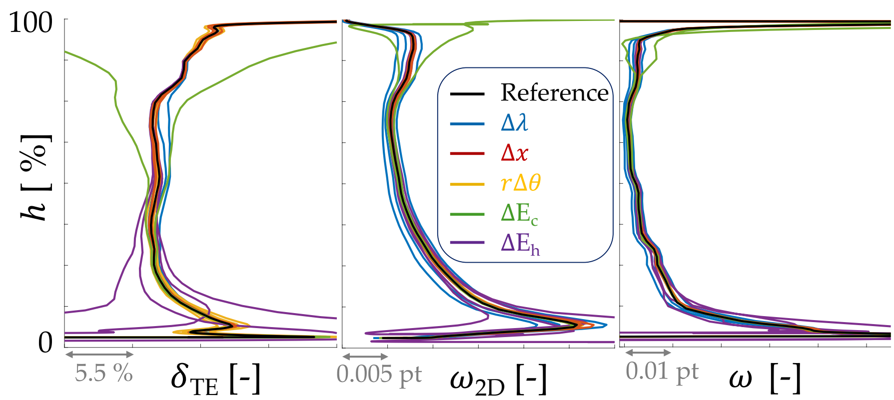

Figure 5.11: Variation of the deviation angle δ_{TE}, profile loss coefficient ω_{2D} computed by the empirical correlations and total loss coefficient ω along the S1 blade span h with respect to imposed geometric variability on the S1 blade.

5.2.2 Blade angle variability at the leading edge

Despite the promising results reported above, the impact of other types of geometric variability can still be partially smoothed by the model due to the approximations and empiricism inherent to the TF solver. The leading edge is a critical example as the aforementioned modeling aspects directly impact the propagation of geometric variability precisely in this region. It is also a critical location from an aerodynamic standpoint, since geometric variations occurring at the leading edge are expected to have a particularly strong influence on performance [70]. This section thus aims to evaluate the ability of the through-flow modeling approach to quantify the impact of geometric variabilities at leading edge. First, the camber line at the blade leading edge is modified by ±1.5° over the first 20% of the chord along the blade span. For each simulation, only one blade row is modified. The comparison of compressor performance variation obtained with TF and RANS respectively, is shown in Fig. 5.12.

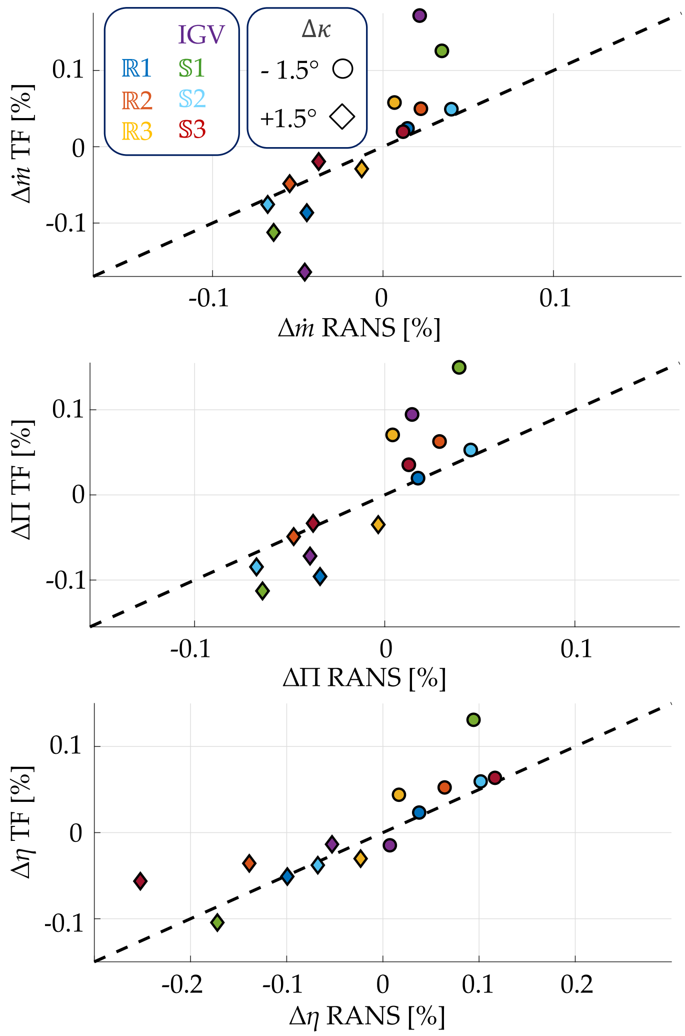

Figure 5.12: Relative variations of the mass-flow rate, the pressure ratio and the isentropic efficiency due to LE blade angle κ variations. Correlations between RANS and TF simulations for which each time a single blade row is modified.

As explained above, a blade geometry modification at the leading edge is mainly felt through the correlations for δ_{TE} and ω because the LE blade angle is one of the main input parameters for these correlations (see Fig. 5.5). As a result, despite the use of the incidence smoothing and the extrapolation of the blade angle at the leading edge, the model is still able to predict performance variations associated with this geometric variability. The global trend is effectively captured by the TF model, although not as accurately as in previous variability tests: the relative performance variation is mainly overestimated by the TF solver, especially in the case of the mass-flow rate and the total pressure ratio, meaning that the correlation sensitivity to the incidence angle has a large contribution in this case. It should also be recalled that the correlation used to determine the optimal incidence angle is itself subject to empirical uncertainty. This uncertainty modifies the δ_{TE} and ω_{2D} polars, thereby introducing an error in the estimation of both loss and deviation angle. The error in the estimation of δ_{TE} in turn yields an incidence at the inlet of the downstream blade row that differs from the expected value. As a consequence, this error propagates progressively from one blade row to the next, amplifying its impact on the overall performance prediction.

5.2.3 Rotor tip gap variability

The impact on performance of increasing and decreasing the tip gap by 50% for the rotors of the compressor is shown in Fig. 5.13. For each simulation, only one blade row is modified. As expected, the TF model significantly underestimates the performance variability compared with the RANS simulations.

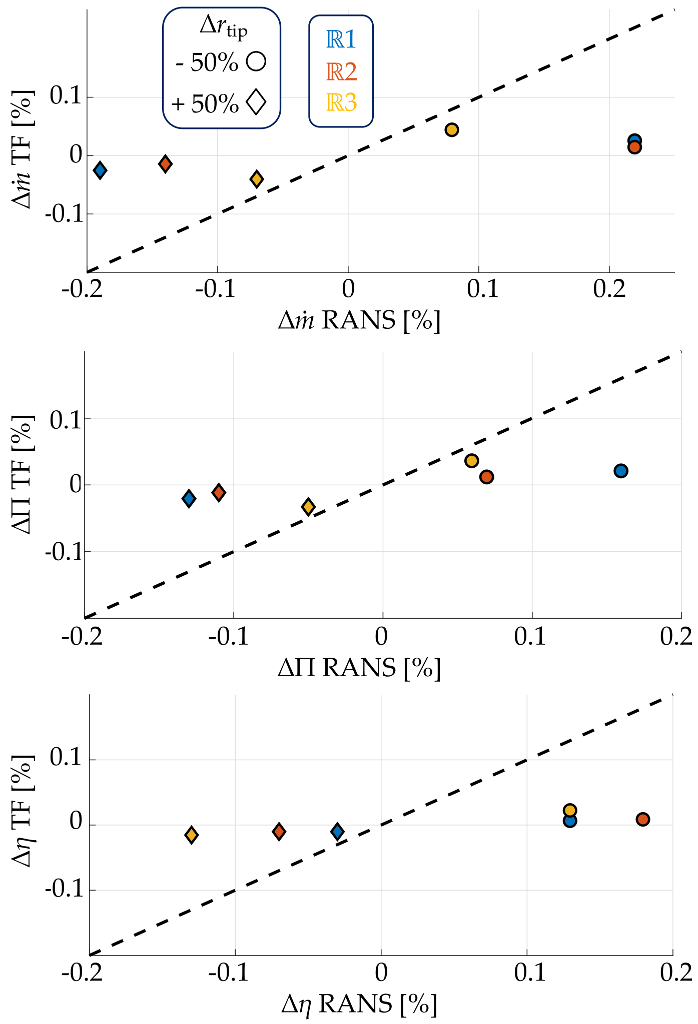

Figure 5.13: Relative variations of the mass-flow rate, the pressure ratio and the isentropic efficiency due to variabilities of the tip gap size. Correlations between RANS and TF simulations for which each time a single rotor blade row is modified.

This discrepancy arises because the TF solver can only capture axisymmetric variations, whereas tip-leakage losses in the rotor tip region are predominantly three-dimensional and strongly non-axisymmetric. In the present formulation, the only mechanism that can be represented near the casing is the development of an axisymmetric tangential shear layer induced by the adverse axial pressure gradient along the casing. However, this shear layer extends over only about 1% of the blade span, which has a limited impact on the compressor performance. In reality, the dominant tip-leakage phenomenon is driven by the pressure difference between the pressure and suction sides of the blade, which generates a strongly non-axisymmetric leakage jet across the tip gap. Consequently, a dedicated tip-gap model is required to introduce these non-axisymmetric effects by modelling the associated blockage, deviation, and loss as a function of the tip-gap size. Without such a model, the TF solver can only reproduce a limited fraction of the real loss mechanisms associated with tip leakage, leading to a systematically underestimated sensitivity of compressor performance to tip-gap variations.

5.2.4 Blade thickness variability

The blade thickness is a parameter directly linked to the blockage-factor terms in the body-force formulation and also enters the empirical correlations through the input parameter $t_{\max}$, which is required to evaluate both i^* and δ_{TE}. In this study, the thickness distribution at 20% (root) and 80% (tip) of the blade span is modified by ±10%, as illustrated in Fig. 5.14. To achieve this, a smooth geometric transition is introduced around the targeted region in order to avoid discontinuities in the thickness distribution. The airfoils within the affected spanwise zone are therefore thickened or thinned via a homothetic transformation, such that the chord length and the camber line remain unchanged. For each simulation, only one blade row is modified.

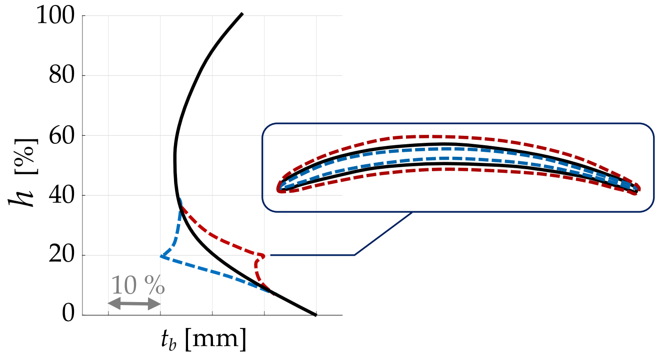

Figure 5.14: Sketch of the geometric variations of the blade thickness t_b at 20% of the blade span h: thickening (red) and thinning (blue) by 10%.

The resulting performance variations obtained with RANS and TF simulations are compared in Fig. 5.15. The TF model predicts the performance variations with acceptable accuracy. The mass-flow rate is the best-captured quantity, as the blockage term directly affects the local meridional velocity. The isentropic efficiency is the least accurately predicted, since it is strongly influenced by loss models that remain incomplete. It should also be noted that the performance variations associated with thickness changes are the smallest observed in this study, except for the tip-gap variability. Indeed, thickness variations affect only a limited portion of the blade span, unlike most of the other geometric variations previously investigated, which influence the entire blade height. Consequently, the overall impact on performance is reduced. Nevertheless, the TF model is able to qualitatively capture the performance trends induced by these thickness variations. A dedicated analysis of the choking mass-flow would also be of interest, once the correlations have been complemented to improve their validity under off-design conditions.

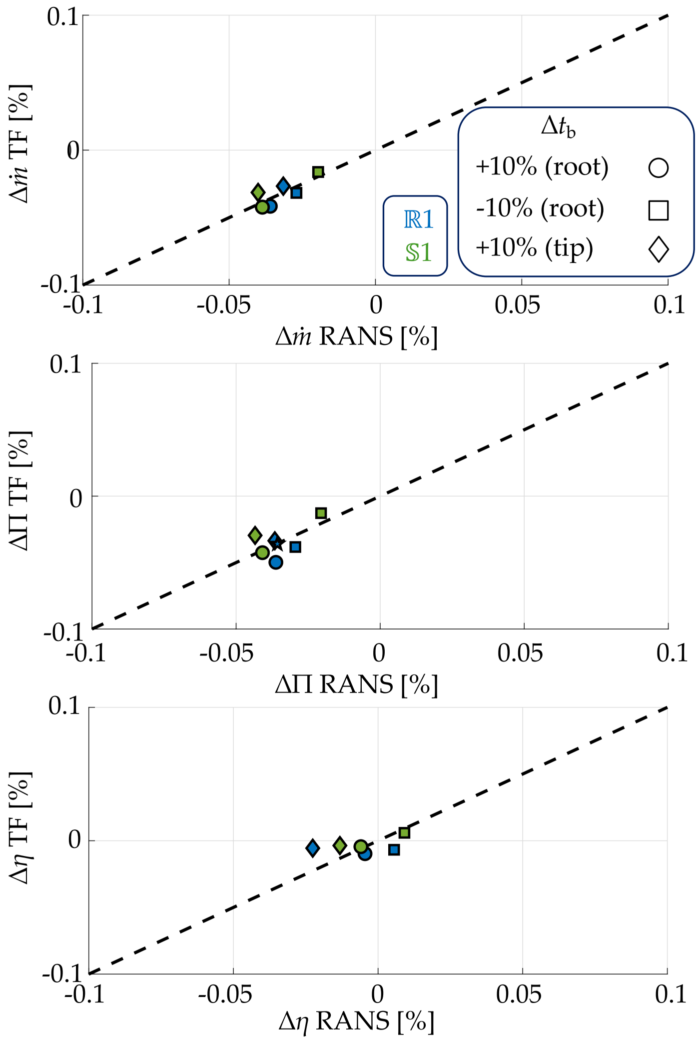

Figure 5.15: Relative variations of the mass-flow rate, the pressure ratio and the isentropic efficiency due to variabilities of the blade thickness. Correlations between RANS and TF simulations for which each time a single rotor blade row is modified.

5.3 Concluding remark

The results in this chapter hint that the TF model can accurately capture the qualitative trends of performance variations for most types of geometric variability considered. However, certain limitations have been identified, particularly in the case of tip-gap variations, for which the accuracy of the TF model strongly depends on the predictive quality of the underlying correlations, and the leading-edge blade angle, where the epistemic uncertainty stemming from the aforementioned aspects can have a large contribution. In addition, discrepancies are also observed in the prediction of isentropic efficiency. This suggests that, provided refined and complementary correlations are available, the TF solver could be effectively embedded within a multi-fidelity framework to efficiently propagate geometric uncertainties in turbomachinery design while reducing reliance on costly RANS simulations. For instance, RANS could be used to evaluate the nominal operating point, whereas the TF model could be employed to investigate the performance deltas induced by geometric variability. Similarly, RANS computations could be exploited to calibrate or adjust the correlations, thereby improving the overall robustness of the approach.

Chapter 6

Conclusion

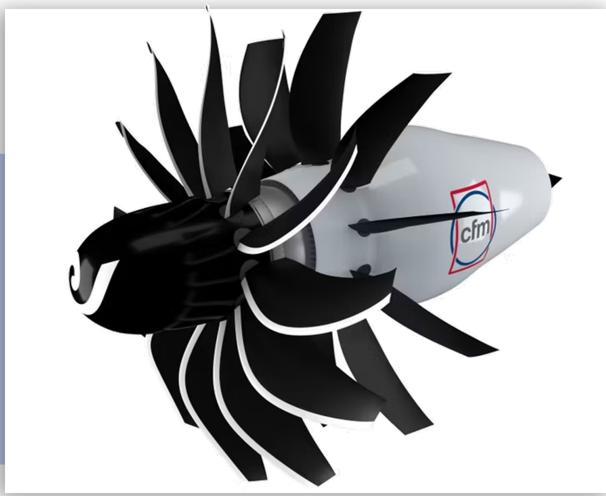

The objective of the present work was to evaluate a viscous CFD-based through-flow solver complemented with state-of-the-art empirical correlations, and the adequacy of this modeling approach to quantify the impact of geometric variability on the performance of axial compressors. This was motivated by the fact that a TF solver could serve as an efficient tool for propagating geometric uncertainties in a multi-fidelity approach, rather than relying exclusively on expensive 3-D RANS computations. This chapter summarizes the main findings of the present work and outlines perspectives for future research.

6.1 Summary and conclusions

After a comprehensive review of the state-of-the-art on through-flow modeling approaches in Chapter 2, a Navier–Stokes-based through-flow solver, relying on a finite-volume method coupled to a time-marching procedure, has been employed to solve the axisymmetric equations derived in Chapter 3. A body-force formulation consisting in imposing the local direction of the flow and the losses is used to represent the blade forces. This approach relies on prescribed radial distributions of the trailing-edge deviation angle δ_{TE} and of the loss coefficient ω.

In Chapter 4, the model has been validated against two test cases: the CME2 compressor stage and a low-pressure axial compressor designed by Safran Aero Boosters. First, the TF simulations were fed with the exact radial distribution of the correlation parameters using RANS input data in order to isolate the modeling error from correlation empiricism. Classical empirical correlations for the deviation angle and the loss coefficient, derived from cascade data, were then introduced and assessed. Subsequently, improved correlations were developed and implemented to better account for Mach number effects and modern blade profiles.

The study has enabled the identification and characterisation of the main sources of model error in the TF solver. The results have shown that these modelling errors remain relatively limited, provided that the key parameter distributions of δ_{TE} and ω are accurately known. Despite its reduced-order nature, the TF solver is capable of reproducing the mean-flow field and the overall performance levels with reliable accuracy when compared with the reference RANS simulations across the range of operating conditions. This demonstrates both the predictive capability of the model, which is essential in preliminary design phases, and its reproducibility, which is crucial for its use in advanced design stages. Moreover, this observation supports the use of the TF solver within a multifidelity framework, combining few 3D RANS with multiple TF simulations. In this context, the distributions of δ_{TE} and ω could be inferred directly from RANS simulations, improving the reliability of the TF predictions or ensuring at least a much better coherence with that obtained by RANS. Such an approach is particularly relevant in late design phases where the geometry is already fixed. However, the consistent use of high-fidelity data in the calibration of deviation and loss correlations raises an important modelling issue. When correlations informed by RANS data are directly embedded into a Navier–Stokes-based through-flow solver, there is a risk of double counting certain loss mechanisms, as part of the viscous effects may already be captured by the axisymmetric formulation. Although this effect remains relatively limited in multi-stage compressors, where the endwall boundary layers typically remain thin compared to the blade span, care must be taken when transferring loss information across fidelity levels. This issue is closely related to the broader question of loss breakdown, namely how to consistently separate profile, secondary, and leakage losses when transferring information across fidelity levels. Ideally, the losses should be decomposed to identify which contributions are already accounted for in the TF formulation. However, carrying out such a decomposition from RANS in a robust and systematic way is still a significant challenge [157]. The use of an Euler-based formulation could also be considered. However, a Navier–Stokes formulation remains fundamentally advantageous as it provides more realistic velocity profiles and gradients near the annulus walls. This becomes especially valuable when local flow information is required in advanced design phases, for instance to define boundary conditions for higher-fidelity simulations or to perform data matching with experimental measurements. In addition, it inherently captures the development of endwall boundary layers between the blade rows, which are not resolved in an Euler-based formulation. This leads to a more realistic prediction of the incidence upstream of the blades, which is particularly important when assessing compressor operability under off-design conditions.

In earlier design stages, however, such high-fidelity information is typically unavailable, and empirical correlations must therefore be introduced to prescribe the distributions of δ_{TE} and ω. The deficiencies and limitations of these correlations have proven to be the dominant source of error in the TF predictions. This conclusion is particularly important, as it indicates that improving the deviation and loss models, together with their streamwise distributions, is a key requirement for enhancing the reliability of TF-based performance predictions. In this context, when empirical correlations are used, the issue of double counting does not arise. A Navier–Stokes formulation therefore becomes advantageous, as it naturally accounts for part of the loss mechanisms and reduces the need for additional empirical modelling.

Modifications of the correlations have thus been introduced in order to improve the prediction in the scope of this work. Specifically, the dominant term of the deviation angle correlation, that is the slope parameter in Carter's rule [28], has been modified. Moreover, Mach number effects, based on the work of König et al. [114], have been introduced in the loss coefficient correlation because some underestimation of the loss had been noticed in the Lieblein's correlation. As a result, the TF predictions were drastically improved compared to the case based on classical correlations and the performance curves show a satisfactory agreement. Moreover, the linear law predicted by the deviation angle correlation reproduces fairly well the deviation angle behavior in a range relatively close to the optimal incidence angle i^*, i.e., the incidence angle that achieves minimal loss, but fails to predict off-design conditions. Furthermore, secondary-flow effects have not been explicitly addressed in the present work. Introducing dedicated correlations to account for these mechanisms would therefore constitute an important step toward improving the predictive capability of the model. These secondary-flow structures intensify under off-design operating conditions and have a strong influence on both effective turning and loss generation. The flow topology associated with these mechanisms is extremely complex and strongly dependent on blade geometry, blade loading, stacking strategy and operating point, making their modelling particularly challenging.

Chapter 5 aimed at evaluating the ability of the TF model, based on a Navier–Stokes formulation and complemented with modified correlations derived from the state of the art, to predict the effects of geometric variability. The results obtained in this chapter suggest that the TF model can capture the qualitative performance trends induced by most types of geometric variability analysed, particularly in terms of compression ratio. However, discrepancies are observed in the trend prediction of the isentropic efficiency, which can largely be attributed to the shortcomings of the loss correlations. These correlations would need to be complemented in order to better capture the associated loss mechanisms, such as secondary flows.

In addition, two cases reveal clear limitations. The first concerns tip-gap variations, for which the TF solver underestimates the impact due to its inability to represent the inherently three-dimensional leakage mechanisms occurring in the rotor tip region. Consequently, a dedicated tip-gap model is required to introduce these non-axisymmetric effects within the through-flow framework, by modelling the associated blockage, deviation, and losses as a function of the tip-gap size. Such a model could also contribute to predicting compressor stability and operability in tip-critical configurations.

The second limitation is related to leading-edge perturbations, where the sensitivity of the correlations and epistemic uncertainties can play a dominant role. In particular, two major sources of epistemic uncertainty have been identified that may smear out the effect of geometric variability: the leading-edge incidence correction and the reconstruction of the camber line from arbitrary blade geometries. Strategies to mitigate these uncertainties have been proposed, such as smoothing the incidence correction over an optimal chordwise extent and enforcing a monotonic extrapolation of the camber line in order to remove non-physical artefacts introduced by preprocessing algorithms.

These findings confirm that, provided refined and complementary correlations are available, the TF solver can be effectively embedded within a multi-fidelity framework to propagate geometric uncertainties efficiently while significantly reducing reliance on costly RANS simulations. This constitutes a proof of concept for the multi-fidelity strategy envisioned in the MARIETTA project. It should nevertheless be recalled that the axisymmetric formulation of the TF approach inherently restricts the modeling of geometric variability to blade-to-blade consistent perturbations within a given row. This precludes the representation of circumferentially non-uniform variations, such as mistuning.

6.2 Suggestions and perspectives for future work

To address the limitations highlighted above and to further extend the capabilities of the proposed through-flow modeling framework, several avenues for investigation should be explored in future work.

6.2.1 Comprehensive set of correlations

A first and obvious direction for improvement is the refinement of the existing empirical correlations. The modeling of the deviation angle is already satisfactory in the near-design regime, but its linear formulation must be corrected at high incidence in order to improve predictions on the stall side of the performance curves. The modeling of profile losses however remains the central limitation of the body-force approach. First, a specific validation and recalibration of the profile-loss correlation should be carried out to enhance its accuracy at negative incidence [61]. Even with perfectly calibrated polars for δ_{TE} and $\omega_{2\mathrm{D}}$, the prediction of losses and turning remains strongly dependent on the accuracy of the optimal incidence i^*. If i^* is poorly estimated, the level of loss and turning is inevitably misrepresented, regardless of the quality of the underlying loss and deviation correlations. As shown in this work, i^* is highly sensitive to the blade angle obtained during the reconstruction of the camber line. In situations where the blade geometry is known, such as during an optimisation phase, and the design flow angle β^* is available, this angle could instead be used as a reference to define the incidence variations in term of $\beta - \beta^*$. Such a formulation would also contribute to improving the robustness of the model with respect to leading-edge geometric perturbations and therefore to a more reliable prediction of the uncertainties associated with leading-edge variability.

In addition, explicitly accounting for secondary-flow effects is essential. Several empirical secondary-flow models exist in the literature, yet they must be used carefully: the axisymmetric Navier–Stokes formulation already captures part of the endwall shear and heat-transfer effects through the boundary-layer solution, raising the question of how to combine empirical secondary-flow correlations with the physics already resolved by the solver in a consistent manner. Moreover, most of these correlations, such as that of Roberts et al. [162], exhibit no dependence on incidence. Nevertheless, previous studies [168] have shown that such models can be coupled with Navier–Stokes-based through-flow solvers, and Manfredi and Fontaneto [131] has identified a particularly promising set of correlations for modern compressor configurations. Future work should also aim at developing correlations capable of accounting for the impact of endwall contouring and shroud treatments, which are increasingly used to control secondary flows and losses in modern compressor designs but are not explicitly represented in current through-flow modeling frameworks.

In this context, an important phenomenon to model is the tip-gap leakage flow, which used to be treated separately from the other secondary flows. Although this topic was not discussed in Chapter 4, the two potential-vortex models proposed by Lakshminarayana [116] were evaluated. As shown in Fig. 6.1, the first model, based on semi-empirical relations, provides a reasonable estimation of the mass-averaged total-pressure loss coefficient and yielded acceptable loss levels for both test cases considered in this work. The second approach, which predicts the radial and pitchwise extent of the tip-gap loss region, significantly overestimated the radial penetration of the leakage-induced vortex.

For the CME2 stage, the predicted influence zone extended to nearly 40% of the blade height. This behavior indicates that a recalibration, as well as further physical assessment, is required before the model can be reliably applied. For these reasons, this correlation was not included in the present study.

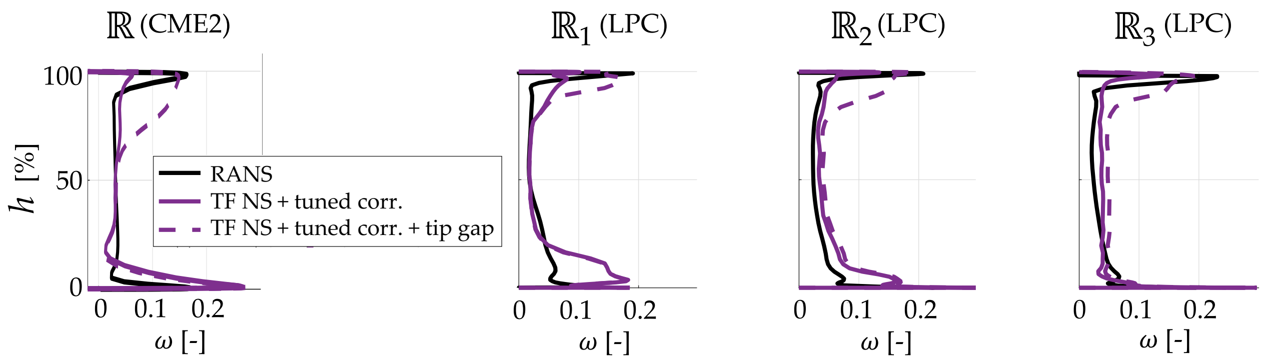

Figure 6.1: Comparison between TF simulations using the tuned correlations, with and without the tip gap loss model, and pitch-wise averaged 3D RANS simulation of the CME2 rotor (left) and the low-pressure compressor (LPC) rotors (right) at nominal conditions (OP1). Loss coefficient ω along the rotor blade height h.

A key aspect that should also be modelled is the aerodynamic blockage associated with secondary flows. For instance, the local blockage and deviation generated by tip-leakage flows or hub-corner vortices should be incorporated into the TF solver. When complemented by a low-empiricism model describing the radial influence zone of the tip-leakage vortex in the meridional plane, such an approach would enable the prediction of both the local and global impact of leakage flows, which are currently underestimated due to their inherently three-dimensional nature. This could be achieved by introducing an additional contribution to the blockage factor b [112]. It would also be appropriate to extend the blockage factor to non-bladed regions in order to represent the blockage induced by wakes, which plays a significant role in redistributing momentum and losses downstream of blade rows. This would need to be complemented by a model for radial mixing.

Furtermore, the correlations implemented in the present work provide only a relation based on the blade row LE and TE and rely on a linear streamwise distribution of the correlation outputs. The development of models capable of prescribing this streamwise behaviour would therefore represent a significant improvement, especially at off-design conditions [143]. In this regard, previous studies [182] have attempted to characterise how the circumferential velocity evolves inside the blade passage but these models have proven to lack generality.

Finally, care should be taken not to remain confined within the classical through-flow correlations that have largely remained unchanged for several decades. Many existing correlations were originally developed for simplified blade geometries, such as NACA airfoils, and their direct applicability to modern, highly three-dimensional blade designs is therefore questionable. This calls for more appropriate modeling strategies, either through the definition of correlations tailored to restricted and well-defined blade design philosophy, for instance for a specific manufacturer. In this perspective, data-driven and machine-learning-based methodologies appear particularly promising.

6.2.2 Toward less empiricism

The present study has shown that the dominant source of error in the through-flow solver originates from the empiricism embedded in the correlations. Although these correlations offer a convenient and computationally efficient way to reproduce cascade physics, they rely on extensive experimental databases whose acquisition and maintenance are costly. Moreover, the long-term sustainability of such empirical foundations becomes increasingly questionable as compressor architectures evolve beyond the range of the historical datasets. In view of the capabilities of modern computing resources, a promising approach is to reduce the level of empiricism by introducing high-order models capable of providing higher-fidelity information that is specific to the machine and operating point under consideration. As discussed by several authors, solving the flow within periodic cascade streamsurfaces can replace the empirical closure entirely and provide the blade forces directly. A noteworthy contribution in this direction is the work of Kravtsoff [112], who revisited potential-flow techniques for axial compressors: the deviation angle and the loss coefficient stemming from profile loss are computed using the Hess & Smith method [84], with viscous effects incorporated through a von Kármán integral boundary-layer formulation.

Further strategies consist in numerically coupling axisymmetric through-flow solvers with the non-axisymmetric stress terms introduced by Adamczyk's averaging procedure. Closure models for these stresses would constitute a major step toward universal through-flow solvers applicable to a wide range of compressor designs. Harmonic balance techniques have already been proposed to treat the unsteady and circumferential stresses [33, 188]. They remain computationally efficient when restricted to a limited number of harmonics. Finally, progress in turbulence modeling could also play a role in improving viscous through-flow simulations. Classical eddy-viscosity models rely on the Boussinesq hypothesis. This assumption is known to induce modeling errors and is still under active investigation.

6.2.3 Geometric variations & design optimization

The results obtained from the sensitivity analysis of geometric variations are encouraging and have also enabled the identification of key areas for improvement in the TF model in order to enhance its capability to predict the impact of geometric variability. Future work should extend the assessment of the through-flow model to additional forms of blade deformation to obtain a more complete analysis of its predictive capabilities, as well as to off-design operating conditions, in order to assess compressor operability. In particular, investigating cross-variations of geometric parameters represents an important next step. Owing to the high dimensionality of the geometric variability space, suitable reduction techniques will be required to ensure computational tractability [8]. In this context, Latin Hypercube Sampling [120] appears well suited for generating representative sets of variations in a Monte-Carlo propagation. Ultimately, the objective is to evaluate the model using realistic blade deformations measured from manufactured blades. Within this framework, a promising approach would be to improve the correlations on the fly by enriching the through-flow model with information from high-fidelity simulations in the multi-fidelity approach.

Although the through-flow model is inherently axisymmetric, mistuned blade rows could nevertheless be treated in a statistical sense by considering azimuthal averages of the blade-row geometries.

Another, more explicit method would consist in extending the model toward a three-dimensional formulation, as explored in Gong [69], Thollet [185]. Such approaches have been successfully employed to investigate surge and stall inception [35], inlet distortion, and boundary-layer ingestion effects [36], as well as intake-fan interactions [150] through body-force formulations based on the lift & drag analogy. These methods constitute formal extensions of axisymmetric through-flow solvers, in which the prescribed body-force distribution is redistributed over the full annulus as a spatially varying function, thereby enabling the prediction of three-dimensional flow features obtained by superimposing local deviations onto an axisymmetric baseline solution. An illustration of such an azimuthally varying body-force distribution is provided in Fig. 6.2.

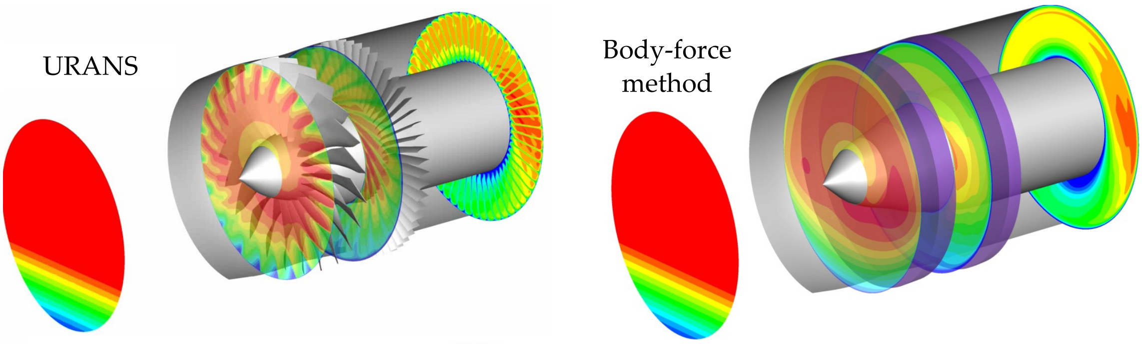

Figure 6.2: Illustration of inlet distortion prediction using (left) a blade-resolved mesh and (right) a body-force formulation. Adapted from Thollet [185].

A similar strategy could be envisioned for the modeling of mistuning. Instead of introducing azimuthal variations of the flow variables, one could introduce azimuthally varying geometric information directly into the body-force terms. In this framework, the body-force distribution would include the passag-to-passage geometric differences, allowing the solver to capture the effects of mistuning while maintaining a significantly reduced computational cost compared to fully three-dimensional simulations. However, this does not imply that such a model could replace full-annulus RANS simulations, as it would not resolve secondary-flow structures with the same level of fidelity. This would therefore open the door to hybrid multi-fidelity strategies in which certain blade rows are represented by high-fidelity RANS simulations while others are treated using body forces. This selective refinement would drastically decrease the computational cost while still enabling a detailed investigation of the impact of geometric variability and mistuning on compressor performance. Moreover, most three-dimensional body-force methods described in the literature have relied heavily on the lift-and-drag analogy, which differs substantially from the body-force model employed in the present work. A benchmark between these approaches would therefore be of significant interest.

Finally, the through-flow framework also holds promise for design optimization, particularly within an adjoint-based methodology [52, 121]. Given the low computational cost of TF simulations, direct finite-difference evaluations of design sensitivities may also remain a viable option. Such capabilities would allow including the TF solver in robust, gradient-based design loops at both preliminary and advanced design stages.

6.2.4 Transonic regime

The test cases discussed throughout this thesis were exclusively subsonic. Nevertheless, the continued development of modern aircraft engines motivates new research efforts aimed at supporting the design of next-generation, high-efficiency turbomachine architectures. For instance, the introduction of geared-engine configurations, which decouple the fan speed from that of the compressor–turbine shaft, enables engines with high bypass ratios, thereby improving both propulsive and thermal efficiency. However, the higher core rotational speeds made possible by such architectures drive compressor stages into highly transonic operating regimes. This highlights the necessity of extending through-flow modeling capabilities toward the transonic domain, where shock and compressibility effects become important contributors to overall performance. In particular, identifying the mechanisms responsible for entropy production, as well as their spatial extent and intensity under unconventional operating conditions, remains essential for technological maturation.

Although TF models using the analysis-mode formulation, like the through-flow solver introduced in this thesis, are capable of capturing shock structures [40], as illustrated by the Rotor37 [6] simulation in Fig. 6.3, the fidelity of these predicted shocks must be interpreted with care. Shocks in TF simulations are inherently axisymmetric by nature, whereas the actual shocks are usually not, which should in theory result in a distributed rather than abrupt flow variation. Additional correlations, such as those proposed by Manfredi and Fontaneto [131], would be required to model shock-induced losses adequately. Nevertheless, such losses cannot be inferred from two-dimensional cascade, as shocks depend strongly on the three-dimensional blade design.

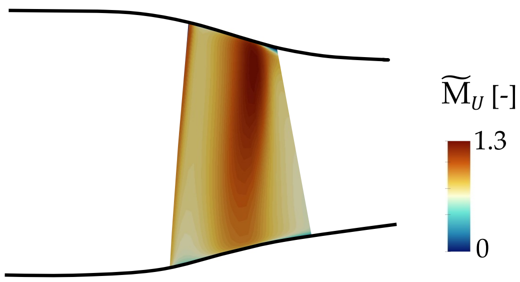

Figure 6.3: Contour of the rotating Mach number of the Rotor37 from the TF simulations.

In addition, an alternative formulation of the blockage factor, often referred to as the *normal blockage* and evaluated along the streamwise direction in the blade-to-blade plane, should be implemented to improve the flow prediction. As emphasized in Baralon [12], the classical circumferential blockage, although consistent with the averaged governing equations, can lead to a poor quality of the solution in the analysis mode when the performance is sought knowing the real geometry. However, the normal blockage is generally not required for subsonic configurations [168, 112].

Finally, Baralon [12] also showed that the incidence correction applied in the analysis mode may lead to an incorrect shock position and an inaccurate level of shock-induced loss. A more refined incidence-correction strategy could therefore be beneficial, for instance by replacing the linear smoothing used in this work with a higher-order C^2-continuous curve for the flow angle. Alternatively, the use of higher-order blade-force models may offer a more fundamental solution. In particular, Kravtsoff [112] demonstrated that when the mean-flow angle distribution is obtained from a potential-flow computation with sufficient fidelity, no incidence correction is needed at all, since the flow angle at the leading edge becomes naturally continuous.

6.3 Closing remarks

As a conclusion, the work presented in this thesis confirms that through-flow methods still have a significant role to play in the future of turbomachinery design. One of the major challenges facing both research and industry in the coming years is the ability to design increasingly complex propulsion systems within a genuinely multidisciplinary framework. In this context, the present study highlights the continued relevance and practical value of reduced-order models, at a time when substantial effort is being directed toward high-fidelity approaches such as LES. These high-fidelity tools will undoubtedly remain essential, not only for resolving complex unsteady flow physics but also for informing, calibrating, and enriching new generations of low-order models that can be embedded within through-flow solvers. Beyond compressors, the methodology could be extended to turbines and fans, provided that appropriate loss and deviation models are developed for these components. Finally, it should be emphasized that the through-flow model developed here has been applied in analysis mode, i.e., for known geometries typical of advanced design stages. An important task for future work could be to equip this framework with a true design mode, enabling geometry generation within the through-flow environment.

Bibliography

[1] J. J. Adamczyk. Model equation for simulating flows in multistage turbomachinery. Technical report, NASA TM-86869, 1984.

[2] J. J. Adamczyk. Aerodynamic Analysis of Multistage Turbomachinery Flows in Support of Aerodynamic Design. *ASME Journal of Turbomachinery*, 122(23):189–217, 1999. doi: 10.1115/1.555439.

[3] J. J. Adamczyk, R. A. Mulac, and M. L. Celestina. A model for closing the inviscid form of the average-passage equation system. *ASME Journal of Turbomachinery*, 108(2):180–186, October 1986. doi: 10.1115/1.3262035.

[4] J. Adkins, G. G. and J. Smith, L. H. Spanwise mixing in axial-flow turbomachines. *Journal of Engineering for Power*, 104(1):97–110, January 1982. doi: 10.1115/1.3227271.

[5] H. A. Aguirre, V. Pachidis, and I. Templalexis. An analytical shock-loss model fully integrated to a streamline curvature method for axial-flow compressors. In *Proceedings of the ASME Turbo Expo*, volume 2C, Pheonix, US, June 2019. doi: 10.1115/GT2019-91701.

[6] A. A. Ameri. Nasa rotor 37 cfd code validation. Technical report, NASA/CR—2010-216235, 2009.

[7] J. D. Anderson. *Fundamentals of Aerodynamics*. McGraw-Hill Education, New-York, US, 5th edition, 2011.

[8] M. Arnst and R. Ghanem. Probabilistic equivalence and stochastic model reduction in multiscale analysis. *Computer Methods in Applied Mechanics and Engineering*, 197(43):3584–3592, 2008. ISSN 0045-7825. doi: https://doi.org/10.1016/j.cma.2008.03.016.

[9] M. S. Attia. A Semi-Viscous Method For Designing Axial Compressors. In *41st AIAA Joint Propulsion Conference and Exhibit*, pages 1–8, Tucson, Arizona, US, 10-13 July 2005. doi: 10.2514/6.2005-4540.

[10] R. H. Aungier. *Axial-Flow Compressors*. ASME Press, January 2003. doi: 10.1115/1.801926.

[11] M. Banjac, M. V. Petrovic, and A. Wiedermann. Secondary flows, endwall effects, and stall detection in axial compressor design. *Journal of Turbomachinery*, 137(5), May 2015. doi: 10.1115/1.4028648.

[12] S. Baralon. *On multistage analysis of transonic compressors : from axisymmetric throughflow time-marching to unsteady three dimensional methods*. PhD thesis, Chalmers university of technology, 2000.

[13] S. Baralon, L.-E. Erikson, and U. Hall. Validation of a throughflow time-marching finite-volume solver for transonic compressors. In *Proceedings of the ASME Turbo Expo*, volume 1, Stockholm, Sweden, 1–4 June 1998.

[14] S. Baralon, L.-E. Eriksson, and U. Håll. Evaluation of higher-order terms in the throughflow approximation using 3D Navier-Stokes computations of a transonic compressor rotor. In *Proceedings of the ASME Turbo Expo*, volume 1, Indianapolis, US, June 1999. doi: 10.1115/99-GT-074.

[15] F. Bardoux. *Modélisation des interactions instationnaires rotor-stator en turbomachine multi-étages*. PhD thesis, Ecole centrale de Lyon, 2000.

[16] B. Beachkofski and R. Grandhi. Probabilistic system reliability for a turbine engine airfoil. In *Proceedings of the ASME Turbo Expo*, volume 5, pages 171–179, Vienna, Austria, 14-17 June 2004. doi: 10.1115/GT2004-53381.

[17] T. Benamara, P. Breitkopf, I. Lepot, and C. Sainvitu. LPC blade and non-axisymmetric hub profiling optimization using multi-fidelity non-intrusive pod surrogates. In *Proceedings of the ASME Turbo Expo*, volume 2C: Turbomachinery, Charlotte, US, June 2017. doi: 10.1115/GT2017-65106.

[18] D. Bestle and P. Flassig. Optimal aerodynamic compressor blade design considering manufacturing noise. In *Proceedings of the ISSMO conference*, London, UK, 8–9 July 2010.

[19] C. Bosman and H. Marsh. An improved method for calculating the flow in turbo-machines, including a consistent loss model. *Journal of Mechanical Engineering Science*, 16(1):25–31, 1974. doi: 10.1243/JMES_JOUR_1974_016_006_02.

[20] M. L. Brand. *An improved blade passage model for estimating off-design axial compressor performance*. PhD thesis, Massachusetts Institute of Technology, Boston, US, 2013.

[21] A. Budo, V. E. Terrapon, M. Arnst, K. Hillewaert, S. Mouriaux, B. Rodriguez, and J. Bartholet. Application of a viscous through-flow model to a modern axial low-pressure compressor. In *Proceedings of the ASME Turbo Expo*, volume 2A, Virtual, Online, 7-11 June 2021. doi: 10.1115/GT2021-59926.

[22] A. Budo, K. Hillewaert, M. Arnst, T. Le Men, and V. E. Terrapon. Quantification of geometric variability effects through a viscous through-flow model: sensitivity analysis of the manufacturing tolerance effects on performance of modern axial-flow compressor blades. In *Proceedings of the ASME Turbo Expo*, volume 13C, Boston, US, 26-30 June 2023. doi: 10.1115/GT2023-102800.

[23] A. Budo, K. Hillewaert, J. Bartholet, and V. E. Terrapon. Assessment of geometrical variability effects through a viscous through-flow model applied to modern axial-flow compressor blades.

In *15th European Conference on Turbomachinery Fluid dynamics and Thermodynamics*, volume no. 307, Budapest, Hungary, 24-28 April 2023.

[24] A. Budo, J. Bartholet, T. Le Men, K. Hillewaert, and V. E. Terrapon. Preliminary assessment of geometric variability effects through a viscous through-flow model applied to modern axial-flow compressor blades. *International Journal of Turbomachinery, Propulsion and Power*, Volume 10 (2): 6, 2025. doi: https://doi.org/10.3390/ijtpp10020006.

[25] M. Burigana, T. Verstraete, and S. Lavagnoli. Turbine endwall contouring through advanced optimization techniques. *Journal of Turbomachinery*, 145(8), April 2023. doi: 10.1115/1.4062211.

[26] L. Cambier, S. Heib, and S. Plot. The onera elsa cfd software: input from research and feedback from industry. *Mechanics & Industry*, 14(3):159–174, 2013. doi: 10.1051/meca/2013056.

[27] T. Cao, P. Hield, and P. G. Tucker. Hierarchical immersed boundary method with smeared geometry. *Journal of Propulsion and Power*, Volume 33(5):1151–1163, 2017. doi: 10.2514/1.B36190.

[28] A. Carter. The Low Speed Performance Of Related Aerofoils In Cascades. Technical Report 19, Aeronautical Research Council, 1950.

[29] M. Casey. A mean line prediction method for estimating the performance characteristic of an axial compressor stage. In *ImechE*, volume Turbomachinery—Efficiency Prediction and Improvement: C264/87, London, UK, 1987.

[30] M. Casey and C. Robinson. A new streamline curvature throughflow method for radial turbomachinery. In *Proceedings of the ASME Turbo Expo*, volume 6, pages 2119–2130, June 2008. doi: 10.1115/GT2008-50187.

[31] L. Castillon, G. Billonnet, J. Riou, S. Péron, and C. Benoit. A technological effect modeling on complex turbomachinery applications with an overset grid numerical method. *Journal of Turbomachinery*, 136(10), July 2014. doi: 10.1115/1.4027997.

[32] M. Çetin, A. S. Ücer, C. Hirsch, and G. K. Serovy. Application of modified loss and deviation correlations to transonic axial compressors. In *AGARD*, volume R-745, 1987.

[33] D. Charbonnier. *Développement D'un Modèle De Tensions Déterministes Instationnaires Adpaté à La Simulation De Turbomachines Multi-étagées*. PhD thesis, Ecole Cntrale de Lyon, Lyon, france, 2004.

[34] T. Chen, P. Vasanthakumar, and L. He. Analysis of unsteady blade row interaction using nonlinear harmonic approach. *Journal of Propulsion and Power*, 17(3):651–658, 2001. doi: 10.2514/2.5792.

[35] R. V. Chima. A three-dimensional unsteady cfd model of compressor stability. In *Proceedings of the ASME Turbo Expo*, volume 6, pages 1157–1168, Barcelona, Spain, May 2006. doi: 10.1115/GT2006-90040.

[36] C. Crea, J. Marty, R. Barrier, S. Cochon, and G. Dufour. Body force modelling of a multi-stage high-pressure compressor under inlet distortion. *International Journal of Turbomachinery, Propulsion and Power*, 10(2), 2025. doi: 10.3390/ijtpp10020012.

[37] H. F. Creveling and R. H. Carmody. Axial Flow Compressor Computer Program For Calculating Off-Design Performance. Technical Report 10873, NASA, 1968.

[38] N. A. Cumpsty. *Compressor Aerodynamics*. Longman, London, UK, 5th edition, 1989.

[39] N. A. Cumpsty and J. H. Horlock. Averaging nonuniform flow for a purpose. *Journal of Turbomachinery*, 128(1):120–129, February 2005. doi: 10.1115/1.2098807.

[40] S. V. Damle, T. Q. Dang, and D. R. Reddy. Throughflow method for turbomachines applicable for all flow regimes. *Journal of Turbomachinery*, 119(2):256–262, April 1997. doi: 10.1115/1.2841108.

[41] T. Q. Dang and T. Wang. Design of multi-stage turbomachinery blading by the circulation method: Actuator duct limit. In *Proceedings of the ASME Turbo Expo*, volume 1, Cologne, Germany, June 1992.

[42] W. N. Dawes. Toward improved throughflow capability: The use of three-dimensional viscous flow solvers in a multistage environment. *Journal of Turbomachinery*, 114(1):8–17, January 1992. doi: 10.1115/1.2928002.

[43] J. de Laborderie and S. Moreau. Prediction of tonal ducted fan noise. *Journal of Sound and Vibration*, Volume 372:105–132, 2016. ISSN 0022-460X. doi: https://doi.org/10.1016/j.jsv.2016.02.032.

[44] J. J. Defoe, M. Etemadi, and D. K. Hall. Fan performance scaling with inlet distortions. *Journal of Turbomachinery*, 140(7):071009, June 2018.

[45] A. Demeulenaere. Conception et développement d'une méthode inverse pour la génération d'aubes de turbomachines. *PhD Thesis*, pages 69–76, 1997.

[46] J. D. Denton. Throughflow calculations for transonic axial flow turbines. *Journal of Engineering for Power*, 100(2):212–218, April 1978. doi: 10.1115/1.3446336.

[47] J. D. Denton. An improved time-marching method for turbomachinery flow calculation. *Journal of Engineering for Power*, 105(3):514–521, July 1983. doi: 10.1115/1.3227444.

[48] J. D. Denton. Loss mechanisms in turbomachines. In *Proceedings of the ASME Turbo Expo*, volume 2, Cincinnati, US, May 1993. doi: 10.1115/93-GT-435.

[49] J. D. Denton. Some limitations of turbomachinery CFD. In *Proceedings of the ASME Turbo Expo*, volume 7, pages 735–745, Glasgow, UK, 14-18 June 2010. doi: 10.1115/GT2010-22540.

[50] J. D. Denton and W. N. Dawes. Computational Fluid Dynamics For Turbomachinery Design. In *Proceedings of the Institution of Mechanical Engineers, Part C: Journal of Mechanical Engineering*, volume 213(2), pages 107–124, 1999. doi: 10.1243/0954406991522211.

[51] J. D. Denton and L. Xu. The exploitation of three-dimensional flow in turbomachinery design. *Proceedings of the Institution of Mechanical Engineers, Part C: Journal of Mechanical Engineering Science*, 213(2):125–137, 1998. doi: 10.1243/0954406991522220.

[52] C. Dosne. *Development and implementation of adjoint formulation of explicit body-force models for aero-propulsive optimizations*. PhD thesis, Institut Polytechnique de Paris, Paris, France, 2025.

[53] E. A. Dow and Q. Wang. The Implications of Tolerance Optimization on Compressor Blade Design. *Journal of Turbomachinery*, 137(10), October 2015. ISSN 0889-504X. doi: 10.1115/1.4030791. 101008.

[54] M. Drela and H. Youngren. A user's guide to Mises 2.63. Technical report, MIT - Aerospace Computational Design Laboratory, February 2008.

[55] C. Dufour. Application and calibration of a viscous throughflow model to axial flow compressor blades subject to geometric variability. Master's thesis, University of Liège, 2022.

[56] J. Dunham. A new endwall model for axial compressor throughflow calculations. *Journal of Turbomachinery*, 117(4):533–540, october 1995. doi: 10.1115/1.2836565.

[57] P. A. Durbin and B. A. Pettersson Reif. *Statistical Theory and Modeling for Turbulent Flows*. John Wiley & Sons, Ltd, Chichester, UK, 2010. doi: 10.1002/9780470972076.

[58] M. Emory, J. Larsson, and G. Iaccarino. Modeling of structural uncertainties in reynolds-averaged navier-stokes closures. *Physics of Fluids*, 25(11), October 2013. doi: 10.1063/1.4824659.

[59] J. Fang, Y. Gao, Y. Liu, L. Lu, Y. Yao, and C. Le Ribault. Direct numerical simulation of a tip-leakage flow in a planar duct with a longitudinal slit. *Physics of Fluids*, Volume 31(12), 2019. ISSN 10897666. doi: 10.1063/1.5124163.

[60] G. Fay, M. Lawerenz, , and H. Przewozny. Calculation of pitch averaged viscous flow in annular compressor cascade. *Computational Methods in Experimental Measurements*, IX(22):185–194, 1999.

[61] L. E. Ferrer-Vidal, M. Schneider, A. Allegretti, and V. Pachidis. A loss and deflection model for compressor blading at high negative incidence. *Journal of Turbomachinery*, 141(12):121001, October 2019. doi: 10.1115/1.4044967.

[62] S. Föllner, V. Amedick, B. Bonhoff, D. Brillert, and F.-K. Benra. Model validation of an Euler-based 2D-Throughflow Approach For multistage Axial Turbine Analysis. In *Proceedings of the ASME Turbo Expo*, volume 29(4), pages 185–186, London, UK, 22–26 June 2020.

[63] S. J. Gallimore. Spanwise mixing in multistage axial flow compressors: Part ii—throughflow calculations including mixing. *Journal of Turbomachinery*, 108(1):10–16, July 1986. doi: 10.1115/1.3262009.

[64] S. J. Gallimore. Viscous throughflow modeling of axial compressor bladerows using a tangential blade force hypothesis. *Journal of Turbomachinery*, 120(4):662–670, october 1998. doi: 10.1115/1.2841775.

[65] S. J. Gallimore, J. J. Bolger, N. A. Cumpsty, M. J. Taylor, P. I. Wright, and J. M. M. Place. The use of sweep and dihedral in multistage axial flow compressor blading—part i: University research and methods development. *Journal of Turbomachinery*, 124(4):521–532, 11 2002. doi: 10.1115/1.1507333.

[66] V. E. Garzon and D. L. Darmofal. Impact of Geometric Variability on Axial Compressor Performance. *Journal of Turbomachinery*, 125(4):692–703, December 2003. doi: 10.1115/1.1622715.

[67] H. Glauert. *Airplane Propellers*, volume IV. Springer, Berlin, Germany, 1935.

[68] B. Godard and E. De Jaeghere. Methodologies for turbofan inlet aerodynamics prediction. In *AIAA Aviation 2017 Forum*, Denver, US, 5-9 June 2017. doi: 10.2514/6.2017-3413.

[69] Y. Gong. *A computational model for rotating stall and inlet distortions in multistage compressors*. PhD thesis, Massachusetts Institute of Technology, Boston, US, 1999.

[70] M. N. Goodhand, R. J. Miller, and H. W. Lung. The Impact of Geometric Variation on Compressor Two-Dimensional Incidence Range. *Journal of Turbomachinery*, Volume 137(2), Setember 2014. ISSN 0889-504X. doi: 10.1115/1.4028355.

[71] N. Gourdain. *Simulation Numerique des Phenomenes de Decollement Tournant dans les Compresseurs Axiaux*. PhD thesis, Ecole Centrale de Lyon, Lyon, France, 2005.

[72] N. Gourdain. Prediction of the unsteady turbulent flow in an axial compressor stage. part 1: Comparison of unsteady rans and les with experiments. *Computers & Fluids*, Volume 106:119–129, 2015. doi: https://doi.org/10.1016/j.compfluid.2014.09.052.

[73] J. S. Gray, C. A. Mader, G. K. W. Kenway, and J. R. R. A. Martins. Coupled aeropropulsive optimization of a three-dimensional boundary-layer ingestion propulsor considering inlet distortion. *Journal of Aircraft*, 57(6):1014–1025, 2020. doi: 10.2514/1.C035845.

[74] E. Greitzer, C. Tan, and M. Graf. *Internal Flow: Concepts and Applications*, volume 3, pages 244–278. Cambridge University Press, Cambridge, UK, 2007.

[75] R. Guido. Blade profile loss model development for axial-flow fans and compressors performance prediction using through-flow simulations. Master's thesis, Politecnico Di Torino, 2017.

[76] B.-A. Gustafson. A simple method for supersonic compressor cascading performance prediction. In *Proceedings of the ASME Turbo Expo*, volume 1A, New Orleans, US, March 1976. doi: 10.1115/76-GT-64.

[77] C. M. Gutiérrez, A. Stuermer, C. Clemen, and A. Grimminger. Validation of actuator disk simulations of cror propulsion systems at low-speed flight conditions. In *30th AIAA Applied Aerodynamics Conference*, 25-28 June 2017. doi: 10.2514/6.2012-2787.

[78] D. K. Hall. *Analysis of civil aircraft propulsors with boundary layers ingestion*. PhD thesis, Massachusetts Institute of Technology, Boston, US, 2015.

[79] E. Hall, D. Topp, and R. Delaney. Task 7 - adpac user's manual. Technical report, NASA CR195472, 1995.

[80] D. Hänel, R. Schwane, and G. Seider. On the accuracy of upwind schemes for the solution of the Navier-Stokes equations. *AIAA*, 87-1105, 1987.

[81] L. He and W. Ning. Efficient approach for analysis of unsteady viscous flows in turbomachines. *AIAA Journal*, 36(11):2005–2012, 1998. doi: 10.2514/2.328.

[82] Y. He, J. Sun, P. Song, and X. Wang. Preference-inspired multi-objective throughflow-design optimization approach of axial flow compressor and its application. In *Proceedings of the ASME Turbo Expo*, volume 2D, Virtual, Online, 21–25 September 2020. doi: 10.1115/GT2020-14489.

[83] M. Hendler, M. Lockan, D. Bestle, and P. Flassig. Component-specific preliminary engine design taking into account holistic design aspects. *International Journal of Turbomachinery, Propulsion and Power*, Volume 3, April 2018. doi: 10.3390/ijtpp3020012.

[84] J. L. Hess and A. M. O. Smith. Calculation of potential flow about arbitrary bodies. *Progress in Aerospace Sciences*, 8:1–138, 1967. ISSN 0376-0421. doi: https://doi.org/10.1016/0376-0421(67)90003-6.

[85] K. Hillewaert. *Development of the discontinuous Galerkin method for high-resolution, large scale CFD and acoustics in industrial geometries*. PhD thesis, Université Catholique de Louvain, 2013.

[86] C. Hirsch. End-wall boundary layers in axial compressors. *Journal of Engineering for Power*, 96(4):413–426, October 1974. doi: 10.1115/1.3445867.

[87] C. Hirsch. CFD methodology and validation for turbomachinery flows. *AGARD Lecture series 195*, Turbomachinry Design Using CFD, 1994.

[88] C. Hirsch. *Numerical Computation of Internal and External Flows: The Fundamentals of Computational Fluid Dynamics*. Butterworth-Heinemann, Oxford, UK, 2^{nd} edition, 2007. ISBN 978-0-7506-6594-0. doi: https://doi.org/10.1016/B978-0-7506-6594-0.X5037-1.

[89] C. Hirsch and J. Denton. Through flow calculations in axial turbomachines. Technical report, AGARD Advisory Report 175, 1981.

[90] C. Hirsch and G. Warzee. A finite-element method for through flow calculations in turbomachines. *Journal of Fluids Engineering*, 98(3):403–414, September 1976.

[91] C. Hirsch and G. Warzee. An integrated quasi-3D finite element calculation program for turbomachinery flows. *Journal of Engineering for Power*, 101(1):141–148, January 1979. doi: 10.1115/1.3446435.

[92] J. H. Horlock. *Axial flow compressors*. Butterworth, London, UK, 1958.

[93] J. H. Horlock. On entropy production in adiabatic flow in turbomachines. *Journal of Basic Engineering*, 93(4):587–593, December 1971. doi: 10.1115/1.3425313.

[94] J. H. Horlock. *Actuator Disk Theory: Discontinuities in Thermo-fluid Dynamics*. McGraw-Hill, New-York, US, 1978.

[95] J. H. Horlock and J. D. Denton. A review of some early design practice using computational fluid dynamics and a current perspective. *Journal of Turbomachinery*, 127(1):5–13, February 2005. ISSN 0889-504X. doi: 10.1115/1.1650379.

[96] J. H. Horlock and H. J. Perkins. Annulus wall boundary layers in turbomachines. Technical report, AGARD Advisory Report 185, 1974.

[97] M. A. Howard and S. J. Gallimore. Viscous throughflow modeling for multistage compressor design. *Journal of Turbomachinery*, 115:2, April 1993. doi: 10.1115/1.2929235.

[98] A. R. Howell. Fluid dynamics of axial compressors. In *Proceedings of the Institution of Mechanical Engineers*, volume 153(1), pages 441–452, 1945. doi: 10.1243/PIME_PROC_1945_153_049_02.

[99] A. R. Howell and W. J. Calvert. A new stage stacking technique for axial-flow compressor performance prediction. *Journal of Engineering for Power*, 100(4):698–703, October 1978. doi: 10.1115/1.3446425.

[100] L. Högner, A. Nasuf, P. Voigt, M. Voigt, K. Vogeler, M. Meyer, C. Berridge, and F. Goenaga. Analysis of high pressure turbine nozzle guide vanes considering geometric variations. In *Proceedings of the ASME Turbo Expo*, volume 2C, 13-17 June 2016. doi: 10.1115/GT2016-57502.

[101] A. Jameson, W. Schmidt, and E. Turkel. Numerical solution of the euler equations by finite volume methods using runge kutta time stepping schemes. In *14th Fluid and Plasma Dynamics Conference*, 1981.

[102] I. K. Jennions and P. Stow. A quasi-three-dimensional turbomachinery blade design system: Part i — throughflow analysis. *Journal of Engineering for Gas Turbines and Power*, 107(2):301–307, April 1985. doi: 10.1115/1.3239715.

[103] I. K. Jennions and P. Stow. The importance of circumferential non-uniformities in a passage-averaged quasi-three-dimensional turbomachinery design system. In *Turbo Expo*, volume 1, September 1985. doi: 10.1115/85-IGT-63.

[104] J. Ji, J. Hu, S. Ma, and R. Xu. A computational method of rotating stall and surge transients in axial compressor. *Energies*, 15(14), 2022. doi: 10.3390/en15145246.

[105] L. Jian, W. Dongrun, T. Jinfang, Z. Mingmin, and Q. Xiaoqing. The effects of incidence and deviation on the CFD-based throughflow analysis. In *Proceedings of the ASME Turbo Expo*, London, UK, 2020.

[106] I. Johnsen and R. Bullock. Aerodynamic Design of Axial-Flow Compressors. Technical Report SP-36, NASA, 1965.

[107] M. Joly, T. Verstraete, and G. Paniagua. Full Design of A Highly Loaded And Compact Contra-rotating Fan Using Multidisciplinary Evolutionary Optimization. In *Proceedings of the ASME Turbo Expo*, volume 6B, pages 1–10, Glasgow, UK, 14-18 June 2013. doi: 10.1115/GT2013-94433.

[108] T. Kiffer, G. Dufour, R. Gojon, W. Thollet, and L. L. de Vega. Extension and validation of the body force method to a propeller blade. In *AIAA Aviation 2023 Forum*, San Diego, US, 12-16 June 2023. doi: 10.2514/6.2023-3378.

[109] G. Kiwada. *Development of a Body Force Description for Compressor Stability Assessment*. PhD thesis, Massachusetts Institute of Technology, Boston, Us, 2008.

[110] C. C. Koch and J. Smith, L. H. Loss sources and magnitudes in axial-flow compressors. *Journal of Engineering for Power*, 98(3):411–424, July 1976. doi: 10.1115/1.3446202.

[111] A. P. Kottapalli. Development of a Body Force Model for Centrifugal Compressors. Master's thesis, Massachusetts Institute of Technology, Boston, Us, 2013.

[112] F. Kravtsoff. *Axial compressor modeling with CFD-based throughflow and potential approach*. PhD thesis, Ecole centrale de Lyon, 2023.

[113] C. I. Kundu, P.K. *Fluid Mechanics*, pages 733–756. Elsevier, fourth edition, 2008.

[114] W. M. König, D. K. Hennecke, and L. Fottner. Improved Blade Profile Loss And Deviation Angle Models For Advanced Transonic Compressor Bladings: Part I - A Model For Subsonic Flow. *ASME Journal of Turbomachinery*, 118(1):73–80, 1996. doi: 10.1115/1.2836610.

[115] W. M. König, D. K. Hennecke, and L. Fottner. Improved blade profile loss and deviation angle models for advanced transonic compressor bladings: Part II — a model for supersonic flow. *Journal of Turbomachinery*, 118(1):81–87, January 1996. doi: 10.1115/1.2836610.

[116] B. Lakshminarayana. Methods of predicting the tip clearance effects in axial flow turbomachinery. *Journal of Basic Engineering*, 92(3):467–480, September 1970. doi: 10.1115/1.3425036.

[117] B. Lakshminarayana and R. Davino. Mean velocity and decay characteristics of the guidevane and stator blade wake of an axial flow compressor. *Journal of Engineering for Power*, 102(1):50–60, January 1980. doi: 10.1115/1.3230231.

[118] A. Lange, K. Vogeler, V. Gümmer, H. Schrapp, and C. Clemen. Introduction of a parameter based compressor blade model for considering measured geometry uncertainties in numerical simulation. *ASME Journal of Turbomachinery*, 59937:1–11, 2009.

[119] A. Lange, M. Voigt, K. Vogeler, H. Schrapp, E. Johann, and V. Gümmer. Probabilistic CFD simulation of a high-pressure compressor stage taking manufacturing variability into account. In *Proceedings of the ASME Turbo Expo*, volume 6, pages 617–628, Glasgow, Scotland, June 2010. doi: 10.1115/GT2010-22484.

[120] A. Lange, M. Voigt, K. Vogeler, E. Johann, R. Royce, C. Kg, and D. Dahlewitz. Principal component analysis on 3D scanned compressor blades for probabilistic CFD simulation. In *AIIA Conference*, 1762, pages 1–16, Granada, Spain, 3–7 September 2012. doi: 10.2514/6.2012-1762.

[121] M. T. Latour. Body force modeling of axial turbomachinery for analysis and design optimization. Master's thesis, Delft University of Technology, Delft, The Netherlands, 2020.

[122] K. L. Lewis. Spanwise transport in axial-flow turbines; part 2: Throughflow calculations including spanwise transport. *Journal of Turbomachinery*, 116(2), March 1994. doi: 10.1115/1.2928352.

[123] J. Li, D. Wu, J. Teng, M. Zhu, and X. Qiang. The effects of incidence and deviation on the cfd-based throughflow analysis. In *Turbo Expo*, volume Volume 2A: Turbomachinery, September 2020. doi: 10.1115/GT2020-14293.

[124] S. Lieblein. Analysis of Experimental Low-Speed Loss And Stall Characteristics of Two-Dimensional Compressor Blade Cascades. Technical Report RM E57A28, NACA, 1957.

[125] S. Lieblein. Loss and stall analysis of compressor cascades. *Journal of Basic Engineering*, 81(3): 387–397, September 1959. doi: 10.1115/1.4008481.

[126] S. Lieblein. Incidence and deviation-angle correlations for compressor cascades. *Journal of Basic Engineering*, 82(3):575–584, September 1960. doi: 10.1115/1.3662666.

[127] B. Liu, S. Chen, , and H. F. Martin. A primary variable throughflow code and its application to last stage reverse flow in lp steam turbine. In *International Joint Power Generation Conference*, volume 15010, 2000.

[128] S. Liu, T. Pan, and Q. Li. An improved body force model to simulate blade loading variation under various operating conditions in transonic axial flow compressor. *Journal of Turbomachinery*, 146(10):101002, April 2024. doi: 10.1115/1.4065238.

[129] J. P. Longley. Calculating stall and surge transients. In *Proceedings of the ASME Turbo Expo*, volume 6, pages 125–136, Montreal, Canada, May 2007. doi: 10.1115/GT2007-27378.

[130] L. López de Vega, G. Dufour, F. Blanc, and W. Thollet. A machine learning based body force model for analysis of fan-airframe aerodynamic interactions. In *International conference proceedings: Global Power and Propulsion Society Conference*, Montréal, Canada, 5-7 May 2018.

[131] M. Manfredi and F. Fontaneto. Transonic axial compressors loss correlations: Part i — analysis and update of loss models. In *Proceedings of the ASME Turbo Expo*, volume 2A, London, UK, September 2020. doi: 10.1115/GT2020-14713.

[132] F. E. Marble. *Section C. Three-Dimensional Flow in Turbomachines*, pages 83–166. Princeton University Press, Princeton, 1964.

[133] H. Marsh. A digital computer program for the through-flow fluid mechanics in an arbitrary turbomachine using a matrix method. Technical report, Aeronautical Research Council, R&M 3509, 1966.

[134] G. L. Mellor and G. M. Wood. An axial compressor end-wall boundary layer theory. *Journal of Basic Engineering*, 93(2):300–314, June 1971. doi: 10.1115/1.3425231.

[135] M. R. Mendenhall and S. B. Spangler. Theoritical study of ducted fan performance. Technical report, NASA CR-1494, Washington, US, January 1970.

[136] Q. J. Minaker and J. J. Defoe. Prediction of crosswind separation velocity for fan and nacelle systems using body force models: Part 1: Fan body force model generation without detailed stage geometry. *International Journal of Turbomachinery, Propulsion and Power*, 4(4), 2019. doi: 10.3390/ijtpp4040043.

[137] S. Mishra, C. Schwab, and J. Šukys. Multi-level monte carlo finite volume methods for nonlinear systems of conservation laws in multi-dimensions. *Journal of Computational Physics*, Volume 231 (8):3365–3388, 2012. ISSN 0021-9991. doi: https://doi.org/10.1016/j.jcp.2012.01.011.

[138] F. K. Moore and E. M. Greitzer. A theory of post-stall transients in axial compression systems: Part i—development of equations. *Journal of Engineering for Gas Turbines and Power*, 108(1):68–76, January 1986. ISSN 0742-4795. doi: 10.1115/1.3239887.

[139] A. W. H. Morris and R. G. Hoare. Secondary loss measurements in a cascade of turbine blades with meridional wall profiling. In *Proceedings of the ASME Turbo Expo*, Houston, US, September 1975.

[140] R. Nigmatullin and M. J. Ivanov. The mathematical models of flow passage for gas turbine engines and their components. *Mathematical Models of Gas Turbine Engines and their Components*, 1994.

[141] R. Nigro. *Uncertainty Quantification for Robust Design of Axial Compressors*. PhD thesis, University of Mons, Mons, Belgium, 2018.

[142] R. A. Novak. Streamline curvature computing procedures for fluid-flow problems. *Journal of Engineering for Power*, 89(4):478–490, October 1967.

[143] R. Pacciani, M. Marconcini, and A. Arnone. A CFD-Based Throughflow Method with Three-Dimensional Flow Features Modelling. *International Journal of Turbomachinery, Propulsion and Power*, Volume 2(3):1–12, 2017. ISSN 2504186X. doi: 10.3390/ijtpp2030011.

[144] V. A. Pachidis. *GasTurbine Advanced Performance Simulation*. PhD thesis, Cranfield University, 2005.

[145] H. Pantel, F. Falissard, and G. Dufour. Assessment of reynolds-averaged Navier–Stokes/Blade Element Theory body force method for propeller modeling. *AIAA journal*, 62:758–775, 2024. doi: https://doi.org/10.2514/1.J063302.

[146] K. D. Papailiou. Boundary layer optimization for the design of high turning axial flow compressor blades. *Journal of Engineering for Power*, 93(1):147–154, January 1971. doi: 10.1115/1.3445387.

[147] S. Pazireh. *Body Force Modeling of Axial Turbomachines Without Calibration*. PhD thesis, University of Windsor, Ontario, Canada, 2020.

[148] S. Pazireh and J. J. Defoe. A new loss generation body force model for fan/compressor blade rows: An artificial-neural-network based methodology. *International Journal of Turbomachinery, Propulsion and Power*, 6(1), 2021. doi: 10.3390/ijtpp6010005.

[149] G. Persico and S. Rebay. A penalty formulation for the throughflow modeling of turbomachinery. *Computers & Fluids*, 60:86–98, 2012. ISSN 0045-7930. doi: https://doi.org/10.1016/j.compfluid.2012.03.001.

[150] A. Peters. *Ultra-short nacelles for low fan pressure ratio propulsors*. PhD thesis, Massachusetts Institute of Technology, Boston, US, 2014.

[151] M. V. Petrovic, G. S. Dulikravich, and T. J. Martin. Optimization of Multistage Turbines Using A Through-Flow Code. *Proceedings of the Institution of Mechanical Engineers, Part A: Journal of Power and Energy*, Volume 215(5):559–569, 2001. doi: 10.1243/0957650011538802.

[152] M. V. Petrovic, A. Wiedermann, and M. B. Banjac. Development and validation of a new universal through flow method for axial compressors. In *Proceedings of the ASME Turbo Expo*, volume 7, pages 579–588, Orlando, US, June 2009. doi: 10.1115/GT2009-59938.

[153] E. W. Pfitzinger, W. Riess, R. Decuypere, and G. Dibelius. A new concept for loss and deviation prediction in throughflow calculations of axial flow compressors. In *Turbomachinery: fluid dynamics and thermodynamics*, pages 117–126, 1987.

[154] R. N. Pinto, A. Afzal, L. V. D'Souza, Z. Ansari, and A. D. Mohammed Samee. Computational Fluid Dynamics in Turbomachinery: A Review of State of the Art. *Archives of Computational Methods in Engineering*, Volume 24(3):467–479, 2017. ISSN 18861784. doi: 10.1007/s11831-016-9175-2.

[155] D. Pollard and J. P. Gostelow. Some experiments at low speed on compressor cascades. *Journal of Engineering for Power*, 89(3):427–436, July 1967. doi: 10.1115/1.3616709.

[156] G. Raina, Y. Bousquet, D. Luquet, E. Lippinois, and N. Binder. Loss breakdown in axial turbines: A new method for vortex loss and wake detection from 3d rans simulations. *Journal of Turbomachinery*, 147(6), November 2024. doi: 10.1115/1.4067033.

[157] G. Raina, Y. Bousquet, D. Luquet, E. Lippinois, and N. Binder. Analysis of interactions among loss-generating mechanisms in axial flow turbines. *International Journal of Turbomachinery, Propulsion and Power*, 10(2), June 2025. doi: 10.3390/ijtpp10020011.

[158] C. M. Rhie, A. J. Gleixner, D. A. Spear, C. J. Fischberg, and R. M. Zacharias. Development and application of a multistage navier–stokes solver: Part i—multistage modeling using bodyforces and deterministic stresses. *Journal of Turbomachinery*, 120(2):205–214, April 1998. doi: 10.1115/1.2841395.

[159] M. Ricci, R. Pacciani, M. Marconcinin, and A. Arnone. Secondary flow and radial mixing modelling for CFD-based through-flow methods: an axial turbine application. *Energy Procedia*, 148:218–225, 2018. ISSN 1876-6102. doi: https://doi.org/10.1016/j.egypro.2018.08.071. ATI 2018 - 73rd Conference of the Italian Thermal Machines Engineering Association.

[160] M. Ricci, R. Pacciani, M. Marconcini, P. Macelloni, S. Cecchi, and C. Bettini. CFD-Based Throughflow Analysis of Transonic Flows in Steam Turbines. In *Proceedings of the ASME Turbo Expo*, 90851, pages 1–10, Phoenix (AZ), US, 17-21 June 2019. ISBN 9780791858578. doi: 10.1115/GT2019-90851.

[161] M. Righi, V. Pachidis, L. Könözsy, and L. Pawsey. Three-Dimensional Through-Flow Modelling of Axial Flow Compressor Rotating Stall and Surge. *Aerospace Science and Technology*, Volume 78: 271–279, 2018. ISSN 12709638. doi: 10.1016/j.ast.2018.04.021.

[162] W. B. Roberts, G. K. Serovy, and D. M. Sandercock. Modeling the 3-d flow effects on deviation angle for axial compressor middle stages. *Journal of Engineering for Gas Turbines and Power*, 108(1): 131–137, January 1986. doi: 10.1115/1.3239859.

[163] W. B. Roberts, G. K. Serovy, and D. M. Sandercock. Design point variation of three-dimensional loss and deviation for axial compressor middle stages. *Journal of Turbomachinery*, 110(4):426–433, October 1988. doi: 10.1115/1.3262215.

[164] Safran. Rapport intégré. https://web.safran-group.com/ri2023/, 2023. Accessed on July 2024.

[165] N. Salvat. *Modeling of shaft precessional motions induced by unilateral and frictional blade/casing contacts in aircraft engines*. PhD thesis, McGill University, 2015.

[166] N. Sayari and A. Bölcs. A new throughflow approach for transonic axial compressor stage analysis. In *Proceedings of the ASME Turbo Expo*, volume 1, June 1995. doi: 10.1115/95-GT-195.

[167] M. T. Schobeiri. Advanced compressor loss correlations, part i: Theoretical aspects. *International Journal of Rotating Machinery*, 3(3), 1997. doi: https://doi.org/10.1155/S1023621X9700016X.

[168] J.-F. Simon. *Contribution to Throughflow Modelling for Axial Flow Turbomachines*. PhD thesis, University of Liège, Liège, Belgium, 2007.

[169] J.-F. Simon and O. Léonard. Modeling of 3-D losses and deviations in a throughflow analysis tool. *Journal of Thermal Science*, 16:208–214, 2007. doi: 10.1007/s11630-007-0208-x.

[170] Skywin. MARIETTA: Technico-economical control of manufacturing tolerances. https://www.skywin.be/fr/node/391, 2020. Accessed on July 2024.

[171] B. R. Smith. A Near Wall Model for The k-l Two Equation Turbulence Model. In *AIIA Conference*, 2386, pages 1–8, 1994. doi: 10.2514/6.1994-2386.

[172] B. R. Smith. Prediction of Hypersonic Shock Wave Turbulent Boundary Layer Interactions with the k-l Two Equation Turbulence Model. In *AIIA Conference: 33rd Aerospace Sciences Meeting and Exhibit*, Paper 95-0232, pages 1–9, 1995.

[173] L. H. Smith. The radial-equilibrium equation of turbomachinery. *Journal of Engineering for Power*, 88(1):1–12, January 1966. doi: 10.1115/1.3678471.

[174] D. A. Spence. Growth of the turbulent wake close behind an aerofoil at incidence. Technical report, Aeronautical Research Council - technical report 125, 1953.

[175] A. Spurr. The prediction of 3D transonic flow in turbomachinery using a combined throughflow and blade-to-blade time marching method. *International Journal of Heat and Fluid Flow*, 2(4): 189–199, 1980. doi: https://doi.org/10.1016/0142-727X(80)90013-2.

[176] J. Starke. The effect of the axial velocity density ratio on the aerodynamic coefficients of compressor cascades. *Journal of Engineering for Power*, 103(1):210–219, January 1981. doi: 10.1115/1.3230700.

[177] Statistica. Number of scheduled passengers boarded by the global airline industry from 2004 to 2022. https://www.statista.com/statistics/564717/airline-industry-passenger-traffic-globally/, 2022. Accessed on July 2024.

[178] S. Stollenwerk and E. Kügeler. Deterministic stress modeling for multistage compressor flowfields. In *Proceedings of the ASME Turbo Expo*, volume 6B, San Antonio, US, 3-7 June 2013. doi: 10.1115/GT2013-94860.

[179] J. A. Storer and N. A. Cumpsty. Tip leakage flow in axial compressors. *Journal of Turbomachinery*, 113(2):252–259, April 1991. doi: 10.1115/1.2929095.

[180] M. Stridh. Modeling of Unsteady Flow Effects in Throughflow Calculations. Master's thesis, Chalmers University of Technology, Gothenburg, Sweden, 2003.

[181] A. Sturmayr. *Evolution of a 3D structured Navier-Stokes solver towards advanced turbomachinery applications*. PhD thesis, Vrije Universiteit Brussel, 2004.

[182] A. Sturmayr and C. Hirsch. Shock representation by Euler throughflow models and comparison with pitch-averaged Navier-Stokes solutions. In *14th Conference of the International Society for Air Breathing Engines*, 1999.

[183] W. C. Swan. A practical method of predicting transonic-compressor performance. *Journal of Engineering for Power*, 83(3):322–330, July 1961. doi: 10.1115/1.3673194.

[184] International Air Transport Association. Covid-19: Airline industry outlook. https://www.iata.org/en/iata-repository/publications/economic-reports/airline-industry-economic-performance---october-2021---presentation/, 2021. Accessed on July 2024.

[185] W. Thollet. *Body force modeling of fan-airframe interactions*. PhD thesis, University of Toulouse, 2017.

[186] W. Thollet, G. Dufour, X. Carbonneau, and F. Blanc. Body-force modeling for aerodynamic analysis of air intake – fan interactions. *International Journal of Numerical Methods for Heat & Fluid Flow*, 26(7):2048–2065, September 2016. doi: 10.1108/HFF-07-2015-0274.

[187] W. Thollet, G. Dufour, X. Carbonneau, and F. Blanc. Assessment of body force methodologies for the analysis of intake-fan aerodynamic interactions. In *Proceedings of the ASME Turbo Expo*, volume 2C, Seoul, North Korea, June 2016. doi: 10.1115/GT2016-57014.

[188] J.-P. Thomas. *Modélisation des Tensions Circonférentielles en Simulation Méridienne d'Ecoulements en Turbomachines*. PhD thesis, University of Liège, Liège, Belgium, 2012.

[189] P. Tucker. Computation of unsteady turbomachinery flows: Part 1—progress and challenges. *Progress in Aerospace Sciences*, 47(7):522–545, 2011. ISSN 0376-0421. doi: https://doi.org/10.1016/j.paerosci.2011.06.004.

[190] J. Tyacke, N. R. Vadlamani, W. Trojak, R. Watson, Y. Ma, and P. G. Tucker. Turbomachinery simulation challenges and the future. *Progress in Aerospace Sciences*, 110:100554, 2019. ISSN 0376-0421. doi: https://doi.org/10.1016/j.paerosci.2019.100554.

[191] A. S. Ucer and R. P. Shreeve. A viscous axisymmetric throughflow prediction method for multi-stage compressors. In *Proceedings of the ASME Turbo Expo*, Cologne, Germany, 1-4 June 1992.

[192] A. G. van de Wall, J. R. Kadambi, and J. J. Adamczyk. A transport model for the deterministic stresses associated with turbomachinery blade row interactions. *Journal of Turbomachinery*, 122 (4):593–603, 02 2000. doi: 10.1115/1.1312802.

[193] B. Van Leer. Flux-vector splitting for the euler equations for real gases. *Journal of Computational Physics*, 79(1):227–230, 1982. doi: 10.1016/0021-9991(88)90013-7.

[194] B. Van Leer, J. L. Thomas, P. L. Roe, and R. W. Newsome. A comparison of numerical flux formulas for the Euler and Navier-Stokes equations. *AIAA*, 87-1104, 1987.

[195] J. Veres. Axial and centrifugal compressor mean line flow analysis method. In *47th AIAA Aerospace Sciences Meeting Including The New Horizons Forum and Aerospace Exposition AIAA*, volume 1641, Orlando, US, January 2009. doi: 10.2514/6.2009-1641.

[196] S. Vilmin, E. Lorrain, C. Hirsch, and M. Swoboda. Unsteady flow modeling across the rotor/stator interface using the nonlinear harmonic method. In *Proceedings of the ASME Turbo Expo*, volume 6, pages 1227–1237, Barcelona, Spain, May 2006. doi: 10.1115/GT2006-90210.

[197] T. Von Kármán. Compressibility effects in aerodynamics. *Journal of the Aeronautical Sciences*, 8(9): 337–356, 1941. doi: 10.2514/8.10737. URL https://doi.org/10.2514/8.10737.

[198] T. Von Kármán. Über laminare und turbulente reibung. *Journal of Applied Mathematics and Mechanics*, 1.4:233–252, 1967. ISSN 00442267. doi: 10.1002/zamm.19210010401.

[199] D. Wang and S. Zhang. An approximate time domain nonlinear harmonic method for analyzing unsteady flows with multiple fundamental modes. *Journal of Turbomachinery*, 144(12), September 2022. doi: 10.1115/1.4055266.

[200] A. Wiedermann and M. V. Petrovic. Through-flow Modeling of Single- and Two-Shaft Gas Turbines at Wide Operating Range. In *Proceedings of the ASME Turbo Expo*, volume 75, pages 1–9, Oslo, Norway, 11-15 June 2018. doi: 10.1115/GT201875394.

[201] D. C. Wisler. *Advanced Compressor and Fan Systems*. General Electric Aircraft Engine Business Group, 1988.

[202] D. C. Wisler, R. C. Bauer, and T. H. Okiishi. Secondary flow, turbulent diffusion and mixing in axial-flow compressors. *Journal of Turbomachinery*, 109(4), October 1987. doi: 10.1115/1.3262127.

[203] C.-H. Wu. A general through-flow theory of fluid flow with subsoniv and supersonic velocity in turbomachines of arbitrary hub and casing shapes. Technical report, NACA 2302, Washington, US, March 1951.

[204] C.-H. Wu. A general theory of three-dimensional flow in subsonic and supersonic turbomachines of axial, radial, and mixed-flow types. Technical report, NACA 2604, Washington, US, January 1952.

[205] D. Wu, H. Wang, K. Zhang, B. Zhao, and X. Lin. Research on adaptive cnc machining arithmetic and process for near-net-shaped jet engine blade. *Journal of Intelligent Manufacturing*, 31(3): 717–744, 2020. doi: 10.1007/s10845-019-01474-z.

[206] L. Xu. Assessing viscous body forces for unsteady calculations. *Journal of Turbomachinery*, 125(3): 425–432, August 2003. doi: 10.1115/1.1574823.

[207] Z. Yao and C. Hirsch. Throughflow model using 3D Euler or Navier-Stokes solver. In *European Conference on Turbomachinery Fluid dynamics and Thermodynamics*, Erlangen, Germany, 1-3 March 1995.

[208] H. Zeng, X. Zheng, and M. Vahdati. A method of stall and surge prediction in axial compressors based on three-dimensional body-force model. *Journal of Engineering for Gas Turbines and Power*, 144(3):031021, January 2022. doi: 10.1115/1.4053103.

[209] X. Zheng and H. Yang. End-wall boundary layers and blockages of multistage axial compressors under different conditions. *Journal of Propulsion and Power*, 33(4):908–916, 2017. doi: 10.2514/1.B36251.

Appendix A

Compressible flows

Perfect gaz

In the case of the calorically perfect gas, the pressure p is given by

$$p = \rho r_{gas} T, \tag{A.1}$$

where r_{gas} is the gas constant, and the specific internal energy E and enthalpy H by

$$E = c_v T \quad \text{and} \quad H = E + \frac{p}{\rho} = \left(c_v + r_{gas}\right) T = c_p T \ , \tag{A.2}$$

where c_v and c_p are the constant specific heat capacity at constant volume and at constant pressure respectively. They are linked to the gas constant by

$$r_{gas} = c_p - c_v \ . \tag{A.3}$$

The behaviour of the gas is represented by the non-dimensional ratio of the heat capacities

$$\gamma = \frac{c_p}{c_v}. \tag{A.4}$$

Air is almost entirely composed of the bi-atomic gases N_2 and O_2 and therefore $\gamma = 7/5$. The molar weight is about $30\,\mathrm{g\,mol^{-1}}$ so that $R \approx 287.058\,\mathrm{J\,kg^{-1}\,K^{-1}}$. Then the heat capacities becomes for air

$$c_v = \frac{r_{gas}}{\gamma - 1} \approx 718\,\mathrm{J\,kg^{-1}\,K^{-1}} \quad \text{and} \quad c_p = \frac{\gamma r_{gas}}{\gamma - 1} \approx 1005\,\mathrm{J\,kg^{-1}\,K^{-1}}. \tag{A.5}$$

Finally, the total quantities are given by

$$E_t = E + \frac{V^2}{2} = c_v T + \frac{V^2}{2} \quad \text{and} \quad H_t = H + \frac{V^2}{2} = E_t + \frac{p}{\rho} = c_p T + \frac{V^2}{2}. \tag{A.6}$$

Newtonian Fluid

A Newtonian fluid is a fluid for which the viscous stresses are linearly proportional to the local strain rate. The proportionality constant, i.e. the dynamic viscosity μ, is defined by the Sutherland's law, as

$$\mu = \frac{\beta_{\text{gas}}\sqrt{T}}{1 + C_{\text{gas}}/T}\,, \tag{A.7}$$

where β_{gas} and C_{gas} are two parameters depending on the nature of the considered gas.

Moreover, the thermal conductivity k is proportional to the dynamic viscosity by

$$k = \frac{\gamma r_{gas}}{\gamma - 1}\frac{\mu}{\text{Pr}_{\text{gas}}}\,, \tag{A.8}$$

where Pr_{gas} is the Prandtl number. The gas parameters are specified for air at standard atmosphere conditions.

Entropy

The entropy is a variable of state given by the Gibbs relation,

$$ds = \frac{dH}{T} - \frac{v}{T}dp = c_p\frac{dT}{T} - r_{gas}\frac{dp}{p}, \tag{A.9}$$

where $v = \frac{1}{\rho}$ is the specific volume. For a calorically perfect gas, the entropy is given by

$$s_2 - s_1 = c_p \ln\frac{T_2}{T_1} - r_{gas}\ln\frac{p_2}{p_1} = r_{gas}\left(\frac{\gamma}{\gamma-1}\ln\frac{T_2}{T_1} - \ln\frac{p_2}{p_1}\right) = r_{gas}\ln\left[\frac{p_1}{p_2}\cdot\left(\frac{T_2}{T_1}\right)^{\frac{\gamma}{\gamma-1}}\right]. \tag{A.10}$$

Isentropic flow

An isentropic flow is an adiabatic and reversible process so that

$$dE = \delta q + \delta w = 0 - pdv = -pdv\,. \tag{A.11}$$

As a result, $ds = 0$ and Eq. A.10 becomes

$$\frac{p_2}{p_1} = \left(\frac{\rho_2}{\rho_1}\right)^{\gamma} = \left(\frac{T_2}{T_1}\right)^{\gamma/(\gamma-1)} \quad \text{or} \quad pv^{\gamma} = \text{cst}\,. \tag{A.12}$$

The speed of sound is given by $a = \sqrt{\gamma r_{gas} T}$. Moreover, from the energy conservation for an adiabatic flow,

$$c_pT + \frac{V^2}{2} = c_pT_0 = \text{cst} \quad \text{or} \quad \frac{\gamma r_{gas}T}{\gamma-1} + \frac{V^2}{2} = \frac{a^2}{\gamma-1} + \frac{V^2}{2} = \frac{a_0^2}{\gamma-1} = \text{cst}, \tag{A.13}$$

the following relations are found:

$$\frac{T_t}{T} = 1 + \frac{\gamma - 1}{2}\mathrm{M}^2\,, \qquad \frac{p_t}{p} = \left(1 + \frac{\gamma - 1}{2}\mathrm{M}^2\right)^{\gamma/(\gamma-1)}\,, \quad \frac{\rho_t}{\rho} = \left(1 + \frac{\gamma - 1}{2}\mathrm{M}^2\right)^{1/(\gamma-1)}\,. \tag{A.14}$$

Rankine-Hugoniot equations

For upstream Mach numbers $M_1 < 5$, an oblique shock over a wedge is weak, and its angle α satisfies the transcendental equation

$$\cot\alpha = \frac{\tan\Theta}{2}\frac{\mathrm{M}_1^2(\gamma + \cos 2\alpha) + 2}{\mathrm{M}_1^2\sin^2\alpha - 1}\,, \tag{A.15}$$

where Θ is the wedge angle and α the shock angle. By applying the normal shock relationships for the components of the velocity or Mach number normal to the shock,

$$\mathrm{M}_{\mathrm{n1}} = \mathrm{M}_1 \sin\alpha \quad \text{and} \quad \mathrm{M}_{\mathrm{n2}} = \mathrm{M}_2 \sin(\alpha - \Theta)\,, \tag{A.16}$$

and considering continuous tangential velocity across the shock, an exact solution can be obtained. Across a shock, the upstream quantities (1) and the downstream quantities (2) are linked by [113]

$$\begin{aligned} M_2^2 &= \frac{1 + [(\gamma-1)/2]M_1^2}{\gamma M_1^2 - (\gamma-1)/2}\,, \\ \frac{\rho_2}{\rho_1} = \frac{u_1}{u_2} &= \frac{(\gamma+1)M_1^2}{2 + (\gamma-1)M_1^2}\,, \\ \frac{p_2}{p_1} &= 1 + \frac{2\gamma}{\gamma+1}\left(M_1^2 - 1\right)\,, \\ \frac{T_2}{T_1} = \frac{H_2}{H_1} &= \left[1 + \frac{2\gamma}{\gamma+1}\left(M_1^2 - 1\right)\right]\frac{2 + (\gamma-1)M_1^2}{(\gamma+1)M_1^2}\,. \end{aligned} \tag{A.17}$$

Appendix B

One-dimensional solver for supersonic flows

Finite Volume solver

The set of averaged equations 2.26 defining the supersonic flow can be rewritten in the following conservative form:

$$\frac{\partial \overline{\mathbf{U}}}{\partial t} + \frac{\partial \overline{\mathbf{F}}}{\partial x} = \overline{\mathbf{S}}\,, \tag{B.1}$$

with

$$\overline{\mathbf{U}} = b \begin{bmatrix} \overline{\rho} \\ \overline{\rho}\widetilde{V}_x \\ \overline{\rho}\widetilde{V}_y \\ \overline{\rho}\widetilde{E}_t \end{bmatrix}, \quad \overline{\mathbf{F}} = b \begin{bmatrix} \overline{\rho}\widetilde{V}_x \\ \overline{\rho}\widetilde{V}_x\widetilde{V}_x + \overline{p} \\ \overline{\rho}\widetilde{V}_y\widetilde{V}_x \\ \overline{\rho}\widetilde{H}_t\widetilde{V}_x \end{bmatrix}, \quad \overline{\mathbf{S}} = - \begin{bmatrix} 0 \\ p\Big|_{y_0} \frac{\partial y_0}{\partial x} + \frac{\partial}{\partial x}\left(b\overline{\rho V_x'' V_x''}\right) \\ [p]_{y_0}^{y_1} + \frac{\partial}{\partial x}\left(b\overline{\rho V_y'' V_x''}\right) \\ \frac{\partial}{\partial x}\left(b\overline{\rho H_t'' V_x''}\right) \end{bmatrix}. \tag{B.2}$$

This set of equations is solved by the finite volume method. This technique is based on the integral form of Eq. B.1. This formulation is conservative. The computational domain is divided into cell-centered control volumes Φ to which the conservation principles are applied:

$$\int_{\Phi} \frac{\partial \overline{\mathbf{U}}}{\partial t}\, d\Phi + \int_{\Phi} \frac{\partial \overline{\mathbf{F}}}{\partial x}\, d\Phi = \int_{\Phi} \overline{\mathbf{S}}\, d\Phi. \tag{B.3}$$

The application of the Gauss's theorem leads to

$$\frac{\partial}{\partial t} \int_{\Phi} \overline{\mathbf{U}}\, d\Phi + \oint_{\Sigma} \overline{\mathbf{F}} n_x\, d\Phi = \int_{\Phi} \overline{\mathbf{S}}\, d\Phi, \tag{B.4}$$

where n_x is the x-component of the normal to the contour Σ. Finally, if Σ is equal to the sum of the N_i segments constituting the edge of the element i, the equations are discretized as

$$\frac{\partial \overline{\mathbf{U}}_i}{\partial t} + \frac{1}{\Phi} \sum_{j=1}^{N_i} \int_{\Sigma_j} \overline{\mathbf{F}} n_x \, d\Sigma = \overline{\mathbf{S}}_i, \tag{B.5}$$

where $\overline{\mathbf{U}}_i$ and $\overline{\mathbf{S}}_i$ represent the averaged values over the cell i:

$$\overline{\mathbf{U}}_i = \frac{1}{\Phi_i} \int_{\Phi_i} \overline{\mathbf{U}} \, d\Phi_i, \quad \overline{\mathbf{S}}_i = \frac{1}{\Phi_i} \int_{\Phi_i} \overline{\mathbf{S}} \, d\Phi_i \; . \tag{B.6}$$

Since the problem is 1-D, the preceding equations can be written

$$\frac{\partial \overline{\mathbf{U}}_i}{\partial t} = -\frac{\overline{\mathbf{f}}_{i+\frac{1}{2}} - \overline{\mathbf{f}}_{i-\frac{1}{2}}}{\Delta x_i} + \overline{\mathbf{S}}_i, \tag{B.7}$$

where $\overline{\mathbf{f}}$ and Δx are the face-averaged fluxes and the cell length. This relation is still exact but **spatial schemes** have to be used in order to approximate the convective fluxes using neighbour cell values. Therefore the solver compute the solution of

$$\frac{\partial \overline{\mathbf{U}}_i}{\partial t} = -\frac{\overline{\mathbf{f}^*}_{i+\frac{1}{2}} - \overline{\mathbf{f}^*}_{i-\frac{1}{2}}}{\Delta x_i} + \overline{\mathbf{S}}_i, \tag{B.8}$$

where $\overline{\mathbf{f}}^*$ are the numerical cell-averaged fluxes.

These convective fluxes are computed using a flux-vector splitting schemes. This upwind method account for the the direction of wave propagation. In this case, the van Leer's scheme [193] is used: the convective fluxes are split into a positive and a negative part, that is,

$$\overline{\mathbf{f}^*}_{i+\frac{1}{2}} = \overline{\mathbf{f}^+}_{i+\frac{1}{2}} \left(\overline{\mathbf{U}}_L \right) + \overline{\mathbf{f}^-}_{i+\frac{1}{2}} \left(\overline{\mathbf{U}}_R \right). \tag{B.9}$$

$\overline{\mathbf{f}}^+$ corresponds to the information propagating from the left to the right and depends on a left state $\overline{\mathbf{U}}_L$ while $\overline{\mathbf{f}}^-$ corresponds to the information propagating from the right to the left and depends on a right state $\overline{\mathbf{U}}_R$, as shown in Fig. B.1. The splitting operation is done according to the Mach number normal

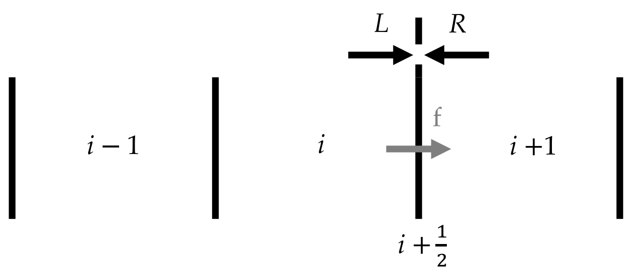

Figure B.1: Left and right state at cell $i + \frac{1}{2}$ for a cell-centered discretization.

to the face considered, i.e.

$$(\widetilde{\mathrm{M}}_n)_{i+\frac{1}{2}} = \left(\frac{\widetilde{V_n}}{\widetilde{a}}\right)_{i+\frac{1}{2}}, \tag{B.10}$$

where $\widetilde{V}_n = \widetilde{V}_x n_x + \widetilde{V}_y n_y$. This Mach number is obtained from

$$(\widetilde{\mathrm{M}}_n)_{i+\frac{1}{2}} = \widetilde{\mathrm{M}}_L^+ + \widetilde{\mathrm{M}}_R^-, \tag{B.11}$$

where the split Mach numbers are given by

$$\widetilde{\mathrm{M}}_L^+ = \begin{cases} \widetilde{\mathrm{M}}_L & \text{if } \widetilde{\mathrm{M}}_L \geq 1, \\ \frac{1}{4}\left(\widetilde{\mathrm{M}}_L + 1\right)^2 & \text{if } |\widetilde{\mathrm{M}}_L| < 1, \\ 0 & \text{if } \widetilde{\mathrm{M}}_L \leq -1, \end{cases} \tag{B.12}$$

and

$$\widetilde{\mathrm{M}}_R^- = \begin{cases} 0 & \text{if } \widetilde{\mathrm{M}}_R \geq 1, \\ \frac{1}{4}\left(\widetilde{\mathrm{M}}_R - 1\right)^2 & \text{if } |\widetilde{\mathrm{M}}_R| < 1, \\ \widetilde{\mathrm{M}}_R & \text{if } \widetilde{\mathrm{M}}_R \leq -1. \end{cases} \tag{B.13}$$

If $-1 < \mathrm{M}_n < 1$ (subsonic flow), the flux parts are defined as

$$\overline{\mathbf{f}}^{\pm}_{i+\frac{1}{2}} = \pm\frac{\overline{\rho}\widetilde{a}}{4}\left(1 \pm \widetilde{M}_n\right)^2 b \begin{pmatrix} 1 \\ \widetilde{V}_x \pm \left(2\widetilde{a} \mp \widetilde{V}_n\right)\frac{n_x}{\gamma} \\ \widetilde{V}_y \\ \frac{\widetilde{a}^2}{\gamma+1}\left(\frac{2}{\gamma-1} \pm 2\widetilde{M}_n - \widetilde{M}_n^2\right) + \frac{\widetilde{V}_x^2+\widetilde{V}_y^2}{2} + \frac{k}{2} \end{pmatrix}. \tag{B.14}$$

The kinetic energy of the spatial stress $k = \frac{1}{\overline{\rho}}\left(\overline{\rho V_x'' V_x''} + \overline{\rho V_y'' V_y''}\right)$ has been added for consistency with the definition of the averaged total enthalpy that is used in the fluxes $\overline{\mathbf{F}}$:

$$\widetilde{H_t} = \widetilde{h} + \frac{1}{2}\widetilde{V_k}\widetilde{V_k} + \frac{1}{2}\frac{\overline{\rho V_k'' V_k''}}{\overline{\rho}}, \tag{B.15}$$

where h is the enthalpy. More generally, the corresponding spatial stress terms must also be included in the non-linear equations presented above, i.e. Eqs. B.14-B.10 to ensure a fully consistent averaged formulation. For supersonic flow, the fluxes reduce to

$$\overline{\mathbf{f}}^{+}_{i+\frac{1}{2}} = \overline{\mathbf{f}}(\overline{\mathbf{U}}_L) \qquad \overline{\mathbf{f}}^{-}_{i+\frac{1}{2}} = 0 \qquad \text{if } \widetilde{\mathrm{M}}_n \geq +1, \tag{B.16}$$

$$\overline{\mathbf{f}}^{+}_{i+\frac{1}{2}} = 0 \qquad \overline{\mathbf{f}}^{-}_{i+\frac{1}{2}} = \overline{\mathbf{f}}(\overline{\mathbf{U}}_R) \qquad \text{if } \widetilde{\mathrm{M}}_n \leq -1. \tag{B.17}$$

The van Leer's scheme is well adapted for the Euler equations. However, it performs not so well in the case of the Navier-Stokes equations [194, 80]. In order to compute the fluxes, the left and the right states of flow variables first have to be interpolated to cell faces. The interpolation method used is the Monotonic Upstream Scheme for Conservation Laws (MUSCL) [45] reconstruction, which leads to the following expressions in 1-D:

$$\overline{\mathbf{U}}^L_{i+\frac{1}{2}} = \overline{\mathbf{U}}_i + \frac{\Delta x_i}{4\overline{\Delta x}}\left[\left(\overline{\mathbf{U}}_i - \overline{\mathbf{U}}_{i-1}\right)\left(\frac{1+\frac{\epsilon}{2}-\chi\frac{\Delta x_i}{\overline{\Delta x}}}{1-\frac{\epsilon}{2}}\right) + \left(\overline{\mathbf{U}}_{i+1} - \overline{\mathbf{U}}_i\right)\left(\frac{1-\frac{\epsilon}{2}+\chi\frac{\Delta x_i}{\overline{\Delta x}}}{1+\frac{\epsilon}{2}}\right)\right], \tag{B.18}$$

$$\overline{\mathbf{U}}^R_{i-\frac{1}{2}} = \overline{\mathbf{U}}_i - \frac{\Delta x_i}{4\overline{\Delta x}}\left[\left(\overline{\mathbf{U}}_i - \overline{\mathbf{U}}_{i-1}\right)\left(\frac{1+\frac{\epsilon}{2}+\chi\frac{\Delta x_i}{\overline{\Delta x}}}{1-\frac{\epsilon}{2}}\right) + \left(\overline{\mathbf{U}}_{i+1} - \overline{\mathbf{U}}_i\right)\left(\frac{1-\frac{\epsilon}{2}-\chi\frac{\Delta x_i}{\overline{\Delta x}}}{1+\frac{\epsilon}{2}}\right)\right], \tag{B.19}$$

where

$$\begin{aligned}\overline{\Delta x} &= \frac{1}{2}\left(\Delta x_{i+\frac{1}{2}} + \Delta x_{i-\frac{1}{2}}\right) = \frac{1}{2}\left(\frac{\Delta x_i + \Delta x_{i+1}}{2} + \frac{\Delta x_i + \Delta x_{i-1}}{2}\right),\\ \epsilon &= \frac{\Delta x_{i+\frac{1}{2}} - \Delta x_{i-\frac{1}{2}}}{\overline{\Delta x}},\\ \Delta x_i &= x_{i+\frac{1}{2}} - x_{i-\frac{1}{2}}.\end{aligned} \tag{B.20}$$

The parameter χ qualifies the reconstruction: the reconstruction is second-order accurate, i.e. an exact approximation of a linear function, except when χ equals $1/3$: the reconstruction is third-order accurate, which means it is an exact approximation of a quadratic function.

Temporal scheme

For simplicity, an explicit temporal scheme is used to reach the steady state (time-marching). The explicit euler schemes yields

$$\frac{\overline{\mathbf{U}}_i^{n+1} - \overline{\mathbf{U}}_i^{n}}{\Delta t} = -\frac{\overline{\mathbf{f}}^{*n}_{i+\frac{1}{2}} - \overline{\mathbf{f}}^{*n}_{i-\frac{1}{2}}}{\Delta x} + \overline{\mathbf{S}}_i, \tag{B.21}$$

so that

$$\overline{\mathbf{U}}_i^{n+1} = \overline{\mathbf{U}}_i^{n} - \frac{\Delta t}{\Delta x}\left(\overline{\mathbf{f}}^{*n}_{i+\frac{1}{2}} - \overline{\mathbf{f}}^{*n}_{i-\frac{1}{2}}\right) + \Delta t\overline{\mathbf{S}}_i. \tag{B.22}$$

Boundary conditions

Because the flow is supersonic, all the characteristics are positive and the flow boundary conditions are only imposed at the inlet. Since the MUSCL reconstruction is a 3-point stencil, the cell-centered approach leads to define additional nodes at boundaries, as shown in Fig. B.2). These nodes are defined so that $\Delta x_a = 0 \Leftrightarrow x_{a-\frac{1}{2}} = x_a = x_{a+\frac{1}{2}} = x_{i-\frac{1}{2}}$ In this case, all the flow variables are known at the inlet node a so that the right state of the first face is known: $\overline{\mathbf{U}}^R_{i-\frac{1}{2}} = \overline{\mathbf{U}}_a$. On the other hand, the left state of the second face $\overline{\mathbf{U}}^L_{i+\frac{1}{2}}$ can be computed automatically by Eq. B.18 because the layout of boundary nodes is taken into account by the coefficients. At the outlet of the domain, no flow variable

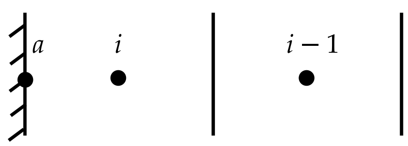

Figure B.2: Boundary conditions for MUSCL reconstruction.

is imposed since the flow is supersonic. An upwind formulation of the MUSCL reconstruction is therefore used for the last finite volume:

$$\overline{\mathbf{U}}^{L}_{i+\frac{1}{2}} = \overline{\mathbf{U}}_i + \frac{\Delta x_i}{4\Delta x}\left(\overline{\mathbf{U}}_i - \overline{\mathbf{U}}_{i-1}\right)\left(\frac{1+\frac{\epsilon}{2}-\chi\frac{\Delta x_i}{\Delta x}}{1-\frac{\epsilon}{2}}\right), \tag{B.23}$$

$$\overline{\mathbf{U}}^{R}_{i-\frac{1}{2}} = \overline{\mathbf{U}}_i - \frac{\Delta x_i}{4\Delta x}\left(\overline{\mathbf{U}}_i - \overline{\mathbf{U}}_{i-1}\right)\left(\frac{1+\frac{\epsilon}{2}+\chi\frac{\Delta x_i}{\Delta x}}{1-\frac{\epsilon}{2}}\right). \tag{B.24}$$

Averaging procedure for the 2-D flow-field

In order to do a comparison with the solution of the averaged equations, the exact two-dimensional flow field has to be averaged according to Eq. 2.17 and Eq. 2.19. In this case, these averaging process become

$$\overline{Q} = \frac{1}{b}\left(Q_1\Delta y_1 + Q_2\Delta y_2\right) \quad \text{and} \quad \widetilde{Q} = \frac{1}{b\overline{\rho}}\left(\rho_1 Q_1\Delta y_1 + \rho_2 Q_2 \Delta y_2\right). \tag{B.25}$$

The definition of Δy_1 and Δy_2 is shown in Fig. B.3. Then, for consistency with the finite volume formulation, these averaged values have to be averaged over the associated n cells according to Eq. B.6. The averaged flow field is thus fully known.

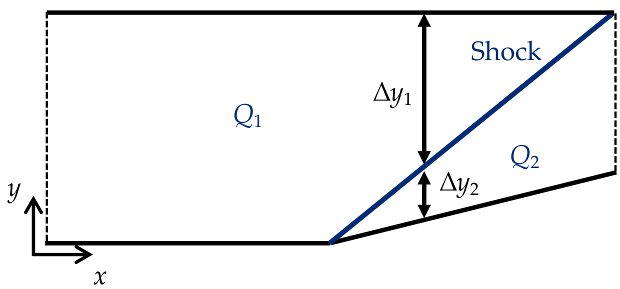

Figure B.3: Flow over a wedge problem definition.

The wall forces have also to be averaged over the elements using Eq. B.6. In this case, the values of the flow variables are constant along the upper and the lower walls. Therefore, the value at element mid-point can be directly used. On the other hand, the stresses have to be computed to close the averaged equations for the simulation. They appear as a flux so that the finite volume approach has to be taken into account for consistency. The procedure is:

- knowing the averaged variables through Eq. B.25, the fluctuations can be computed on the computational domain,
- then, the spatial stresses are computed at the cells edges.
- Finally, the fluxes are computed using the finite volume discretization and the edges values.